uOttawa

Novel Approaches for Interpretation of the THMC behaviors of Unfrozen and Frozen Unsaturated Soils

YAO LI

Thesis submitted to the
University of Ottawa
in partial fulfillment of the requirements
for the Doctorate in Philosophy degree in Civil Engineering

Department of Civil Engineering
Faculty of Engineering
University of Ottawa

ABSTRACT

The soils in arid and semi-arid regions are typically in an unsaturated state. Three phases; namely solids (i.e., soil), liquid (i.e., water) and pore-air (i.e., gas) commonly exist in unsaturated soils. Soil mechanics for unsaturated soils are widely used towards understanding the hydro-mechanical behavior of unsaturated soils. The major focus of these studies during the past three decades is directed towards interpreting and predicting the flow, shear strength and volume change behaviors of unsaturated soils using the saturated soil properties and the soil water characteristic curve (SWCC) as a tool. However, for rigorous understanding, the coupled influence of thermo-hydro-mechanical-chemo (THMC) behavior of unsaturated soils is required. Such studies would be valuable for interpreting the influence of climate changes on the fundamental behavior of both frozen and unfrozen soils. To achieve this goal, the focus of this PhD thesis has been directed towards investigating the THMC behaviors of unsaturated soils with emphasis on water retention behaviors for unsaturated unfrozen and frozen soils.

A multi-modal or bimodal SWCC can be used as an effective tool for developing a fundamental understanding and predicting the behavior of unsaturated soils considering the influence of macro and microstructure. Such an approach will be valuable for all soils, including unimodal SWCC which is a special case of bimodal SWCC. For addressing this objective, a hypothesis is introduced to link the soil pore size distribution (PoSD) curve to the bimodal SWCC. The relationships between the soil PoSD curve and the bimodal SWCC equations are discussed extending the proposed hypothesis using two equations: namely, the rigid equation and the simplified equation for the two well-known traditional unimodal SWCC equations from the literature. The calibration processes built for both the equations performance was evaluated for various types of soils. The results suggest that both the modified equations provide excellent comparison with the measured data. The rigid equations provide comprehensive information about the macropores and the micropores of the bimodal SWCC; however, the simplified equations facilitate a flexible yet simple curve-fitting process. The relationships between the proposed equations and the available methods for the bimodal SWCC from the literature are also discussed. In addition, a technique is developed based on regression analysis to estimate the key features for bimodal SWCCs.

Novel models are derived from the pore-size distribution (PoSD) curve of the SWCC to predict the SWCCs for coarse- and fine-grained soils and linked to the well-known SWCC fitting equations from literature. Three simple methods are proposed for predicting the scanning SWCCs of coarse-grained soils, extending this philosophy. A modified SWCC model is built based on the theoretical background developed for the PoSD curve that can predict the SWCC of fine-grained soils taking account influence of the initial water content and stress state. In addition, a coupled SWCC model is proposed as a part of this study for explaining the influence of multiple soil parameters.

To model soil freezing characteristics curve (SFCC) of unsaturated frozen soils, SFCC models with well-defined model parameters are developed extending thermodynamics principles and are linked to well-known SWCC models from the literature. Various zones in the SFCC are discussed along with providing rational explanation for the hysteretic effects using the proposed models. In addition, comparisons are provided between the measured and the predicted results using the proposed models successfully highlighting the effects of salinity and the initial water content on the frozen unsaturated soils.

Finally, the proposed generalized THMC framework is successfully used to explain the complex behaviors of unsaturated soils. The developed models are promising and can be used as valuable tools for numerical modeling of the THMC behaviors of unsaturated soils in all environments.

ACKNOWLEDGMENTS

The studies presented in this Ph.D. thesis were conducted at the Department of Civil Engineering, University of Ottawa under the supervision of Prof. Sai K. Vanapalli. I would like to express my deepest appreciation to Dr. Vanapalli as well as his family for ongoing mentorship and significant support. Dr. Vanapalli has a humble and sincere attitude to research, and his optimistic philosophy towards both research and life has been a precious and unforgettable memory to me. His guidance and consistent feedback were indispensable throughout my Ph.D. journey, particularly during the pandemic, and without his support, this thesis would not have been possible.

The joint Ph.D. study program offers opportunities to learn advanced courses from both University of Ottawa and Carleton University. Prof. Siva Sivathayalan, Prof. Mohammad Rayhani, and Prof. Hossein Bonakdari provide excellent courses that benefit a lot.

The financial supports received from China Scholarship Council (CSC) and University of Ottawa joint doctoral scholarship, the Natural Sciences and Engineering Research Council of Canada (NSERC) are gratefully acknowledged.

I would like to thank thesis committee members, Prof. Annan Zhou, Prof. Rozalina Dimitrova, Prof. Julio Angel Infante Sedano, and Prof. Mehdi Pouragha. I would like to sincerely appreciate all teachers, who challenge and help the students to get better. My appreciations extend to faculty officers, Luc and Jean-Claude. Many thanks also to my colleagues and friends from our research group: Junping, Penghai, Ruixia, Xiuhan, Mengxi, Mingshu, Xinting, Hongyu, N'eem Tavakkoli, Maha Saleh, Xingyi, Junjie, Pan, Aolin, Xinye, Roberto Alves, Ziwen, Hao, and Alpesh.

Most importantly, none of this could have happened without my family. I am extremely grateful to my parents for providing me with unfailing support and continuous encouragement throughout my years of study. I would also like to thank my grandmother, who always offered her encouragement and support through calls.

TABLE OF CONTENTS

LIST OF FIGURES

LIST OF TABLES

CHAPTER 1

Introduction

1.1 Background

Unsaturated soils are widely distributed around the world, especially in arid and semi-arid regions (Fredlund and Rahardjo 1993). Figure 1.1 shows a nine-month global precipitation map in the year 2022 (data source: drought.gov). Red areas in the map have been increasing highlighting decrease in the precipitation in various regions compared to the earlier years. Many of such highlighted regions are suffering from extreme climate events (e.g., hotter weather and less precipitation) (Gens 2010) due to the influence of global climate patterns in recent decades. Due to this reason, the natural ground water table (GWT) depth has been steadily decreasing in such regions. The soils above the GWT are typically characterized as unsaturated soils and their behavior is significantly different from saturated soils (Fredlund and Rahardjo 1993). Many other soils such as compacted soils, expansive soils, collapsible and residual soils are typically in a state of unsaturated condition. Several researchers have contributed towards better understanding the mechanics of unsaturated soils to analyze the hydro-mechanical behaviors of the soils above the GWT (e.g., Bishop 1959, Alonso et al. 1990, Fredlund and Rahardjo 1993, Vanapalli et al. 1996, Wheeler et al. 2003, Lu and Likos 2006, Sheng et al. 2008, Delage et al. 2010, Tang et al. 2011, Ng et al. 2020).

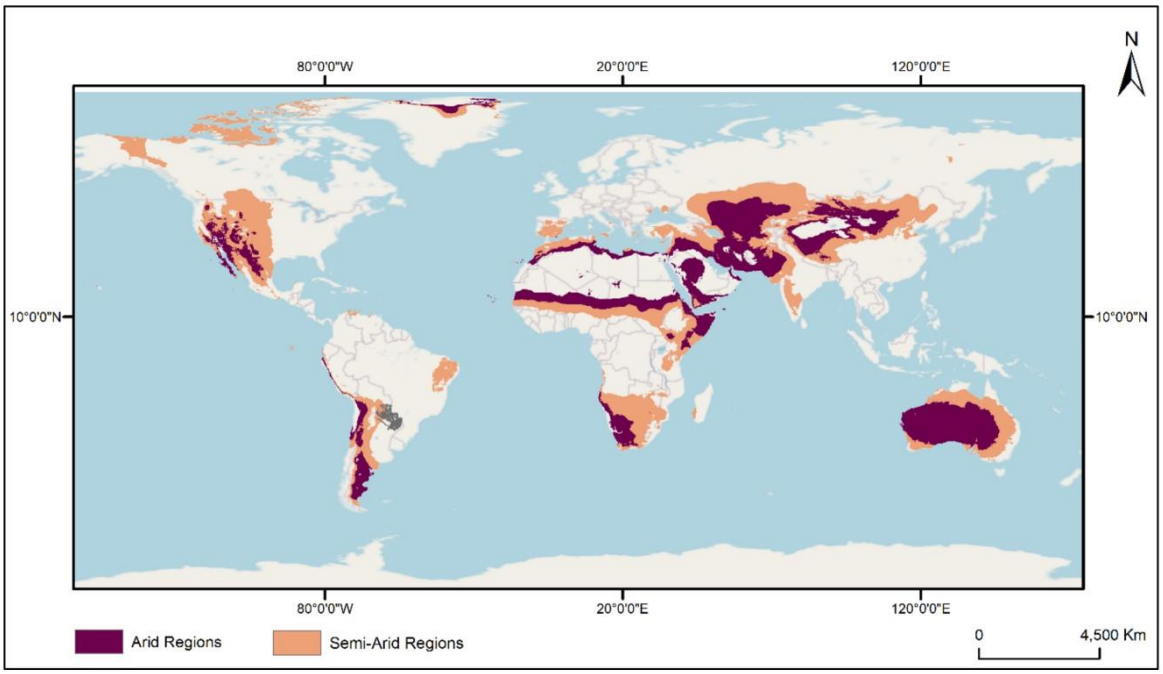

Figure 1.1 Global distribution of arid and semi-arid regions (Collected from Qader et al. 2021).

Hydro-mechanical behavior of unsaturated soils are signficantly different in comparison to saturated soils (Bishop 1959, Fredlund and Morgenstern 1977, Houlsby 1997, Lu et al. 2010, Alonso et al. 2010). Unsaturated soils constitute of three phases; namely, solid phase (i.e., soil solids), liquid phase (i.e., pore-water), and gaseous phase (i.e., pore-air). More importantly, soils above the GWT (i.e., unsaturated soils) have a continuous energy interaction with the atmosphere due to the influence of hydrologic cycles. The distinct responses of soil solids, pore-water and pore-air under different loadings lead to unique behaviors that influence the engineering behavior of unsaturated soils (i.e., flow, volume change, and shear strength behavior) (Fredlund et al. 1994, Vanapalli et al. 1996, Vanapalli et al. 1999, Wheeler et al. 2003, Sun et al. 2007a, Rahardjo et al. 2019).

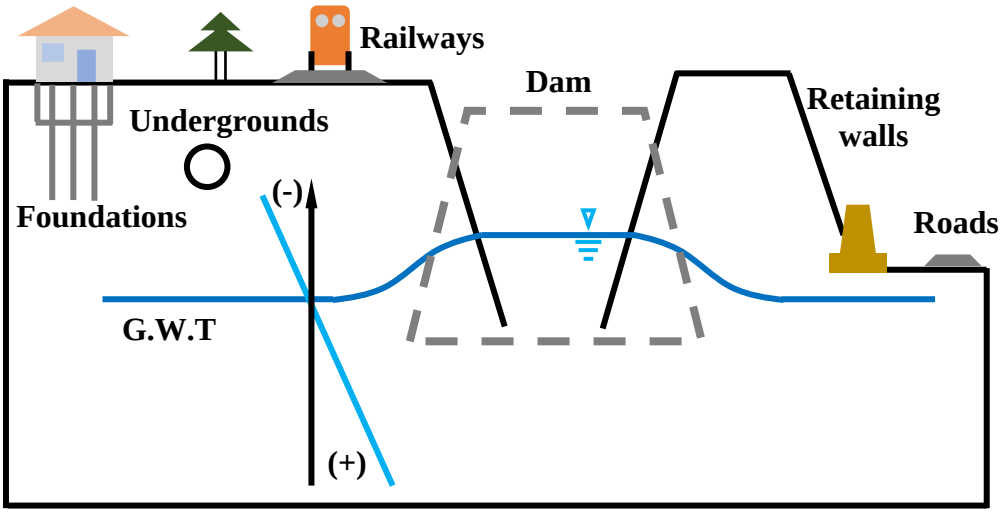

Figure 1.2 Typical infrastructures in unsaturated soils.

Several infrastructures such as shallow and deep foundations, retaining walls, embarkments, pavements are placed or constructed in unsaturated soils, as shown in Figure 1.2. These infrastructures are vital for providing civil facilities that enhance quality of day-to-day activities for humans (e.g., residential and service structures such as hospitals and schools, water supply, drainage facilities using pipe lines, and transporation facilities that include pavements and railways).

The mechanical behavior (i.e., shear strength and volume change) of saturated soils can be reasonably explained using the effective stress equation proposed by Terzaghi (1943), which can be considered as a single stress state variable within the framework of continuum

mechanics. Effective stress, $\boldsymbol{\sigma'}$ is defined as the difference between the total stress $\boldsymbol{\sigma}$ and the pore liquid water pressure $\boldsymbol{u}_{lw}$;

$$\boldsymbol{\sigma}' = \boldsymbol{\sigma} - u^{lw}\boldsymbol{\delta} \tag{1.1}$$

where $\boldsymbol{\delta} = \delta_{ij}$ is Kroneckor delta ($\delta_{ij} = 1$ for $i = j$; $\delta_{ij} = 0$ for $i \neq j$).

Bishop (1959) extended the definition introduced by Terzaghi (1943) for explaining the effective stress in unsaturated soils. The equation below is suggested using total stress $\boldsymbol{\sigma}$, pore-water (liquid) pressure $\boldsymbol{u}^{lw}$, and pore-air pressure $\boldsymbol{u}^{air}$.

$$\boldsymbol{\sigma}' = \boldsymbol{\sigma} - u^{air}\boldsymbol{\delta} + \chi\left(u^{air} - u^{lw}\right)\boldsymbol{\delta}, \quad 0 \leq \chi \leq 1 \tag{1.2}$$

where χ is a factor which is suggested to be a function of degree of saturation.

Some researchers have highlighted limitations of χ factor in explaining experimental results of the mechanical (i.e., volume change and shear strength) behaviour of unsaturated soils (e.g., Jennings and Burland 1962; Bishop and Blight 1963). The factor χ is not only influenced by the degree of saturation of water; but also, due to drying-wetting cycles associated with soil hysteresis (Bishop and Blight 1963). Over the past quarter century, many functions or relationships have been proposed for the factor χ in the literature (e.g., Khalili and Khabbaz 1998; Nuth and Laloui 2008; Lu et al. 2010; Alonso et al. 2010; D'Onza et al. 2011; Zhang and Lu 2020; Niu et al. 2021).

Fredlund and Morgenstern (1977) suggested any two sets of the three independent stress state variables; namely, net normal stress ($\boldsymbol{\sigma}$ - $u^{air}\boldsymbol{\delta}$), effective stress ($\boldsymbol{\sigma}$ - $u^{lw}\boldsymbol{\delta}$), and matrix suction ($u^{air}$ - u^{lw})$\boldsymbol{\delta}$ as shown in Eq. (1.3) can be used for explaining the unsaturated soils behaviors.

$$\begin{Bmatrix} \boldsymbol{\sigma} - u^{air}\boldsymbol{\delta} \\ \left(u^{air} - u^{lw}\right)\boldsymbol{\delta} \end{Bmatrix} \text{ or } \begin{Bmatrix} \boldsymbol{\sigma} - u^{lw}\boldsymbol{\delta} \\ \left(u^{air} - u^{lw}\right)\boldsymbol{\delta} \end{Bmatrix} \text{ or } \begin{Bmatrix} \boldsymbol{\sigma} - u^{air}\boldsymbol{\delta} \\ \boldsymbol{\sigma} - u^{lw}\boldsymbol{\delta} \end{Bmatrix} \tag{1.3}$$

The choice of stress and strain variables is arbitrary (Fredlund and Morgenstern 1977); this approach has been found to be compatible with work conjugate approach proposed by Houlsby (1997) and thermodynamic framework proposed by Borja (2006).

The complex hydro-mechncial behaviors of unsaturated soils can be reasonably explained extending the mechanics of unsaturated soils. For example, as the water height rises above the ground water table, the pore-water and pore-air is different in the capillary and vadose zones. Buckingham (1908) is the pioneering researcher who described the relationship between water content and soil (matric) suction and used it as a tool in explaining flow behavior of unsaturated soils. The relationship between the water content and soil suction is typically refererred to as the soil water characteristics curve (SWCC), soil-water retention curve (SWRC) or soil-mostirue curve (SMC) and is useful in explaining complex hydro-mechanical behavors of unsaturated soils. A typical SWCC is shown in Figure 1.3.

The SWCC has been found to be a valuable tool for understanding the behavior of unsaturated soils in various fields (i.e., soil science, agriculture, hydrology, geotechnical, geo-environmental and mining engineering fields to list a few). The SWCC relationship can be plotted in different ways; between water content (either volumetric or gravimetric) or degree of saturation and soil suction (Fredlund and Rahardjo 1993). Several researchers have used the SWCC relationship for both interpreting and predicting the hydro-mechanical behaviors of unsaturated soils during the last three decades in the geotechnical engineering field (Alonso et al. 1990, Fredlund et al. 1994, Vanapalli et al. 1996, Wheeler et al. 2003, Rahardjo et al. 2019).

Three different zones can be identified in a typical SWCC; namely, boundary effect zone, transition zone and residual zone which arise in a soil due to an increase in soil suction (or decrease in water content) (see Figure 1.3). The influence of pore-water and pore-air pressures induces different hydro-mechanical behavior characteristics in the different zones. The different response in unfrozen unsaturated soils behavior can be attributed to the influence external environment associated with wetting-drying cycles and hysteris effects. Temperature and chemical effects also influence the hydro-mechanical behavior. To establish the relationship between the SWCCs under THMC response, the fundamental relationships among soil solids, soil pores and pore fluids should be rigorously investigated. The need for such relationships are succinctly discussed below.

First, as the soil is formed by solid particles while water and air are stored within soil pores, the link between soil particles and soil pores should be established (i.e., the link between soil grain size distribution curve and pore size distribution curve). Second, after pore size distribtuion is distinguished, the influential factors on pore size as well as pore- water, air and

ice (at low temperature) should be considered. Third, the link btween the amount of pore-water and soil (matric) suction should be built. Most studies related to the SWCCs and their behavior fall within the scope. For example, typical SWCC eqution (e.g., van Genuchten 1980; Fredlund and Xing 1994) provide the direct link between the amount of water in unsaturated soils and soil matric suction with several model paramaters. However, the variance of pore structure, and drying and wetting cycles contribute to the change of water content within the soil significanly.

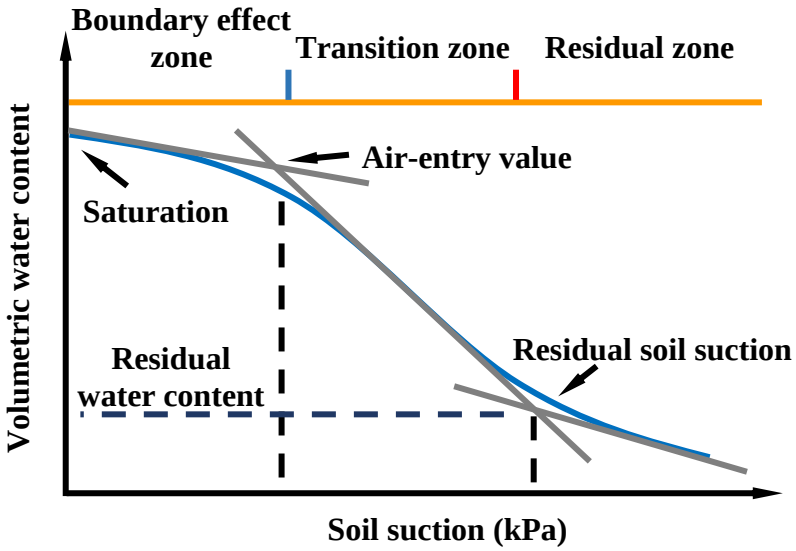

Figure 1.3 Typical soil-water characteristics curve.

At low temperatures, the pore-liquid-water is frozen into ice, the amount of unfrozen water content is gradually changing along with temperature (i.e., soil freezing characteristic curve (SFCC)) as shown in Figure 1.4. The SFCCs also exhibit significant hysteresis behaviors. The unfrozen water content is sensitive to the dissolved salt and initial stress states. Both the SFCC and SWCC constitute powerful tools to understand the temporal and spatial variation of water inside unsaturated soils. For this reason, there is a need to build the links between two curves (e.g., SWCC and SFCC) and develop tools that can provide rational explanation of the behavior of unfrozen and frozen unsaturated soils.

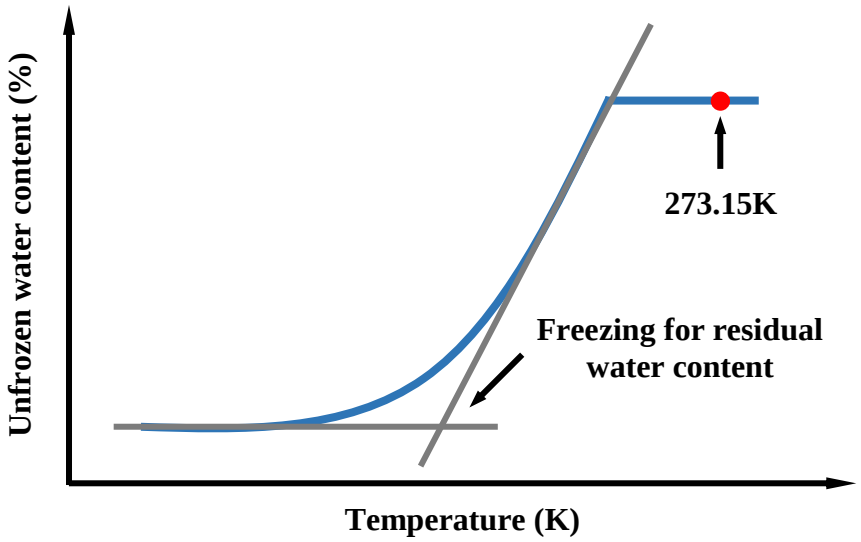

Figure 1.4 Typical soil-freezing characteristics curve.

1.2 Objective, novelty and methodology

The discussion summarized in the earlier paragraphs highlight that both SWCC and SFCC models are key tools to interpret the temporal and spatial distribution of pore-water in unsaturated soils. Such models would provide a valuable platform for understanding the THMC effects on unsaturated soils. For this reason, in this thesis the focus of the investigations were directed towards understanding both the SWCCs and SFCCs behavior considering the influence of THMC effects for achieving comprehensive understanding of the soil behavior in all environments. To achieve this goal, four major novel objectives are addressed through this PhD research program as summarized below:

(i) To develop models for bimodal SWCCs

As the soil is formed by solid particles, and water and air are stored in soil pores, the soil structure influences the SWCC behavior. In other words, soil pore size distribution and the related influential factors should be investigated for rational understanding of the SWCC. Several studies in the literature have suggested that the SWCC can be either unimodal, bimodal or in certain cases multi-modal in nature due to the influence of pore size distribution. Currently, there are several models that have been proposed to highlight unimodal SWCC behavior in the literature. However, models that highlight the links between macropores and micropores in the

bimodal SWCCs are rather limited. There is a need to model bimodal SWCCs within a unified framework for rational understanding of the SWCC behavior. For this reason, in this PhD research, a new method to model bimodal SWCCs based on pore size distribution curve is proposed and the model results are compared with the experimental results in the literature.

(ii) To investigate SWCCs behaviors for both fine- and coarse-grained soils

Several SWCC models are proposed in the literature for both sands and clayey soils; however, there are limited studies that systematically model SWCCs of both fine- and coarse- grained soils considering various influencing parameters. A new model that highlights "ink-bottle" effects on SWCCs of sands is proposed. In addition, models considering the influence of initial water content and stress state effects on the SWCC behavior of fine-grained soils are discussed and modeled.

(iii) To develop SFCC models under THMC effects

The soils near the natural ground surface that are typically in a state of unsaturated condition are exposed to not only wetting and drying cycles but also different (i.e., high or low) temperatures. As discussed earlier, the relationship between temperature (below zero) and unfrozen water content is regarded as soil freezing characteristics curve (SFCC). It is of significance in analyzing the behaviors of frozen soils. The two curves (i.e., SWCC and SFCC) combined provide the water content variation in soil pores that are valuable in understanding the thermo-hydro-mechanical-chemo effects (THMC) of the unsaturated soils. However, there are limited studies that provide a SFCC model that are linked to SWCC models with clear physical meanings of parameters in the literature. For this reason, a set of SFCC models have been developed and linked to the traditional SWCC models. In addition, comparisons are provided for validation purposes using the proposed models with experimental results from the literature.

(iv) To develop generalized THMC framework for unfrozen and frozen unsaturated soils

There are several frameworks available in the literature that focus on the hydro-mechanical behavior of unsaturated soils. However, there is a need for a unified framework for understanding the THMC effects of both unfrozen and frozen unsaturated soils (i.e., for all soil environments). Such a novel framework would be valuable for rigorous understanding, interpretation, and modeling the behavior of unsaturated soils, especially considering the

effects of climate change. In this thesis, a novel thermodynamic framework that highlights the THMC behaviors of unsaturated soils is proposed and validated.

1.3 Layout

This proposal is divided into seven chapters as summarized below.

(i) Chapter 1 presents the background introduction related to the thesis topic, research objectives, and layout of the thesis.

(ii) Chapter 2 presents a comprehensive literature review on modeling SWCCs.

(iii) Chapter 3 proposes models for bimodal SWCCs.

(iv) Chapter 4 presents SWCC models for both fine- and coarse- grained soils.

(v) Chapter 5 proposes a model for SFCCs under THMC effects.

(vi) Appendices in Chapters 4 and 5 present a unified thermodynamic framework for unsaturated soils addressing THMC effects.

(vii) Chapter 6 presents the conclusions and future work.

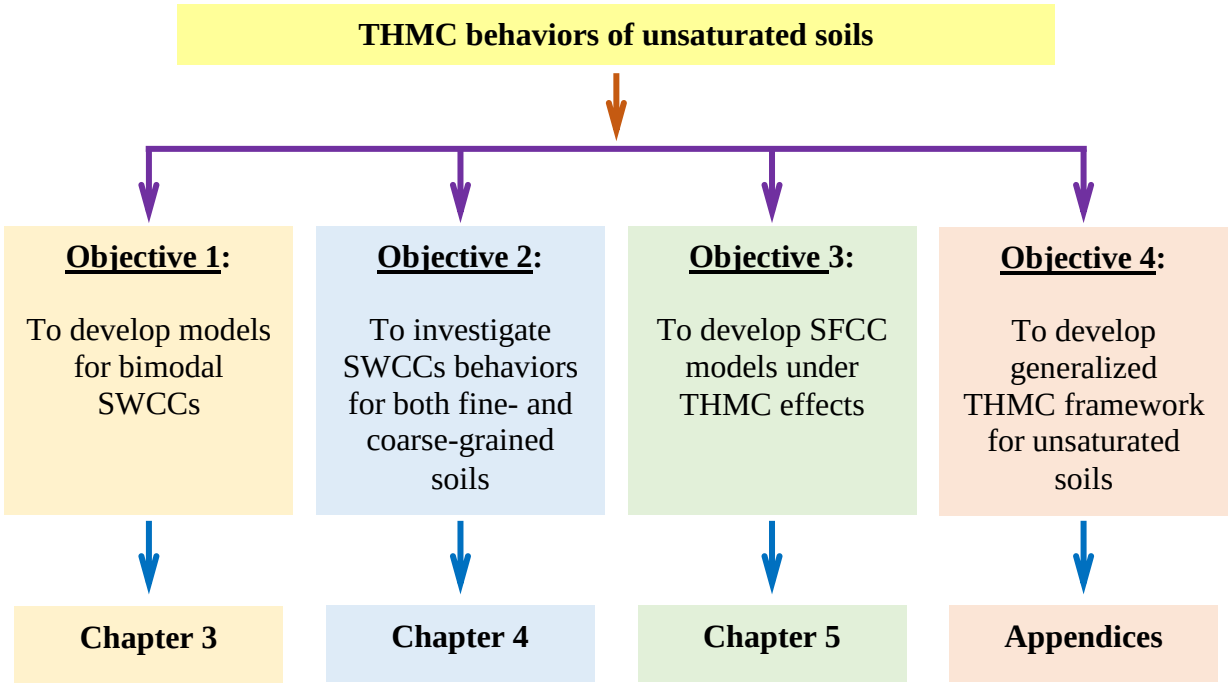

Figure 1.5 Research scope and major objectives of the thesis.

CHAPTER 2

Literature Review

2.1 Introduction

In this chapter, a comprehensive review of methods for modeling the soil-water characteristic curve (SWCC) behavior is summarized. The published studies from the literature are used for discussing methods for interpreting water content variation with respect to soil (matric) suction. In addition, the various factors that influence the SWCC behavior are reviewed based on the theoretical and numerical approaches.

2.2 Equations for Fitting SWCCs

The amount of water that is filled in the soil pores can be expressed as following mathematical relationship (Fredlund and Xing 1994).

$$\theta(r) = \int_{r_{min}}^{r} f(r)dr \tag{2.1}$$

where θ is volumetric water content, r is pore radius, r_{min} is the minimum pore radius, $f(r)$ is pore size distribution function.

Extending the Young-Laplace equation (or the capillary law) shown in Eq. (2.2), the pore radius can be expressed as a functional relationship of soil matric suction shown in Eq. (2.3).

$$r = \frac{2T_s cos\beta}{\psi} \tag{2.2}$$

$$\theta(r) = \int_{\psi_{max}}^{\psi} f\left(\frac{2T_s cos\beta}{\psi}\right) d\left(\frac{2T_s cos\beta}{\psi}\right) = \int_{\psi_{min}}^{\psi} f\left(\frac{2T_s cos\beta}{\psi}\right) \frac{2T_s cos\beta}{\psi^2} d\psi \tag{2.3}$$

where T_s is surface tension, and β is contact angle. The relationship between soil matric suction and volumetric water content (i.e., SWCC) can be built (Fredlund and Xing 1994) based on Eq. (2.3), by introducing various pore size distribution functions. Eqs. (2.1) to (2.3) presents a brief basis for modeling SWCCs. The available SWCC equations based on the above theory are listed in Table 2.1.

Table 2.1 Typical SWCC equations in the literature.

Eq. # and References	Equations	Note
Eq. (2.4) Gardner (1958)	$S = \frac{1}{1 + a\psi^n}$	a, m, and n are model parameters. ψ_{AEV} is air-entry value
Eq. (2.5) Brooks and Corey (1964)	$\begin{cases} S = 1, & \psi < \psi_{AEV} \\ S = \left(\frac{\psi}{a}\right)^{-n}, & \psi > \psi_{AEV} \end{cases}$	
Eq. (2.6) Brutsaert (1966)	$\frac{S - S_{res}}{1 - S_{res}} = \frac{1}{1 + (a\psi)^n}$	
Eq. (2.7) Farrel and Larson (1972)	$\psi = \psi_0 \exp\left(a(\theta_0 - \theta)\right)$	
Eq. (2.8) Campbell (1974)	$\psi = \psi_{AEV}(\theta/\theta_s)^{-b}$	
Eq. (2.9) van Genuchten (1980)	$\frac{S - S_{res}}{1 - S_{res}} = \frac{1}{[1 + (a\psi)^n]^m}$	
Eq. (2.10) Tani (1982)	$\frac{S - S_{res}}{1 - S_{res}} = \left(1 + \frac{a - \psi}{a - n}\right) \exp\left(-\frac{a - \psi}{a - n}\right)$	
Eq. (2.11) Williams et al. (1987)	$\ln(\psi) = n + m\theta$	
Eq. (2.12) McKee and Bumb (1987)	$\frac{S - S_{res}}{1 - S_{res}} = \frac{1}{1 + \exp\left(\frac{\psi - a}{b}\right)}$	
Eq. (2.13) Fredlund and Xing (1994)	$\begin{cases} S = C(\psi) \frac{1}{\left[\ln\left(\exp(1) + \left(\frac{\psi}{a}\right)^n\right)\right]^m} \\ C(\psi) = 1 - \frac{\ln\left(1 + \frac{\psi}{\psi_{res}}\right)}{\ln(1 + \frac{10^6}{\psi_{res}})} \end{cases}$	

Eq. (2.14) Kosugi (1994)

$$\begin{cases} \dfrac{S - S_{res}}{1 - S_{res}} = 1, \psi < \psi_{AEV} \\ \dfrac{S - S_{res}}{1 - S_{res}} = \dfrac{1}{2}\operatorname{erfc}\left(\dfrac{\ln\left(\dfrac{\psi_{AEV} - \psi}{\psi_{AEV} - \psi_{mode}}\right) - \sigma^2}{\sqrt{2}\pi\sigma}\right), \psi > \psi_{AEC} \end{cases}$$

Eq. (2.15) Pachepsky et al. (1995)

$$\theta = \frac{\theta_0}{2}\operatorname{erfc}\left(\frac{1}{\sigma\sqrt{2}}\ln\left(\frac{\psi}{\psi(\theta_0/2)}\right)\right)$$

Eq. (2.16) Assouline et al. (1998)

$$\frac{S - S_{res}}{1 - S_{res}} = 1 - \exp(-a(\psi^{-1} - \psi_{res}^{-1})^n)$$

Eq. (2.17) Webb (2000)

$$\log_{10}(\psi) - \log_{10}(\psi_{res}) = \gamma(S - S_{res})$$

Eq. (2.18) Pham and Fredlund (2008)

$$\begin{aligned} w(\psi) = [&w_1(\psi)f_1(\psi, \psi_{AEV}) - w_2(\psi)f_2(\psi, \psi_{AEV}) \\ &- f_3(\psi, \psi_{AEV})]f_4(\psi, \psi_{res}) \\ &+ w_3(\psi)f_5(\psi, \psi_{res}) + f_6(\psi, \psi_{res}) \end{aligned}$$

Eq. (2.19) Li and Vanapalli (2022b)

$$\frac{S - S_{res}}{1 - S_{res}} = \frac{1}{\exp(n(a\psi)^m)}$$

Leong and Rahardjo (1997), and Sillers and Fredlund (2001) evaluated the performance of various SWCC models. Fayer and Simmons (1995) proposed a new correction function for the entire suction range. Groenevelt and Grant (2004) modeled SWCC over residual soil suction. Tuller and Or (2005) divided the SWCC behavior into two regions and proposed a model for low saturation range. Khlosi et al. (2006) modified Kosugi (1994) model to fit the entire suction range. Schneider and Goss (2012) extended Webb (2000) model to the oven dryness. Resurreccion et al. (2011) and Oh et al. (2012) evaluated distinct SWCC models performance from saturation to oven dryness.

2.3 Prediction SWCCs from the Pore Size Distribution Curve

The SWCC is widely used as a tool towards interpreting and predicting the several properties of unsaturated soils. Several methods or techniques are available for measuring the SWCC using direct or indirect testing methods (i.e., hanging column technique, axis translation technique, filter paper method, and dewpoint potentiometer method) (Nam et al. 2010).

However, these measurement methods are either expensive or time-consuming. To simplify the procedure of obtaining SWCCs, some indirect prediction methods based on easily measured soil physical properties are developed in the literature. In comparison to the measurement of the SWCC, the soil physical properties can be readily tested with limited cost that typically include grain size distribution (GSD), bulk density, and void ratio (Romero-Ruiz et al. 2018). The function to relate different soil characteristics and properties with one another is also termed pedotransfer functions (PTFs, Bouma 1989). Some widely used SWCC based on PTFs proposed in the literature as summarized below.

2.3.1 Physico-empirical models

One of the pioneering works to build relationships between soil matric suction, pore space, and water content was originally proposed by Visser (1966). A well-known physico-empirical model was proposed by Arya and Paris (1981). Later, a more comprehensive and thoughtful version was developed by Arya et al. 1999. In this model, the soil pore volume is calculated from grain size information using the information of particle density, bulk density as well as void ratio. The main concept of the model is to build the relationships between soil grain size and soil pore size based on the information of pore volume. Once the pore size is calculated, the capillary law is then applied to estimate the corresponding soil suction. Several separate points for soil matric suction versus volumetric water content are then generated to form the SWCC using the gathered information.

Following the above model, various other physico-empirical models were either proposed or comprehensively discussed in the literature (Arya and Dierolf 1992, Basile and D'Urso 1997, Simms and Yanful 2001, Wösten et al. 2001, Chan and Govindaraju 2004, Nimmo et al. 2007, Van Looy et al. 2017). The key features of physico-empirical models can be summarized as follows. First, the relationship between the pore volume and GSD curve or other soil physical properties is developed. Second, the soil (matric) suction is estimated based on the pore size (or volume) typically using the Capillary law. As discussed earlier, this methodology is useful in developing the relationship between GSD curve and the SWCCs. Such relationships are of significance as the soil is recognized as porous media. The method is a simple approach to predict the SWCCs from GSD curve that is of low cost and reasonable accuracy. However, discrete SWCC points are obtained by using empirical parameters extending this approach and have some limitations. To overcome such limitations, various physico-empirical models that were proposed in the literature are succinctly summarized below.

The flexible SWCC model that has been found to be useful for different types of soils proposed by van Genuchten (1980) has been used as a tool to fit the cumulative GSD curve information combining the concepts in Arya and Paris (1981) together to develop simple SWCC models. For example, Haverkamp and Parlange (1986) presented a physico-empirical SWCC prediction model based on the similarity between GSD curve and SWCC. Based on this approach, a modified van Genuchten (1980) SWCC model was developed using the GSD curve. A similar approach has also been developed by Smettem and Gregory (1996). Later, Zhuang et al. (2001) considered the shape effect of soil particles from GSD curve use van Genuchten-type model to propose a more rigorous model (van Genuchten 1980). Some further modifications based on Arya and Paris (1981) model is also available in the literature (e.g., Arya et al. 2008; Nasta et al. 2009; Jaafar and Likos 2011; Mohammadi et al. 2011; Meskini-Vishkaee et al. 2014; Antinoro et al. 2014; Wan et al. 2019; Alves et al. 2020).

Another approach by considering the shape of the pore channel was proposed by Tyler and Wheatcraft (1989). In their proposed approach, the fractal dimension was used to describe the tortuosity of the pore channels based on Arya and Paris (1981) model. Following the method, Perrier et al. (1996) proposed a SWCC model considering the fractal PoSD. Comegna et al. (1998) proposed a model to determine the fractal dimension of pore trace. Distinct fractal models for predicting SWCCs following similar approaches are also available in the literature (Bird et al.1996; Bird et al. 2000; Huang et al. 2005; Ghanbarian-Alavijeh and Hunt 2012).
As soil pores are surrounded by soil particles, it is of significance to evaluate exactly the size of soil particles near the soil pore. However, more rigorous theoretical models are required for reliable estimation because soil particles are randomly packed. Recently, the possibility theorem was incorporated into physico-empirical model to evaluate the arrangement of random soil particles. The possibility theorem is a useful tool for solving the random arrangement of soil particles. Based on the possibility theorem, some recent advances were made for modeling the SWCC are in the literature (e.g., Rahimi and Rahardjo 2016; Wan et al. 2019; Cheng et al. 2019; Zhai et al. 2020).

The SWCC behavior is commonly observed to be unimodal in nature for different soils from experimental studies. However, SWCC behavior is also multi-modal in nature in soils that are gap-graded in nature and in soils where water adsorption characteristics on surface of clay size particles due to influence of minerals (e.g., Burger and Shackelford 2001). There has been a significant interest in building physico-empirical models based on GSD curve for predicting

the multi-modal SWCC behavior in recent years. Research contributions of Della Vecchia et al. (2015) and Pouragha et al. (2021) are pioneering works in this direction. However, the mechanism for the formation of multi-modal SWCC is still under discussion.

The physico-empirical methods are widely accepted and adopted to empirically model the SWCCs in various fields that include soil science and geotechnical engineering. Some classical physico-empirical models for SWCC prediction are summarized in the book edited by Pachepsky and Rawls (2004). Several researchers have also summarized state-of-the-art reviews on the related topics related empirical models for SWCCs in the literature (Wösten et al. 2001; Vereecken et al. 2016; Van Looy et al. 2017; Vereecken et al. 2022).

2.3.2 Statistical estimation

Several statistical estimation methods were developed in the literature to understand the relationships between the SWCCs and soil physical properties and many influential factors such as the GSD curve and initial soil density. In comparison with physico-empirical methods, these statistical estimation methods build straightforward links among distinct variables. The statistical models provide a better performance when the database is large enough (Nemes et al. 2001). The general equation for the statistical estimation methods can be summarized below.

$$df(x_1, x_2, \dots x_n) = \frac{\partial f}{\partial x_1} dx_1 + \frac{\partial f}{\partial x_2} dx_2 + \cdots + \frac{\partial f}{\partial x_n} dx_n \tag{2.20}$$

where x_1, x_2, and x_n refer to variables that account for the target function f.

The target function typically is the degree of saturation, S due to its significant influence on the SWCC. The coefficient (i.e., $\partial S / \partial x_n$) is determined by statistical estimation from the dataset. The statistical method provides a reliable estimation over a large range of suction for soils from the related soil physical properties when a large volume of dataset is used. However, one of the limitations of this method is that it does not provide a fundamental understanding of how the SWCC is influenced by various properties. In other words, a comprehensive understanding of how the coefficients in the model are influenced is not well understood. In addition, the results are also sensitive to the selected database. To overcome this limitation, the statistical method can be combined with other methods (e.g., Schaap et al. 2001; Zhang and Schaap 2017, Li and

Vanapalli 2022a), such as the physico-empirical models or the new techniques as the Artificial Intelligence (AI) models. The combination methods will be discussed in a later section.

Two distinct approaches are typically used in statistical estimation methods; the first one is the direct estimation of SWCCs from soil properties; while the second one is the indirect method in which the SWCC is obtained from the estimated model parameters of SWCC equations.

2.3.2.1 Direct SWCC estimation

In this method, the SWCC is directly estimated from statistical methods using the soil physical properties that typically include the information of bulk density and GSD curves. As there are wide applications of SWCCs, some researchers (e.g., Pidgeon (1972), Cameron (1978), Gupta and Larson (1979), De Jong and Loebel (1982), Aina and Periaswamy (1985), Dijkerman (1988), Bruand (1990), Bruand et al. (1994), Walczak et al. (2006)) built and validated statistical regression models for directly predicting several points in SWCCs.

One widely accepted and pioneering approach of this method was proposed by Gupta and Larson (1979). In this study, soil fractions, organic matter, and bulk density are used to estimate water content at certain soil matric suction. A similar statistical estimation model by additionally adding one constant can also be found in the literature, which was presented by Rawls et al. (1982). Ahuja et al. (1985) proposed a simplified statistical estimation model. Later, Rawls and Brakensiek (1985) proposed a multiple regression model. Some further improved models are also available (Rawls et al. 1991, Pachepsky et al. 1998, Pachepsky and Rawls 1999).

A piecewise SWCC statistical model covering a large soil suction range was presented by Saxton et al. (1986). Mbagwu and Mbah (1998) directly estimated water content from saturation percentage. A comprehensive study for the SWCC estimation was summarized by Saxton and Rawls (2006).

2.3.2.2 Estimation via SWCC equations

Some milestone SWCCs models published in the literature are widely used in soil science, agriculture, geotechnical and geo-environmental engineering fields (e.g., BC model (Brooks and Corey 1964), VG model (van Genuchten 1980), and FX model (Fridlund and Xing 1994). There is a keen interest in correlating the model parameters of these SWCC equations with soil

physical properties via statistical estimation methods. As both VG and FX models are derived from the PoSD curve and as soil pores shapes have a strong correlation with the soil particles, such an indirect estimation method has received significant interest in the literature.

Brakensiek (1977) is one of pioneering works related to the estimation of the SWCC based on the BC model. This study has provided good validation of empirically estimated air-entry value with the measured values. Later studies by Clapp and Hornberger (1978) suggested that the BC model parameters are strongly related to soil texture. Brakensiek et al. (1981), McCuen et al. (1981), and Cosby et al. (1984) evaluated and discussed the link between the BC model parameters and soil textures for large volume of soil hydraulic data. Ghosh (1980) fitted the parameter in the BC model for some soils using soil physical properties (i.e., the percentages of sand, silt, and clay). Williams et al. (1983) estimated SWCC model parameters for different groups of soils. Hutson and Cass (1987) modified Campbell (1974) SWCC model and estimated the parameter via multiple regression. Aubertin et al. (1996) estimated air-entry value from GSD information. Tomasella and Hodnett (1998) estimated BC model parameter by linear regression for Brazilian Amazonia soils. Mayr and Jarvis (1999) proposed a statistical model to estimate BC model parameters from soil properties. Sakaki et al. (2014) estimated air-entry value from soil grain size.

After the VG model was published and widely accepted, there has been a keen interest in correlating the model parameters with soil physical properties. Carsel and Parrish (1988) estimated the VG parameters' variance for each class of soils. Wösten and van Genuchten (1988), Vereecken et al. (1989), Vereecken et al. (1990), and Gonçalves et al. (1997) developed regression models for predicting VG parameters and hydraulic conductivities, respectively. Rajkai and Várallyay (1992) and Rajkai et al. (1996) proposed regression models for estimating SWCC parameters based on GSD information. Further, van den Berg et al. (1997) and Scheinost et al. (1997) estimated VG models by mean grain diameter and its standard deviation. Tinjum et al. (1997), Zacharias and Wessolek (2007), and Li et al. (2007) estimated parameters in VG model with various initial water contents. Chiu et al. (2012) built a statistical estimation model using Bayesian probabilistic selection. Puhlmann and von Wilpert (2012) presented a multiple linear regression model for predicting the VG model parameters for forest soils.

After the FX model for SWCC was developed in 1994, several indirect estimation methods were developed using the FX model SWCC parameters. Fredlund et al. (1996) built the link

between grain diameter and the FX model. Fredlund et al. (2002) further improved the model and evaluated various estimation models in the literature. Vanapalli and Catana (2005) estimated various SWCC model parameters using soil properties and a measured SWCC data point that lies in the transition zone. Sung et al. (2005), Chin et al. (2010), Jensen et al. (2015), and Chai and Khaimook (2020) estimated FX model parameters using easily measured soil properties for reliably predicting the SWCC.

Several researchers have reviewed, examined or evaluated statistical models in the literature (Mishra et al. 1989, Williams and Ahuja 1992, Tietje and Tapkenhinrichs 1993, Kern 1995, Wösten et al. 1995, Cresswell and Paydar 1996, Nandagiri and Prasad 1997, Romano and Santini 1997, Wagner et al. 1998, Schaap and Leij 1998, Minasny et al. 1999, Zapata et al. 2000, Tomasella et al. 2000, Wagner et al. 2001, Cornelis et al. 2001, Romano and Palladino 2002, Tomasella et al. 2003, Mermoud and Xu 2006, Merdun 2010, Vereecken et al. 2010, Zou et al. 2015, and Vereecken et al. 2016).

2.3.3 Artificial Intelligent prediction

With the rising interests in artificial intelligence (AI) techniques (Rumelhart et al. 1986), several researchers proposed SWCC predictions based on AI models that were based on similar procedures discussed in previous sections. AI prediction models for SWCCs can also be divided into two main categories: direct and indirect prediction methods. As the name suggests, the SWCCs are predicted directly in the first method. While in the second model (i.e., an indirect method), SWCC model parameters are first estimated, and the estimated values are used in the prediction of the SWCC. The AI prediction methods can also be divided into distinct categories based on the adopted AI models. A succinct discussion on AI prediction models is summarized below.

Pachepsky et al. (1996) was one of the pioneers to directly predict SWCC points from soil texture and bulk density by artificial neural networks (ANN) model. Tamari et al. (1996) was a pioneer to predict soil hydraulic conductivity by ANN. Typically, higher model prediction accuracy is achieved by ANN model in comparison with indirect statistical estimation of parameters from VG model. Nemes et al. (2003) evaluated the prediction accuracy for direct SWCC estimation using distinct inputs. Jain et al. (2004) developed ANN model for direct predicting SWCC and compared it with fitting models.

Another pioneering work was conducted by Schaap and Bouten (1996), in their study, both direct and indirect SWCC predictions from VG model using soil texture information, bulk density and organic matter based on ANN models were investigated. Later Schaap et al. (1998), and Schaap and Leij (1998) tested and evaluated the SWCC prediction accuracy with distinct levels of input variables based on ANN models. A comprehensive version with details named as 'Rosetta' was later provided by Schaap et al. (2001). Patil and Rajput (2009) evaluated 'Rosetta' performance. A further developed version (i.e., 'Rosetta 3') was available in Zhang and Schaap (2017). Other ANN prediction models for SWCCs are also available in the literature. Minasny and McBratney (2002), Minasny et al. (2004), Børgesen et al. (2008) improved the ANN model performance based on VG model. Haghverdi et al. (2012) directly predicted SWCCs using ANN model from limited data.

For direct SWCC estimation from ANN model, Koekkoek and Booltink (1999) developed ANN models for several points in SWCCs. Børgesen and Schaap (2005), and Moreira de Melo and Pedrollo (2015) predicted several points in SWCCs by ANN model. Baker and Ellison (2008) combined a few individual ANNs together to gain more robust prediction results for several points in SWCCs.

Lamorski et al. (2008) developed support vector machines (SVM) approach, which belongs to a different category of AI model to directly predict various points related to the SWCC. Twarakavi et al. (2009) predicted the VG model parameters using SVM. Pachepsky et al. (1998) directly estimated SWCC points by group method of data handling (GMDH) technique. Ungaro et al. (2004) estimated both BC model parameters and SWCC points by GMDH model. Nemes et al. (2006) adopted the k-nearest neighbor algorithm to directly predict water content from soil properties. Garg et al. (2014) compared multi-gene genetic programming, ANN, and SVM model performance on predicting SWCCs using soil suction and effective stress as input variables. Amanabadi et al. (2019) compared the prediction performance for various models. Li and Vanapalli (2022b) predicted SWCCs by combining multivariate adaptive regression splines (MARS) and Arya and Paris (1981) methods together. Li et al. (2022) developed a database and estimated various unsaturated soil properties by random forest regression and ANN. Some typical SWCC prediction models based on soil properties are listed below.

Table 2.2 Typical models for predicting the SWCC from the GSD curve.

Eq. # and References	Equations and Notations
Eq. (2.21) Arya and Paris (1981) and Arya et al. (1999)	$\begin{cases} \theta_{vi} = S_f \sum_{j=1}^{j=i} \rho_b (W_i/\rho_P) e \\ \psi_i = 2T_s cos\theta / [\rho_w g R_i \{2e[3\,W_i/(4\rho_P \pi R_i^3)]^{1-\alpha_{AP}}/3\}^{1/2}] \end{cases}$ where, θ_{vi} is the average volumetric water content represented by pore volume that corresponds to ith grain size range, S_f is scale factor and defined as the ratio of theoretical volumetric water content to porosity, ρ_b is bulk density, W_i is solid mass per unit mass in the ith grain size range, ρ_P is particle density, e is void ratio, ψ_i is soil suction, T_s is surface tension, θ is contact angle, ρ_w is water density, g is acceleration of gravity, R_i is the mean grain size in ith grain size range, and α_{AP} is fitting parameter.
Eq. (2.22) Tyler and Wheatcraft (1989)	$\psi_i = 2T_s cos\theta / [\rho_w g R_i\,(2eN_i^{1-D}/3)^{1/2}]$ where, N_i is the number of particles with radius R_i, and D is fractal dimension.
Eq. (2.23) Fredlund et al. (2002)	$p(\phi) = p_1 \left[\frac{1}{\ln\{\exp(1) + \left[\frac{10^{-\log(d_e)-1}}{p_2}\right]^{p_3}\}} \right]^{p_4} + p_5$ where, p_1, p_2, p_3, p_4 and p_5 are fitting parameters, d_e is effective grain diameter, and $p(\phi)$ is the value for either m_f or n_f in Fredlund and Xing (1994) model.
Eq. (2.24) Chin et al. (2010)	$a_f = -2.4x + 722; n_f = 0.07x^{0.4}; m_f = 0.015x^{0.7};$ $\psi_r = 914\exp(-0.002x)\,; x = eP_{200}$ where, a_f, n_f and m_f are fitting parameters in Fredlund and Xing (1994) equation, ψ_r is residual suction, and x is combination of void ratio e and percentage at soil passing standard sieve No. 200, P_{200}.
Eq. (2.25) Zhai et al. (2020)	$A_{void}^{Total} = \sum_{i=1}^{N} P_i P_j P_k \left(s_{tri} - 0.5\alpha_t r_k^2 - 0.5\beta_t r_i^2 - 0.5\gamma_t r_j^2\right);$ $r_{tangen} = \frac{1}{r_i} + \frac{1}{r_j} + \frac{1}{r_k} + 2\sqrt{\frac{1}{r_i r_j} + \frac{1}{r_j r_k} + \frac{1}{r_k r_i}};$ $\psi = 2T_s cos\theta / \left(\rho_w g r_{tangen}\right); S = \frac{A^m}{A_{void}^{Total}}$ where, A_{void}^{Total} is total void area, P_i, P_j and P_k are the probabilities filling the triangle between particles with radii of r_i, r_j and r_k, s_{tri} is the area of triangle, α_t, β_t and γ_t are three angles of the triangle, r_{tangen} is the circle that is tangent to all three particles, ψ is soil suction, S is degree of saturation, and A^m is the total area filled with water.

2.4 Models for multi-modal SWCCs

A SWCC can be either unimodal or bimodal in nature based on the pore structure of the unsaturated soil (Fredlund and Rahardjo 1993, Ito and Azam 2013, Satyanaga et al. 2017, Zhai et al. 2018). For example, the pore size distribution (PoSD) curve in a well-graded soil usually leads to a SWCC with unimodal features (i.e., continuous *S* shape curve). However, soils with dual-porosity structure constituted with macropores (inter-aggregate pores) and micropores (intra-aggregate pores) is usually associated with varying PoSD curve that contributes to a bimodal SWCC (i.e., it has two continuous *S* shape curve, for example, Li et al. 2009a, 2009b, Li et al. 2014, Qiao et al. 2021).

During the last three decades, many researchers have proposed various bimodal SWCC equations. These equations from literature can be summarized into three categories. The first category of methods uses piecewise equations to fit the bimodal SWCCs (Wilson et al. 1992, Burger and Shackelford 2001). In these methods, the bimodal SWCC is divided into two unimodal curves that respectively correspond to the macropores and micropores. Each of these curves is independently fitted using a unimodal SWCC equation with distinct fitting parameters. The merging point (i.e., ψ_j in Eq. (2.26)) between these two parts is typically determined arbitrarily (Wijaya and Leong 2016). One of the key limitations of this method is the location of merging point of the two curves that significantly affects the curve fitting process. Such a technique contributes to various SWCC fitting parameters at the merging point of the two curves (Burger and Shackelford 2001, Wijaya and Leong 2016). This method can be summarized as below:

$$\theta(\psi) = \begin{cases} f_1(\psi) & \psi \le \psi_j \\ f_2(\psi) & \psi > \psi_j \end{cases} \tag{2.26}$$

where f_1 and f_2 are SWCC functions representing the inter-aggregate pores (macropores) and the intra-aggregate pores (micropores), respectively, and ψ is soil suction.

The second category of methods separates the porosity (i.e., the saturated volumetric water content) into fractions representing the macropores and micropores and uses a continuous equation to describe the bimodal SWCC (Ross and Smettem 1993, Zhang and Chen 2005, Chen et al. 2019). In this method, optimization process of all the parameters can be simultaneously achieved. This method can be summarized below.

$$\theta(\psi) = \theta_{sl} f_1(\psi) + \theta_{ss} f_2(\psi) \tag{2.27}$$

where θ_{sl} and θ_{ss} are saturated volumetric water contents for the macropores and micropores, respectively. The functions f_1 and f_2 have a coupled effect on the entire shape of bimodal SWCC since the optimization process is performed simultaneously (Zhang and Chen 2005).

Based on one hypothesis, (i.e., interaction zone in the PoSD curve predominantly influences the behavior of bimodal SWCC in a limited zone), Li and Vanapalli (2021) proposed a new bimodal SWCC model as shown in Eqs. (2.28). In comparison with Eqs. (2.26) and (2.27), the proposed method is an extension of both methods one and two in the literature.

$$\theta(\psi) = \begin{cases} f_1(\psi) & \psi \le \psi_A \\ \lambda_\beta f_1(\psi) + \left(1 - \lambda_\beta\right) f_3(\psi) & \psi_A < \psi < \psi_B \\ f_3(\psi) & \psi \ge \psi_B \end{cases} \tag{2.28a}$$

or

$$\theta(\psi) = [f_1(\psi)]_{\mathrm{I}} + \left[\lambda_\beta f_1(\psi) + \left(1 - \lambda_\beta\right) f_3(\psi)\right]_{\mathrm{II}} + [f_3(\psi)]_{\mathrm{III}} \tag{2.28b}$$

where the symbol $[]_i$ determines the boundaries in bimodal SWCCs.

2.5 Models for hysteretic SWCCs

A family of SWCC taking account of influence soil hysteresis is required for rigorous modeling the soil behaviors. The water content in the SWCC associated with the wetting branch is less than the drying branch at any given soil suction. Numerous drying and wetting scanning curves are possible within the main drying/wetting SWCCs. The major factors that influence the hysteretic SWCCs (Pham et al. 2005) include: (i) irregular pore structures inside soils or the "ink-bottle" effect; (ii) the contact angle variation during drying and wetting processes; (iii) entrapped air during wetting; (iv) thixotropic regain or aging due to the wetting-drying cyclic history.

Two approaches are widely used for modeling hysteretic SWCC (Pham et al. 2005) in the literature; namely, physical-based (domain) models (e.g., Parlange 1976, Mulem and Miller 1979, Hogarth et al. 1988, Wei and Dewoolkar 2006, Min and Huy 2010, Zhou 2013, Likos et al. 2014, Fu et al. 2020) and empirical models (e.g., Feng and Fredlund 1999, Pham et al. 2003, Zhai et al. 2020).

2.6 Modeling SWCCs under initial states effects

Experimental studies from the literature suggest that the SWCC behavior is significantly influenced by the stress state and initial compaction water content that is strongly related to the pore structure in fine-grained soils (e.g., Vanapalli et al. 1999, Ng and Pang 2000). During the last two decades, several models have been developed to incorporate the influence of initial stress state into SWCC (e.g., Wheeler et al. 2003, Gallipoli et al. 2003, Sun et al. 2007a, Tarantino and Col 2008, Tarantino 2009, Gallipoli 2012, Zhou et al. 2012a, Hu et al. 2013, Zhou and Sheng 2015). Two equations are widely used in literature (e.g., Gallipoli 2012, Hu et al. 2013) for understanding the influence of void ratio changes associated with the stress state on the SWCC and are summarized below.

$$\frac{\theta-\theta_r}{\theta_s-\theta_r}=\left\{\frac{1}{1+[\psi(\phi_c e^{\xi c})]^{n_v}}\right\}^{m_v} \tag{2.33}$$

$$\frac{\theta-\theta_r}{\theta_s-\theta_r}=\left\{\frac{1}{1+[a_0\psi\exp(\xi_c(e-e_0))]^{n_v}}\right\}^{m_v} \tag{2.34}$$

where ϕ_c and ξ_c are fitting parameters, a_0 is parameter a_v value at reference state, e is void ratio, and e_0 is the void ratio at reference state.

Table 2.3 Typical bimodal SWCC equations from the literature.

Eq. # and Refs	Equations and Notations
Eq. (2.29) Gitirana Jr and Fredlund (2004)	$\theta = \frac{S_1 - S_2}{1+(\psi/\sqrt{\psi_{b1}\psi_{res1}})^{d_1}} + \frac{S_2 - S_3}{1+(\psi/\sqrt{\psi_{res1}\psi_{b2}})^{d_2}} + \frac{S_3 - S_4}{1+(\psi/\sqrt{\psi_{b2}\psi_{res2}})^{d_3}} + S_4$ $S_i = \frac{tan\theta_i(1+r_i^2)\ln(\psi/\psi_i^a)}{(1-r_i^2 tan^2\theta_i)} + S_i^a + (-1)^i \frac{(1+tan^2\theta_i)}{(1-r_i^2 tan^2\theta_i)}\sqrt{r_i^2 \ln^2(\psi/\psi_i^a) + \frac{a^2(1-r_i^2 tan^2\theta_i)}{(1+tan^2\theta_i)}}$ where S_1^a=1, S_2^a=S_{res1}, S_3^a=S_b, S_4^a=S_{res2}, S_5^a=0, $\psi_1^a = \psi_{b1}$, $\psi_2^a = \psi_{res1}$, $\psi_3^a = \psi_{b2}$, $\psi_4^a = \psi_{res2}$, $\psi_5^a = 10^6$, $\theta_i = -(\lambda_{i-1} + \lambda_i)/2$, $r_i = \tan[(\lambda_{i-1} + \lambda_i)/2]$, λ_0=0, $\lambda_i = \arctan\{(S_i^a - S_{i+1}^a)/[\ln(\psi_{i+1}^a/\psi_i^a)]\}$, and $d_i = 2\exp[1/\ln(\psi_{i+1}^a/\psi_i^a)]$.
Eq. (2.30) Satyanaga et al. (2013)	$\theta = \left(1 - \frac{\ln(1+\frac{\psi}{\psi_r})}{\ln(1+\frac{10^6}{\psi_r})}\right)\left[\theta_r + (\theta_{s1} - \theta_{s2})\left(1 - erfc\frac{\ln(\frac{\psi_{a1}-\psi}{\psi_{a1}-\psi_{m1}})}{s_1}\right) + (\theta_{s2} - \theta_r)\left(1 - erfc\frac{\ln(\frac{\psi_{a2}-\psi}{\psi_{a2}-\psi_{m2}})}{s_2}\right)\right]$ $erfc = \int_{-\infty}^{X} \frac{1}{\sqrt{2\pi}} \exp\left(-\frac{x^2}{2}\right) dx$ where θ_s is the saturated volumetric water content, ψ_a represents air-entry value, ψ_m represents the matric suction at the inflection point, and s is the geometric standard deviation of SWCC.
Eq. (2.31) Li et al. (2014)	$\theta = \lambda\left(\frac{\theta_s}{\lambda+1} - \theta_r\right)\frac{\sqrt{\psi_{r1}/\psi_{a1}}^{n/\log(\psi_{r1}/\psi_{a1})}}{\psi^{n/\log(\psi_{r1}/\psi_{a1})} + \sqrt{\psi_{r1}/\psi_{a1}}^{n/\log(\psi_{r1}/\psi_{a1})}} + \left(\frac{\theta_s}{\lambda+1} - \theta_r\right)\frac{(l\psi_{r1})^m}{\psi^m + (l\psi_{r1})^m} + \lambda\theta_r \frac{\sqrt{\psi_{r2}/\psi_{a2}}^{n/\log(\psi_{r2}/\psi_{a2})}}{\psi^{n/\log(\psi_{r2}/\psi_{a2})} + \sqrt{\psi_{r2}/\psi_{a2}}^{n/\log(\psi_{r2}/\psi_{a2})}} + \theta_r \frac{(l\psi_{r2})^m}{\psi^m + (l\psi_{r2})^m}$, $\lambda = (\theta_s - \theta_r)/\theta_r$ where l, m, n are fitting parameters.
Eq. (2.32) Wijaya and Leong (2016)	$\theta = \theta_s - m_1(x - x_1) - R_2(x)(m_2 - m_1) - R_3(x)(m_3 - m_2) - R_4(x)(m_4 - m_3) - R_5(x)(m_5 - m_4)$ $R_i(x) = \frac{1}{2}\langle(x - x_1) + \frac{1}{c_i}\ln\left\{\frac{\cosh[c_i(x-x_i)]}{\cosh[c_i(x_i-x_1)]}\right\}\rangle$ $c_i = \frac{2}{\log(\psi_i^+/\psi_i^-)}$, $x = \log(\psi)$, $x_i = \log(\psi_i)$ where x_1 is the value of log (ψ_i) when $\theta = \theta_s$, m_i is the slope of each linear segment i, ψ_i is the matric suction at the intersection point between linear segment i-1 and i, ψ_i^+ is the suction where the SWCC merges into linear segment i, and ψ_i^- is the suction when the SWCC departs from segment i-1.

2.7 Modeling SWCC considering THMC effects

There is extensive information in the literature to understand and interpret the influence of hydro-mechanical behavior of unsaturated soils using the SWCC. Several models have been proposed in the literature for predicting the SWCCs considering the influence of temperature effects (e.g., Hansson et al. 2004, Jacinto et al. 2009, Zhou et al. 2014, Wan et al. 2015, Ghavam-Nasiri et al. 2019, Cai et al. 2022). The influence of different types of salts and concentrations were also investigated on the behavior SWCCs in the literature (e.g., Ravi and Rao 2013, He et al. 2016, Wang et al. 2019). There is an urgent need to understand the influence of THMC on SWCCs.

In many scenarios, frozen soils are also in a state of unsaturated condition. The pore-water in unsaturated soils can exist in a partial or fully frozen state as ice when the soil is subjected to a low temperature. The initial freezing point of water within the soils is lower than the fusion point of pure water due to certain factors such as the high pore pressures (e.g., Koopmans and Miller 1966, Banin and Anderson 1974, Black and Tice 1989, Ren and Vanapalli 2019). The relationship between the unfrozen water content and temperature which is referred to as the soil freezing characteristic curve (SFCC) is used for understanding, interpreting, and predicting the behavior of frozen unsaturated soils with a temperature lower than 0 °C (e.g., Kurylyk and Watanabe 2013, Teng et al. 2020).

In recent decades, two approaches have been used for modeling SFCC behavior in the literature (e.g., Kurylyk and Watanabe 2013, Zhang and Lu 2021): the first approach is based on semi-empirical or empirical methods (e.g., Black and Tice 1989, Kozlowski 2007); while the second approach is based on exploiting the similarities with the SWCC (e.g., Liu and Yu 2013, Wang et al. 2017, Zhou et al. 2018, Teng et al. 2020, Jin et al. 2020, Wan and Yang 2020, Kong et al. 2022).

CHAPTER 3

A Novel Modeling Method for the Bimodal Soil-Water Characteristic Curve

3.1 Introduction

The soil-water characteristic curve (SWCC) describes the relationship between water content or degree of saturation and the soil suction (Fredlund and Rahardjo, 1993). The water content in this relationship can be either gravimetric or volumetric. The SWCC is also referred to in the literature using different terms; namely, soil moisture curve and soil-water retention curve. During the last 25 years, the variation of thermo-hydro-mechanical-chemo (THMC) properties with respect to suction have been predicted using the SWCC along with the saturated soil properties (for example, Vanapalli et al., 1996; Xu et al., 2003; Fredlund et al., 2011; Zhu et al., 2013; Siemens et al., 2014; Yin and Vanapalli, 2018; Alves et al., 2020). There is a growing interest during the last two decades to design various geotechnical infrastructures such as the slopes, pavements, retaining walls, pipelines, shallow and deep foundations (Tsaparas et al., 2002; Qi and Vanapalli, 2015; Cary and Zapata, 2016; Ren and Vanapalli, 2020; Chen et al., 2021; Rong and McCartney, 2021) for unsaturated soils using the SWCC as a tool.

A typical SWCC can be either unimodal or bimodal in nature based on the pore structure of the unsaturated soils (Fredlund and Rahardjo, 1993; Nemes et al., 2001; Ito and Azam, 2013; Satyanaga et al., 2017; Zhai et al., 2018) (see Figure 3.1). For example, the pore size distribution (PoSD)curve in a well-graded soil usually leads to a SWCC with unimodal features (i.e., continuous *S* shape curve). However, soils with dual-porosity structure constituted with macropores (inter-aggregate pores) and micropores (intra-aggregate pores) is usually associated with varying PoSD curve that contributes to a bimodal SWCC (i.e., it has two continuous *S* shape curve) (for example, Li et al., 2009a, 2009b; Li et al., 2014; Qiao et al., 2021).

Several traditional equations are available in the literature for fitting (for example, van Genuchten, 1980; Fredlund and Xing, 1994) or predicting the unimodal SWCC behavior (for example, Arya and Paris (1981).

The contents presented in this chapter are published in Computers and Geotechnics.
Li, Y., Vanapalli, S.K., 2021. *A novel modeling method for the bimodal soil-water characteristic curve*. Comp. Geotech. 138, 104318. doi: 10.1016/j.compgeo.2021.104318.

A typical prediction equation that relates the SWCC to basic soil properties include physico-empirical equations and statistical estimation methods (Arya and Paris, 1981; Fredlund et al., 2002; Vanapalli and Catana, 2005; Chin et al., 2010; Zhai et al., 2020; Li and Vanapalli, 2021). The SWCC fitting equations are smooth mathematical relationships that are widely used in the prediction of the unsaturated soil functions such as the permeability and the shear strength for use in engineering and agriculture applications (for example, Fredlund et al., 1994; Vanapalli et al., 1999; Zhan et al., 2012; Zhai et al., 2017).

The bimodal SWCCs are different from unimodal SWCC and are not typically described by traditional equations (Burger and Shackelford, 2001; Satyanaga et al., 2013; Li et al., 2014; Wijaya and Leong, 2016). In this Chapter, a hypothesis is introduced to link the soil PoSD curve to the bimodal SWCC. The relationships between the PoSD curve and the bimodal SWCC equations are used in extending the proposed hypothesis to propose two novel equations; namely, the rigid equation and the simplified equation by modifying two widely used unimodal SWCC equations from the literature; namely van Genuchten (1980) and Fredlund and Xing (1994) equations. The proposed bimodal SWCC equations can be used as valuable tools for reliably predicting various properties of unsaturated soils; similar to the unimodal SWCC equations. In addition, they can be used in the finite element methods for analyzing the complex nonlinear THMC behavior of unsaturated soils.

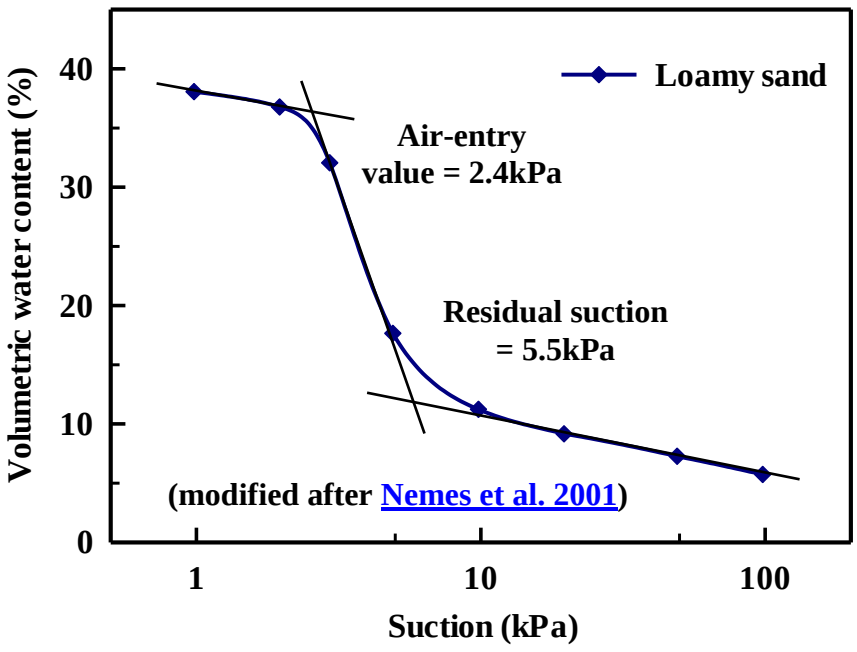

(a) Typical unimodal soil-water characteristic curve

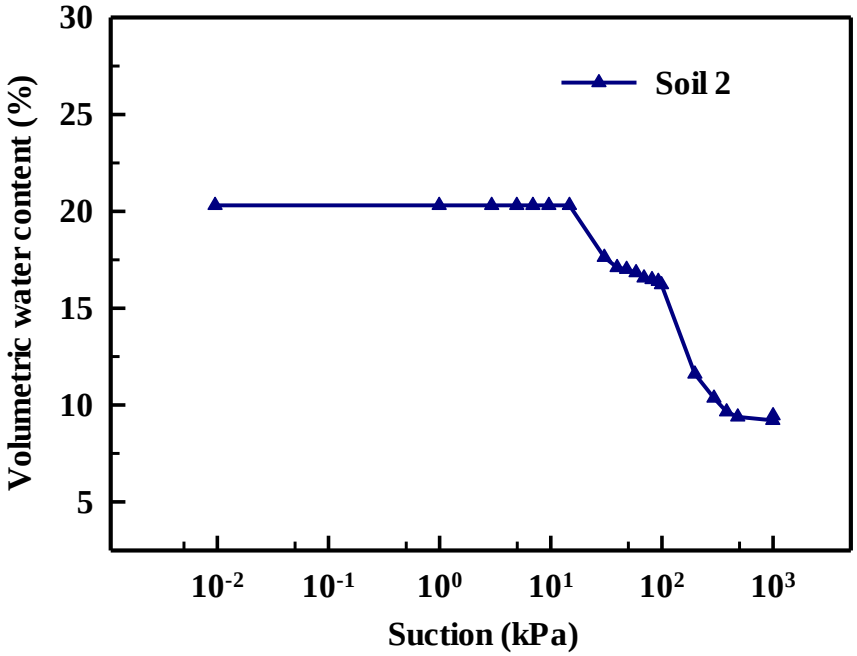

Figure 3.1 Typical unimodal and bimodal soil-water characteristic curves.

3.2 Background literature

During the last three decades, many researchers have proposed various bimodal SWCC equations. These equations from literature can be summarized into three categories. The first category of methods uses piecewise equations to fit the bimodal SWCCs (Wilson et al., 1992; Burger and Shackelford, 2001). In these methods, the bimodal SWCC is divided into two unimodal curves that respectively correspond to the macropores and micropores. Each of these curves is independently fitted using a unimodal SWCC equation with distinct fitting parameters. The merging point (i.e., ψ_j in Eq. (3.1)) between these two parts is typically determined arbitrarily (Wijaya and Leong, 2016). One of the key limitations of this method is the location of merging point of the two curves that significantly affects the curve fitting process. Such a technique contributes to various SWCC fitting parameters at the merging point of the two curves (Burger and Shackelford, 2001, Wijaya and Leong, 2016). This method can be summarized as below:

$$\theta(\psi) = \begin{cases} f_1(\psi) & \psi \le \psi_j \\ f_2(\psi) & \psi > \psi_j \end{cases} \tag{3.1}$$

where f_1 and f_2 are SWCC functions representing the inter-aggregate pores (macropores) and the intra-aggregate pores (micropores), respectively, and ψ is soil suction.

The second category of methods separates the porosity (i.e., the saturated volumetric water content) into fractions representing the macropores and micropores and uses a continuous equation to describe the bimodal SWCC (Ross and Smettem, 1993; Zhang and Chen, 2005; Chen et al., 2019). In this method, optimization process of all the parameters can be simultaneously achieved. This method can be summarized below.

$$\theta(\psi) = \theta_{sl} f_1(\psi) + \theta_{ss} f_2(\psi) \tag{3.2}$$

where θ_{sl} and θ_{ss} are saturated volumetric water contents for the macropores and micropores, respectively.

The functions f_1 and f_2 have a coupled effect on the entire shape of bimodal SWCC since the optimization process is performed simultaneously (Zhang and Chen, 2005).

The third category of methods extends an independent parameter approach to determine the bimodal SWCC. This method is based on several fitting parameters that need to be estimated extending graphical construction methods for the bimodal SWCCs. Different equations are used for determining the fitting the parameters in these methods (Gitirana Jr and Fredlund, 2004; Liu et al., 2013; Satyanaga et al., 2013; Wijaya and Leong, 2016). The equations in this method focus on flexibility rather than strongly relating them to the bimodal PoSD curve (Satyanaga et al., 2013; Qiao et al. 2021). Table 3.1 summarizes four representative equations of this method from the literature (i.e., Eqs. (3), (4), (5), and (6) in Table 3.1).

In this Chapter, two piecewise-form bimodal SWCC equations are proposed that are linked with the bimodal PoSD curve. Both these equations incorporate advantages of various methods. First, it is based on the traditional unimodal SWCC equations that were found to be valuable tools for providing a rational basis for explaining the THMC behavior of unsaturated soils. Second, various parameters required in identifying salient features of the SWCC can be determined using graphical construction methods, which simplify curve-fitting procedures. In addition, a technique is developed based on regression analysis to estimate the key features that include the air-entry and the residual suction values of the bimodal SWCC without bias. The

proposed equations can be used as tools for rational interpretation and prediction of the THMC properties of unsaturated soils that exhibit dual pore structure.

3.3 Derivation for the bimodal soil water characteristic curve

3.3.1 Basic relationships for bimodal SWCC

The volumetric water content, θ in unsaturated soils can be expressed as Eq. (3.7) since it describes the amount of water stored in the pores and each pore is characterized by radius r (Fredlund and Xing, 1994):

$$\theta(R) = \int_{R_{min}}^{R} f(r)\, dr \tag{3.7}$$

where $\theta(R)$ represents the volumetric water content when the water fills all pores with radii less than or equal to R, R_{min} is the minimum radius of pores inside the soil, and $f(r)$ is the density function of pore volume with respect to pore radius r.

The volumetric water content can be rewritten as Eq. (3.9), by including Young-Laplace equation (i.e., Eq. (3.8)):

$$r = \frac{2T_s cos\beta}{\psi} \tag{3.8}$$

$$\theta(\psi) = \int_{\psi_{max}}^{\psi} f\left(\frac{2T_s cos\beta}{h}\right) d\left(\frac{2T_s cos\beta}{h}\right) = \int_{\psi}^{\psi_{max}} f\left(\frac{2T_s cos\beta}{h}\right) \frac{2T_s cos\beta}{h^2}\, dh \tag{3.9}$$

where T_s is surface tension of water, β is contact angle, ψ_{max} is the maximum soil suction corresponding to the minimum pore size, and h is a dummy variable of integration representing suction.

The above equations are based on the local equilibrium hypothesis (Hypothesis I, Mualem, 1976), which suggests that at a given suction for a specific pore radius, all pores with larger radii are fully filled with air, while the pores with smaller radii are totally filled with water (Fredlund and Xing, 1994).

Table 3.1 Bimodal SWCC equations for the third category of methods from the literature.

Eq. # and Refs	Equations and Notations
Eq. (3.3) Gitirana Jr and Fredlund (2004)	$\theta = \frac{S_1 - S_2}{1+(\psi/\sqrt{\psi_{b1}\psi_{res1}})^{d_1}} + \frac{S_2 - S_3}{1+(\psi/\sqrt{\psi_{res1}\psi_{b2}})^{d_2}} + \frac{S_3 - S_4}{1+(\psi/\sqrt{\psi_{b2}\psi_{res2}})^{d_3}} + S_4$ $S_i = \frac{tan\theta_i(1+r_i^2)\ln(\psi/\psi_i^a)}{(1-r_i^2 tan^2\theta_i)} + S_i^a + (-1)^i \frac{(1+tan^2\theta_i)}{(1-r_i^2 tan^2\theta_i)} \sqrt{r_i^2 \ln^2(\psi/\psi_i^a) + \frac{a^2(1-r_i^2 tan^2\theta_i)}{(1+tan^2\theta_i)}}$ where S_1^a=1, S_2^a=S_{res1}, S_3^a=S_b, S_4^a=S_{res2}, S_5^a=0, $\psi_1^a = \psi_{b1}$, $\psi_2^a = \psi_{res1}$, $\psi_3^a = \psi_{b2}$, $\psi_4^a = \psi_{res2}$, $\psi_5^a = 10^6$, $\theta_i = -(\lambda_{i-1} + \lambda_i)/2$, $r_i = \tan[(\lambda_{i-1} + \lambda_i)/2]$, λ_0=0, $\lambda_i = \arctan\{(S_i^a - S_{i+1}^a)/[\ln(\psi_{i+1}^a/\psi_i^a)]\}$, and $d_i = 2\exp[1/\ln(\psi_{i+1}^a/\psi_i^a)]$.
Eq. (3.4) Satyanaga et al. (2013)	$\theta = \left(1 - \frac{\ln(1+\frac{\psi}{\psi_r})}{\ln(1+\frac{10^6}{\psi_r})}\right)\left[\theta_r + (\theta_{s1} - \theta_{s2})\left(1 - erfc\frac{\ln(\frac{\psi_{a1}-\psi}{\psi_{a1}-\psi_{m1}})}{s_1}\right) + (\theta_{s2} - \theta_r)\left(1 - erfc\frac{\ln(\frac{\psi_{a2}-\psi}{\psi_{a2}-\psi_{m2}})}{s_2}\right)\right]$ $erfc = \int_{-\infty}^{X} \frac{1}{\sqrt{2\pi}} \exp\left(-\frac{x^2}{2}\right) dx$ where θ_s is the saturated volumetric water content, ψ_a represents air-entry value, ψ_m represents the matric suction at the inflection point, and s is the geometric standard deviation of SWCC.
Eq. (3.5) Li et al. (2014)	$\theta = \lambda\left(\frac{\theta_s}{\lambda+1} - \theta_r\right)\frac{\sqrt{\psi_{r1}/\psi_{a1}}^{n/\log(\psi_{r1}/\psi_{a1})}}{\psi^{n/\log(\psi_{r1}/\psi_{a1})} + \sqrt{\psi_{r1}/\psi_{a1}}^{n/\log(\psi_{r1}/\psi_{a1})}} + \left(\frac{\theta_s}{\lambda+1} - \theta_r\right)\frac{(l\psi_{r1})^m}{\psi^m + (l\psi_{r1})^m} + \lambda\theta_r \frac{\sqrt{\psi_{r2}/\psi_{a2}}^{n/\log(\psi_{r2}/\psi_{a2})}}{\psi^{n/\log(\psi_{r2}/\psi_{a2})} + \sqrt{\psi_{r2}/\psi_{a2}}^{n/\log(\psi_{r2}/\psi_{a2})}} + \theta_r \frac{(l\psi_{r2})^m}{\psi^m + (l\psi_{r2})^m}$, $\lambda = (\theta_s - \theta_r)/\theta_r$ where l, m, n are fitting parameters.
Eq. (3.6) Wijaya and Leong (2016)	$\theta = \theta_s - m_1(x - x_1) - R_2(x)(m_2 - m_1) - R_3(x)(m_3 - m_2) - R_4(x)(m_4 - m_3) - R_5(x)(m_5 - m_4)$ $R_i(x) = \frac{1}{2}\langle(x - x_1) + \frac{1}{c_i}\ln\left\{\frac{\cosh[c_i(x-x_i)]}{\cosh[c_i(x_i-x_1)]}\right\}\rangle$ $c_i = \frac{2}{\log(\psi_i^+/\psi_i^-)}$, $x = \log(\psi)$, $x_i = \log(\psi_i)$ where x_1 is the value of log (ψ_i) when $\theta = \theta_s$, m_i is the slope of each linear segment i, ψ_i is the matric suction at the intersection point between linear segment i-1 and i, ψ_i^+ is the suction where the SWCC merges into linear segment i, and ψ_i^- is the suction when the SWCC departs from segment i-1.

Based on Eq. (3.9), the volumetric water content can be calculated at various soil suction values, if the PoSD curve for a soil is well defined. Two well-known equations for unimodal SWCC; namely, van Genuchten equation (van Genuchten, 1980) (i.e. Eq. (3.10)), and Fredlund and Xing equation (Fredlund and Xing, 1994) (i.e. Eqs. (3.11)) are developed in the literature extending the above philosophy.

$$\frac{\theta-\theta_r}{\theta_s-\theta_r} = \left[\frac{1}{1+(a_v\psi)^{n_v}}\right]^{m_v} \tag{3.10}$$

$$\theta = C(\psi)\frac{\theta_s}{\{\ln[e+(\psi/a_f)^{n_f}]\}^{m_f}} \tag{3.11a}$$

$$C(\psi) = 1 - \frac{\ln(1+\psi/\psi_r)}{\ln(1+10^6/\psi_r)} \tag{3.11b}$$

where e is base of natural logarithm, a_v, m_v, n_v, a_f, m_f, and n_f are fitting parameters, θ_s and θ_r are saturated and residual volumetric water content, respectively, and $C(\psi)$ is the correction function for Fredlund and Xing equation.

For simplicity purposes in the remainder of this Chapter, van Genuchten equation (i.e., Eq. (3.10)) and Fredlund and Xing equation (i.e., Eq. (3.11)) are referred to as VG and FX equations, respectively.

The PoSD curve can be expressed as the sum of PoSD curve functions for macropores and micropores of soils with dual-porosity structure (Zhang and Chen, 2005), as given below:

$$f(r) = f_s(r) + f_L(r) \tag{3.12}$$

where $f_L(r)$ and $f_S(r)$ are PoSD curve functions for macropores and micropores, respectively. Based on Eq. (3.9), water content can be expressed as the sum of water stored in the macropores and the micropores:

$$\theta(\psi) = \int_{\psi}^{\psi_{max}}\left[f_S\left(\frac{2T_s cos\beta}{h}\right) + f_L\left(\frac{2T_s cos\beta}{h}\right)\right]\frac{2T_s cos\beta}{h^2}dh \tag{3.13}$$

The saturated volumetric water content can be expressed as Eq. (3.14) when the Eq. (3.13) is integrated over the suction range (Zhang and Chen, 2005):

$$\theta_s = \theta_s + \theta_{sL} \tag{3.14}$$

where θ_{ss} and θ_{sL} are saturated volumetric water content for the micropores and the macropores, respectively. Eq. (3.13) can also be written as:

$$\theta(\psi) = \int_0^{\psi_r} g(h)\, dh + \int_{\psi_r}^{\infty} g(h)\, dh \tag{3.15a}$$

$$g(h) = [f_s\left(\frac{2T_s cos\beta}{h}\right) + f_L\left(\frac{2T_s cos\beta}{h}\right)]\frac{2T_s cos\beta}{h^2} \tag{3.15b}$$

where ψ_r is the residual suction value. The amount of water drained from the soil equals to the residual volumetric water content, θ_r when soil suction exceeds the residual suction value.

Thus, based on Eqs. (3.15a), and (3.15b), the residual water content can be expressed as:

$$\theta_r = \theta_{rs} + \theta_{rL} \tag{3.16}$$

where θ_{rs} and θ_{rL} are residual volumetric water content for the micropores and the macropores, respectively. Therefore, Eqs. (3.15a), and (3.15b) can be expressed as:

$$\theta_s = \left(\Delta\theta_{sp} + \Delta\theta_{Lp}\right) + (\theta_{rs} + \theta_{rL}) \tag{3.17}$$

where $\Delta\theta_{sp}$ and $\Delta\theta_{Lp}$ are the differences between saturated and residual volumetric water content for the micropores and the macropores, respectively.

If Eq. (3.17) is separated into two parts that correspond to the micropores and the macropores, the following equations are derived:

$$\theta_s = (\Delta\theta_{sp} + \theta_{rs}) + (\Delta\theta_{Lp} + \theta_{rL}) \tag{3.18}$$

$$\theta_{ss} = \Delta\theta_{sp} + \theta_{rs} \tag{3.19a}$$

$$\theta_{sL} = \Delta\theta_{Lp} + \theta_{rL} \tag{3.19b}$$

Some key observations can be derived from the Eqs. (3.18) and (3.19). These equations suggest that the total variation of volumetric water content for bimodal SWCC can be regarded as the

sum of water content variations of the micropores and the macropores; in addition, they can be performed independently. These equations are valuable; however, they do not provide the required information to link PoSD curve to the bimodal SWCC. The peak points from the micropores to the macropores can be clearly distinguished for most soils, as shown in Figure 3.2. The boundary between the macropores and the micropores however remains questionable for some soils (Miguel and Bonder, 2012). Such a behavior can be attributed to the pore sizes that are not constant under various scenarios for some soils, e.g., expansive clays (Vanapalli et al., 1999; Gitirana Jr and Fredlund, 2004; Zhou, 2013).

3.3.2 Hypothesis to relate bimodal SWCC equations

To alleviate the limitations discussed in the earlier paragraph, another hypothesis, which is referred to as hypothesis II is proposed to explain the bimodal nature of the SWCC. As shown in Figure 3.3, the interaction zone in the PoSD curve predominantly influences the behavior of bimodal SWCC in stage II. This is the only zone that is influenced by both the macropores and the micropores. This hypothesis suggests that there is combined contribution of both macropores and the micropores to the bimodal SWCC in stage II (as shown in Figure 3.3). The boundary between the macropores and micropores is difficult to distinguish from the PoSD curve. However, the interaction zone in the PoSD curve (i.e., stage II in bimodal SWCC) can be determined graphically based on this hypothesis. Therefore, functions of both the macropores and the micropores can be applied together to model the behavior in stage II.

A corollary can also be introduced extending hypothesis II. The micropores have little or no effect on stage I of the bimodal SWCC and the macropores have little or no influence on stage III of the bimodal SWCC, as per this corollary. This means that the macropores are filled with air at the end of stage II, while the micropores are filled with water at the start of stage II. This discussion suggests that it is reasonable to assume the behavior in stage II is influenced by both the macropores and the micropores. However, the exact contribution of the macropores and the micropores in PoSD curve to stage II is uncertain. Nevertheless, some relationships can be derived based on the hypothesis and the corollary, extending the graphical construction method (Vanapalli et al., 1998) as shown in Figure 3.3(b).

$$\Delta\theta_{Lp} = \Delta\theta_{Lp}^{H} - \alpha^{H}\Delta\theta_{M} \quad (3.20a)$$

$$\Delta\theta_{sp} = \Delta\theta_{sp}^{H} - (1 - \alpha^{H})\Delta\theta_{M} \quad (3.20b)$$

where $\Delta\theta_{Lp}^{H}$ is the difference of volumetric water content between saturated water content and the water content at the end of stage II, $\Delta\theta_{sp}^{H}$ is the difference of volumetric water content between the volumetric water content at the start of stage II and residual water content, $\Delta\theta_M$ is the volumetric water change at stage II, and α^H is the pore size influence factor. $\Delta\theta_{Lp}^{H}$, $\Delta\theta_{sp}^{H}$, and $\Delta\theta_M$ are all determined graphically (i.e., Fig. 3.3(b)), and the equations to find them from existing points are listed below:

$$\Delta\theta_{Lp}^{H} = \theta_s - \theta_{Mb} \tag{3.21a}$$

$$\Delta\theta_{sp}^{H} = \theta_{Ma} - \theta_r \tag{3.21b}$$

$$\Delta\theta_M = \theta_{Ma} - \theta_{Mb} \tag{3.21c}$$

where θ_{Ma}, and θ_{Mb} are the volumetric water content at points M_a and M_b, respectively.

The above equations can be used for developing relationships for volumetric water content using VG and FX equations to piecewise-form bimodal SWCC equations. For example, Eq. (3.10) can be modified to define stage I of the bimodal SWCC equation as given below:

$$\frac{\theta' - \theta_{rL}}{\Delta\theta_{Lp}} = \left[\frac{1}{1+(a_{v1}\psi)^{n_{v1}}}\right]^{m_{v1}} \tag{3.22}$$

where a_{v1}, n_{v1}, and m_{v1} are fitting parameters.

The pseudo volumetric water content θ' is introduced here because it needs to be converted into the global axis (i.e., the measured volumetric water content in bimodal SWCC, θ). To fit the entire bimodal SWCC based on Eqs. (3.18), (3.19a), and (3.19b), the pseudo water content θ' in the above equation (i.e., Eq. (3.22)) can be expressed as:

$$\theta' = \theta - \Delta\theta_{sp} - \theta_{rs} \tag{3.23}$$

The equation below is derived based on hypothesis II by incorporating Eqs. (3.20a), (3.20b), and (3.23) into Eq. (3.22):

$$\frac{\theta - \Delta\theta_{sp}^{H} + (1-\alpha^H)\Delta\theta_M - \theta_{rs} - \theta_{rL}}{\Delta\theta_{Lp}^{H} - \alpha^H\Delta\theta_M} = \left[\frac{1}{1+(a_{v1}\psi)^{n_{v1}}}\right]^{m_{v1}} \tag{3.24}$$

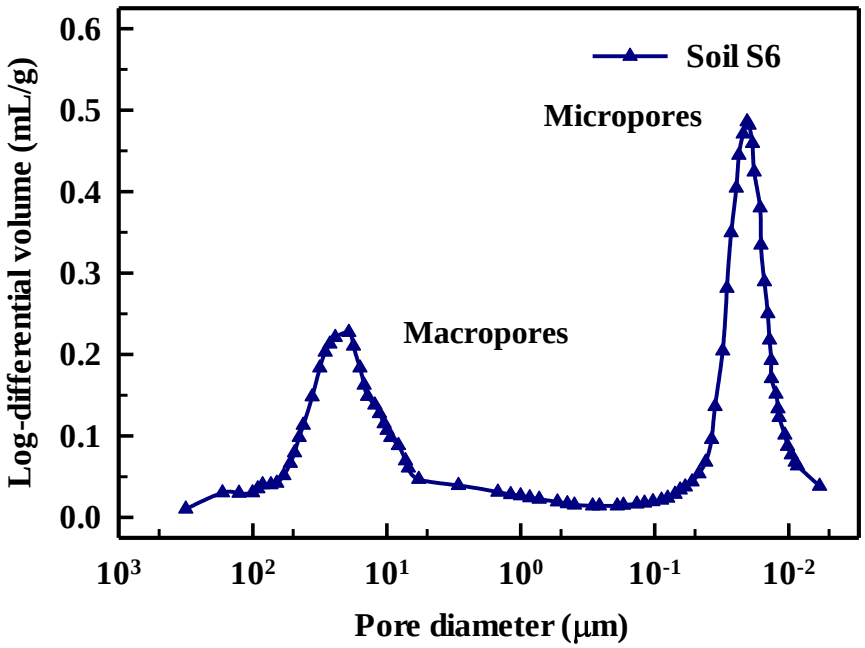

(a) Bimodal pore size distribution curve

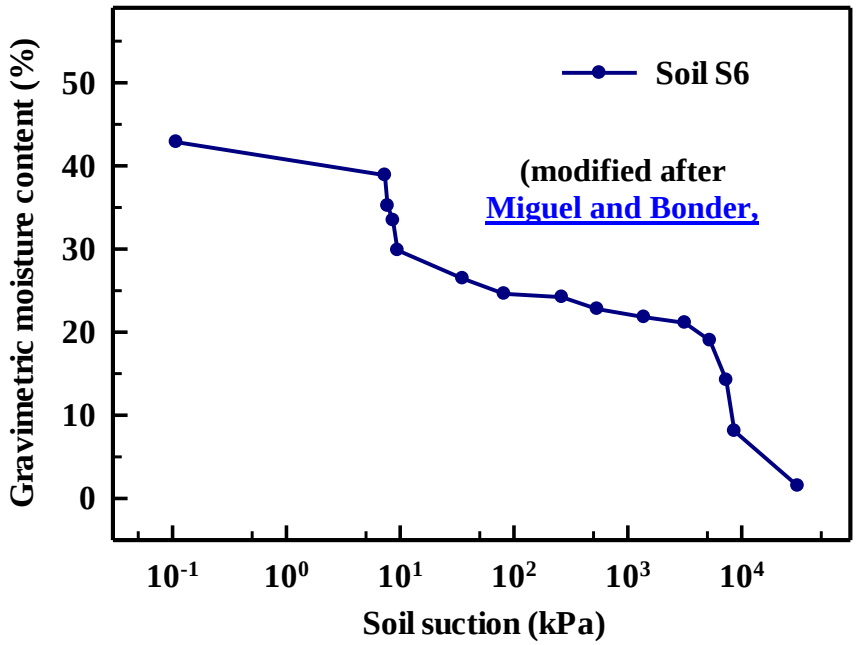

(b) The corresponding bimodal soil-water characteristic curves

Figure 3.2 Bimodal pore size distribution curve and corresponding SWCC.

From Eq. (3.16), Eq. (3.24) can be simplified as:

$$\frac{\theta-\Delta\theta_{sp}^{H}+(1-\alpha^{H})\Delta\theta_{M}-\theta_{r}}{\Delta\theta_{Lp}^{H}-\alpha^{H}\Delta\theta_{M}}=[\frac{1}{1+(a_{v1}\psi)^{n_{v1}}}]^{m_{v1}} \tag{3.25}$$

In the above equation, except α^{H}, the other four parameters on the left side (i.e., $\Delta\theta_{Lp}^{H}$, $\Delta\theta_{sp}^{H}$, $\Delta\theta_{M}$, and θ_{r}) can be determined extending graphical construction method (i.e., Figure 3.3(b)). For the bimodal SWCC equation in stage III, it can be expressed as:

$$\frac{\theta'-\theta_{rs}}{\Delta\theta_{sp}}=[\frac{1}{1+(a_{v3}\psi)^{n_{v3}}}]^{m_{v3}} \tag{3.26}$$

Based on hypothesis II and the corollary, in stage III, the macropores are filled with air. Thus, from Eq. (3.18), the pseudo water content θ' can be written as:

$$\theta'=\theta-\theta_{rL} \tag{3.27}$$

By substituting Eqs. (3.16) and (3.27) into Eq. (3.26), the following equation is derived:

$$\frac{\theta-\theta_{r}}{\Delta\theta_{sp}^{H}-(1-\alpha^{H})\Delta\theta_{M}}=[\frac{1}{1+(a_{v3}\psi)^{n_{v3}}}]^{m_{v3}} \tag{3.28}$$

Eqs. (3.25) and (3.28) describe the bimodal SWCC behaviors in stage I and III, respectively. The contribution of various types of pore structures can be evaluated by a parameter α^{H}, which is referred to as the pore size influence factor in stage II that takes account of both the macropores and micropores. However, the influence from the macropores and micropores can be different at various points in stage II. For example, the macropores may contribute more to the data close to M_a, while the micropores can exert more influence on the data points close to M_b as shown in Figure 3.3. Thus, it is reasonable to introduce a floating parameter β^{HD} to allocate the contribution of the macropores and the micropores to each point in stage II of the bimodal SWCC. Therefore, the volumetric water content in stage II (i.e., θ_{II}) can be expressed as:

$$\theta_{II}=(1-\beta^{HD})\theta_{I}+\beta^{HD}\theta_{III} \tag{3.29}$$

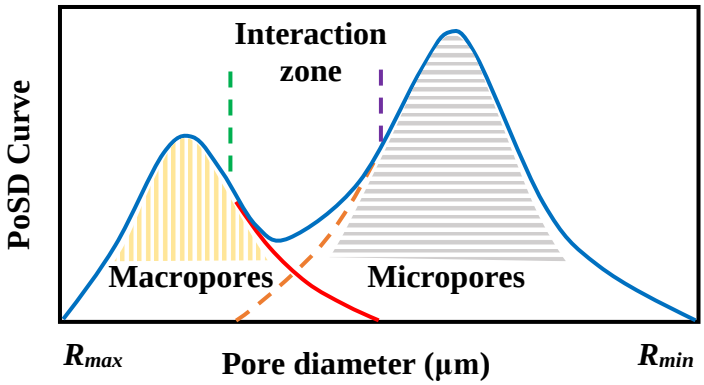

(a) Bimodal pore size distribution curve

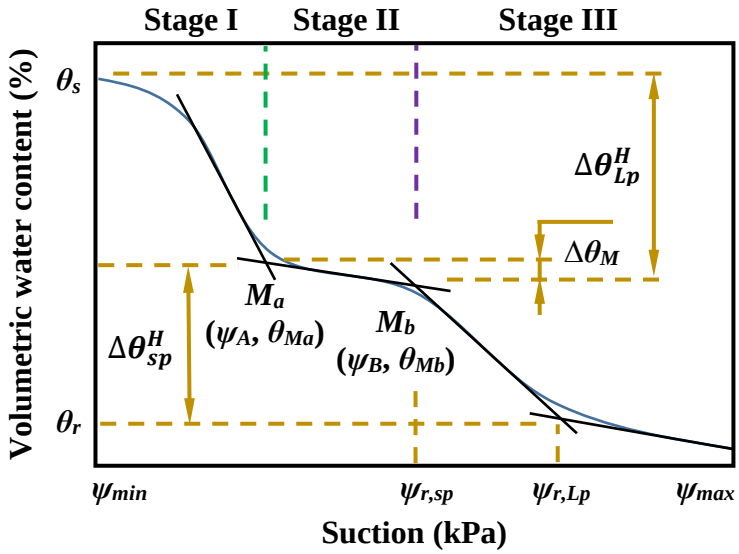

(b) The corresponding bimodal soil-water characteristic curves

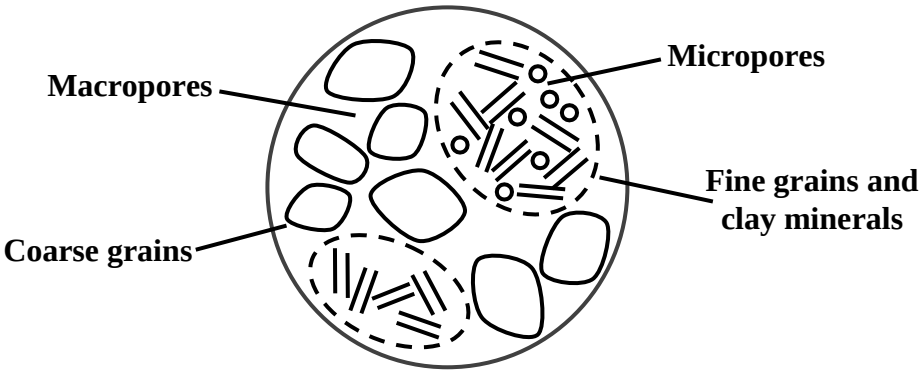

(c) Illustration of macropores and micropores

Figure 3.3 Conceptual model for bimodal SWCC.

where θ_I and θ_{III} are the volumetric water contents calculated from Eqs. (3.25), and (3.28) using soil suction in stage II, respectively. The floating parameter β^{HD} can be determined for each point in stage II as a function (i.e., $\beta^{HD} = \beta^{HD}(\psi)$). Since the pore size influence parameter α^H describes the entire contribution of the macropores and the micropores, the relationships can be expressed as below.

$$\alpha^H = \frac{1}{\psi_B - \psi_A} \int_{\psi_A}^{\psi_B} \beta^{HD}(\psi)\, d\psi \tag{3.30}$$

Based on Eqs. (3.25), (3.28), (3.29), and (3.30), the proposed bimodal SWCC equation equations are summarized as below:

$$\frac{\theta_I - \Delta\theta_{sp}^H + (1-\alpha^H)\Delta\theta_M - \theta_r}{\Delta\theta_{Lp}^H - \alpha^H \Delta\theta_M} = \left[\frac{1}{1+(a_{v1}\psi)^{n_{v1}}}\right]^{m_{v1}} \text{ for } \psi \le \psi_A \tag{3.31a}$$

$$\frac{\theta_{III} - \theta_r}{\Delta\theta_{sp}^H - (1-\alpha^H)\Delta\theta_M} = \left[\frac{1}{1+(a_{v3}\psi)^{n_{v3}}}\right]^{m_{v3}} \text{ for } \psi \ge \psi_B \tag{3.31b}$$

$$\theta_{II} = (1-\beta^{HD})\theta_I + \beta^{HD}\theta_{III} \text{ for } \psi_A < \psi < \psi_B \tag{3.31c}$$

$$\alpha^H = \frac{1}{\psi_B - \psi_A} \int_{\psi_A}^{\psi_B} \beta^{HD}(\psi)\, d\psi \tag{3.31d}$$

where the symbols θ_I, θ_{II}, and θ_{III} are used to distinguish the water content in stage I, II, and III, respectively.

In Eq. (3.31), as mentioned above, θ_I and θ_{III} are calculated from Eqs. (3.31a) and (3.31b) respectively using the suction range in stage II (i.e., from ψ_A to ψ_B in Figure 3.3(b)).

For the calibration of this equation (i.e., Figure 3.4(a)), parameters $\Delta\theta_{Lp}^H$, $\Delta\theta_{sp}^H$, and $\Delta\theta_M$ in Eqs. (3.31a), and (3.31b) can be determined based on a graphical construction method. First, a value from zero to one should be assumed for α^H. The fitting parameters a_{v1}, n_{v1}, and m_{v1} in stage I and a_{v3}, n_{v3}, and m_{v3} in stage III are calibrated using bimodal SWCC data in stage I and stage III, respectively. Second, θ_I and θ_{III} are calculated for the suction range in stage II, using parameters from the first step. This procedure facilitates calibrating β^{HD} from each point in stage II of the bimodal SWCC. Third, obtain new α^H by calculating β^{HD} from Eq. (3.31d) and check the difference between the calculated values. The calibration process is terminated if these two values are close (e.g., the difference is less than 0.0001). If this is not achieved, the

first step is repeated with the calculated α^H and iterative calibration is continued until appropriate parameters are found. In other words, a rigorous iteration technique is required for the calibration process.

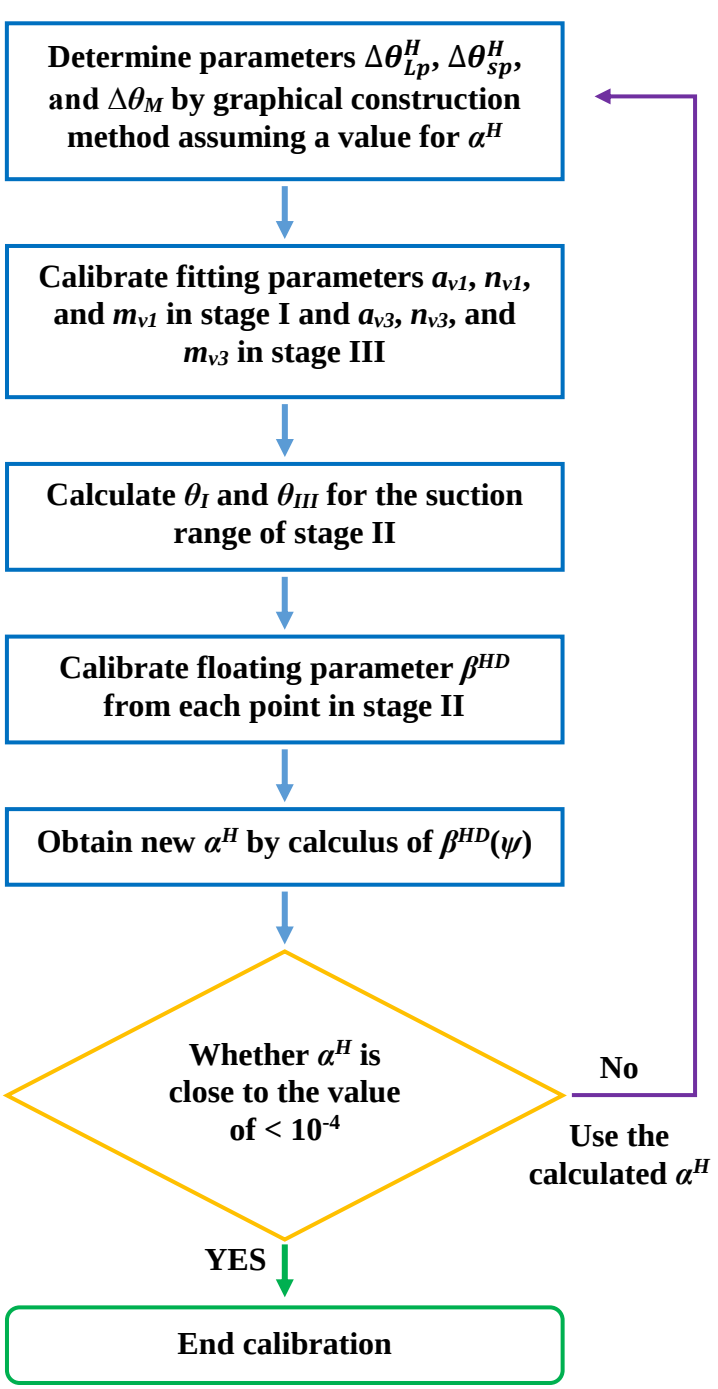

(a) Calibration process for the rigorous model

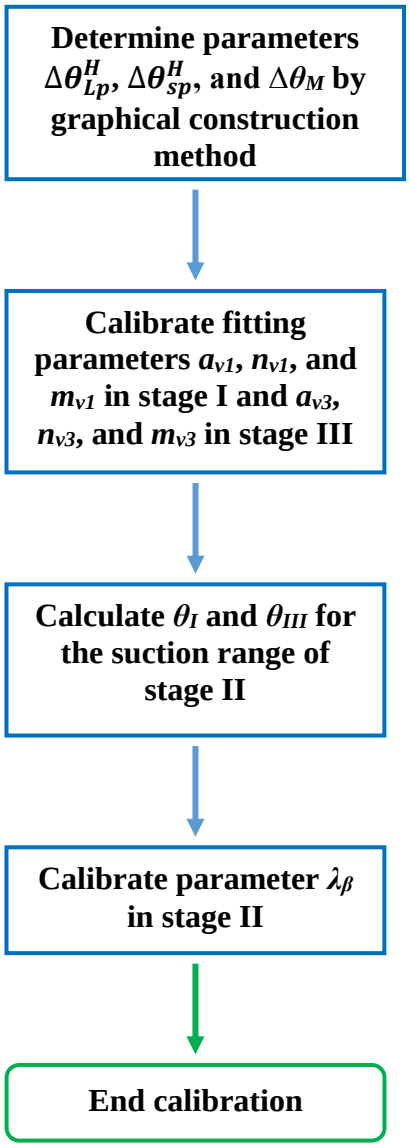

(b) Calibration process for the simplified model

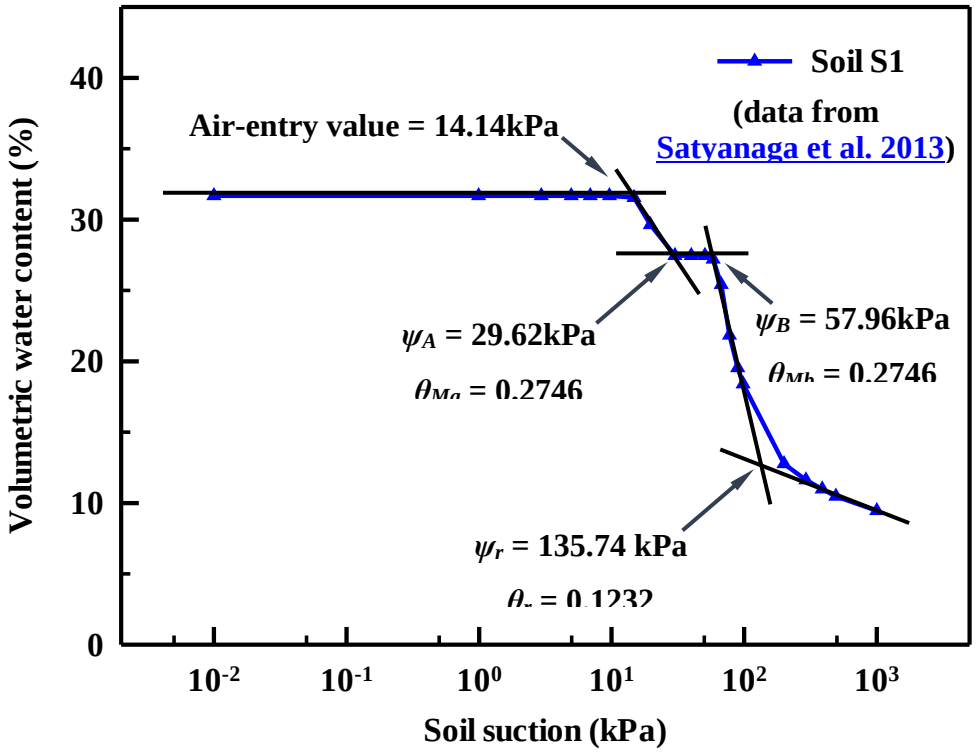

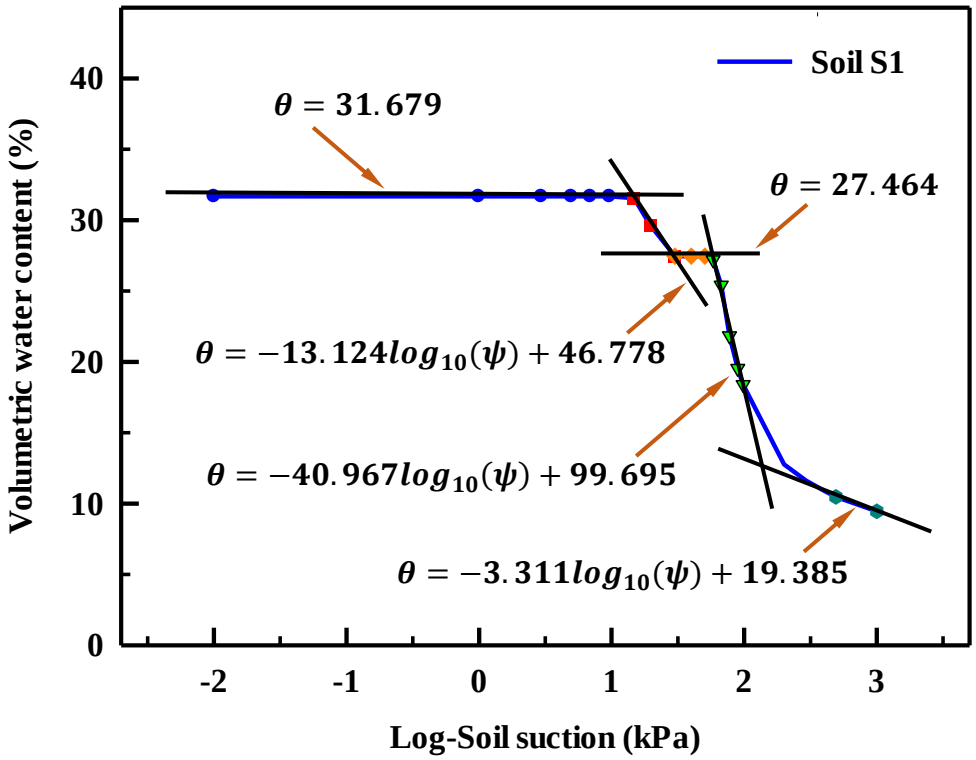

(c) Linear regression method to derive bimodal SWCC parameters

Figure 3.4 Calibration processes for proposed models.

The suitable parameters can be precisely determined by extending this calibration technique; however, it is tedious. In some scenarios, when the data for stage II of bimodal SWCC is limited (i.e., only a few data points are available), the calculation procedure for the two calibration steps may not provide a reliable value of α^H. The hypothesis II in certain scenarios, as discussed, cannot reliably determine the macropores and the micropores. For this reason, to alleviate these limitations, a simplified bimodal SWCC equation is proposed.

$$\frac{\theta_I - \Delta\theta_{sp}^H + \Delta\theta_M - \theta_r}{\Delta\theta_{Lp}^H} = \left[\frac{1}{1+(a_{v1}\psi)^{n_{v1}}}\right]^{m_{v1}} \quad \text{for } \psi \le \psi_A \tag{3.32a}$$

$$\frac{\theta_{III} - \theta_r}{\Delta\theta_{sp}^H} = \left[\frac{1}{1+(a_{v3}\psi)^{n_{v3}}}\right]^{m_{v3}} \quad \text{for } \psi \ge \psi_B \tag{3.32b}$$

$$\theta_{II} = \lambda_\beta \theta_I + (1-\lambda_\beta)\theta_{III} \quad \text{for } \psi_A < \psi < \psi_B \tag{3.32c}$$

where λ_β is a static model parameter.

This equation is relatively simple to derive volumes for both the micropores and the macropores in comparison with the rigid equation (i.e., Eqs. (3.31a), (3.31b), and (3.31c)). However, a larger range of the macropores and the micropores information is required for the development of each equation (i.e., Eqs. (3.32a), and (3.32b)) that can individually cover the entire variation of volumetric water content in stage II for the bimodal SWCC.

The calibration process for using simplified equations for bimodal SWCC is summarized with the aid of Figure 3.4(b). First, parameters $\Delta\theta_{Lp}^H$, $\Delta\theta_{sp}^H$, and $\Delta\theta_M$ in Eqs. (3.32a). and (3.32b) can be determined using the graphical construction method (i.e., Figure 3.3(b)). Second, Eqs. (3.32a), and (3.32b) can be used for fitting the measured bimodal SWCC data in stage I and III, respectively. The corresponding values of θ_I and θ_{III} can then be calculated using the suction range for stage II. Finally, Eq. (3.32c) can be calibrated from the measured points in stage II by finding a best-fit smoothening parameter λ_β value between zero to one. The λ_β value is set from zero to one based on the hypothesis II because it assumes that the volumetric water content in stage II is combined influenced by the macropores and the micropores.

A statistical linear regression method (Fomby et al. 1984) can be introduced to determine parameters $\Delta\theta_{Lp}^H$, $\Delta\theta_{sp}^H$, and $\Delta\theta_M$ as shown in Figure 3.4(c) to alleviate the graphical construction method. In this method, soil suction is expressed on a logarithmic scale to find a

linear part for each segment, and a linear regression equation for each segment of bimodal SWCC curve is individually developed. The merging point between two linear regressions equations approximately represents the same bimodal SWCC properties as derived from graphical construction method. The key advantage of the regression method is that it determines both the unimodal and bimodal SWCC parameters (for example, air-entry value, $\Delta\theta_{Lp}^{H}$, $\Delta\theta_{sp}^{H}$, $\Delta\theta_{M}$, θ_r, and ψ_r) based on statistical basis without the operator bias in the graphical construction method. In the present study, parameters for soils S1, S4 and S6 (Miguel and Bonder, 2012; Satyanaga et al., 2013) are highlighted by this method. Due to the calculation difficulties associated with the value of zero on logarithmic scale, the saturated water content is estimated for a soil suction value at 0.001 kPa for soils S1 and S4. For soil S6, the saturated water content is estimated as 0.4293 for soil suction at 0.1 kPa. Due to limited information, residual water contents are estimated as 0.090 and 0.015 for soils S1 and S6, respectively; and the residual suction is estimated as 300 kPa for soil S1.

The modified FX equation for the bimodal SWCC can be written as:

$$\theta_I = \left[1 - \frac{\ln\left(1+\frac{\psi}{\psi_{r,Lp}}\right)}{\ln\left(1+\frac{10^6}{\psi_{r,Lp}}\right)}\right] \frac{\theta_s}{\{\ln[e+(\psi/a_{f1})^{n_{f1}}]\}^{m_{f1}}} \qquad \text{for } \psi \le \psi_A \tag{3.33a}$$

$$\theta_{III} = \left[1 - \frac{\ln\left(1+\frac{\psi}{\psi_{r,sp}}\right)}{\ln\left(1+\frac{10^6}{\psi_{r,sp}}\right)}\right] \frac{\Delta\theta_{sp}^{H} - (1-\alpha^{H})\Delta\theta_M + \theta_r}{\{\ln[e+(\psi/a_{f3})^{n_{f3}}]\}^{m_{f3}}} \qquad \text{for } \psi \ge \psi_A \tag{3.33b}$$

$$\theta_{II} = (1-\beta^{HD})\theta_I + \beta^{HD}\theta_{III} \qquad \text{for } \psi_A < \psi < \psi_B \tag{3.33c}$$

$$\alpha^{H} = \frac{1}{\psi_B - \psi_A}\int_{\psi_A}^{\psi_B} \beta^{HD}(\psi)\, d\psi \tag{3.33d}$$

where $\psi_{r,sp}$ and $\psi_{r,Lp}$ are residual suction values for micropores and macropores, respectively and both of them can be determined using graphical construction method (Vanapalli et al., 1998) as shown in Figure 3.3(b). Here, $\psi_{r,Lp}$ is set as the same suction value as point M_b.

Based on above equations, a simplified equation can be expressed as below for calibration purposes.

$$\theta_I = \left[1 - \frac{\ln\left(1+\frac{\psi}{\psi_{r,Lp}}\right)}{\ln\left(1+\frac{10^6}{\psi_{r,Lp}}\right)}\right] \frac{\theta_s}{\{\ln[e+(\psi/a_{f1})^{n_{f1}}]\}^{m_{f1}}} \qquad \text{for } \psi \le \psi_A \tag{3.34a}$$

$$\theta_{III} = \left[1 - \frac{\ln\left(1+\frac{\psi}{\psi_{r,sp}}\right)}{\ln\left(1+\frac{10^6}{\psi_{r,sp}}\right)}\right] \frac{\Delta\theta_{sp}^{H} + \theta_r}{\{\ln[e+(\psi/a_{f3})^{n_{f3}}]\}^{m_{f3}}} \qquad \text{for } \psi \geq \psi_A \tag{3.34b}$$

$$\theta_{II} = \lambda_\beta \theta_I + (1 - \lambda_\beta)\theta_{III} \qquad \text{for } \psi_A < \psi < \psi_B \tag{3.34c}$$

The calibration processes for the above two sets of equations (i.e. Eqs. (3.33) and (3.34)) are similar to the modified VG equations for bimodal SWCC (i.e., Eqs. (3.31) and (3.32)). The summary of the calibration process is shown in Figure 3.4. The relationships between gravimetric, volumetric water content and degree of saturation (i.e., Eq. (3.35), Eqs. (3.31), (3.32), (3.33), and (3.34)) can be expressed as below.

$$S = \frac{w}{w_s} = \frac{\theta}{\theta_s} \tag{3.35}$$

where S is the degree of saturation, w is the gravimetric water content, w_s and θ_s are the saturated water content in gravimetric and volumetric forms.

The target function as introduced from Fredlund and Xing (1994) is used here to find the best-fitting parameters (i.e., a, m, and n). It is expressed as the sum of squared deviations of the measured water content θ_{obv} and the predicted values θ_{pred} as listed below:

$$O(a,m,n) = \min\left(\sum\left(\theta_{pred} - \theta_{obv}\right)^2\right) \tag{3.36}$$

where O () is the objective function, min () is the function to find minimum values. To compare the equation performance, the coefficient of determination (R^2) is adopted:

$$R^2 = \frac{[\sum_{i=1}^{N}(\theta_{obv} - \bar{\theta}_{obv})(\theta_{pred} - \bar{\theta}_{pred})]^2}{\sum_{i=1}^{N}(\theta_{obv} - \bar{\theta}_{obv})^2 \sum_{i=1}^{N}(\theta_{pred} - \bar{\theta}_{pred})^2} \tag{3.37}$$

where $\bar{\theta}_{obv}$ and $\bar{\theta}_{pred}$ are the mean values for the observed and the predicted water contents, respectively.

3.4 Results

Figure 3.5 presents performance of the modified VG equation for bimodal SWCC (i.e., Eq. (3.32)). Four sand-silt mixtures (i.e., soils S1-S4) are gathered from the literature (Satyanaga

et al., 2013). For each soil, three stages in the bimodal SWCC are highlighted. The modified VG equations for the bimodal SWCC are compared with the measured SWCC. All the equation parameters are determined by the described calibration procedures as shown in Figure 3.4(b). The parameter details and references are listed in Table 3.2.

The R^2 values for all soils are above 0.990; the value for soil S4 is a little lower at 0.994 because a few predicted points depart slightly from the measured data. The curve shapes reveal that all the features that include air-entry and residual suction values of the macropores and the micropores, respectively are fully captured by the modified VG equations for bimodal SWCC. Both statistical indices and curve shapes suggest that the modified VG equations can be used in the reliable prediction of the bimodal SWCCs with a high degree of accuracy.

Figure 3.6 highlights the details of fitting performance by modified FX equation for bimodal SWCC (i.e., Eq. (3.34)). The various parameters associated with this equation are summarized in Table 3.2. The R^2 values are above 0.995 for all bimodal SWCCs suggesting that most of the prediction points are close to the measured data. Only a few data points slightly deviate from the measured values. The bimodal SWCC shapes are well captured by the extended equation. Most importantly, key details of the macropores and the micropores are fully described including the information of air-entry and residual suction values.

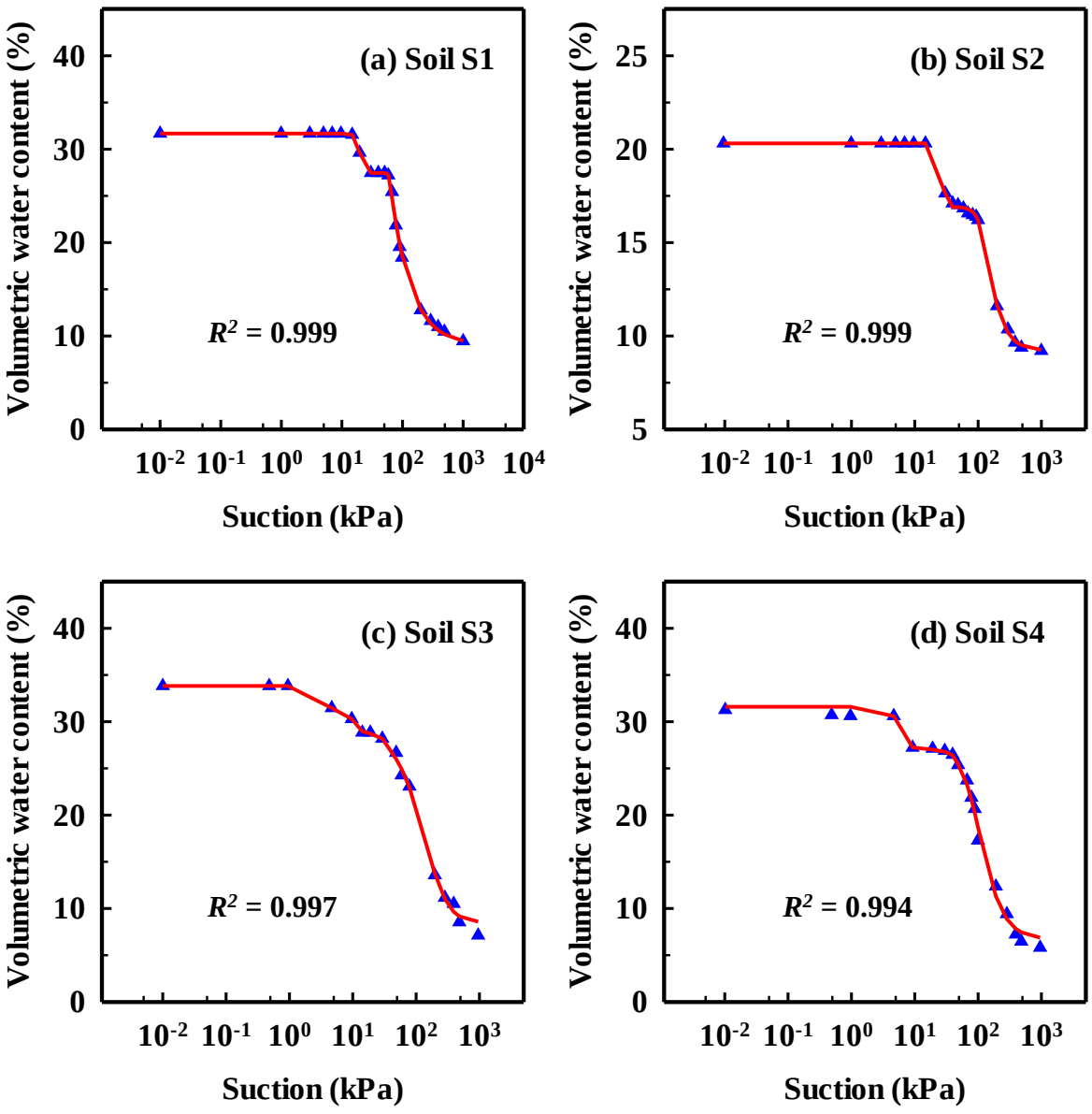

Figure 3.5 Best-fit bimodal SWCC results using the modified VG model.

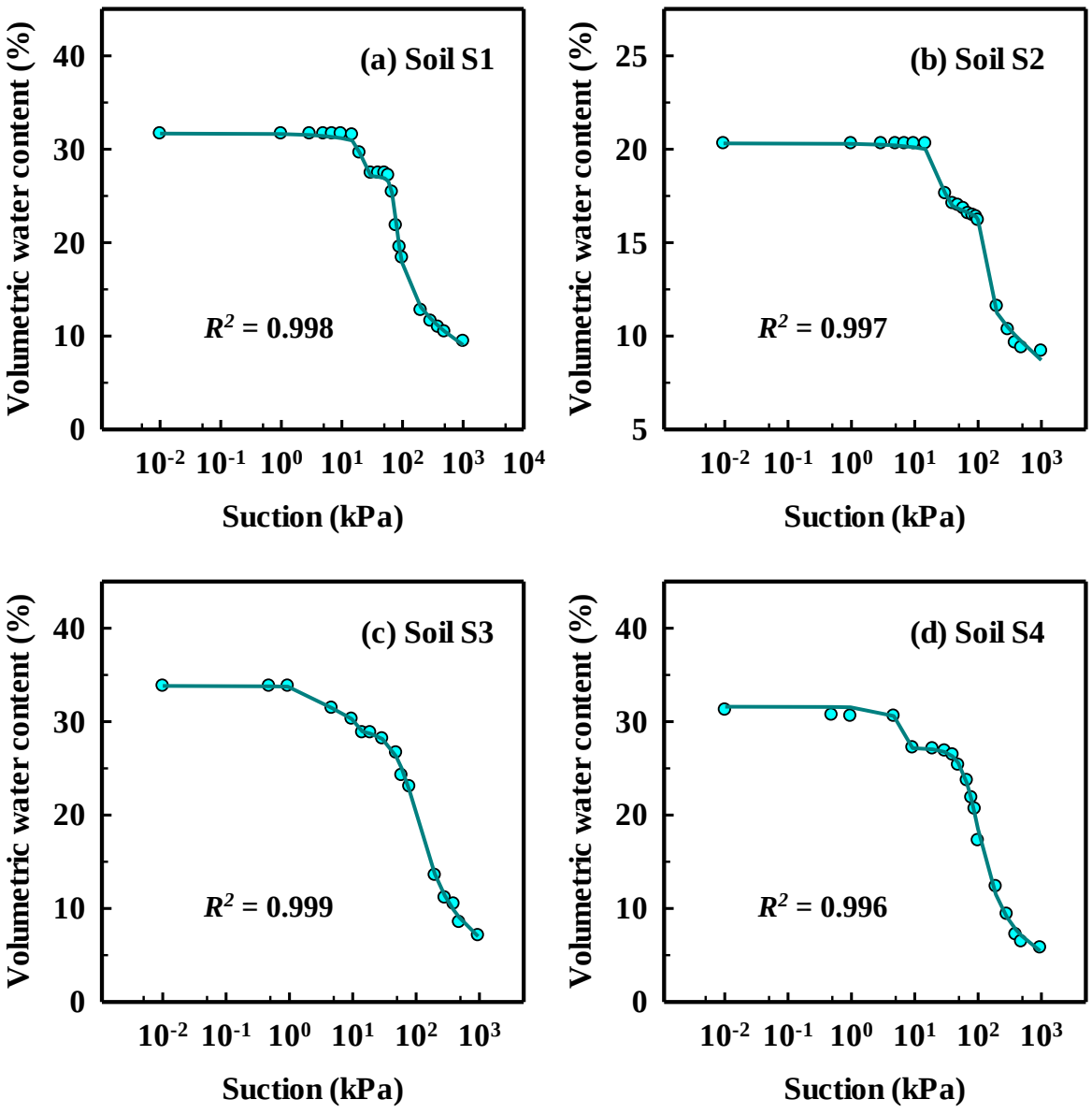

Figure 3.6 Best-fit bimodal SWCC results using the modified FX model.

Table 3.2 Model parameters for the proposed simplified models.

Soil #	θ_s / %	θ_a / %	θ_b / %	θ_r / %	a_{v1}	n_{v1}	m_{v1}	a_{v3}	n_{v3}	m_{v3}	λ_β	References
S1	31.68	27.46	27.46	9.0	0.0434	11.034	4.280	0.0168	42.159	0.0308	1.000	Satyanaga et al. (2013)
S2	20.31	17.10	16.25	9.2	0.0310	24.658	5.261	0.00815	5.459	0.436	0.223	Satyanaga et al. (2013)
S3	33.82	28.84	28.18	8.5	0.519	16.160	0.0380	0.00530	1.806	1.838	0.348	Satyanaga et al. (2013)
S4	31.60	27.25	26.82	6.68	0.0410	3.422	68.899	0.0106	2.897	0.692	0.368	Satyanaga et al. (2013)
S6	42.93	28.67	20.18	1.5	0.150	167.196	0.0140	9.99×10^{-6}	2.329	385.464	0.575	Miguel and Bonder (2012)

Soil #	θ_a / %	θ_r / %	$\psi_{r,lp}$ / kPa	$\psi_{r,sp}$ / kPa	af_1	nf_1	mf_1	af_3	nf_3	mf_3	λ_β	References
S1	27.46	9.0	57.96	300	18.310	43.521	0.0323	68.782	12.915	0.257	0.000	Satyanaga et al. (2013)
S2	17.10	9.2	99.3	400	21.266	41.276	0.0416	100.061	41.209	0.110	0.317	Satyanaga et al. (2013)
S3	28.84	8.5	39.0	480	2.560	9.772	0.0346	69.511	2.645	0.651	0.288	Satyanaga et al. (2013)
S4	27.25	6.68	45.44	382.84	4.613	330.761	0.0191	73.749	3.628	0.644	0.000	Satyanaga et al. (2013)
S6	28.67	1.5	6243.61	10318.50	7.134	87.831	0.101	9455.557	1.838	3.652	1.000	Miguel and Bonder (2012)

The modeling results for Eqs. (3.31) and (3.33) are shown in Figure 3.7 using the data of two soils (i.e., soils S2 and S4). The model parameters and the related references (Satyanaga et al., 2013) are listed in Table 3.3. The R^2 values for Figures. 3.7(a) and (b) are 0.999 and 0.994, respectively. The rigid VG equation (i.e., Eq. (3.31)) is used for soil S2 and S4, respectively in Figures 3.7(a) and (b), which also highlights the variation of floating parameter β^{HD} along with soil suction in stage II. All the information required for the bimodal SWCC is captured by the rigid VG equation; more importantly, the key features of the bimodal SWCC in stage II are fully described by the equation. For soil S4, as shown in Figure 3.7(b), the rigid VG equation performance is a bit weaker when the suction value is high (i.e., around 10^3 kPa) due to overestimated residual water content caused by limited data in the high suction range.

Figures 3.7(c) and (d) present results of the rigid FX equation (i.e., Eq. (3.33)) along with the corresponding floating parameter, β^{HD} values for soils S2 and S4, respectively. R^2 values for soils S2 and S4 are 0.997 and 0.996, respectively. The rigid FX equation has slightly better performance in comparison to the rigid VG equation results as shown in Figures 3.7(a) and (b). The variance of β^{HD} for soil S2 in the rigid FX equation is similar to the value in rigid VG equation (i.e., Figure 3.7(a)); however, it is better for soil S4 because of better performance in high suction ranges. Since β^{HD} values are determined via each point in stage II, the variance in soil S2 reveals that the significance of the macropores and the micropores varies along with the suction. It suggests that hypothesis II is rigorous and reasonable (i.e., the micropores and the macropores exert distinct effects on stage II).

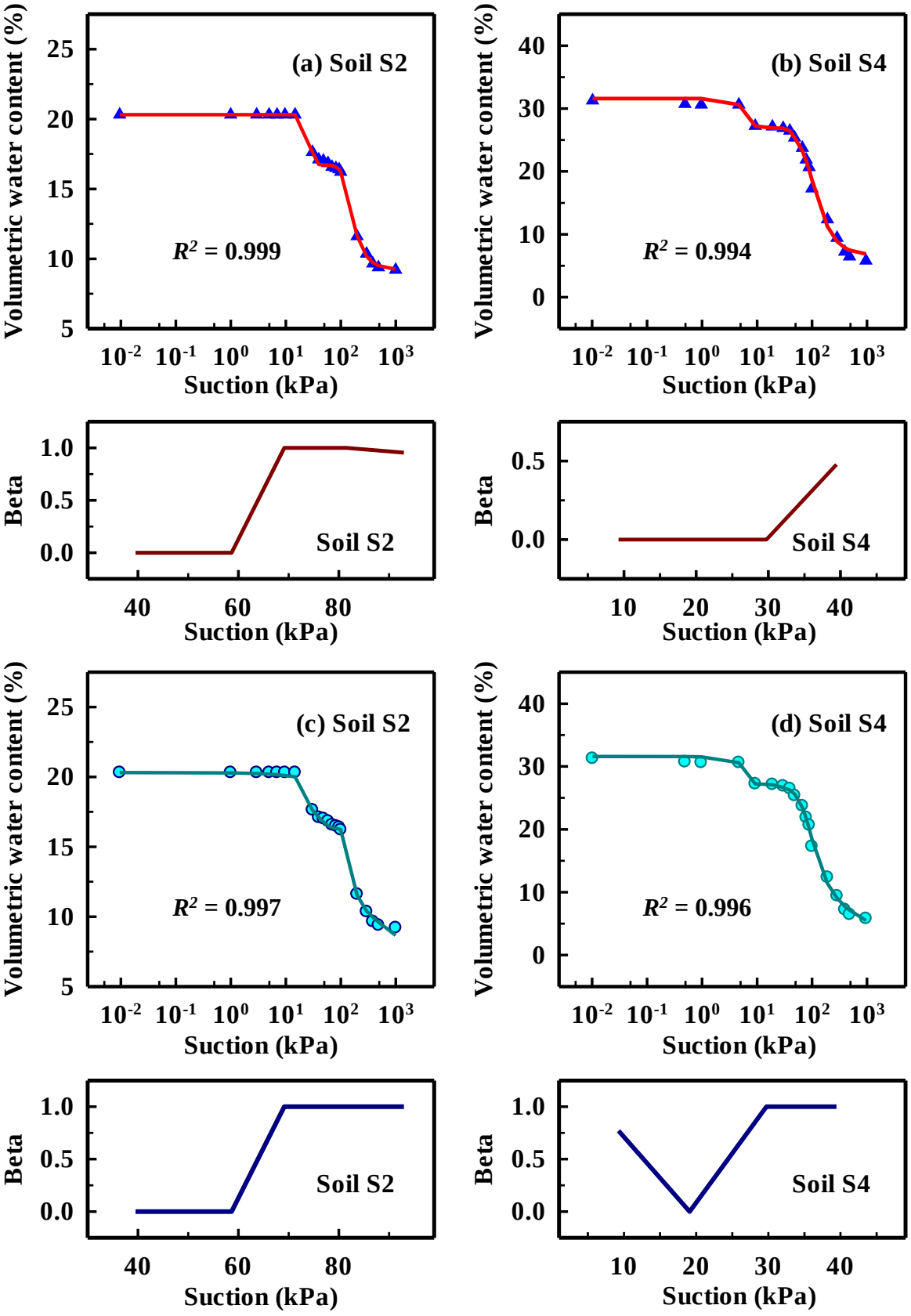

Figure 3.7 Model results for bimodal SWCC using the rigid models.

Table 3.3 Model parameters for the proposed rigid models.

Soil #	θ_s / %	θ_a / %	θ_b / %	θ_r / %	a_{v1}	n_{v1}	m_{v1}	a_{v3}	n_{v3}	m_{v3}	α^H	References
S2	20.31	17.10	16.25	9.2	0.0369	35.377	0.335	0.00810	6.895	0.340	0.5391	Satyanaga et al. (2013)
S4	31.60	27.25	26.82	6.68	0.230	150.447	0.0226	0.0110	3.165	0.611	0.0767	Satyanaga et al. (2013)
Soil #	θ_a / %	θ_r / %	$\psi_{r,lp}$ / kPa	$\psi_{r,sp}$ / kPa	af_1	nf_1	mf_1	af_3	nf_3	mf_3	α^H	References
S2	17.10	9.2	99.3	400	21.148	39.364	0.0421	164.212	394.320	0.0737	0.5439	Satyanaga et al. (2013)
S4	27.25	6.68	45.44	382.84	4.613	330.761	0.0191	74.060	3.853	0.620	0.6232	Satyanaga et al. (2013)

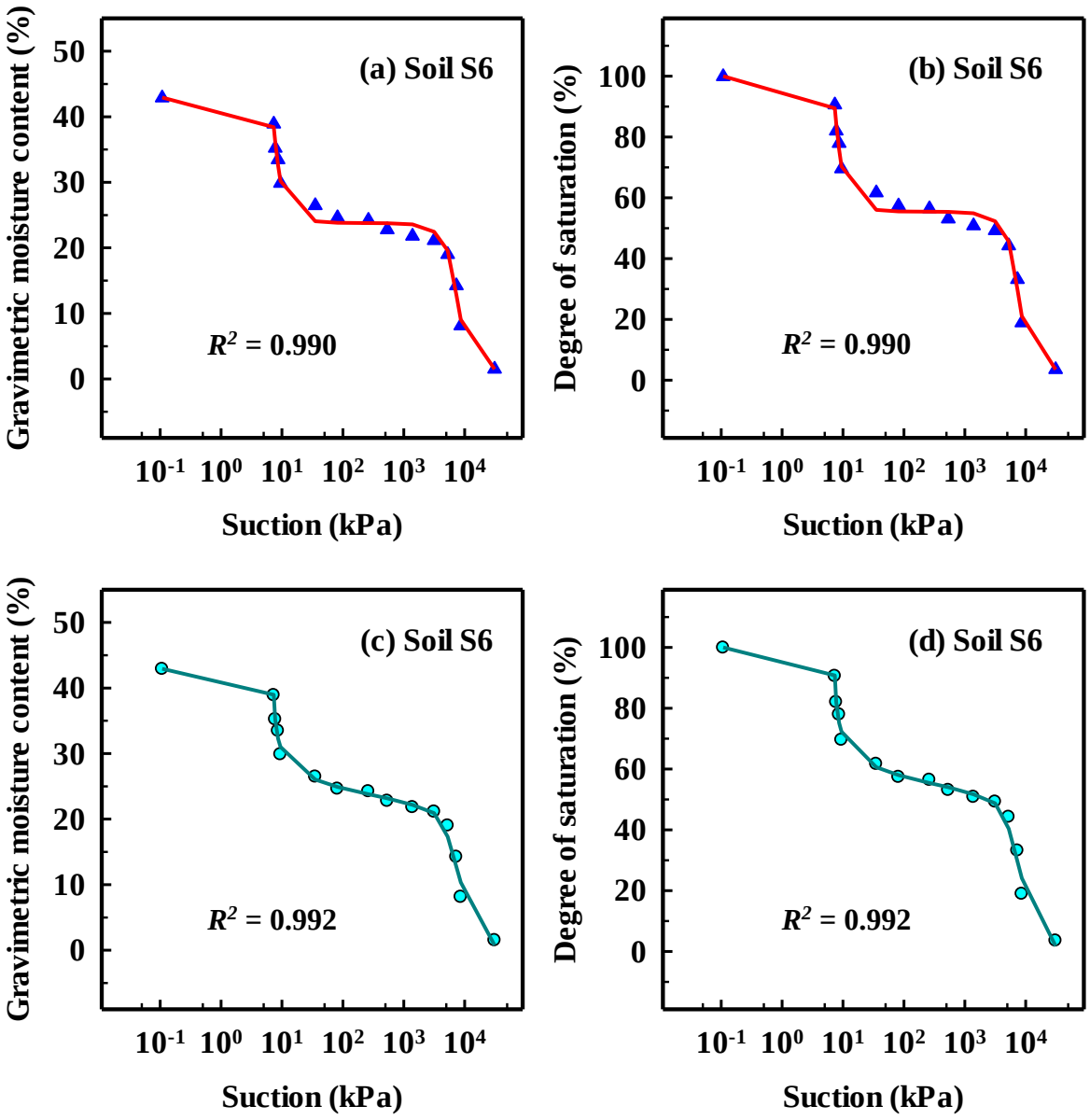

Note: Figures. 3.8(a) and (b) are calibrated based on modified VG model; Figures. 3.8(c) and (d) are based on modified FX model proposed in the manuscript.

Figure 3.8 Bimodal SWCC equations expressed as relationships between degree of saturation and suction and gravimetric water content versus suction.

Figure 3.8 presents the results of the modified VG and FX equations for bimodal SWCC as variations of gravimetric water content and degree of saturation versus suction for sandy-silt clay, respectively (i.e., for soil S6 (Miguel and Bonder, 2012)). The calibration process is based on Figure 3.4(b) and the parameters for the modified VG equation (i.e., Figures 3.8(a) and (b)) and FX (i.e., Figures 3.8(c) and (d)) equation are listed in Tables 3.2. The R^2 values for these four figures are around 0.990. The predicted values in stage II slightly depart from the measured points by using parameter λ_β which describes the overall contribution of micropores and macropores using the proposed simplified VG model (i.e., Eq. (3.32)) (Figures 3.8(a) and (b)). Except for the intersection point, the bimodal SWCC shapes in expression of gravimetric water content and degree of saturation are also reasonably described by both the modified VG and FX equations. These results suggest that Eqs. (3.32) and (3.34) can also be converted to accurately describe bimodal SWCC behaviors using expressions of gravimetric water content and degree of saturation instead of volumetric water content.

Figure 3.9 shows the bimodal SWCC fitting results using the first method from the literature (i.e., Eq. (3.1)). The parameter details of Soils S2 and S4 are highlighted and listed in Table 3.4. Figures 3.9(a) and (b) use van Genuchten (1980) equation, while equations in Figures 3.9(c) and (d) are based on Fredlund and Xing (1994) equation. R^2 values for soil S2 in Figures 3.9(a) and (c) are 1.000 and 0.997, respectively; these values for soil S4 in Figures 3.9(b) and (d) are 0.994 and 0.996, respectively. The equation shapes both for soils S2 and S4 are close to the measured data. Since only one merging point is adopted in the first method (i.e., Eq. (3.1)), it is easy to calibrate the equation; however, the fitting parameters are distinct with various merging points (Satyanaga et al., 2013; Wijaya and Leong, 2016).

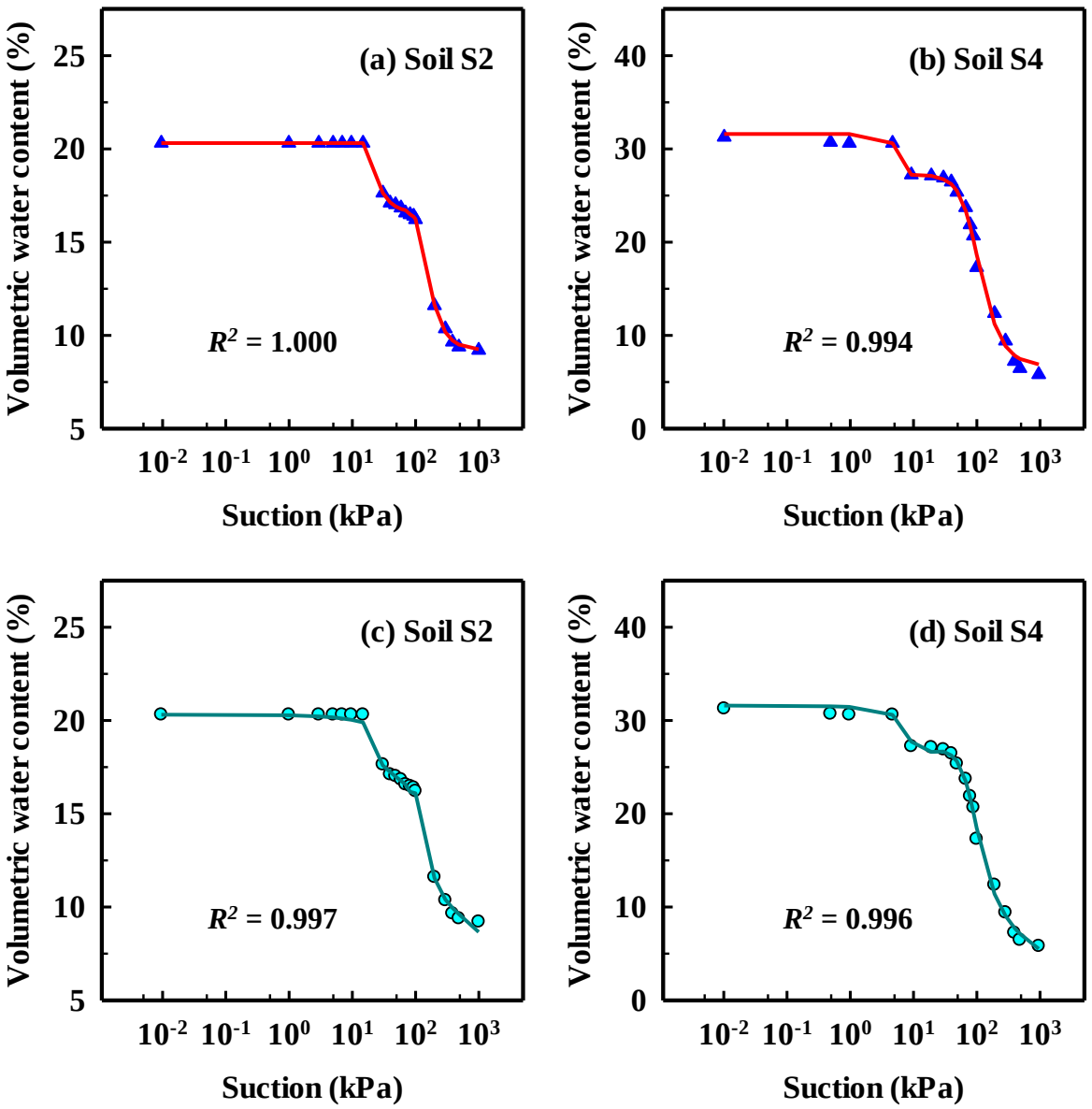

Note: Figures. 3.9(a) and (b) are based on VG model, while Figures. 3.9(c) and (d) are based on FX model extending method one (i.e., Eq. (3.1)).

Figure 3.9 Bimodal SWCC model results using method one.

Table 3.4 Model parameters for method one from the literature.

Soil #	θ_s / %	θ_r / %	θ_j / %	a_{v1}	n_{v1}	m_{v1}	a_{v3}	n_{v3}	m_{v3}	References
S2	20.31	9.2	16.57	0.0552	40.594	0.0597	0.00809	7.968	0.292	Satyanaga et al. (2013)
S4	31.60	6.68	27.11	0.225	45.251	0.112	0.0112	3.162	0.606	Satyanaga et al. (2013)
Soil #	θ_j / %	$\psi_{r,lp}$ / kPa	$\psi_{r,sp}$ / kPa	af_1	nf_1	mf_1	af_3	nf_3	mf_3	References
S2	16.57	69.14	400	20.320	362.099	0.0211	165.494	396.031	0.0723	Satyanaga et al. (2013)
S4	27.11	19.09	382.84	4.641	501.879	0.0160	73.923	3.875	0.618	Satyanaga et al. (2013)

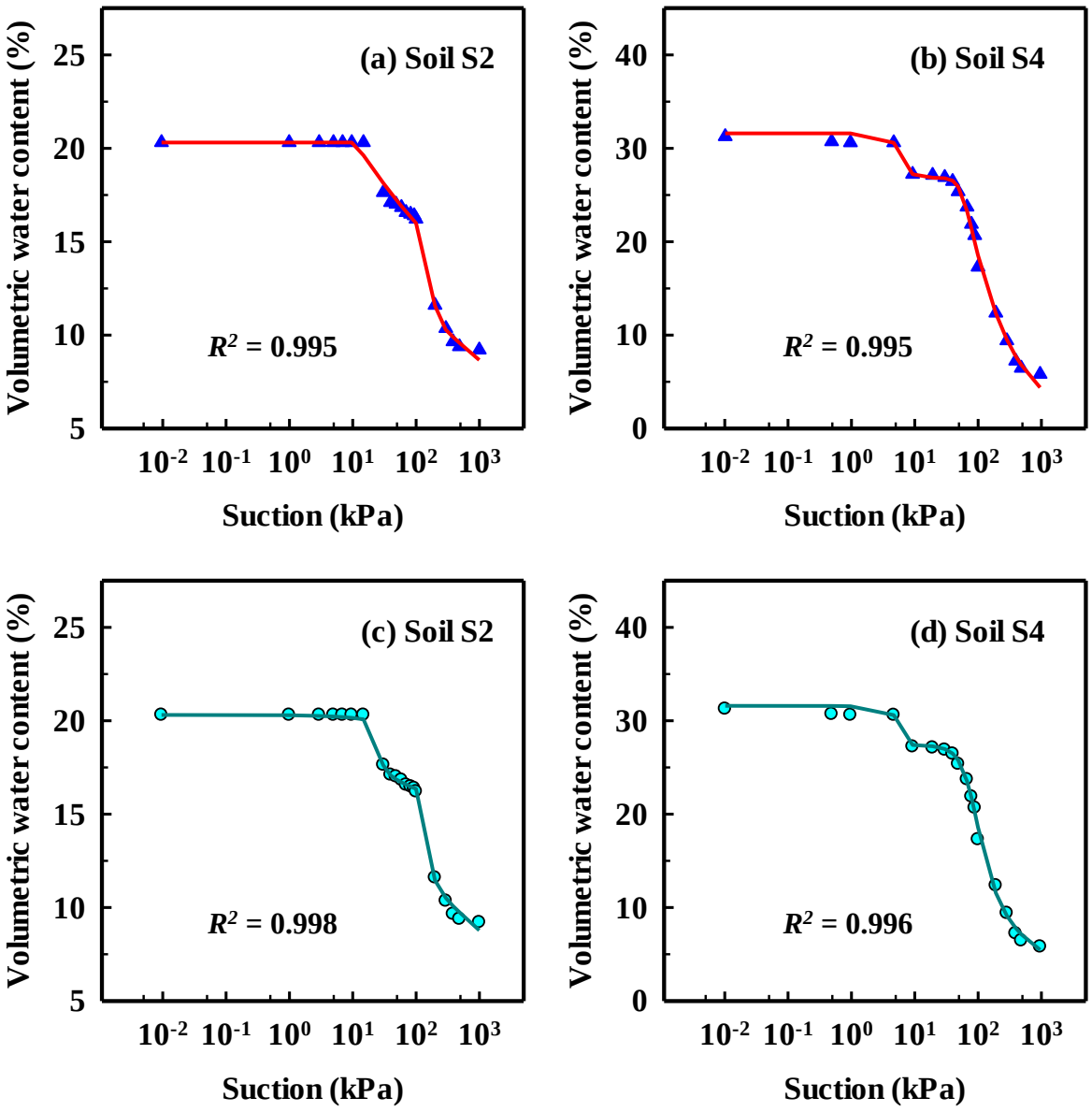

Note: Figures. 3.10(a) and (b) are based on modified VG model; Figures. 3.10(c) and (d) are based on modified FX model extending method two (i.e., Eq. (3.2)).

Figure 3.10 Bimodal SWCC model results by method two.

Table 3.5 Model parameters for method two from the literature.

Soil #	$\theta_{s,L}$ / %	$\theta_{s,s}$ / %	$\psi_{r,L}$ / kPa	$\psi_{r,s}$ / kPa	a_{v1}	n_{v1}	m_{v1}	a_{v3}	n_{v3}	m_{v3}	References
S2	16.25	4.06	-	-	0.0924	43.570	0.00319	0.00603	64.129	0.151	Satyanaga et al. (2013)
S4	4.74	26.86	-	-	0.0264	3.463	342.522	0.0178	5.975	0.107	Satyanaga et al. (2013)
Soil #	$\theta_{s,L}$ / %	$\theta_{s,s}$ / %	$\psi_{r,L}$ / kPa	$\psi_{r,s}$ / kPa	af_1	nf_1	mf_1	af_3	nf_3	mf_3	References
S2	3.86	16.45	30.3	400	21.979	11.055	0.779	150.931	376.672	0.0716	Satyanaga et al. (2013)
S4	4.11	27.49	9.19	382.84	4.704	146.873	2.952	73.346	3.608	0.647	Satyanaga et al. (2013)

Figure 3.10 presents the bimodal SWCC results from the second method in the literature (i.e., Eq. (3.2)). The results in Figures 3.10(a) and (b) are based on the modified VG equation, while Figures 3.10(c) and (d) adopt the modified FX equation. All the parameters are listed in Table 3.5. R^2 are 0.995 both for Figures 3.10(a) and (b), while the values are 0.998 and 0.996 for Figures 3.10(c) and (d), respectively. The equation shapes are close to the measured data and equations are continuous for the entire bimodal SWCC. However, close examination of stage II for Figures 3.10(a), (b), and (d) reveal that method two has limitations to describe all the features of bimodal SWCC because of the mutual influence of $f_1(\psi)$ and $f_2(\psi)$ in all the stages. In addition, as six fitting parameters (i.e., two groups of a, m, and n listed in Table 3.5) need to be calibrated simultaneously; extra costs are inevitable associated with computation time for this method and for developing algorithms to accelerate curve-fitting process.

3.5 Discussion

The hypothesis II can be explained using Figure 3.3 to highlight the influence of the macropores and the micropores. In the stage II, according to this hypothesis, the bimodal SWCC is influenced by the macropores and the micropores (i.e., interaction zone in PoSD curve) as shown in Figure 3.3. Second, the mapping of the interaction zone in PoSD curve is constrained to the stage II of bimodal SWCC. Due to this reason, in certain scenarios, the size of the micropores might be larger than that of the macropores. For example, if the soil pores are typically classified by their surrounding solid skeleton as shown in Figure 3.3(c), (i.e., macropores are formed by coarse-grains while micropores are generated by fine-grains and clay minerals); the soil pores may change when they are subjected to various states of stress (Li et al., 2009a, 2009b; Vanapalli, 2009; Zhang and Lin, 2019; Qiao et al. 2021). Hypothesis I (i.e., the local equilibrium hypothesis proposed by Mualem, (1976)) is acceptable for the interaction zone in PoSD curve if it corresponds to a part of bimodal SWCC. However, it is difficult to precisely determine the corresponding range in the bimodal SWCC for the interaction zone in the PoSD curve since the soil pore sizes are not constant. Generally, macropores have much larger pore sizes than the micropores; the drainage of water from macropores with low suction values can be modeled using Eq. (3.8). However, a smooth transition from macropores to micropores ensures a continuous curve for PoSD curve as shown in Figure 3.2(a). Therefore, hypothesis II is a better choice as it assumes that interaction zone in the PoSD cruve affects bimodal SWCC behavior only in stage II.

Typically, one or two discontinuous points are possible in the modified VG and FX equations

based on the value of λ_β. For example, only one discontinuous point arises when λ_β equals zero or one. For such a scenario, the modified equations are similar to the first category of methods from the literature (i.e., Eq. (3.1)). However, a close examination suggests it is slightly different from the first method because in this technique the merging point is determined arbitrarily for the modified VG and FX equations (i.e., Eqs. (3.32) and (3.34)). In other words, the merging point in this technique is a fixed point. When λ_β equals zero, the merging point is M_a in Figure 3.3(b); while it is point M_b as λ_β equals one. Two discontinuous points arise when λ_β is larger than zero and is less than one that can be identified as M_a and M_b, respectively. However, as most points are well defined in Eqs. (3.32) and (3.34), one or two discontinuous points have negligible effect on the entire bimodal SWCC (Satyanaga et al., 2013; Wijaya and Leong, 2016).

In rigid equations (i.e., Eqs. (3.31), and (3.33)), the calibration procedures are complex and each point in stage II is discontinuous. However, rigid bimodal SWCC equations provide comprehensive information about the macropores and the micropores. As shown in Figures 3.7(a) and (c), in each point the contribution that arises from various types of soil pores is different, which also supports validation for the hypothesis II, used in the present study.

For this method, parameters θ_s, $\Delta\theta_{Lp}^H$, $\Delta\theta_{sp}^H$, $\Delta\theta_M$, θ_r, $\psi_{r,sp}$ and $\psi_{r,Lp}$ can be determined by graphical construction method as shown in Figure 3.3(b) or by using the proposed linear regression method shown in Figure 3.4(c). These parameters determine the water content relationships for bimodal SWCC. Parameters a_{v1}, n_{v1}, m_{v1}, a_{v3}, n_{v3}, and m_{v3} in Eqs. (3.31) and (3.32) (or a_{f1}, n_{f1}, m_{f1}, a_{f3}, n_{f3}, or m_{f3} in Eqs. (3.33) and (3.34)) can be calibrated by experimental results in stage I and III through Eq. (3.36). These parameters are necessary both in method one and two as shown in Eqs. (3.1) and (3.2). Parameters α^H and β^{HD} in rigid models (i.e., Eqs. (3.31) and (3.33)) or parameter λ_β in simplified models (i.e., Eqs. (3.32) and (3.34)) are calibrated by experimental results in stage II. Except parameters determined from bimodal SWCC shapes (i.e., parameters θ_s, $\Delta\theta_{Lp}^H$, $\Delta\theta_{sp}^H$, $\Delta\theta_M$, θ_r, $\psi_{r,sp}$ and $\psi_{r,Lp}$), only one or two parameters are newly introduced. These parameters (i.e., parameters α^H and β^{HD} for rigid models or parameter λ_β for simplified models) are adopted to show water content variation in stage II.

As listed in Tables 3.2 and 3.3, λ_β value varies with soils; however, similar value is obtained

for the same soil in spite of using different equations (i.e., modified FX or VG equation). For example, for soil S3, λ_β equals 0.348 for the modified VG equation, while it is 0.288 for the modified FX equation. These values approximately indicate the rough contribution percentiles from the macropores and the micropores. However, this value only varies significantly for one soil (i.e., α^H values for Soils S1 and S6) listed in Table 3.2. This is caused by the distinct curve shapes resulted from various equations in stage II. To obtain better results, several points in stage II could be introduced to calibrate equations applying for stages I and III.

In the proposed equations (i.e., Eqs. (3.32), and (3.34)), the stage II is determined from the calibrated equation in stage I and III based on the hypothesis II. However, this method is the same as the first method in the literature if the mapping of the interaction zone in PoSD curve to bimodal SWCC is a single point or parameter λ_β equals zero or one (i.e., Eq. (3.1)). This method falls in the category of the second method in the literature (i.e., Eq. (3.2)) when the mapping of the interaction zone is extended to the bimodal SWCC for the entire suction range. Therefore, the proposed method is an extension of both methods one and two. In summary, this method can be written as:

$$\theta(\psi) = \begin{cases} f_1(\psi) & \psi \le \psi_A \\ \lambda_\beta f_1(\psi) + \left(1-\lambda_\beta\right) f_3(\psi) & \psi_A < \psi < \psi_B \\ f_3(\psi) & \psi \ge \psi_B \end{cases} \tag{3.38}$$

or

$$\theta(\psi) = [f_1(\psi)]_{\mathrm{I}} + \left[\lambda_\beta f_1(\psi) + \left(1-\lambda_\beta\right) f_3(\psi)\right]_{\mathrm{II}} + [f_3(\psi)]_{\mathrm{III}} \tag{3.39}$$

where the symbol $[]_{\mathrm{i}}$ in Eq. (3.39) determines the boundary (i.e., stages I, II, and III in bimodal SWCC) applied to inside function.

3.6 Conclusions

In this Chapter, a reasonable hypothesis is introduced based on the features of pore-size distribution (PoSD) curve for predicting the bimodal soil-water characteristic curve (SWCC). From this hypothesis, volumetric water content relationships corresponding to the macropores and micropores in the PoSD curve for bimodal SWCC are developed. Two sets of bimodal SWCC equations are successfully derived from the traditional unimodal SWCC equations; namely, van Genuchten (1980) and Fredlund and Xing (1994) equations.

In addition, the calibration processes for the proposed equations are built. Graphical construction method and regression method are separately developed to estimate the key features for bimodal SWCC. The two parameters (i.e., pore size influence factor, α^H and best-fit smoothening parameter λ_β) were used as tools to evaluate the contribution of the micropores and macropores. Rational description of bimodal SWCC is possible using the proposed bimodal SWCC equations.

The proposed equations can be converted into the available methods in the literature for the bimodal SWCC based on the proposed hypothesis. The results summarized in this Chapter suggest that the proposed equations rigorously describe the bimodal SWCCs for various soils. These equations are promising for use as a continuous function for predicting unsaturated properties of the soils with dual pore structure. In addition, they can be used in numerical models for analyzing the complex behaviors of unsaturated soils.

CHAPTER 4

Models for Predicting the Soil-Water Characteristic Curves for Coarse and Fine-Grained Soils

4.1 Introduction

The relationship between water content (volumetric or gravimetric) or degree of saturation and the soil suction is referred to as the soil-water characteristic curve (SWCC). The SWCC is also widely referred to as the soil moisture curve and soil-water retention curve in the literature. Researchers during the past four decades focused on proposing models for predicting the SWCC in the literature since conventional measurement techniques are time consuming (e.g., Arya and Paris, 1981; Schaap et al., 2001; Chin et al., 2010; Li et al., 2016; Alves et al., 2020; Li and Vanapalli, 2022). The focus of most research studies was mainly directed towards predicting the main drying curve.

During last two decades, complex thermo-hydro-mechanical-chemo (THMC) behaviors of unsaturated soils were also analyzed by many researchers using the SWCC as a tool (e.g. Wheeler and Sivakumar, 1995; Gallipoli et al., 2003; Zhou et al., 2012b**;** Ni et al., 2019; Yang and Vanapalli, 2020; Xu et al., 2020; Rong and McCartney, 2021). The research related to the SWCC has wide applications in water resources, agriculture, soil science, geotechnical, and geo-environmental engineering fields (e.g., Nemes et al., 2001; Qi and Vanapalli, 2015; Cary and Zapata, 2016; Zhu et al., 2020; Cheng et al., 2021). The use of SWCC as a tool is receiving more attention in the recent literature for understanding the influence of climate change on the THMC behavior of unsaturated soils (Bai et al., 2020; Li et al., 2021).

A family of SWCC taking account of influence soil hysteresis is required for rigorous modeling of the soil behavior (Figure. 4.1 (i)). Two approaches are widely used for modeling hysteretic SWCC (Pham et al., 2005) in the literature; namely, physical-based (domain) models (e.g., Parlange, 1976; Mulem and Miller, 1979; Hogarth et al., 1988; Wei and Dewoolkar, 2006; Min and Huy, 2010; Zhou, 2013; Likos et al., 2014; Fu et al., 2020) and empirical models (e.g., Feng and Fredlund, 1999; Pham et al., 2003; Zhai et al., 2020).

Some of the contents presented in this chapter have been published in the Journal of Hydrology. Li, Y., and Vanapalli, S. K. (2022b). *Models for predicting the soil-water characteristic curves for coarse and fine-grained soils*. Journal of Hydrology, 612. doi: 10.1016/j.jhydrol.2022.128248.

Experimental studies from the literature suggest that the SWCC behavior is significantly influenced by the stress state and initial compaction water content that is strongly related to the pore structure in fine-grained soils (e.g., Vanapalli et al., 1999; Ng and Pang, 2000). During the last two decades, several models have been developed to incorporate the influence of initial stress state into SWCC (e.g., Wheeler et al., 2003; Gallipoli et al., 2003; Sun et al., 2007a; Tarantino and Col, 2008; Tarantino, 2009; Gallipoli, 2012; Zhou et al., 2012a; Hu et al., 2013; Zhou and Sheng, 2015). However, the initial water content has a significant influence on the soil-structure that impacts the SWCC behavior, especially in compacted fine-grained soils. The coupled effects of both the initial stress state and initial water contents are not typically incorporated into models for SWCCs. For this reason, there is a need for developing models taking account of the influence of various parameters to reliably predict the SWCCs. Such models would be valuable for various practical applications in water resources, agriculture, soil science, geotechnical, and geo-environmental engineering fields.

In this Chapter, simple, yet novel models are proposed for predicting the family of SWCCs (i.e., main drying and wetting SWCC along with scanning curves considering hysteretic nature) of coarse-grained soils from the pore-size distribution (PoSD) curve using a set of basic functions and boundary conditions. The SWCCs of fine-grained soils are also predicted considering the effects of initial stress state and soil structure associated with the initial water content based on the PoSD curve. The various proposed SWCC models in this study are presented in Figure. 4.1 (ii). Reasonable comparisons were achieved between the experimental and the predicted results of the SWCCs for both coarse and fine-grained soils.

The proposed models are valuable for use in numerical modeling of the complex THMC modeling problems and for predicting various properties of unsaturated soils considering the influences of wetting and drying cycles associated with environmental factors.

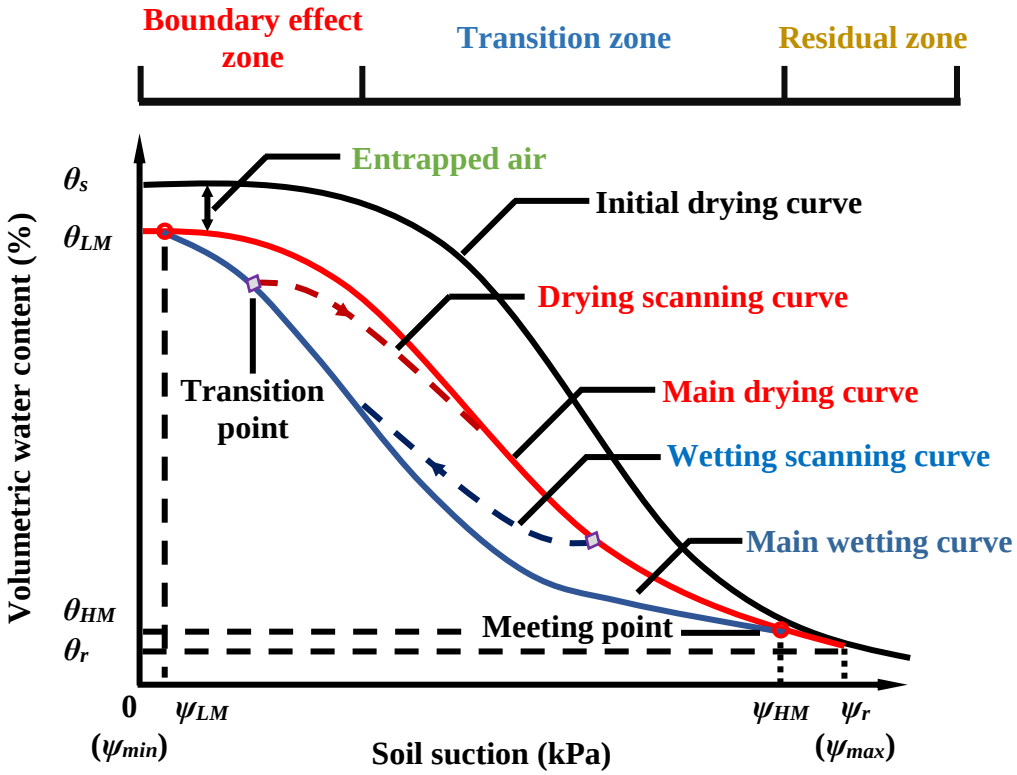

(i) Illustration of the SWCC with hysteresis behavior.

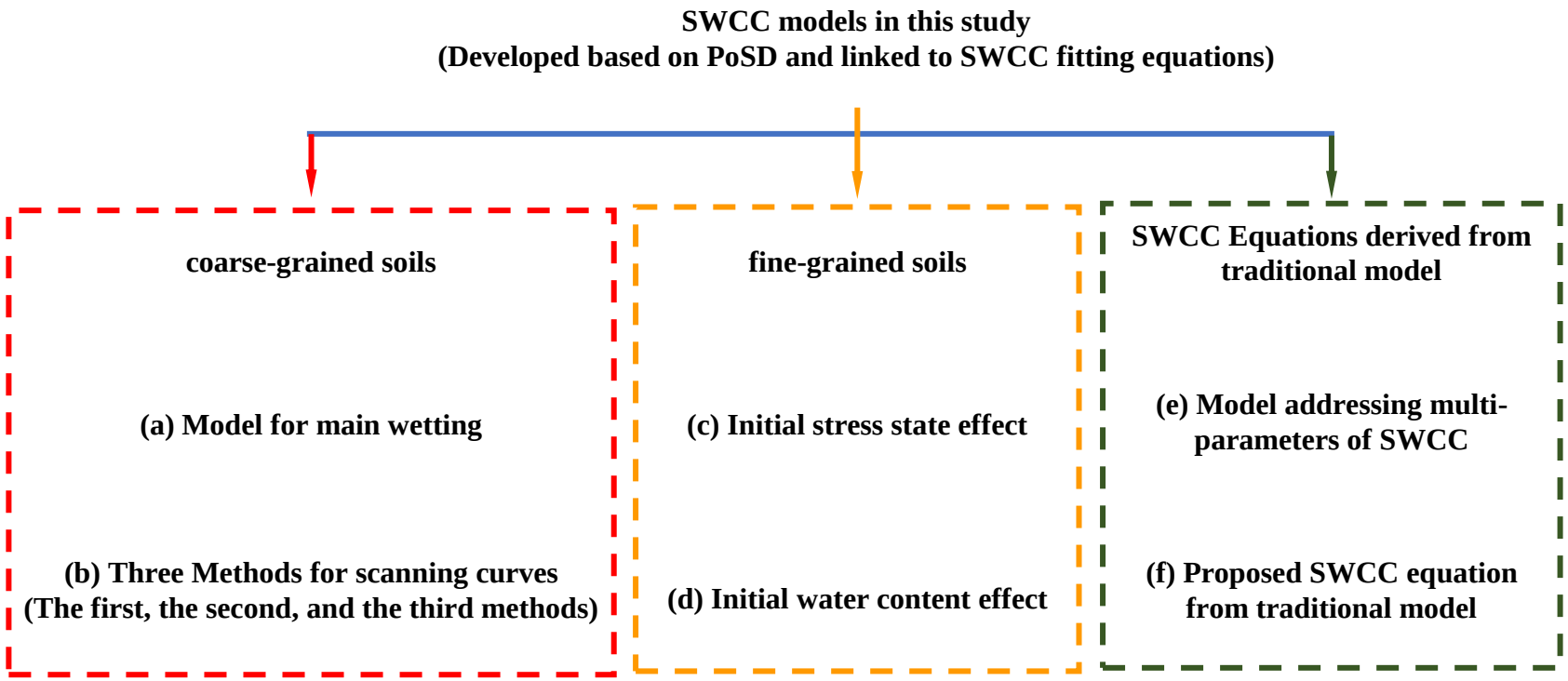

(ii) Proposed SWCC models in this study.

Figure 4.1 Hysteretic SWCCs and proposed SWCC models in this study.

4.2 SWCC models for coarse-grained soils

4.2.1 Model for main wetting curves

The family of SWCC that constitutes main drying and wetting curves taking account of hysteresis effects and scanning curves is required for rational interpretation of the soil behavior. The water content in the SWCC associated with the wetting branch is less than the drying branch at any given soil suction as shown in Figure 4.1 (i). Numerous drying and wetting scanning curves are possible within the main drying/wetting SWCCs. The major factors that influence the hysteretic SWCCs (Pham et al., 2005) include: (i) irregular pore structures inside soils or the 'ink-bottle' effect; (ii) the contact angle variation during drying and wetting processes; (iii) entrapped air during wetting; (iv) thixotropic regain or aging due to the wetting-drying cyclic history.

Water in soils is stored in the interconnected pores (Vanapalli et al., 1996; Li and Vanapalli, 2021), and the pores with radii r can be reasonably described by their pore-size distribution $P(r)$. When the pores with radius less than R are filled with water, the volumetric water content can be expressed as below (Fredlund and Xing, 1994).

$$\theta(R) = \int_{R_{min}}^{R} P(r)dr \tag{4.1}$$

where $\theta(R)$ is the volumetric water content when the pores with radius are smaller than R are filled with water, and R_{min} is the minimum pore size in soils.

The water stored in larger pores drain easily due to desaturation associated with an increase in the soil suction. Since the amount of water in pores can be characterized by pore size r, an inverse relationship between soil suction ψ and pore radius r is conventionally used (Fredlund and Xing, 1994) as shown in Eqs. (4.2).

$$\frac{1}{r} \propto \psi \tag{4.2a}$$

$$\psi = \frac{C}{r} = \frac{2T\cos\alpha}{r} \tag{4.2b}$$

where $C = 2T\cos\alpha$, T is surface tension (unit N·m), α is contact angle between soils and water.

The widely used capillary law (i.e., Eq. (4.2b)) can be introduced into Eq. (4.1) to obtain the

relationship below.

$$\theta(R) = \int_{\psi_{max}}^{\psi} P\left(\frac{C}{h}\right) d\left(\frac{C}{h}\right) = \int_{\psi}^{\psi_{max}} P\left(\frac{C}{h}\right) \frac{C}{h^2} dh \tag{4.3}$$

where h is a dummy variable of integration representing soil suction, and ψ_{max} is the maximum soil suction representing minimum pore radius.

Several SWCC equations have been successfully developed in the literature extending the above philosophy. Two equations (i.e., Eq. (4.4) and Eqs. (4.5)) proposed by van Genuchten (1980) and Fredlund and Xing (1994), respectively are widely used for modeling the SWCCs.

$$\frac{\theta-\theta_r}{\theta_s-\theta_r} = \left[\frac{1}{1+(a_v\psi)^{n_v}}\right]^{m_v} \tag{4.4}$$

$$\theta = C(\psi)\frac{\theta_s}{\{\ln[\exp(1)+(\psi/a_f)^{n_f}]\}^{m_f}} \tag{4.5a}$$

$$C(\psi) = 1 - \frac{\ln(1+\psi/\psi_r)}{\ln(1+10^6/\psi_r)} \tag{4.5b}$$

where θ_s and θ_r are saturated and residual volumetric water contents, respectively, exp () is exponential function, a_v, m_v, and n_v are van Genuchten (1980) equation fitting parameters, a_f, m_f, and n_f are Fredlund and Xing (1994) equation fitting parameters, C (ψ) is the correction function for Fredlund and Xing equation, and ψ_r is residual soil suction.

The corresponding PoSD functions for these two equations are summarized below.

$$g_{dry}(a_v, n_v, m_v, \psi) = \frac{m_v n_v a_v (a_v\psi)^{n_v-1}}{[1+(a_v\psi)^{n_v}]^{m_v+1}} \tag{4.6a}$$

$$f_{dry}(a_f, n_f, m_f, \psi) = \frac{m_f n_f (\psi/a_f)^{n_f-1}}{a_f[\exp(1)+(\psi/a_f)^{n_f}]\{\ln[\exp(1)+(\psi/a_f)^{n_f}]\}^{m_f+1}} \tag{4.6b}$$

where g_{dry} and f_{dry} are PoSD functions for drying branch by van Genuchten equation and Fredlund and Xing equation, respectively.

Several model parameters are typically suggested by various investigators (e.g., Zhou, 2013; Zhou and Sheng, 2015) for fitting wetting branches of SWCC. Eqs. (4.7) and (4.8) belong to this category that use fitting parameters a_v^{wet}(a_f^{wet}), n, and m.

$$\frac{\theta-\theta_{r,wet}}{\theta_s-\theta_{r,wet}} = \left[\frac{1}{1+(a_v^{wet}\psi)^{n_v}}\right]^{m_v} \tag{4.7}$$

$$\theta = C(\psi)\frac{\theta_s}{\{\ln\left[\exp(1)+(\psi/a_f^{wet})^{n_f}\right]\}^{m_f}} \tag{4.8a}$$

$$C(\psi) = 1-\frac{\ln(1+\psi/\psi_{r,wet})}{\ln(1+10^6/\psi_{r,wet})} \tag{4.8b}$$

where a_v^{wet} and a_f^{wet} are model parameters for main wetting curve in van Genuchten and Fredlund and Xing equations, respectively, and $\psi_{r,wet}$ and $\theta_{r,wet}$ are residual soil suction and volumetric water content for main wetting branch, respectively.

This model for fitting wetting branches of SWCC provides a theoretical basis of variation of contact angle during drying and wetting cycles (e.g., Eqs. (4.2) and (4.3)). However, as summarized earlier, various factors affect hysteretic behaviors of the SWCCs (e.g., irregular pore structures inside soils or the "ink-bottle" effect). For this reason, another model is introduced for modelling the main wetting curve.

Based on Eqs. (4.3) and (4.4), the drying branch of SWCC can be expressed as an integral function form using the van Genuchten equation (i.e., Eq. (4.9a)). This equation simply implies that all the pores with radius less than *R* are filled with water during drying process (Mualem, 1976). However, the scenario is distinct in wetting branches, due to the irregular pore structures that can associated with the "ink-bottle" effect as shown in Figure 4.2 (i) (i.e., only part of the pores with radius less than *R* are filled with water) (Zhai et al., 2020). The larger pores obstruct the water soaking process as soil suction during wetting process gradually decreases, as shown in Figure 4.2 (ii).

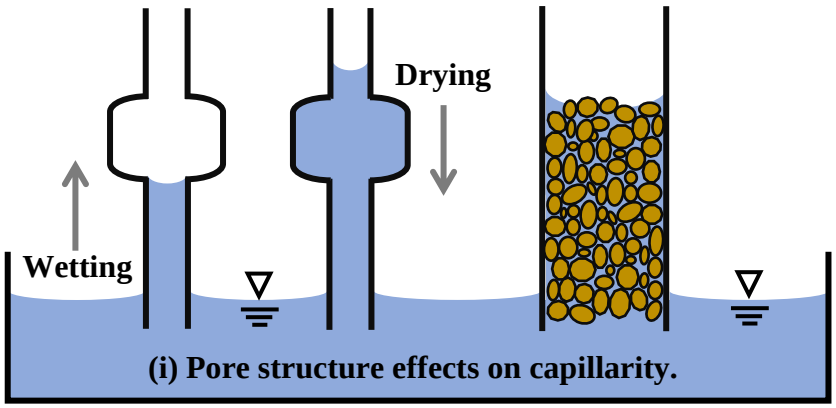

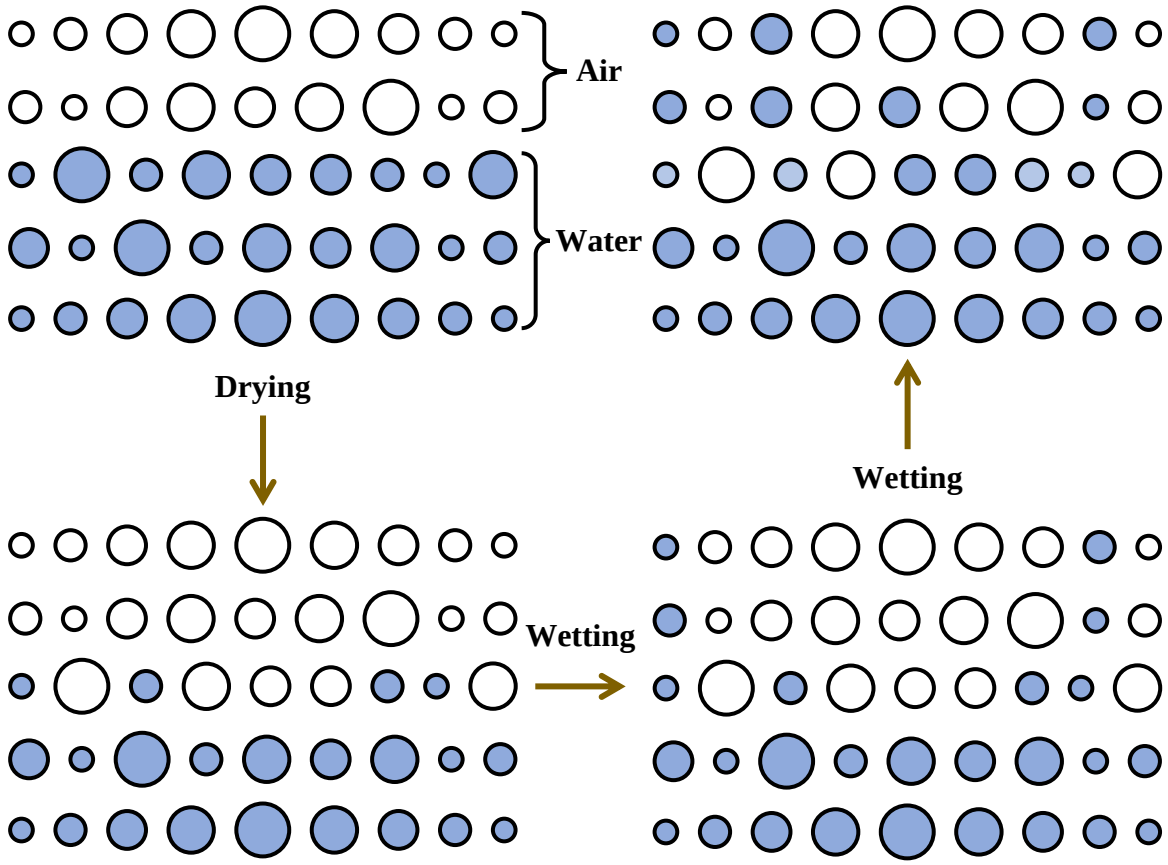

(ii) Conceptual model for soil pores under drying and wetting cycles.

Figure 4.2 Conceptual models for SWCCs with hysteresis.

The PoSD functions (e.g., Eq. (4.9a)) represent the possibility of occurrence of the pores with certain radii R (e.g., Fredlund and Xing, 1994; Zhai et al., 2020). In addition, a new occurrence function F_P (ψ) can also be introduced for modeling irregular pore structure (Zhai et al., 2020). For simplicity purposes, a linear accumulative possibility function with a range that varies from zero to a value of one can be applied. This approach highlights that each size of pore has an equal occurrence chance as shown in Eq. (4.9b).

$$\frac{\theta-\theta_r}{\theta_s-\theta_r}=\int_{\psi_{max}}^{\psi}P(\psi)d\psi=\int_{\psi_{max}}^{\psi}\frac{m_v n_v a_v(a_v\psi)^{n_v-1}}{[1+(a_v\psi)^{n_v}]^{m_v+1}}d\psi \quad (4.9a)$$

$$\frac{\theta-\theta_r}{\theta_s-\theta_r}=F_P(\psi)\cdot\int_{\psi_{max}}^{\psi}P(\psi)d\psi=\left(1-\int_{\psi}^{\psi_{LM}}\frac{1}{\psi_{HM}-\psi_{LM}}d\psi\right)\cdot\int_{\psi_{max}}^{\psi}P(\psi)d\psi=\frac{\psi_{HM}-\psi}{\psi_{HM}-\psi_{LM}}\cdot \int_{\psi_{max}}^{\psi}P(\psi)d\psi \quad (4.9b)$$

where F_P (ψ) is occurrence function, ψ_{LM} and ψ_{HM} are soil suction at meeting points of low suction and high suction, respectively.

Eq. (4.9b) is occurrence function, F_P (ψ) that is independent of the PoSD function. This equation can be applied to all the PoSD functions (e.g., Eqs. (4.6)). For ensuring flexibility of the model, the following Eq. (4.10) is suggested for modeling main wetting curve from the main drying curve.

$$\frac{\theta-\theta_r}{\theta_s-\theta_r}=F_P(\psi)\cdot\int_{\psi_{max}}^{\psi}P(\psi)d\psi\approx\frac{P_a-\psi}{P_a-P_b}\cdot\int_{\psi_r}^{\psi}P(\psi)d\psi=\frac{P_a-\psi}{P_a-P_b}\cdot\int_{\psi_r}^{\psi}\frac{m_v n_v a_v(a_v\psi)^{n_v-1}}{[1+(a_v\psi)^{n_v}]^{m_v+1}}d\psi \quad (4.10)$$

where P_a and P_b are fitting parameters.

Conventionally, minimum soil suction ψ_{min} is approximated as zero, while ψ_{max} is assumed to as ψ_r. However, to ensure F_P (ψ) is consistent with the physical meaning of PoSD function, F_P (ψ) is always zero when it is lower than zero; while F_P (ψ) is set as one when it is larger than one (i.e., Eq. (4.11a)). The model performance of Eqs. (4.11) is highlighted in Figure 4.3.

$$F_P(\psi)=\frac{P_a-\psi}{P_a-P_b}\qquad 0\le F_P(\psi)\le 1 \quad (4.11a)$$

$$\frac{\theta-\theta_r}{\theta_s-\theta_r}=F_P(\psi)\cdot\int_{\psi_r}^{\psi}\frac{m_v n_v a_v(a_v\psi)^{n_v-1}}{[1+(a_v\psi)^{n_v}]^{m_v+1}}d\psi \quad (4.11b)$$

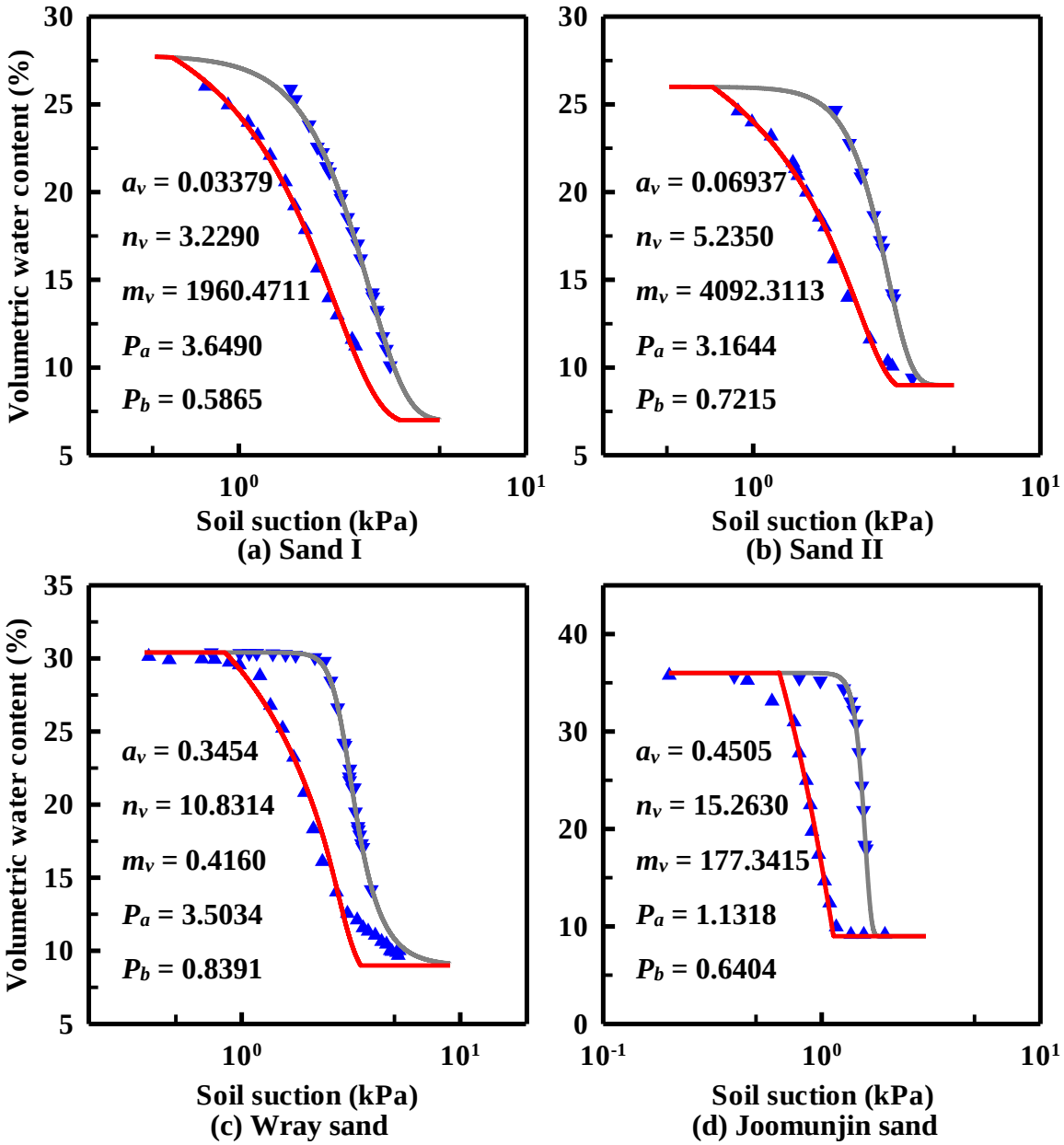

Note: Sands I and II are gathered from Poulovassilis (1970), while Wray sand and Joomunjin sand are gathered from Gillham et al. (1976) and Min and Huy (2010), respectively. P_a and P_b are parameters for modeling main wetting curve from main drying branch.

Figure 4.3 Predictions of main wetting and drying branches for SWCC.

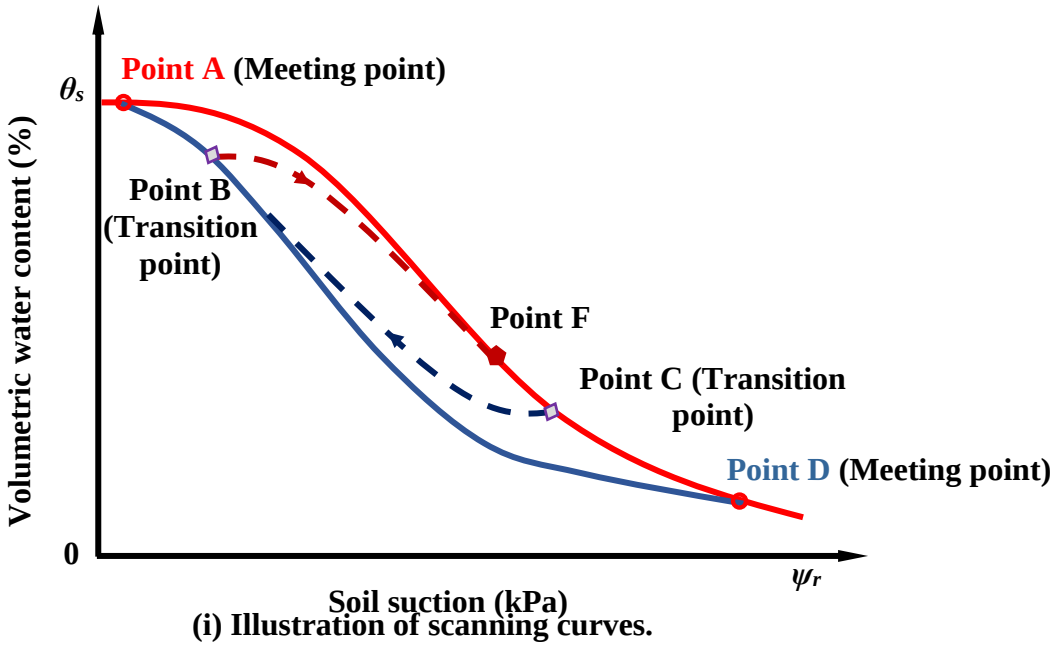

(i) Illustration of scanning curves.

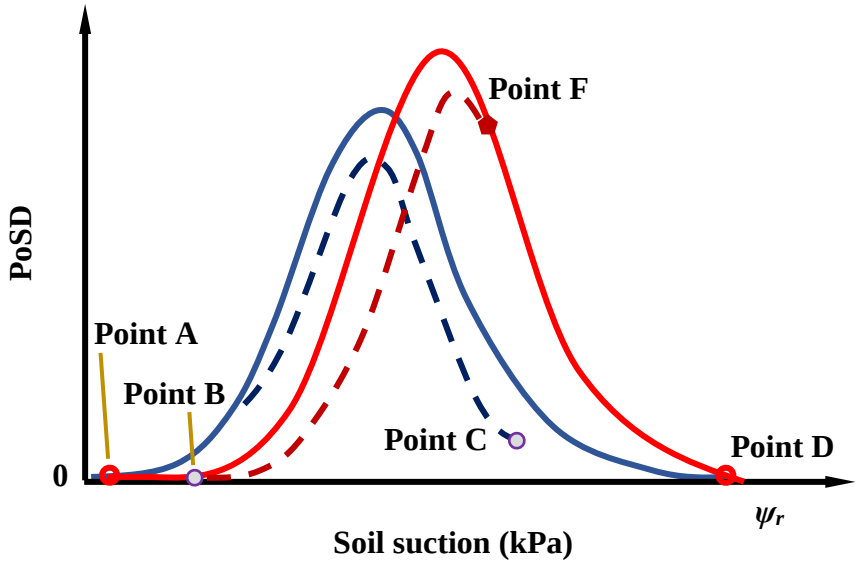

(ii) Illustration of scanning curves from the PoSD curve.

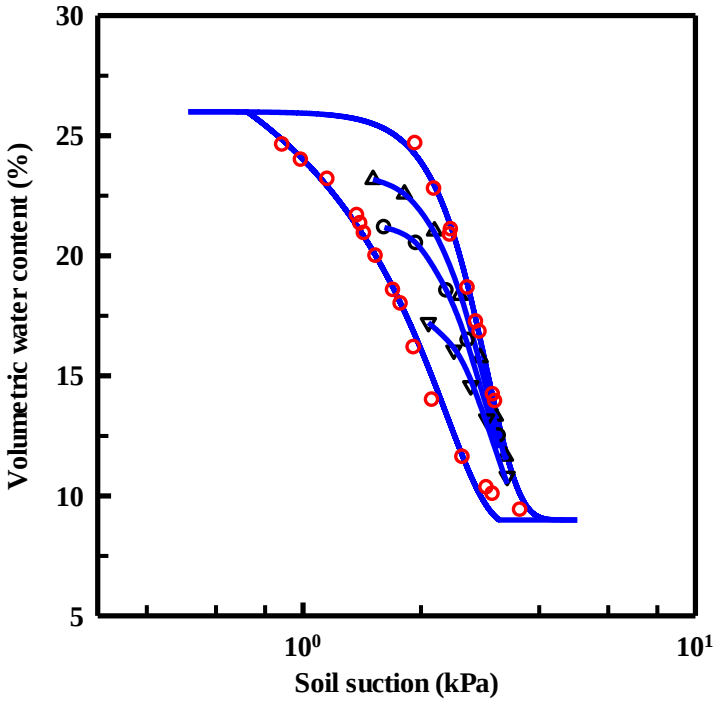

(iii) Flow chart for calibrating scanning curves.

Figure 4.4 Features and calibration flow chart of scanning curves.

4.2.2 Methods of modeling scanning curves

Figures 4.4 (i) and (ii) summarize a typical SWCC with hysteresis and scanning curves; such a hysteretic behavior typically observed in a coarse-grained soil. The terminology and other salient features summarized below as (*a*), *(b)* and (*c*) are useful for explaining the scanning curves characteristics for coarse-grained soils.

4.2.2.1 Scanning curves characteristics of coarse-grained soils

(*a*) The curves shapes for scanning drying and wetting curves are similar to main drying curve and wetting curves, respectively (Pham et al., 2003; Li, 2005; Zhou, 2013).

(*b*) One meeting point (i.e., points D or A in Figure 4.4 (i)) can be found for each main drying and wetting curves.

(*c*) Starting from transition point (i.e., points B or C in Figure 4.4 (i)), the drying or wetting scanning curves are gradually approaching to main drying or wetting curves. Taking account of the above features, in this Chapter, three different methods are proposed that are suitable for coarse-grained soils.

4.2.2.2 The first method

The first method, also referred to as the general method, is built from main drying and wetting curves based on the characteristics of scanning curves summarized in (*a*) and (*c*). As the scanning wetting curve starts from transition point C (e.g., Figure 4.4 (i)), models for main wetting curve (e.g., Eqs. (4.11)) should be modified based on Bayes' theorem of possibility (i.e., Eq. (4.12)). The required Eqs. (4.13) for wetting scanning curves can be derived from Eqs. (4.9b) and (4.12).

$$P(A|B) = \frac{P(B|A)P(A)}{P(B)} \tag{4.12}$$

$$\frac{\theta-\theta_0}{\theta_s-\theta_0} = \frac{\frac{\psi_0-\psi}{\psi_{HM}-\psi_{LM}}}{1-\frac{\psi_{HM}-\psi_0}{\psi_{HM}-\psi_{LM}}} \cdot \frac{\int_{\psi_0}^{\psi} P(\psi)d\psi}{\int_{\psi_{max}}^{\psi_{min}} P(\psi)d\psi - \int_{\psi_{max}}^{\psi_0} P(\psi)d\psi} = \frac{\psi_0-\psi}{\psi_0-\psi_{LM}} \cdot \frac{\int_{\psi_0}^{\psi} P(\psi)d\psi}{\int_{\psi_0}^{\psi_{min}} P(\psi)d\psi} \approx \frac{P_c-\psi}{\psi_0-P_d} \cdot$$

$$\frac{\int_{\psi_0}^{\psi} P(\psi)d\psi}{\int_{\psi_0}^{0} P(\psi)d\psi} = \frac{P_c-\psi}{\psi_0-P_d} \cdot \frac{\int_{\psi_r}^{\psi} P(\psi)d\psi - \int_{\psi_r}^{\psi_0} P(\psi)d\psi}{\int_{\psi_r}^{0} P(\psi)d\psi - \int_{\psi_r}^{\psi_0} P(\psi)d\psi} = F_P^{ws}(\psi) \cdot \frac{\int_{\psi_r}^{\psi} P(\psi)d\psi - \int_{\psi_r}^{\psi_0} P(\psi)d\psi}{1-\int_{\psi_r}^{\psi_0} P(\psi)d\psi} \tag{4.13a}$$

$$F_P^{ws}(\psi) = \frac{P_c-\psi}{\psi_0-P_d} \qquad 0 \le F_P^{ws}(\psi) \le 1 \tag{4.13b}$$

where P_c and P_d are model parameters, θ_0 and ψ_0 are water content and soil suction at transition point (e.g., Point C in Figure 4.4 (i)), respectively.

Similarly, by using Bayes' theorem (i.e., Eq. (4.12)), the model for drying scanning curve can be expressed as following Eqs. (4.14).

$$\frac{\theta-\theta_r}{\theta_0-\theta_r} = 1-\frac{\theta_0-\theta}{\theta_0-\theta_r} = 1-\frac{\frac{\theta_0-\theta}{\theta_s-\theta_r}}{\frac{\theta_0-\theta_r}{\theta_s-\theta_r}} = 1-\frac{\frac{\psi-\psi_0}{\psi_{HM}-\psi_{LM}}\int_{\psi}^{\psi_0} P(\psi)d\psi}{\frac{\psi_{HM}-\psi_0}{\psi_{HM}-\psi_{LM}}\int_{\psi_{max}}^{\psi_0} P(\psi)d\psi} = 1-\frac{\psi-\psi_0}{\psi_{HM}-\psi_0} \cdot \frac{\int_{\psi}^{\psi_0} P(\psi)d\psi}{\int_{\psi_{max}}^{\psi_0} P(\psi)d\psi} =$$

$$1-\frac{\psi-\psi_0}{\psi_{HM}-\psi_0} \cdot \left(1-\frac{\int_{\psi_{max}}^{\psi} P(\psi)d\psi}{\int_{\psi_{max}}^{\psi_0} P(\psi)d\psi}\right) \approx 1-\frac{\psi-P_e}{P_f-\psi_0} \cdot \left(1-\frac{\int_{\psi_r}^{\psi} P(\psi)d\psi}{\int_{\psi_r}^{\psi_0} P(\psi)d\psi}\right) \tag{4.14a}$$

$$\frac{\theta_0-\theta}{\theta_0-\theta_r} = \frac{\psi-P_e}{P_f-\psi_0} \cdot \left(1-\frac{\int_{\psi_r}^{\psi} P(\psi)d\psi}{\int_{\psi_r}^{\psi_0} P(\psi)d\psi}\right) = F_P^{ds}(\psi) \cdot \left(1-\frac{\int_{\psi_r}^{\psi} P(\psi)d\psi}{\int_{\psi_r}^{\psi_0} P(\psi)d\psi}\right) \tag{4.14b}$$

$$F_P^{ds}(\psi) = \frac{\psi-P_e}{P_f-\psi_0} \qquad 0 \le F_P^{ds}(\psi) \le 1 \tag{4.14c}$$

where P_e and P_f are model parameters. Combining Eqs. (4.6a), (4.13) and (4.14), the model for scanning curves using van Genuchten equation can be expressed as following Eqs. (4.15).

$$\frac{\theta_0-\theta}{\theta_0-\theta_r} = F_P^{ds}(\psi)\cdot\left(1-\frac{\int_{\psi_r}^{\psi}P(\psi)d\psi}{\int_{\psi_r}^{\psi_0}P(\psi)d\psi}\right) \tag{4.15a}$$

$$\frac{\theta-\theta_0}{\theta_s-\theta_0} = F_P^{ws}(\psi)\cdot\frac{\int_{\psi_r}^{\psi}P(\psi)d\psi-\int_{\psi_r}^{\psi_0}P(\psi)d\psi}{1-\int_{\psi_r}^{\psi_0}P(\psi)d\psi} \tag{4.15b}$$

$$F_P^{ds}(\psi) = \frac{\psi-P_e}{P_f-\psi_0} \qquad 0 \le F_P^{ds}(\psi) \le 1 \tag{4.15c}$$

$$F_P^{ws}(\psi) = \frac{P_c-\psi}{\psi_0-P_d} \qquad 0 \le F_P^{ws}(\psi) \le 1 \tag{4.15d}$$

$$P(\psi) = g_{dry}(a_v, n_v, m_v, \psi) = \frac{m_v n_v a_v (a_v\psi)^{n_v-1}}{[1+(a_v\psi)^{n_v}]^{m_v+1}} \tag{4.15e}$$

To highlight the effect of transition point on scanning curves (i.e., ψ_0 in Eqs. (4.15c) and (4.15d), Eqs. (4.15c) and (4.15d)) are further transformed into Eqs. (4.16a) and (4.16b), respectively.

$$F_P^{ds}(\psi) = \frac{\psi-P_e}{P_f-\psi_0} = \frac{(\psi-\psi_0)+(\psi_0-P_e)}{P_f-\psi_0} = \beta_d + \lambda_d(\psi-\psi_0) \tag{4.16a}$$

$$F_P^{ws}(\psi) = \frac{P_c-\psi}{\psi_0-P_d} = \frac{(P_c-\psi_0)+(\psi_0-\psi)}{\psi_0-P_d} = \beta_w + \lambda_w(\psi_0-\psi) \tag{4.16b}$$

where β_d and λ_d are model parameters for scanning curves of drying, while λ_w and β_w are parameters for wetting scanning curves. Eqs. (4.17) can be summarized in a simplified form based on Eqs. (4.15) and (4.16).

$$\frac{\theta_0-\theta}{\theta_0-\theta_r} = F_P^{ds}(\psi)\cdot\left(1-\frac{\int_{\psi_r}^{\psi}P(\psi)d\psi}{\int_{\psi_r}^{\psi_0}P(\psi)d\psi}\right) \tag{4.17a}$$

$$\frac{\theta-\theta_0}{\theta_s-\theta_0} = F_P^{ws}(\psi)\cdot\frac{\int_{\psi_r}^{\psi}P(\psi)d\psi-\int_{\psi_r}^{\psi_0}P(\psi)d\psi}{1-\int_{\psi_r}^{\psi_0}P(\psi)d\psi} \tag{4.17b}$$

$$F_P^{ds}(\psi) = \beta_d + \lambda_d(\psi-\psi_0) \qquad 0 \le F_P^{ds}(\psi) \le 1 \tag{4.17c}$$

$$F_P^{ws}(\psi) = \beta_w + \lambda_w(\psi_0-\psi) \qquad 0 \le F_P^{ws}(\psi) \le 1 \tag{4.17d}$$

$$P(\psi) = \frac{m_v n_v a_v (a_v\psi)^{n_v-1}}{[1+(a_v\psi)^{n_v}]^{m_v+1}} \tag{4.17e}$$

Both F_P^{ds} and F_P^{ws} are constrained within zero and a value of one such that they are consistent with the main drying and wetting SWCCs, that were discussed earlier. This model can also be explained using the PoSD curve shown in Figure 4.4 (ii). Water drains from the soil along the main drying curve. However, starting from transition point C, soil is gradually filled with water following wetting scanning curve path. During wetting process when soil suction decreases to

a certain point, only partial pores corresponding to a certain radii R are filled with water. Similarly, drying scanning curves represent the water drainage process from main wetting curve to the main drying curve. In the PoSD curve, this process represents partial drainage of water from soil pores (e.g., Point F in Figure 4.4 (i)). The model (i.e., Eqs. (4.15)) for each scanning curve can be calibrated by Eq. (4.18).

$$O(a,m,n) = \min\left(\sum\left(\theta_{pred} - \theta_{obv}\right)^2\right) \tag{4.18}$$

where O () is the objective function, and θ_{pred} and θ_{obv} are the predicted and measured volumetric water contents, respectively. The calibration process for the first method (i.e., general method) is highlighted in Figure 4.4 (iii). More details regarding calibration are available in later sections.

Based on the salient features of scanning curves in *(b)* and *(c),* one condition for scanning curves should always be satisfied (i.e., all the scanning curves will finally reach the meeting point shown as points A or D in Figure 4.4 (i)). Eqs. (4.19) summarize boundary conditions that are satisfactory for all the scanning curves.

$$\frac{\theta_0 - \theta_{HM}}{\theta_s - \theta_r} \equiv [\beta_d + \lambda_d(\psi_{HM} - \psi_0)] \cdot \int_{\psi_{HM}}^{\psi_0} P(\psi)d\psi \tag{4.19a}$$

$$\frac{\theta_{LM} - \theta_0}{\theta_s - \theta_r} \equiv [\beta_w + \lambda_w(\psi_0 - \psi_{LM})] \cdot \int_{\psi_0}^{\psi_{LM}} P(\psi)d\psi \tag{4.19b}$$

where θ_{LM} and θ_{HM} are volumetric water contents at meeting points of low suction and high suction, respectively.

The scanning curves will intersect on the main drying and wetting curves at different points as shown in Figure 4.1 (i). However, as suction increases or decreases, all the drying or wetting curves, respectively will reach the meeting points (i.e., points D or A in Figure 4.4 (i)) at high or low suction range (i.e., Eqs. (4.19)).

Eqs. (4.17) define two equations along with two parameters for each scanning curve. However, only one set of boundary condition is proposed as shown in Eqs. (4.19). Two simplified methods are proposed to find suitable parameters for using Eqs. (4.17) and (4.19); these methods use two different parameters; namely, β and λ which are summarized below.

4.2.2.3 The second method

The second method (i.e., constant β method), uses Eqs. (4.20), by setting a constant β for each scanning curves in Eqs. (4.17). This constant is obtained by 'trial-and-error' method. Based on the earlier discussions, after β is fixed in Eqs. (4.17), a suitable λ is found by Eqs. (4.19) for each of the scanning curves as shown in the flow chart summarized in Figure 4.4 (iii).

$$\beta_d \equiv constant \tag{4.20a}$$

$$\beta_w \equiv constant \tag{4.20b}$$

4.2.2.4 The third method

The third method (constant λ method) that uses Eqs. (4.21) is achieved by setting λ as a constant in Eqs. (4.17). The 'trial-and-error' method is introduced to find a suitable parameter λ for each scanning curve. The parameter β for each scanning curve is determined using a constant λ value and boundary conditions (i.e., Eqs. (4.19)) for this method. This calibration process is similar for finding parameter β in the second method as shown in Figure 4.4 (iii).

$$\lambda_d \equiv constant \tag{4.21a}$$

$$\lambda_w \equiv constant \tag{4.21b}$$

The above three methods are targeted for predicting the hysteretic behaviors of coarse-grained soils. Typical results for these three methods; namely the first, the second, and the third methods are presented in Figures 4.5, 4.6, and 4.7, respectively. More discussions and modeling results related to the SWCC behaviors of fine-grained are summarized in the later sections.

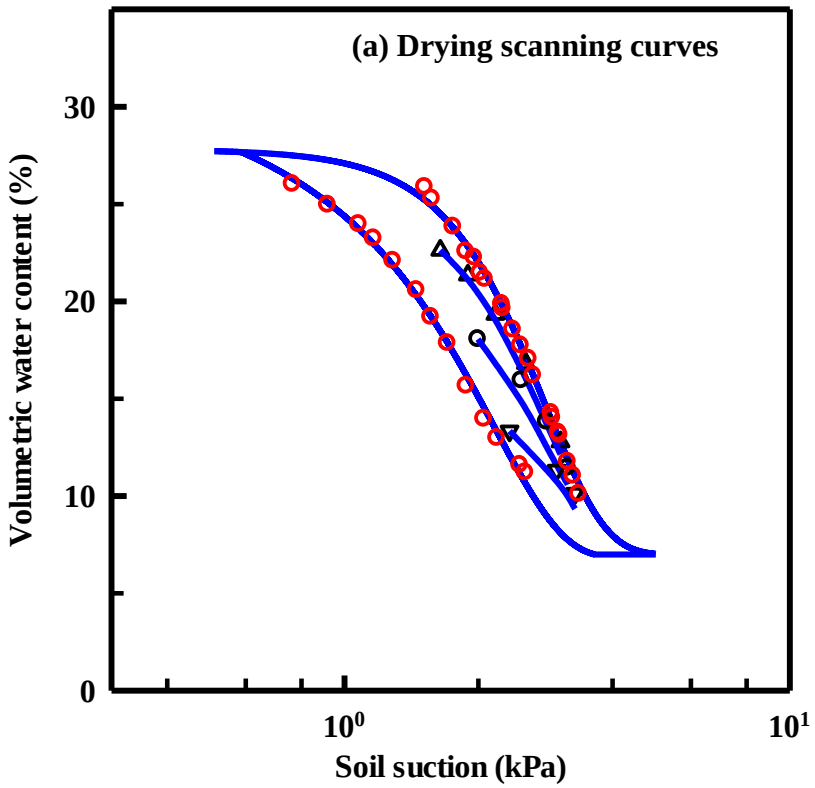
(a) Drying scanning curves
Volumetric water content (%)
30
20
10
0
10^0
10^1
Soil suction (kPa)

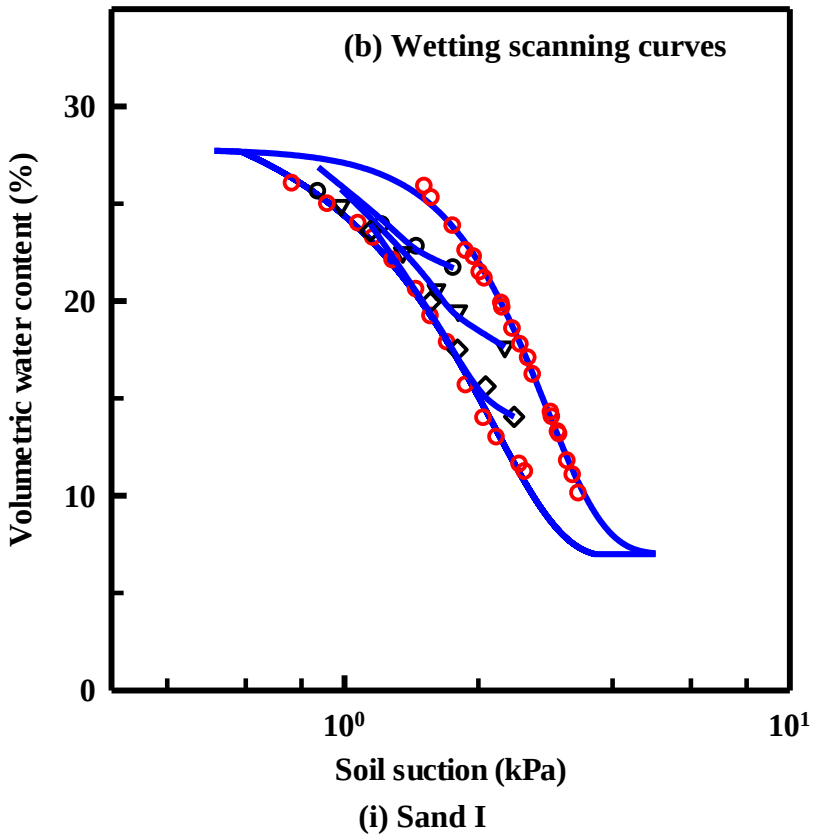
(b) Wetting scanning curves
Volumetric water content (%)
30
20
10
0
10^0
10^1
Soil suction (kPa)

(i) Sand I

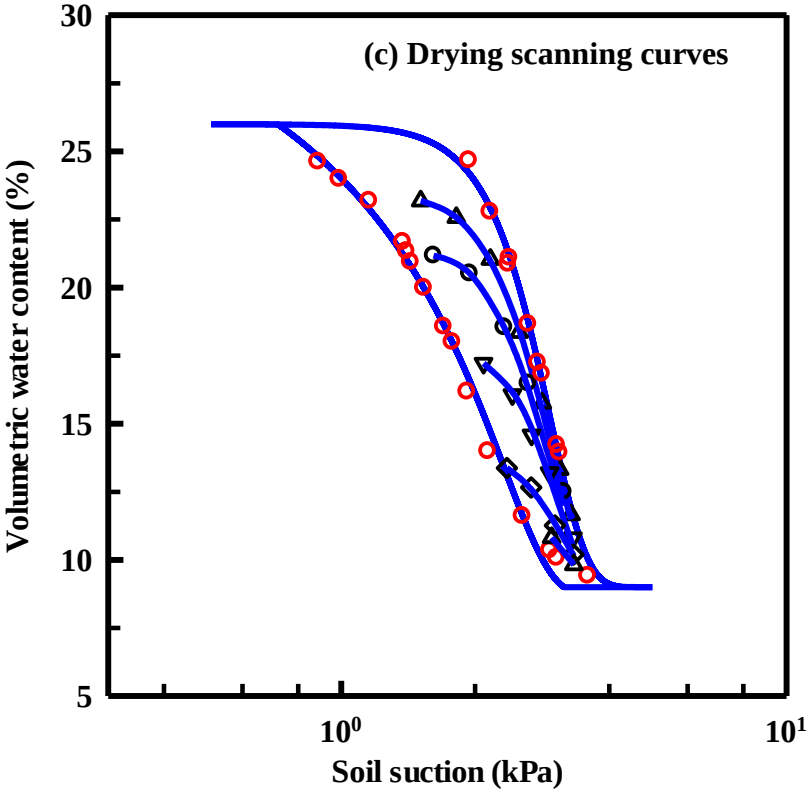
(c) Drying scanning curves
Volumetric water content (%)
30
25
20
15
10
5
10^0
10^1
Soil suction (kPa)

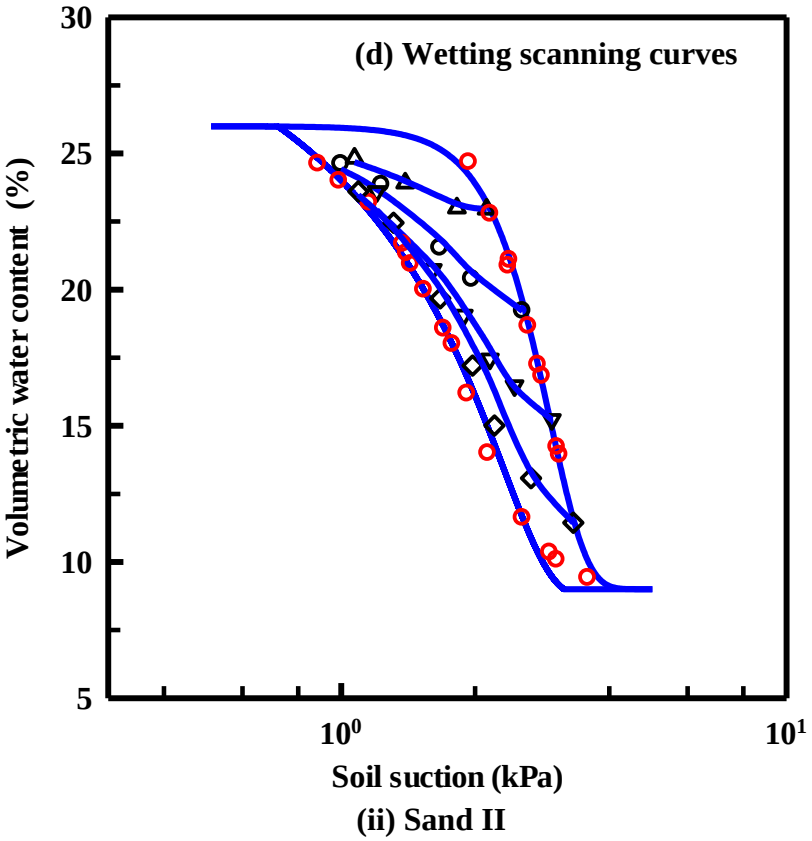
(d) Wetting scanning curves
Volumetric water content (%)
30
25
20
15
10
5
10^0
10^1
Soil suction (kPa)

(ii) Sand II

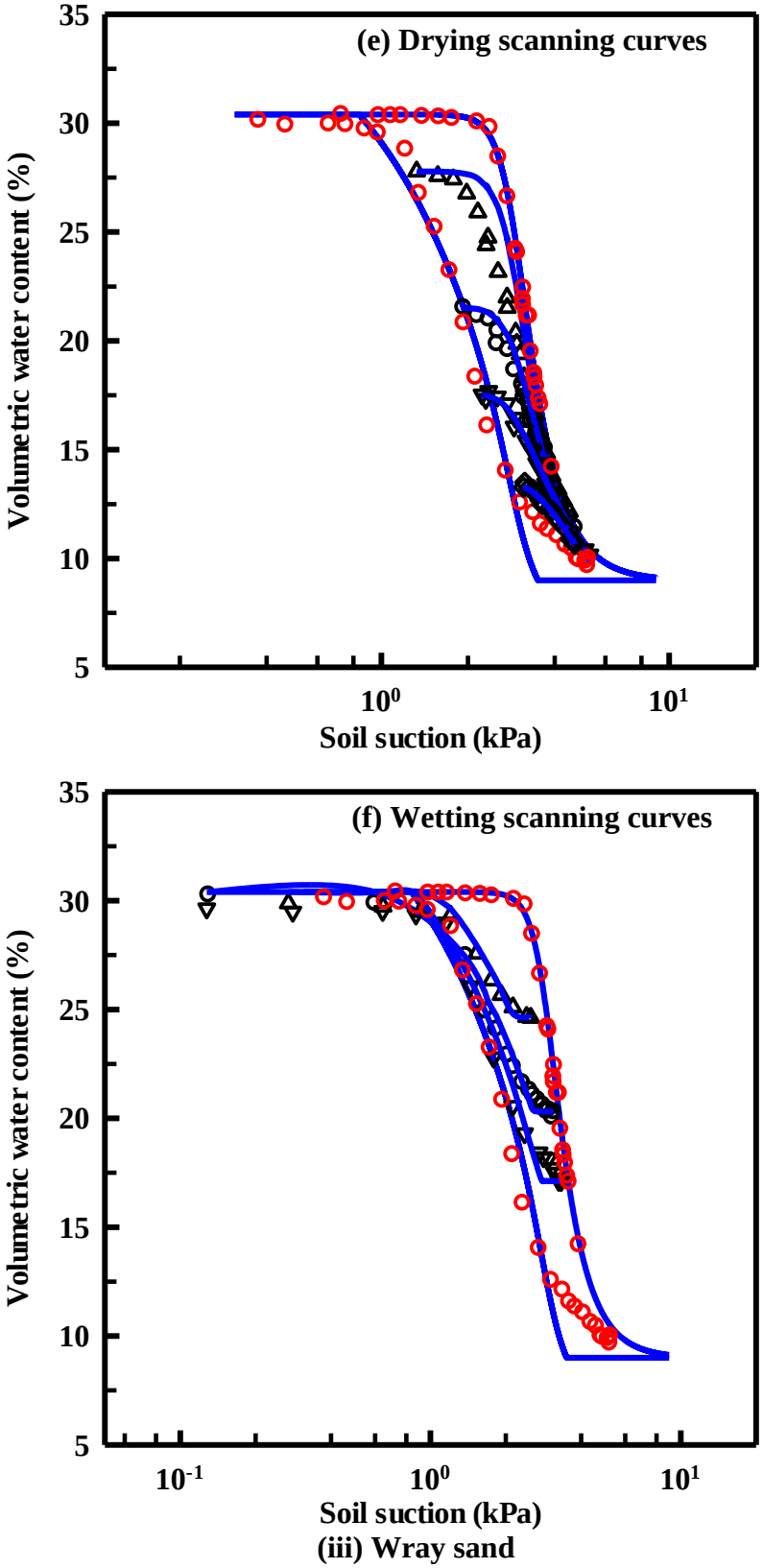

Note: The blue lines are prediction results. The red dots are experimental results for main curves, while the black dots are experimental results for scanning curves.

Figure 4.5 Prediction results for scanning curves using the first method.

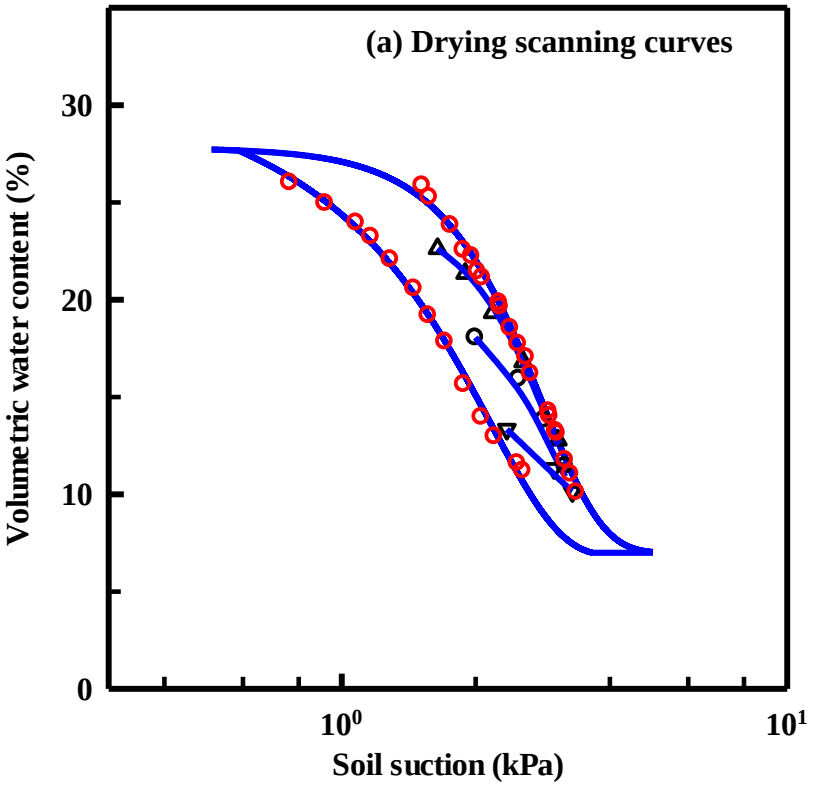
(a) Drying scanning curves
Volumetric water content (%)
30
20
10
0
10^0
10^1
Soil suction (kPa)

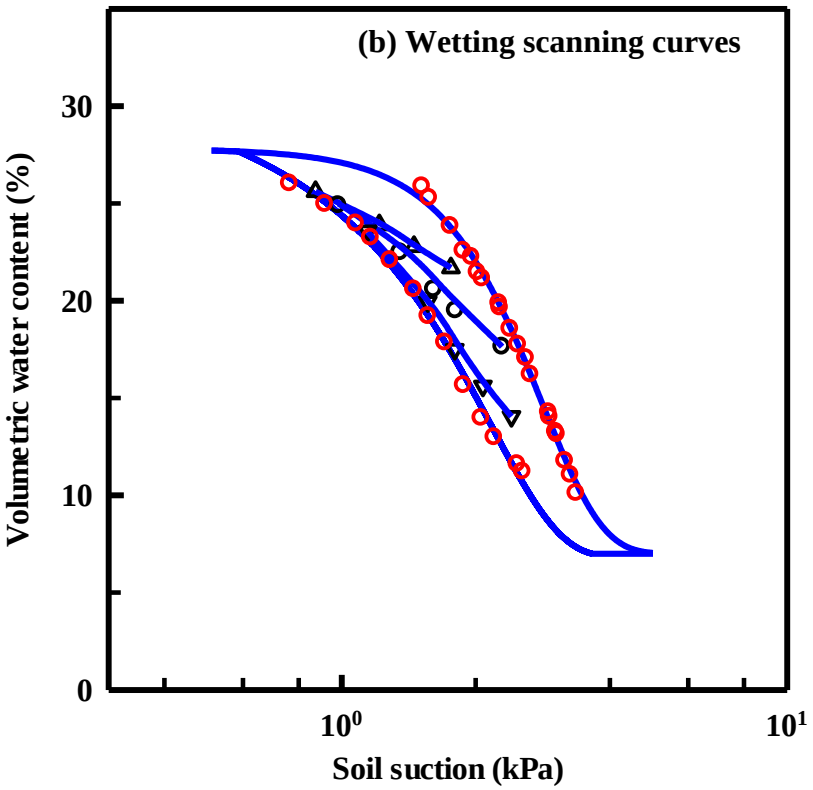
(b) Wetting scanning curves
Volumetric water content (%)
30
20
10
0
10^0
10^1
Soil suction (kPa)

(i) Sand I

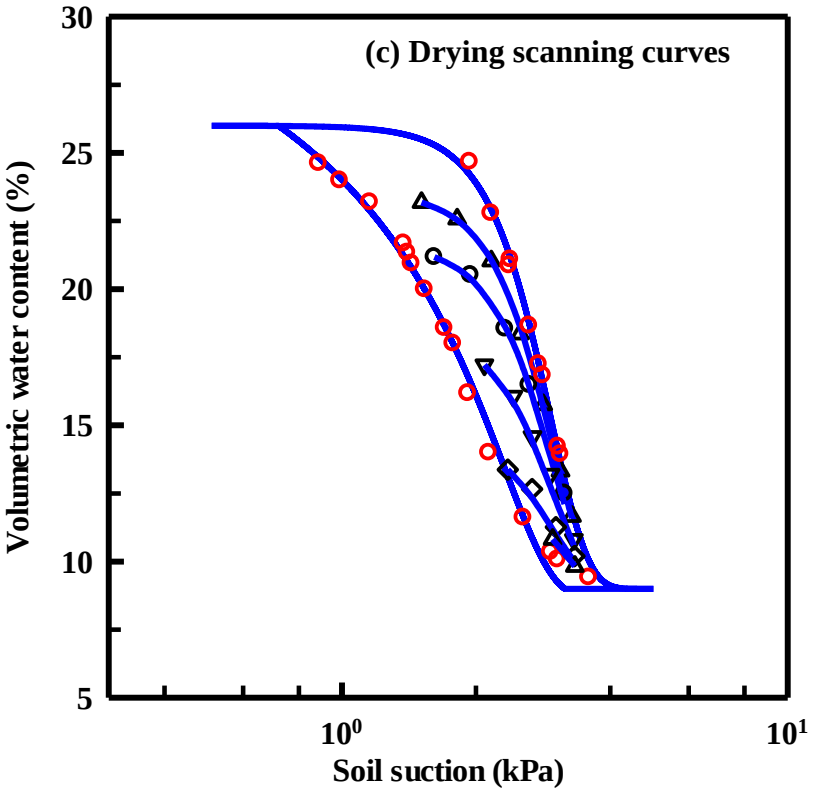
(c) Drying scanning curves
Volumetric water content (%)
30
25
20
15
10
5
10^0
10^1
Soil suction (kPa)

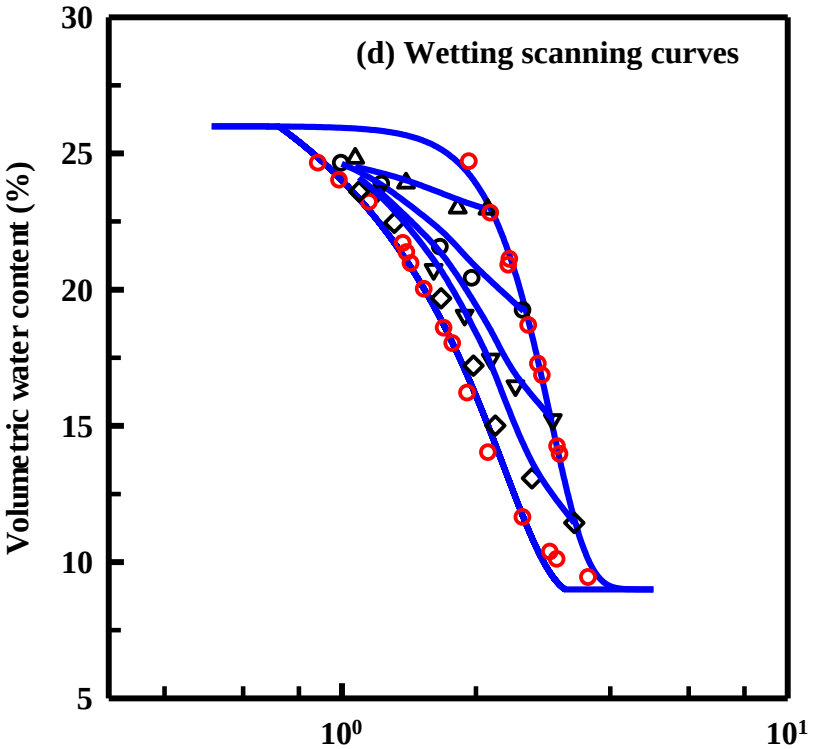
(d) Wetting scanning curves
Volumetric water content (%)
30
25
20
15
10
5
10^0
10^1
Soil suction (kPa)

(ii) Sand II

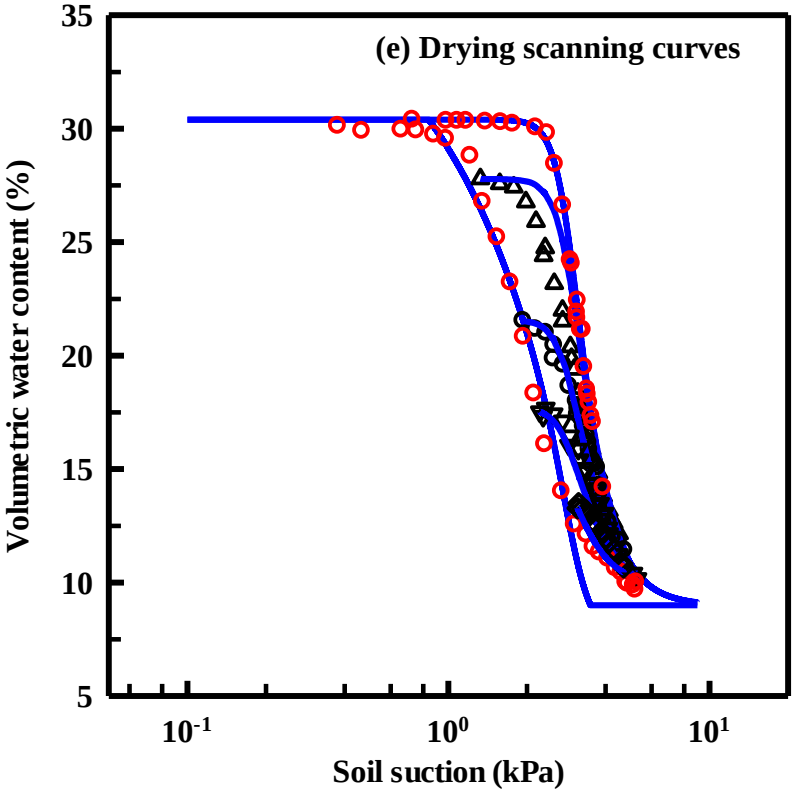

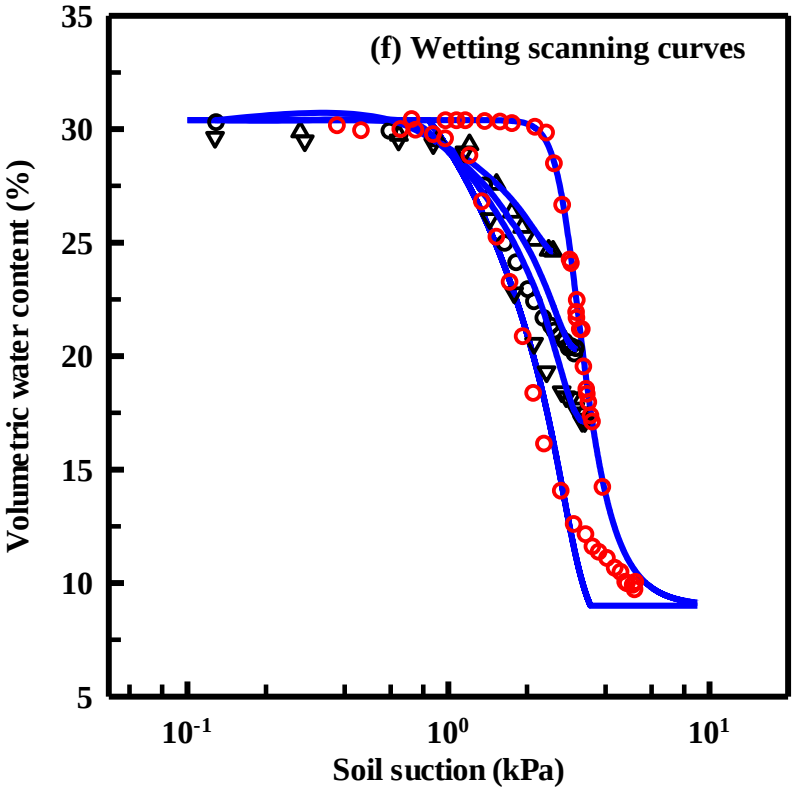

(iii) Wray sand

Note: The blue lines are prediction results. The red dots are experimental results for main curves, while the black dots are experimental results for scanning curves.

Figure 4.6 Prediction results for scanning curves using the second method.

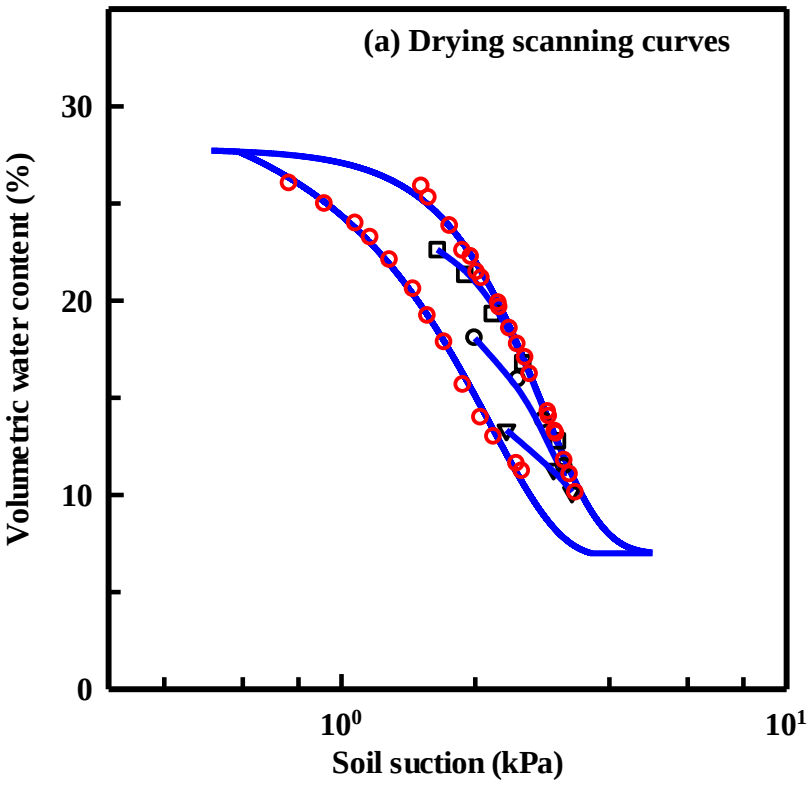
(a) Drying scanning curves
Volumetric water content (%)
30
20
10
0
10^0
10^1
Soil suction (kPa)

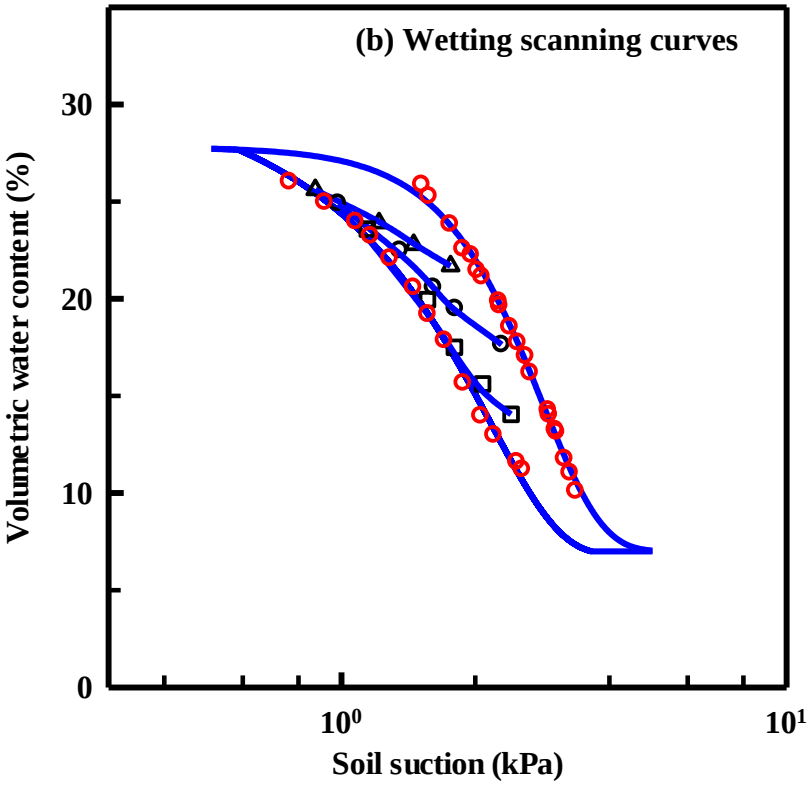
(b) Wetting scanning curves
Volumetric water content (%)
30
20
10
0
10^0
10^1
Soil suction (kPa)

(i) Sand I

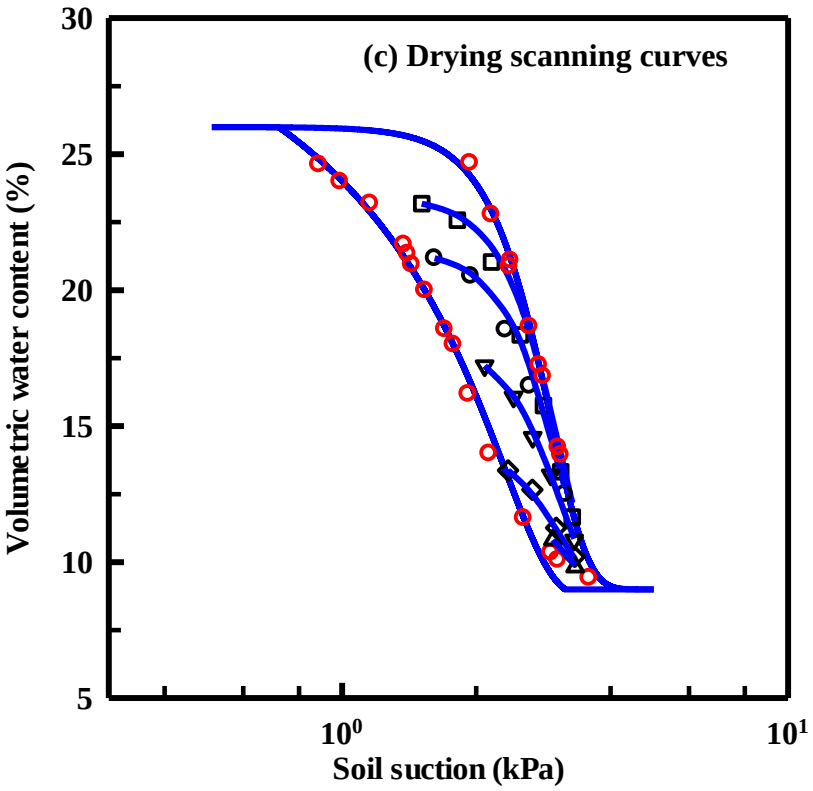
(c) Drying scanning curves
Volumetric water content (%)
30
25
20
15
10
5
10^0
10^1
Soil suction (kPa)

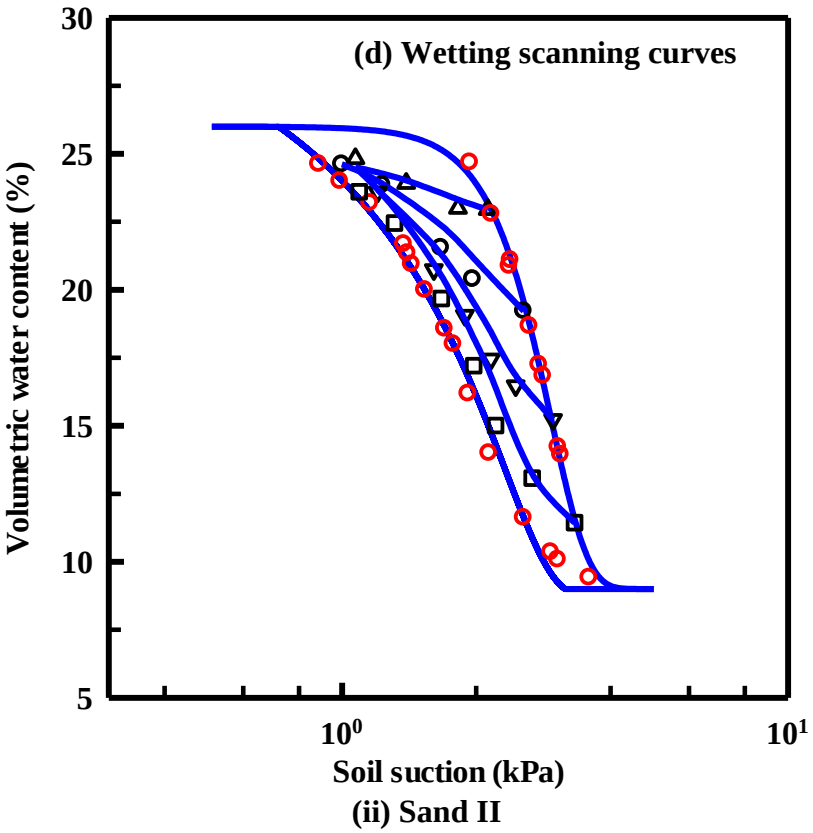
(d) Wetting scanning curves
Volumetric water content (%)
30
25
20
15
10
5
10^0
10^1
Soil suction (kPa)

(ii) Sand II

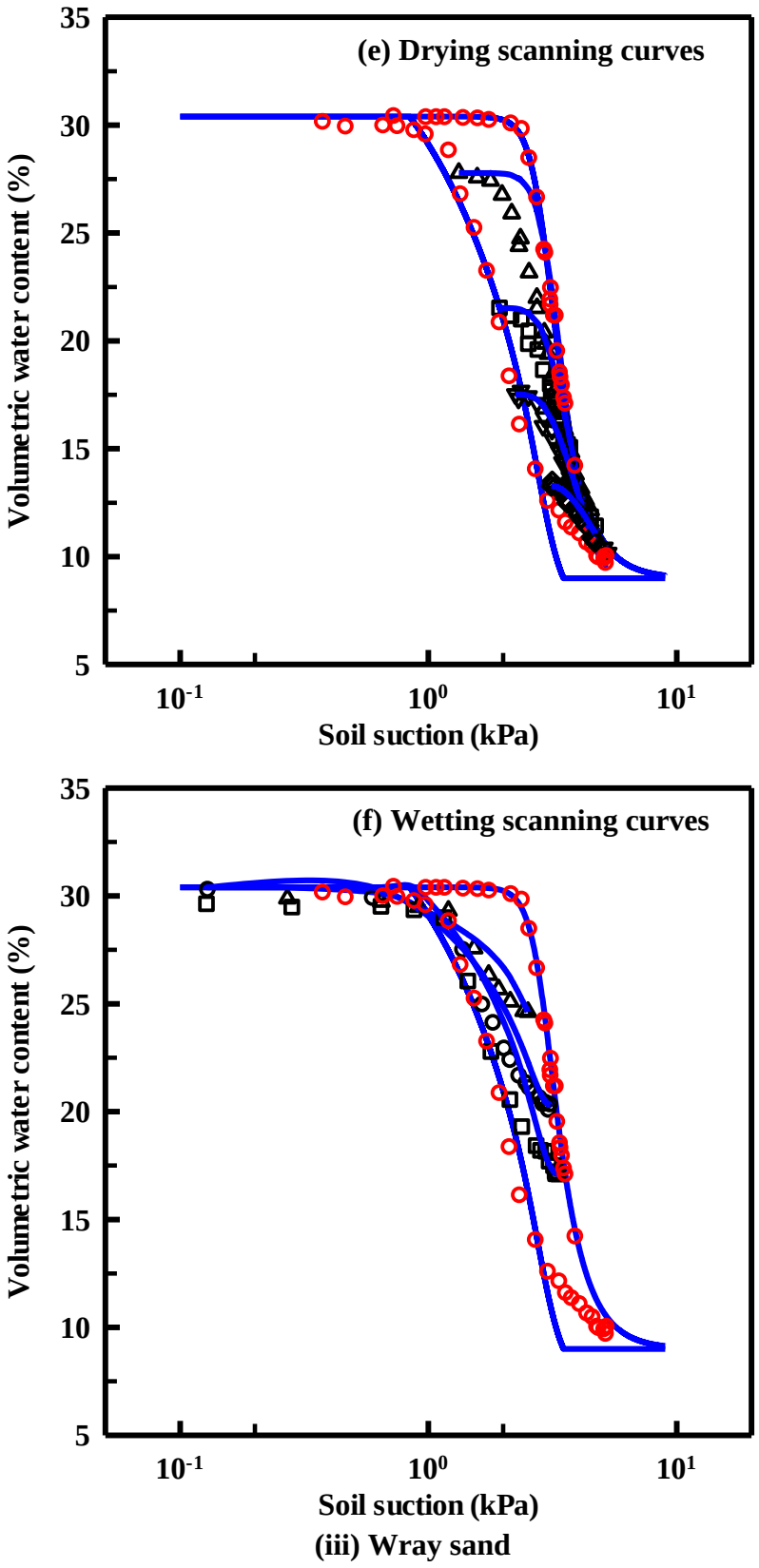

(iii) Wray sand

Note: The blue and cyan lines are prediction results. The red dots are experimental results for main curves, while the black dots are experimental results for scanning curves.

Figure 4.7 Prediction results for scanning curves using the third method.

4.3 SWCC models for fine-grained soils

The SWCC behavior of fine-grained soils is significantly influenced by the initial stress state and the soil structure as shown in Figure 4.8. The relationships between PoSD and how the SWCC behavior is influenced by the void ratio has been discussed extensively in the literature during the last two decades. Two equations, Eqs. (4.22a) and (4.22b) are widely used in the literature (e.g., Gallipoli, 2012; Hu et al., 2013) for understanding the influence of void ratio changes associated with the stress state on the SWCC and are summarized as below.

$$\frac{\theta-\theta_r}{\theta_s-\theta_r}=\left\{\frac{1}{1+[\psi(\phi_c e^{\xi_c})]^{n_v}}\right\}^{m_v} \tag{4.22a}$$

$$\frac{\theta-\theta_r}{\theta_s-\theta_r}=\left\{\frac{1}{1+[a_0\psi\exp(\xi_c(e-e_0))]^{n_v}}\right\}^{m_v} \tag{4.22b}$$

where ϕ_c and ξ_c are fitting parameters, a_0 is parameter a_v value at reference state, e is void ratio, and e_0 is the void ratio at reference state.

4.3.1 Initial stress state effect

In this study, a new model is proposed which is based on Eq. (4.2b) (i.e., $\psi(r) = f(r) = C / r$ and $\psi(r_0) = C / r_0$). The following approximation can be achieved by regarding contact angle as a constant value.

$$\psi(r)=\psi(r_0)+\frac{f'(r_0)}{1!}(r-r_0)+\frac{f''(r_0)}{2!}(r-r_0)^2=\psi(r_0)-\frac{C}{r_0^2}(r-r_0)+\frac{C}{r_0^3}(r-r_0)^2=$$
$$\psi(r_0)\left[1-\frac{1}{r_0}(r-r_0)+\frac{1}{r_0^2}(r-r_0)^2\right] \tag{4.23}$$

where r_0 is the size of soil pores at reference state, r is the radius of soils pores corresponding to another state.

As initial void ratio is directly related to pore radius as shown in Eq. (4.24a), Eq. (4.23) can be written as Eqs. (4.24b) and (4.24c).

$$\begin{cases} e \to r \\ e_0 \to r_0 \end{cases} \tag{4.24a}$$

$$\psi(e) = \psi(e_0)\left[1 - \frac{1}{e_0}(e - e_0) + \frac{1}{e_0^2}(e - e_0)^2\right] \quad (4.24b)$$

$$\psi(e_0) = \psi(e)[1 + \xi_c(e - e_0) + \xi_c^2(e - e_0)^2] \quad (4.24c)$$

$$\frac{\theta - \theta_r}{\theta_s - \theta_r} = \left(\frac{1}{1 + \left\{a_0\psi\left[1 + \xi_c(e - e_0) + \frac{\xi_c^2}{2}(e - e_0)^2\right]\right\}^{n_v}}\right)^{m_v} \quad (4.24d)$$

By substituting Eq. (4.24c) into Eq. (4.4), a new model for incorporating the initial stress state effect can be proposed (i.e., Eq. (4.24d)). This Eq. (4.22) is equivalent to assuming Taylor polynomial of order two to form the exponential equations (i.e., Eqs. (4.22)).

4.3.2 Initial water content effect

As shown in Figure 4.8 (ii), initial stress state decreases first and increases later as initial water content increases for the same compaction effort for fine-grained soils, such as the clays. Several researchers (e.g., Tarantino, 2009; Gallipoli, 2012; Zhou et al., 2012a; Hu et al., 2013) have investigated to understand the influence of initial water content and proposed various models to explain the SWCC behavior.

The models summarized in the earlier section for initial stress state effect can also be applied to analyze the initial water content effect on SWCCs. For example, Eqs. (4.25b) and (4.25c) can be obtained from Eq. (4.25a). In this equation, the pore size decreases with an increase in the initial water content.

$$\begin{cases} w_{i0} \to r_0 \\ w_i \to r \end{cases} \quad (4.25a)$$

$$\psi(w_{i0}) = \psi(w_i)[1 - \xi_i(w_i - w_{i0}) + \xi_i^2(w_i - w_{i0})^2] \quad (4.25b)$$

$$\frac{\theta - \theta_r}{\theta_s - \theta_r} = \left(\frac{1}{1 + \left\{a_0\psi\left[1 - \xi_i(w_i - w_{i0}) + \frac{\xi_i^2}{2}(w_i - w_{i0})^2\right]\right\}^{n_v}}\right)^{m_v} \quad (4.25c)$$

where w_i is initial water content, w_{i0} is initial water content at reference state, and ξ_i is a parameter that takes account of the influence of initial water content effect.

This model can also be explained with the aid of another approach, as discussed below. As highlighted in Figure 4.8 (ii), void ratio decreases (i.e., soils become denser) for initial

compaction water content lower than the optimum water content. The fine-grained soils compacted in this range of water content (i.e., dry of optimum) exhibit flocculated structure and typically have large clod sizes (e.g., Vanapalli et al., 1999). At optimum, soils have lowest void ratio. After optimum, as void ratio increases and the soil attains a dispersed structure (i.e., smaller clod sizes). Since the clod size can be represented by pore radius r (or $\ln(r)$) as initial water content increases, Eqs. (4.26b) and (4.26c) can be built based on Eq. (4.26a).

$$\ln(r_1) - \ln(r_0) = \xi_c(e - e_0) \tag{4.26a}$$

$$\ln(r_1) - \ln(r_0) = -\xi_i(w_i - w_{i0}) \tag{4.26b}$$

$$\frac{r_1}{r_0} = \exp\left(-\xi_i(w_i - w_{i0})(w_i - w_{i0})\right) \tag{4.26c}$$

Typical SWCC models (e.g., van Genuchten equation; Eq. (4.4)) can be applied along with the Eqs. (4.2), (4.3), (4.9a), and (4.26c) to derive the relationship below.

$$\frac{\theta-\theta_r}{\theta_s-\theta_r} = \left\{\frac{1}{1+[a_0\psi\exp(-\xi_i(w_i-w_{i0}))]^{n_v}}\right\}^{m_v} \tag{4.27}$$

It is important to note that Eq. (4.27) does not indicate that SWCC relies only on (4.27). The following Eq. (4.28) suggests that both initial stress state and water content contribute to the overall shapes of SWCCs.

$$\frac{\theta-\theta_r}{\theta_s-\theta_r} = \left\{\frac{1}{1+[a_0\psi\exp(\xi_c(e-e_0)-\xi_i(w_i-w_{i0}))]^{n_v}}\right\}^{m_v} \tag{4.28}$$

Applying second order Taylor polynomial to Eq. (4.28) at w_{i0} and e_0, respectively, the following Eq. (4.29) can be achieved.

$$a_v = a_0\exp\left(\xi_c(e-e_0)-\xi_i(w_i-w_{i0})\right) \cong a_0\left[1+\xi_c(e-e_0)+\frac{\xi_c^2}{2}(e-e_0)^2\right]\left[1-\xi_i(w_i-w_{i0})+\frac{\xi_i^2}{2}(w_i-w_{i0})^2\right] \tag{4.29}$$

Eq. (4.29) is the same as the combined form of Eqs. (4.24d) and (4.25c). These two equations, (i.e., Eqs. (4.24d) and (4.25c)) are derived from two distinct approaches. As shown in Eqs. (4.28) and (4.29), parameters ξ_c and ξ_i affect each other indirectly. For example, for different initial water contents, a_0 is distinct and another ξ_c value must be adopted. In Eqs. (4.25c), (4.27),

(4.28) and (4.29), initial water content w_i can be used; however, in some cases, only initial stress state (void ratio) is provided (e.g., Figure 4.8 (ii)). To express SWCCs behaviors for initial water contents greater than optimum by using the information of initial void ratio, the following Eq. (4.30) is suggested that is based on the information of void ratio.

$$a_v = a_0 \Big/ \left[1 + \xi_i (e - e_0) + \frac{\xi_i^2}{2}(e - e_0)^2\right] \tag{4.30}$$

In the above equation, e_0 denotes void ratio at reference state (i.e., at optimum point). SWCCs for the water contents in dry of optimum zones is adopted to calibrate parameter ξ_i, and void ratio in wet side is used for prediction. Eqs. (4.31a) and (4.31b) are suggested for SWCCs in dry of optimum zones; while Eqs. (4.31c) and (4.31d) are used for prediction of SWCCs for wet of optimum zones. The model results for initial water content and initial stress state effects are highlighted in Figures 4.9 and 4.10, respectively.

$$\frac{\theta - \theta_r}{\theta_s - \theta_r} = \left(\frac{1}{1 + \left\{ a_{d0} \left[1 + \xi_d (e - e_0) + \frac{\xi_d^2}{2}(e - e_0)^2 \right] \psi \right\}^{n_v}} \right)^{m_v} \tag{4.31a}$$

$$\frac{\theta - \theta_r}{\theta_s - \theta_r} = \left(\frac{1}{1 + \left\{ a_{w0} \left[1 + \xi_w (e - e_0) + \frac{\xi_w^2}{2}(e - e_0)^2 \right] \psi \right\}^{n_v}} \right)^{m_v} \tag{4.31b}$$

$$\frac{\theta - \theta_r}{\theta_s - \theta_r} = \left(\frac{1}{1 + \left\{ a_{d0} \Big/ \left[1 + \xi_d (e - e_0) + \frac{\xi_d^2}{2}(e - e_0)^2 \right] \psi \right\}^{n_v}} \right)^{m_v} \tag{4.31c}$$

$$\frac{\theta - \theta_r}{\theta_s - \theta_r} = \left(\frac{1}{1 + \left\{ a_{w0} \Big/ \left[1 + \xi_w (e - e_0) + \frac{\xi_w^2}{2}(e - e_0)^2 \right] \psi \right\}^{n_v}} \right)^{m_v} \tag{4.31d}$$

where a_{d0} and a_{w0} are a_v values at reference state for wetting and drying branches, respectively, ξ_d and ξ_w are respectively parameters of drying and wetting branches for modeling initial state effect (i.e., initial stress state or initial water content).

Eqs. (4.31a) and (4.31b) are general form equations that reflect both initial stress state and water content effects on SWCCs; however, they are expressed in terms of initial stress state. Eqs. (4.31c) and (4.31d) are special cases to reflect initial water content effect on SWCCs in the wet of optimum zone.

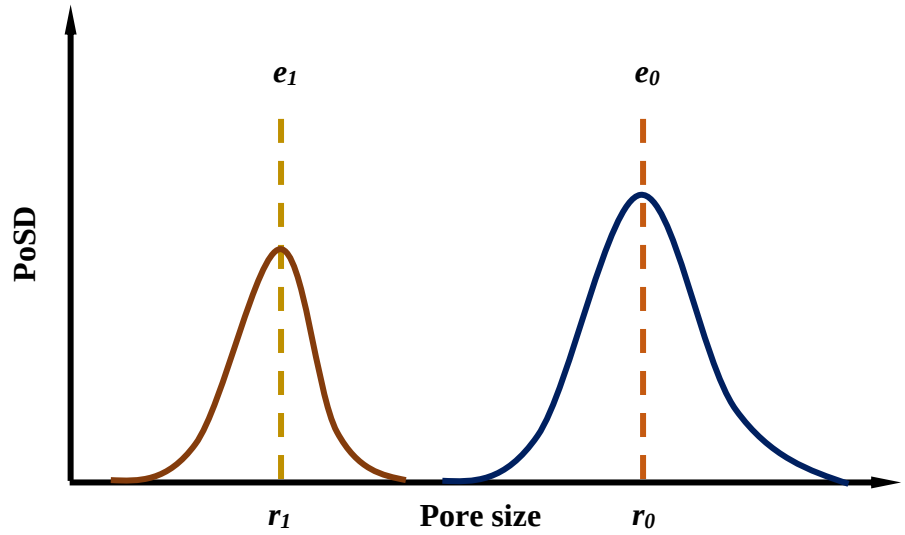

(i) PoSD curves with various initial void ratio.

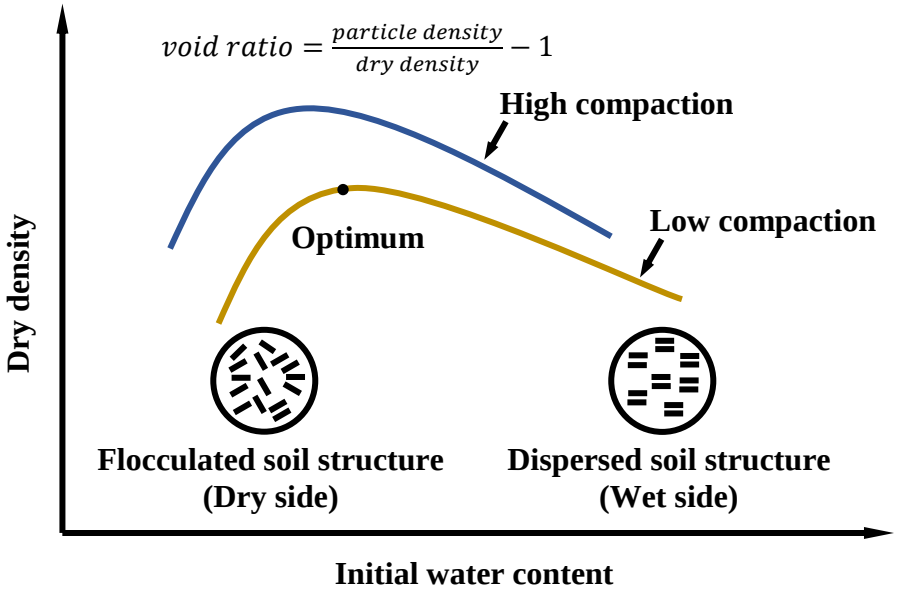

(ii) Relationships between initial water content and void ratio.

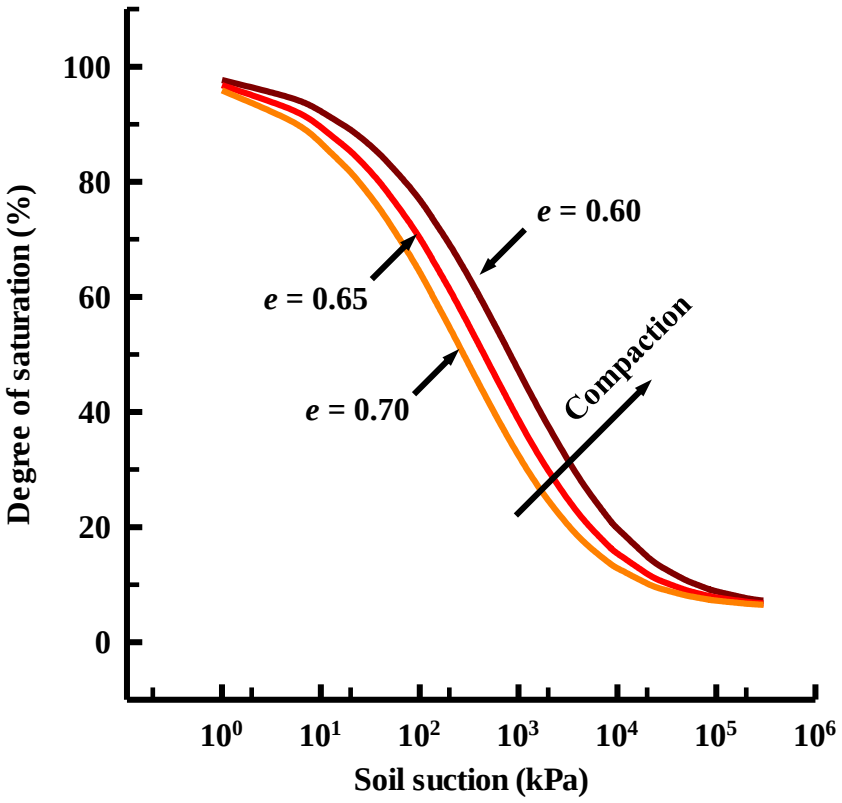

(iii) SWCCs under various stress state.

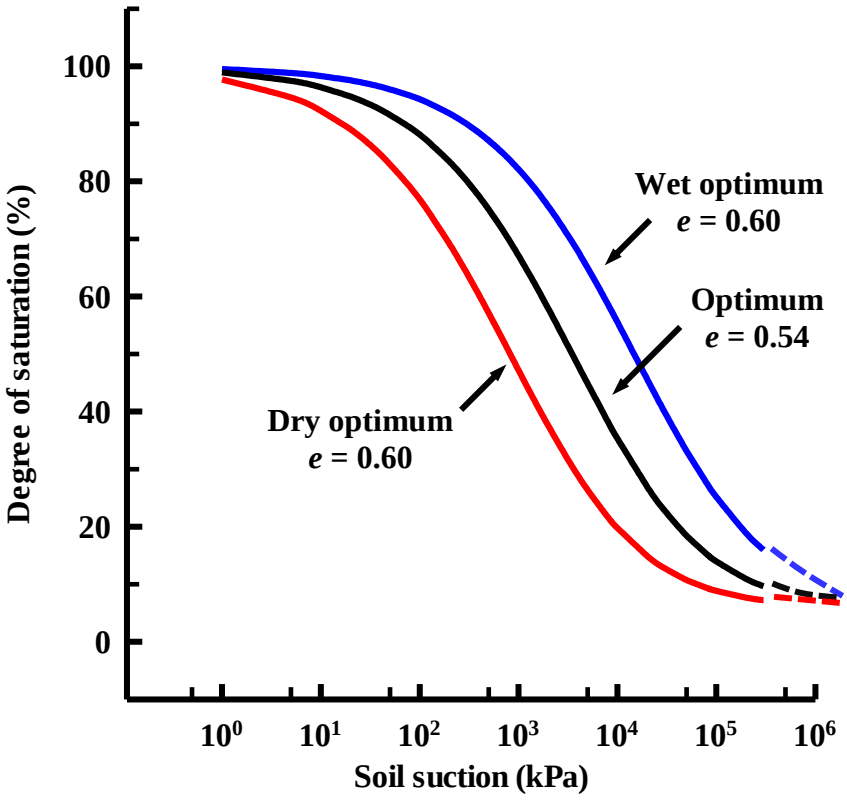

(iv) SWCCs with various initial water content.

Figure 4.8 Initial stress state and water content effects on the SWCCs.

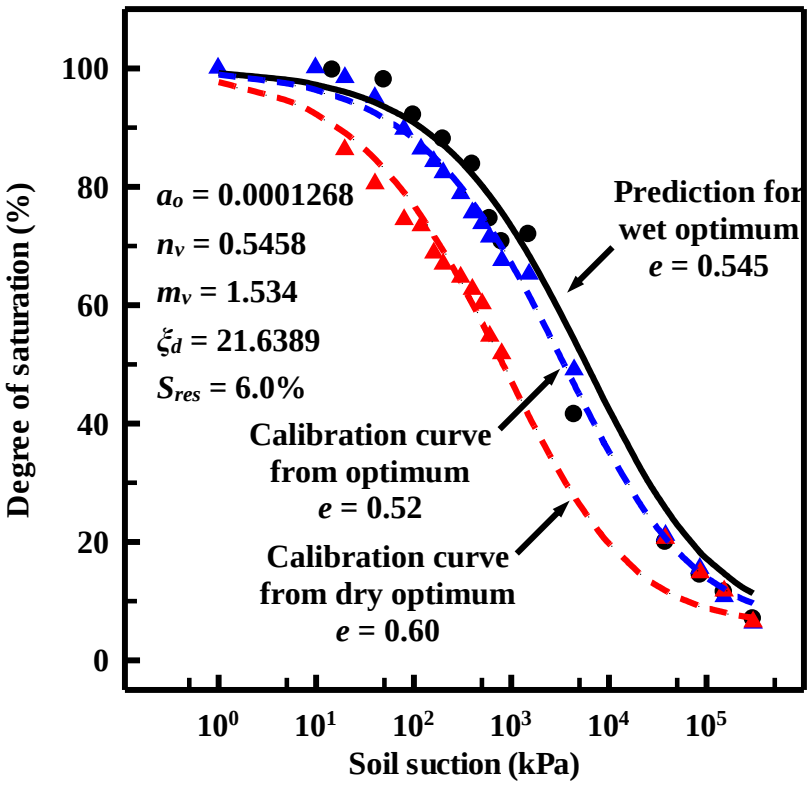

(a) Sandy clay till at 0 kPa equivalent pressure.

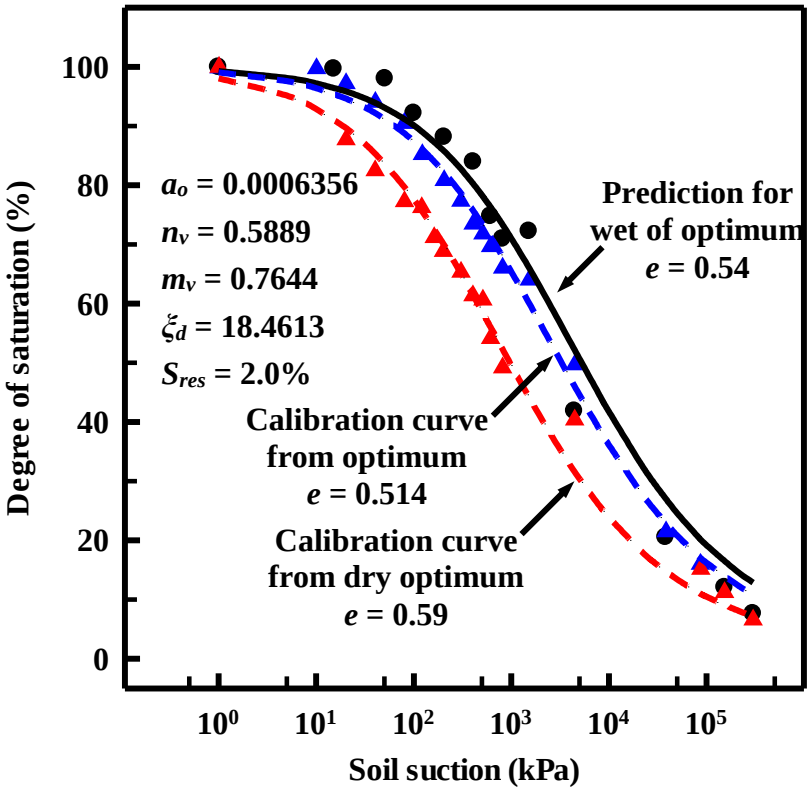

(b) Sandy clay till at 25 kPa equivalent pressure.

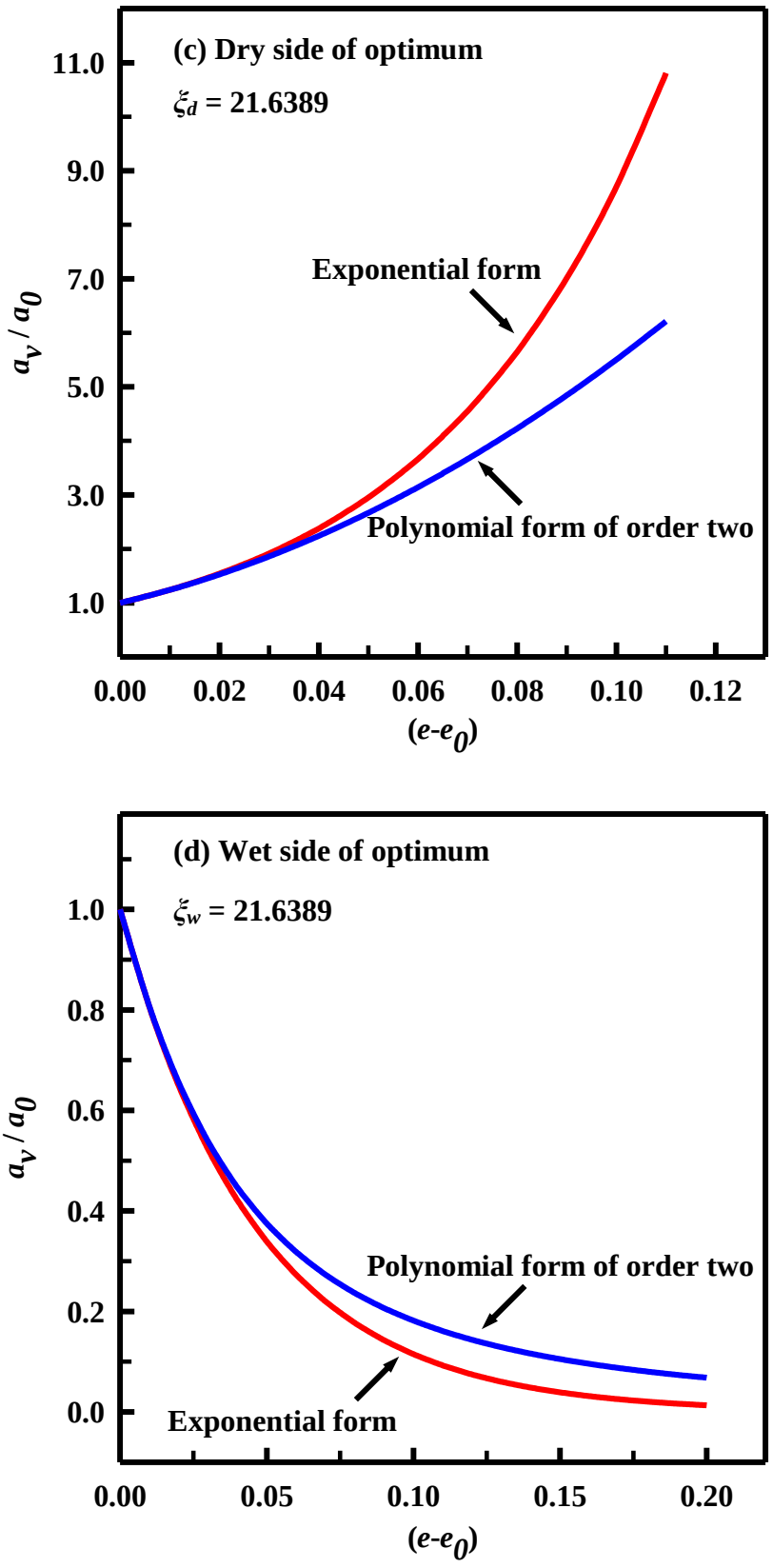

Figure 4.9 Prediction of SWCCs for wet of optimum soil from dry optimum data.

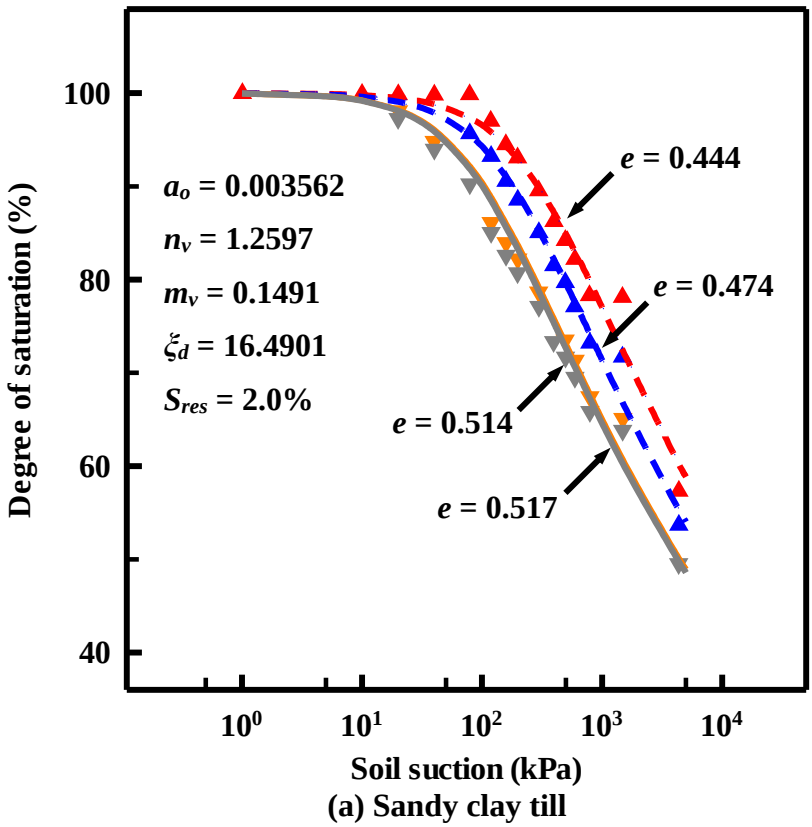

(a) Sandy clay till

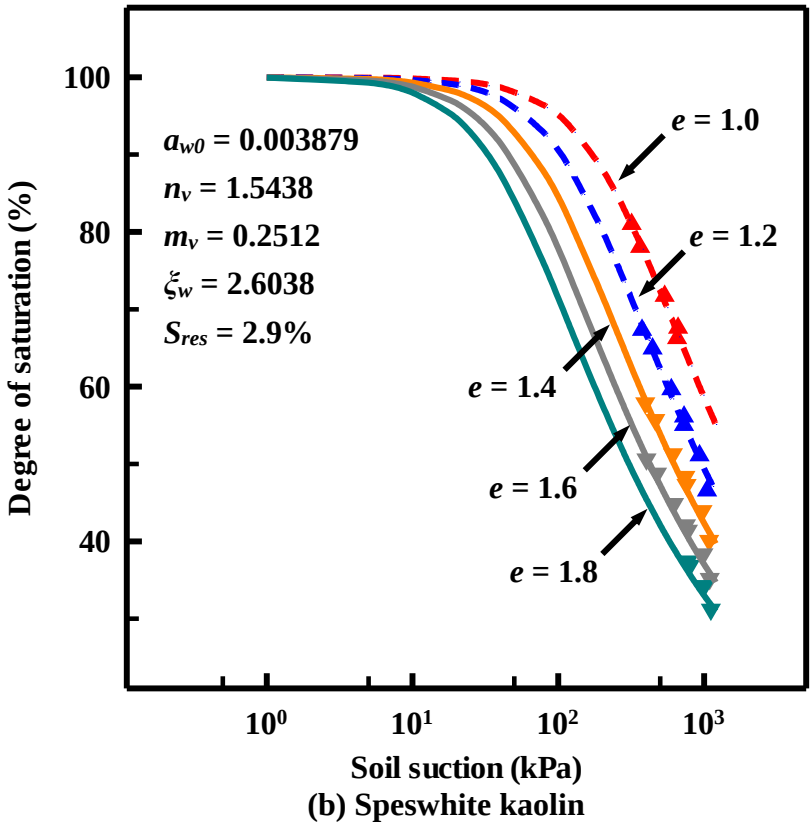

(b) Speswhite kaolin

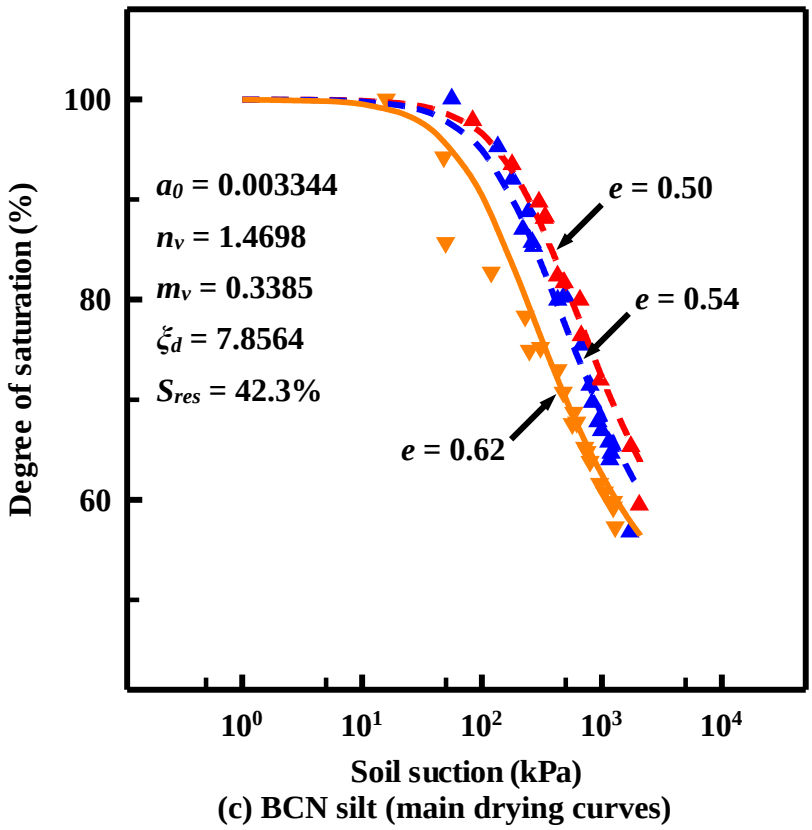

(c) BCN silt (main drying curves)

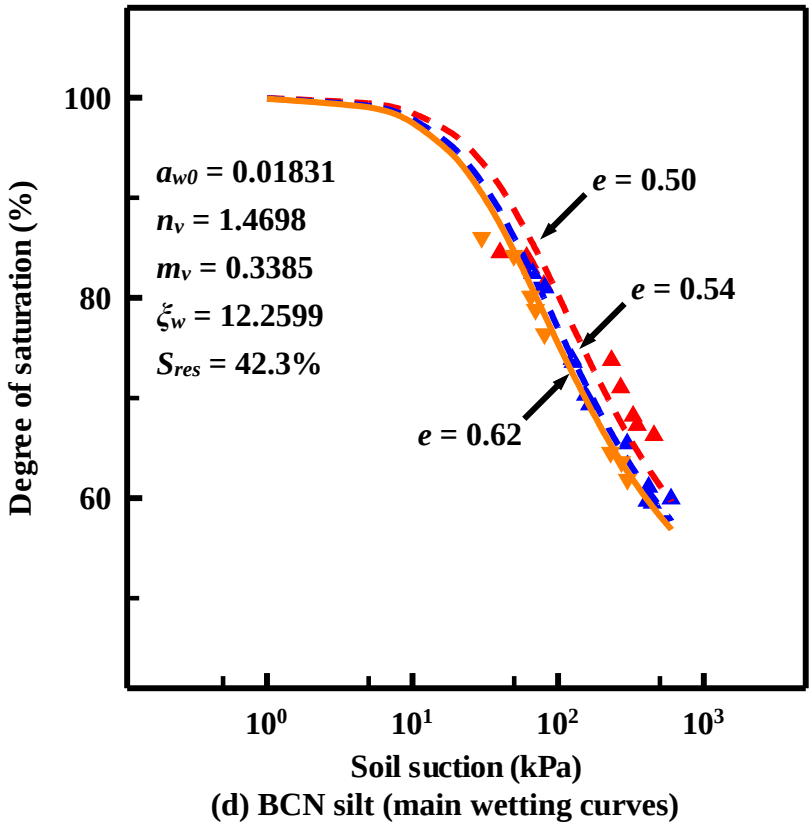

(d) BCN silt (main wetting curves)

Figure 4.10 Prediction of SWCCs under various stress states.

4.4 SWCC equations derived from traditional models

4.4.1 Coupled model for addressing multiple parameters on SWCC

The traditional SWCC modeling equations use parameters for predicting SWCC for a specific set of conditions. However, in this study, a novel model is presented to evaluate and discuss the influence of multi-parameters on the SWCC fitting process, which is summarized below.

$$\frac{\theta-\theta_r}{\theta_s-\theta_r}=\left[\frac{1}{1+(a_v\psi)^{n_v}}\right]^{m_v}=\left\{\frac{1}{1+[(a_v\cdot\psi_{max})(\psi/\psi_{max})]^{n_v}}\right\}^{m_v}=\left\{\frac{1}{1+(a_v\cdot\psi_{max})^{n_v}(\psi/\psi_{max})^{n_v}}\right\}^{m_v} \quad (4.32)$$

As the ratio of ψ to ψ_{max} is a value that is equal to or less than one, the following approximation can be used.

$$1+(a_v\cdot\psi_{max})^{n_v}(\psi/\psi_{max})^{n_v}\cong[1+(\psi/\psi_{max})^{n_v}]^{(a_{v2})^{n_v}} \quad (4.33)$$

The following Eq. (4.34) can be derived by substituting Eq. (4.33) into Eq. (4.4).

$$\frac{\theta-\theta_r}{\theta_s-\theta_r}=\left[\frac{1}{1+(a_v\psi)^{n_v}}\right]^{m_v}\cong\frac{1}{[1+(\psi/\psi_{max})^{n_v}]^{m_v(a_v\cdot\psi_{max})^{n_v}}} \quad (4.34)$$

From Eq. (4.34), various sets of suitable parameters can be obtained; the results derived from such model are shown in Figure 4.11. Only values of parameter ψ_{max} are adjusted in Figures 4.11 (b), (c), and (d).

4.4.2 Proposed SWCC equation from traditional model

A coupled SWCC model is feasible in the form of Eq. (4.35) below which can be obtained from Eq. (4.33) and can be expressed in an exponential form equation as below.

$$1+(a_{v2})^{n_v}(\psi/\psi_{max})^{n_v}\cong\exp\left((a_{v2})^{n_v}\left(\frac{\psi}{\psi_{max}}\right)^{n_v}\right) \quad (4.35)$$

Eq. (4.36) can be derived by substituting Eq. (4.35) into Eq. (4.4).

$$\frac{\theta-\theta_r}{\theta_s-\theta_r}=\left\{\frac{1}{1+(a_v\cdot\psi_{max})^{n_v}(\psi/\psi_{max})^{n_v}}\right\}^{m_v}\cong\frac{1}{\left[\exp\left((a_{v2})^{n_v}\left(\frac{\psi}{\psi_{max}}\right)^{n_v}\right)\right]^{m_v}} \quad (4.36)$$

The above SWCC model can be put in a simplified form as given below.

$$\frac{\theta-\theta_r}{\theta_s-\theta_r}=\frac{1}{\exp(n_{lv}(a_{lv}\psi)^{m_{lv}})} \tag{4.37}$$

where a_{lv}, n_{lv}, and m_{lv} are fitting parameters. This SWCC model performance is evaluated in Figure 4.12. The PoSD function for the modified SWCC is summarized as Eq. (4.38).

$$f(\psi)=\frac{a_{lv}n_{lv}m_{lv}(a_{lv}\psi)^{(m_{lv}-1)}}{\exp(n_{lv}(a_{lv}\psi)^{m_{lv}})} \tag{4.38}$$

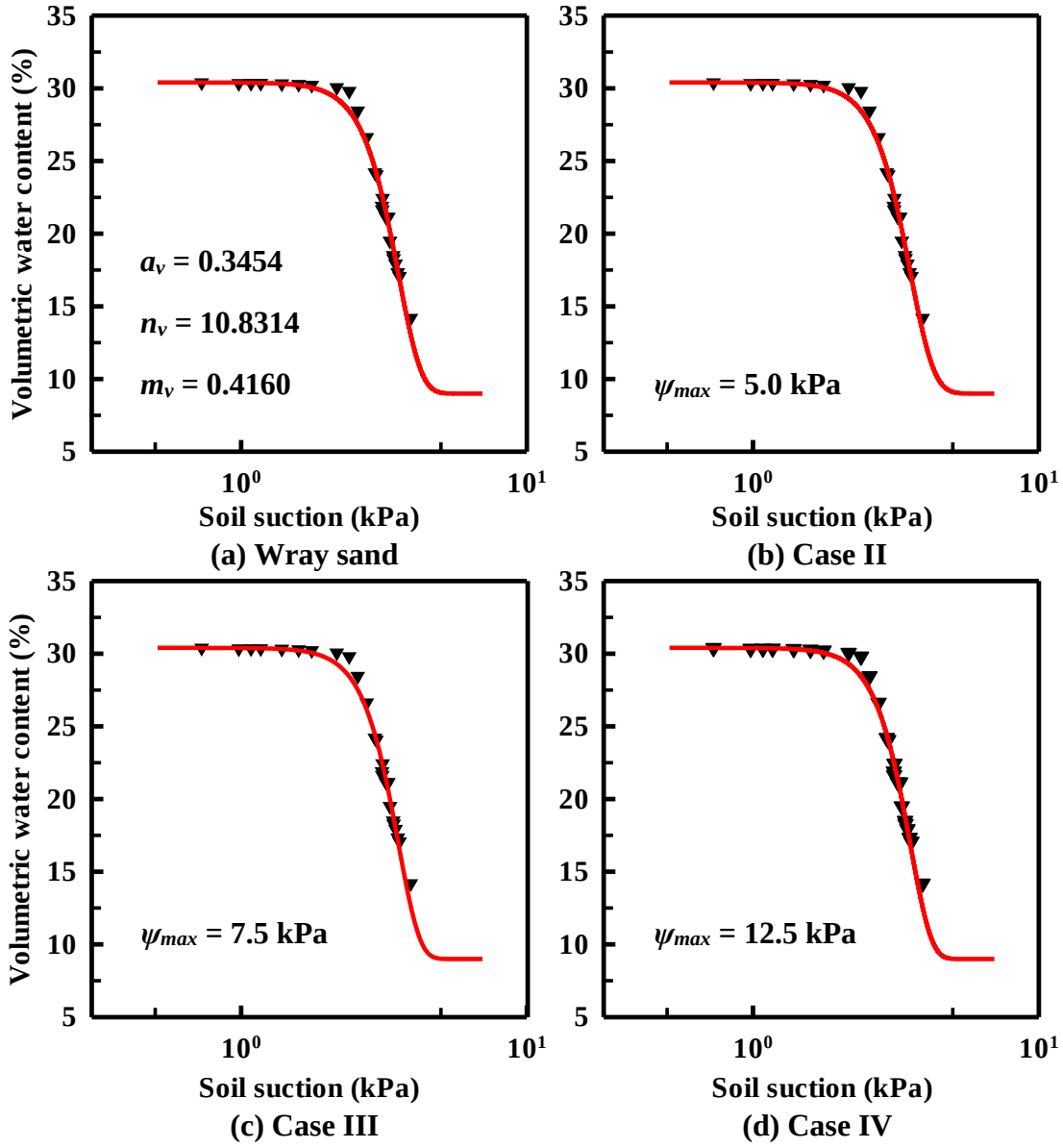

Figure 4.11 Evaluation of multi-parameters on the modeling of SWCC.

The following Eq. (4.39) is used for SWCC model evaluation.

$$R^2 = \frac{\left[\sum_{i=1}^{N}(\theta_{obv}-\bar{\theta}_{obv})(\theta_{pred}-\bar{\theta}_{pred})\right]^2}{\sum_{i=1}^{N}(\theta_{obv}-\bar{\theta}_{obv})^2 \sum_{i=1}^{N}(\theta_{pred}-\bar{\theta}_{pred})^2} \tag{4.39}$$

where $\bar{\theta}_{pred}$ and $\bar{\theta}_{obv}$ are the average values of the predicted and measured volumetric water contents, respectively.

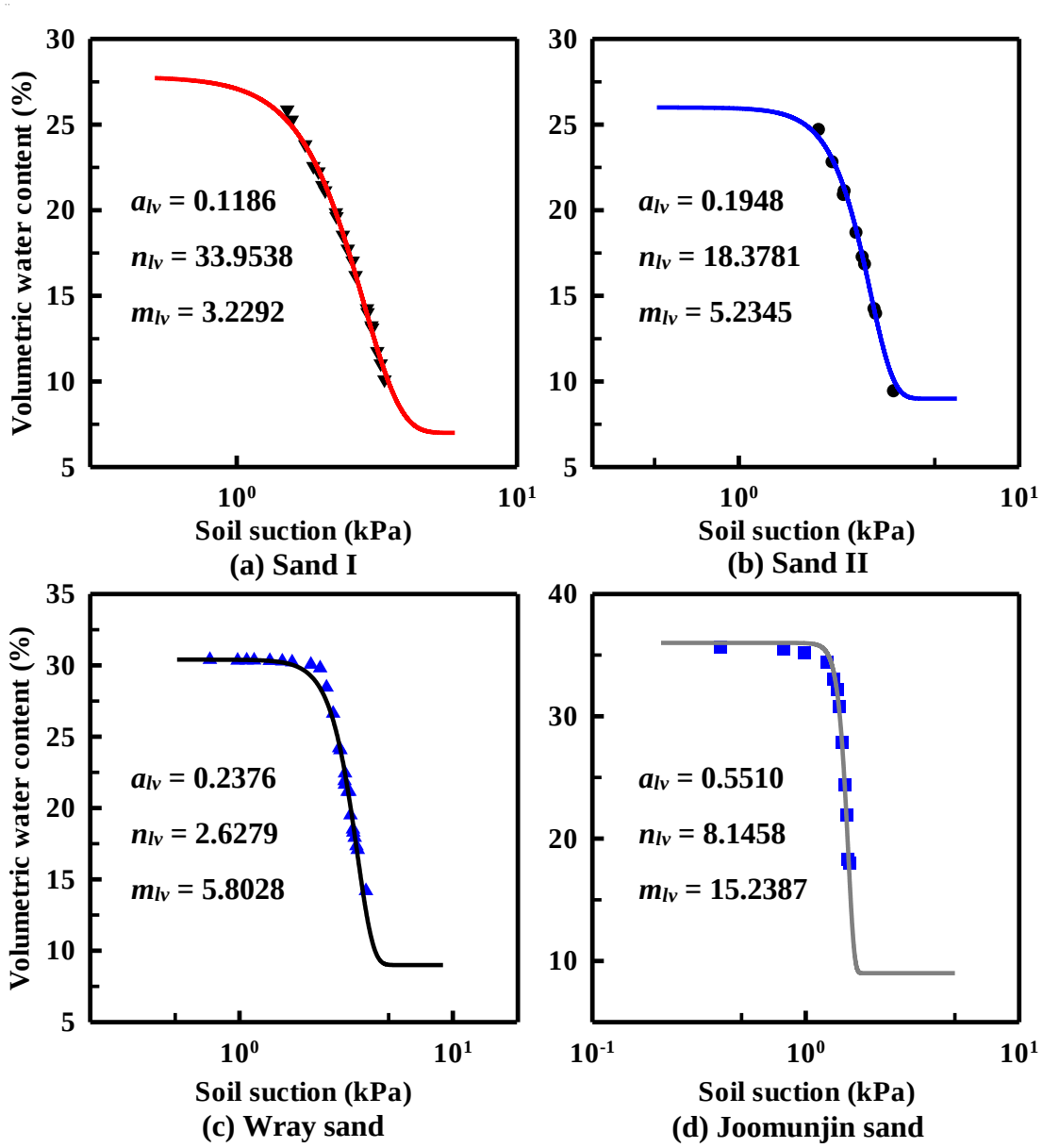

Figure 4.12 Proposed SWCC model performance.

4.5 Results

Figure 4.5 presents the results of scanning curves by the first method (i.e., Eqs. (4.15)). The various parameters used in this method are listed in Table 4.1. Data for Sand I, Sand II, and Wray sand is collected from Poulovassilis (1970), and Gillham et al. (1976), respectively. The intermediate parameters that are used for comparison purposes in this method are listed in Table 4.2. All parameters summarized in Table 4.2 are obtained by using Eq. (4.18). This method used for predicting the scanning curves for Sand I provides good comparisons with measured values as shown in Figures 4.5 (i). For Sand II shown in Figures 4.5 (ii), predicted scanning curves are reasonable; however, some predicted values are slightly different from the measured values. Such a behavior may be attributed to using Eqs. (4.11) for predicting the main wetting branch. Due to this reason, the scanning curve is flat when it is close to transition points. Similar trends in scanning curve predictions can also be observed in Figures 4.5 (iii) for Wray sand.

Figure 4.6 highlights performance of the second method (i.e., Eqs. (4.17) with model constraints Eqs. (4.19) and (4.20)) for predicting the scanning curves of SWCCs for various soils. The various parameters required for this method are listed in Tables 4.1 and 4.3. Table 4.3 summarizes the various intermediate parameters required for calculating or for calibration process. Constant β is determined by 'trial-and-error' method, as discussed earlier. There is a close comparison between the predicted and measured experimental values using the second method (see Figure 4.6 and Eqs. (4.17) with model constraints Eqs. (4.19) and (4.20)). For Sand I in Figures 4.6 (i), all the scanning curves are well predicted. For Sand II shown in Figures 4.6 (ii), the shapes for various scanning curves are well captured. However, the model performance is a bit weaker when it is close to the transition points. The results for Wray sand presented in Figures 4.6 (iii) are similar to Sand II.

Figure 4.7 presents model results using the third method (i.e., Eqs. (4.17) with model constraints Eqs. (4.19) and (4.21)) for predicting the scanning curves. Parameters used for this method are listed in Tables 4.1 and 4.3. In this method, constant λ is calibrated by 'trial-and-error' method, while parameter β is determined by Eqs. (4.19). Most of the scanning curves are well predicted by this method. The results of the third method are similar to the second method.

Table 4.1 Model parameters for the prediction of scanning curves.

Soil #	θ_s / %	a_v	n_v	m_v	θ_r / %	θ_{LM} / %	ψ_{LM} / kPa	θ_{HM} / %	ψ_{HM} / kPa	References
Sand I	27.8	0.03379	3.2290	1960.4711	7.0	25.61	0.87	10.14	3.30	Poulovassilis (1970)
Sand II	26.0	0.06937	5.2350	4092.3113	9.0	24.61	1.00	9.42	3.58	Poulovassilis (1970)
Wray sand	30.4	0.3454	10.8314	0.4160	9.0	29.49	0.91	10.18	5.30	Gillham and Heermann (1976)

Table 4.2 Intermediate model parameters for the proposed first method.

Soil #	Intermediate parameters	Drying scanning curves					Wetting scanning curves				References
		1st	2nd	3rd	4th	5th	1st	2nd	3rd	4th	
Sand I	P_f (P_c)	2.8392	3.4580	5.2929	-	-	1.7921	2.2789	2.4510	-	Poulovassilis (1970)
	P_e (P_d)			0.5000					0.8000		
Sand II	P_f (P_c)	2.9833	3.4580	4.7716	5.4162	5.9671	2.0173	2.5879	2.9903	3.4403	Poulovassilis (1970)
	P_e (P_d)			0.5000					0.5000		
Wray sand	P_f (P_c)	1.8233	6.3829	7.7392	5.7253	-	2.1792	2.5866	2.7947	-	Gillham and Heermann (1976)
	P_e (P_d)		0.0000		2.7389	-			1.3900		

Table 4.3 Intermediate model parameters for the proposed second and third methods.

Soil #	Intermediate parameters	Drying scanning curves					Wetting scanning curves				Method	References
		1st	2nd	3rd	4th	5th	1st	2nd	3rd	4th		
Sand I	λ_d (λ_w)	0.146	0.168	0.001	-	-	0.476	0.373	0.381	-	2	Poulovassilis (1970)
	β_d (β_w)			0.758				0.300				
	λ_d (λ_w)			0.200				0.500			3	
	β_d (β_w)	0.669	0.716	0.569	-	-	0.279	0.119	0.117	-		
Sand II	λ_d (λ_w)	0.033	0.035	0.045	0.044	0.001	0.407	0.452	0.393	0.348	2	Poulovassilis (1970)
	β_d (β_w)			0.933				0.001				
	λ_d (λ_w)			0.200				0.400			3	
	β_d (β_w)	0.586	0.607	0.702	0.743	0.812	0.107	0.180	0.087	0.001		
Wray sand	λ_d (λ_w)	0.049	0.048	0.037	0.001	-	0.525	0.415	0.386	-	2	Gillham and Heermann (1976)
	β_d (β_w)			0.809				0.000				
	λ_d (λ_w)			0.400				0.410			3	
	β_d (β_w)	0.001	0.001	0.001	0.001	-	0.184	0.010	0.001	-		

Note: only one parameter is determined by ‘try-and-error’ method, the remainder parameters are automatically calibrated by constraint Eqs. (4.19).

Figures 4.9 (a) and (b) highlight the model performance for SWCCs measured using the experimental data from Vanapalli et al. (1999) on compacted fine-grained soil specimens. These specimens were prepared with different initial water contents representing dry of optimum, optimum and wet of optimum conditions subjected to equivalent stress 0 and 25 kPa, respectively (the initial stress states are also shown in the figures). Eqs. (4.31a) and (4.31b) are used to predict the data of SWCC at wet of optimum conditions using the data of SWCCs of dry of optimum conditions for calibration.

The model performance shown in Figure 4.9 (a) suggests the SWCCs of wet of optimum conditions are reasonably well predicted. The overall trend of predicted SWCCs (i.e., the dash lines) are close to the measured values. Figure 4.9 (b) presents predicted SWCC under 25 kPa equivalent pressure; the measured points are well predicted by the proposed model.

The variation of parameter a_v using exponential (i.e., Eq. (4.25b)) and polynomial (i.e., Eq. (4.29)) models are shown in Figures 4.9 (c) and (d). For dry of optimum specimens, exponential-form equation leads to higher a_v values as void ratio increases when the parameter value is the same. However, for specimens with water content greater than optimum, a_v results in a lower value compared with the polynomial-form equation. Various equations have similar performance when the initial stress state, e approaches to the reference state e_0.

Figure 4.10 summarizes SWCCs results taking account of the influence of various stress states using Eqs. (4.31) for data collected from Vanapalli et al. (1999), Tarantino and Col (2008), and Tarantino (2009) for sandy clay till, Speswhite kaolin, and Barcelona silt (BCN silt, a sandy clayey silt), respectively. The lines shown with dashes are curves that are used for calibration, while the solid lines are predicted SWCCs. For sandy clay till, as shown in Figure 4.10 (a), the prediction curves provide good agreement with measured points. Because the difference between void ratio of 0.514 and 0.517 is small, both measured data and predictions have some overlap. The model validation can also be supported using the results of various soils as shown in Figures 4.10 (b), (c), and (d).

The model performance for main wetting curves of Speswhite kaolin is presented in Figure 4.10 (b). The predicted SWCCs with different void ratios, e = 1.4, 1.6, and 1.8 are close to experimental results. Figures 4.10 (c) and (d) highlight model performance for main drying and wetting curves of BCN silt (Barcelona silt), respectively. As shown in Figure 4.10 (c), most

data are reasonably well captured by the model (e.g., Eqs. (4.31)) used for prediction.
In Figure 4.10 (d), main wetting curves are well predicted by the Eq. (4.7) as this model is simple and well-accepted in the literature. Since water retention ability is significantly different for soils in dry and wetting processes, the wetting and drying behaviors of SWCCs under various stress states are also different. Therefore, the values of ξ_d and ξ_w herein are also different.

Figure 4.11 provides one possible solution to multi-parametric value problem for modeling SWCC based on Eq. (4.34). As shown in this figure, by setting various ψ_{max} values, the model has almost the same performance as the original van Genuchten equation (i.e., Eq. (4.4) and Figure 4.11 (a)).

Figure 4.12 highlights performance of a modified SWCC model (i.e., Eq. (4.37)). This equation is derived from van Genuchten equation (i.e., Eq. (4.4)) and it is expressed as an exponential form. As shown in the figure, most features of SWCC curves are well captured by the proposed SWCC model (i.e., Eq. (4.37)). The modified model results summarized in Figure 4.12 provides close performance with the traditional SWCC equation (i.e., Eq. (4.4)), as can be seen in Figure 4.3.

5.6 Discussion

Figure 4.2 explains the relationship between main and scanning SWCCs from the PoSD curves. It is of interest to note that the pore structure is not drastically different for hysteretic processes. Since the water content of wetting and drying curves varies for the same soil suction, the variation of scanning curves in the PoSD curve is dependent on the water drainage and storage processes.

Figure 4.3 provides comparison between the measured results of main drying and wetting SWCCs that were fit using van Genuchten (i.e., Eq. (4.4)) and the predictions using the proposed model (i.e., Eqs. (4.11)). The proposed model for predicting wetting branches of SWCC from drying branch is based on the conceptual model of irregular pore structure or “ink-bottle” effect. This model assumes that hysteretic behaviors of SWCCs are dependent on the distinct water soaking paths. This assumption is also consistent with the soils PoSD curve behavior that is not significantly influenced during the drying and wetting cycles. This characteristic is useful in the calculation of PoSD function that is assumed equal to the

derivative function of SWCC models for drying branch (i.e., Eqs. (4.6)). This simplified treatment is widely accepted and used in the literature (e.g., Fredlund and Xing, 1994; Zhai et al., 2020).

Figures 4.5, 4.6 and 4.7 present the results of the proposed three methods (i.e., first, second, and third methods, respectively) for scanning curves. These methods are based on the PoSD curves with clear physical meaning (Li and Vanapalli, 2021) (i.e., Eqs. (4.15) and (4.17)); these are simple methods with only two parameters, and only one parameter needs calibration based on Eqs. (4.19), (4.20), and (4.21) for the second and third methods. The second and the third methods (i.e., the simplified methods in comparison to the first method) are highlighted because one parameter can be fixed by the boundary condition (i.e., Eqs. (4.19)). The constant β and λ for the second and the third methods (i.e., Eqs. (4.20) and (4.21)), respectively, are the only parameter that should be calibrated using experiment of scanning curves. These methods are simple and have relatively high accuracy.

The meeting points listed in Table 4.1 are measured points in main curves or scanning curves. The measured points in scanning curves are used as meeting points in some cases (e.g., Wray sands in Figures 4.5, 4.6 and 4.7) because there are several measured points, for the main wetting curves. If the measured points are sparse in main drying or wetting curves, the measured points in scanning curves can be used as meeting points that contribute reasonably to capture the features of all scanning curves.

In the three methods (i.e., the first, second, and third methods) shown in Figures 4.5, 4.6, and 4.7, respectively, parameters λ and β (i.e., Eqs. (4.15c), (4.15d), (4.17c), and (4.17d)) are restrained to be less than or equal to one. However, as discussed in the earlier section, scanning curves can be used to build water and soil suction relationships between the main curves. The large pores may partially be filled with water (i.e., the number of soil pores with the same amount of water is more in comparison of PoSD curve). The values of parameters λ and β might be larger than one for some points in the scanning curve. However, the constraints (i.e., Eqs. 4.17 (b) and (d)) are applied to ensure relatively reasonable curve shapes.

For the second and the third methods as shown in Figures 4.6 and 4.7, respectively, experimental data of scanning curves is required for calibration purposes. Such a method is acceptable to find a constant β or λ value for well predicting all scanning curves. However, as

discussed in previous paragraph, different constant β or λ values are possible based on 'trial-and-error' method. As discussed earlier, using Eqs. (4.19), various acceptable parameters values can be obtained using two sets of parameters with only one set of boundary condition. As shown in Figure 4.8, SWCC behavior of clayey soils is significantly affected by both initial stress state and initial water content. The mechanisms associated with the differences in the SWCC behavior due to the influence of initial stress state and water content are rather different. Various types of pores in clayey soils that include macropores and micropores are affected due to the influence of different stress state. For example, the soils pores in compacted fine-grained soils are also influenced by initial water content, which contribute to different soil structure. This is strongly related to the soil suction that is dependent on different water contents. Thus, the two major mechanical factors that influence the summarized results in Figure 4.8 (ii) are isotropic mechanical loading and soil suction. Equations for initial stress state and water content are similar; however, the mechanisms are distinct. As for parameters ξ_c and ξ_i, (e.g., Eqs. (4.24d) and (4.25c)) they are independent variables representing two influential factors, but they are affected by each other (e.g., Eqs. (4.28) and (4.29)) since both describe the SWCC (i.e., soil water and suction relationship).

Figures 4.9 (a), (b) and 4.10 (a) present results of sandy clay till using model parameters for van Genuchten equation (i.e., Eq. (4.4)). As per the discussions summarized in the last paragraph, new parameters ξ_c and ξ_i, can be introduced to evaluate initial stress state and water content effects. However, each parameter requires calibration of two curves. A set of more suitable parameters for van Genuchten equations could be obtained with the same two curves. However, due to the inherent anisotropic nature of soils, PoSD curves may vary significantly (Yin and Vanapalli, 2018).

Figure 4.10 summarizes the results from Eqs. (4.31); they are useful for explaining the meaning of the model derived from the PoSD curve (i.e., a polynomial-form relationship between pore size and initial stress state (or initial water content)). The effects associated with initial stress state and water content can be explained using Eq. (4.40), which is obtained by dividing Eq. (4.26a) by Eq. (4.26b).

$$\frac{\ln(r_2)-\ln(r_0)}{\ln(r_1)-\ln(r_0)} = -\frac{\xi_i}{\xi_c}\frac{(w_i-w_{i0})}{(e-e_0)} \tag{4.40}$$

The void ratio represents the ratio of void volume to soil solid volume, and gravimetric water content is the ratio of the mass of water to the mass of soil solids. If the volume and the mass of soil solids are the constant, by dividing density of water in both sides in Eq. (4.40), the following equation can be obtained.

$$\frac{\ln(r_2)-\ln(r_0)}{\ln(r_1)-\ln(r_0)} = -\frac{1}{G_s}\frac{\xi_i}{\xi_c}\frac{(V_w-V_{w0})}{(V_{void}-V_{void0})} \tag{4.41}$$

where G_s is specific gravity of soil solids, V_w and V_{w0} are volumes of water at initial water content and reference state, respectively, V_{void} and V_{void0} are the volume of void at initial stress state and reference state, respectively. Eq. (4.41) can be expressed in differential form as given below.

$$\frac{\Delta\ln(r_2)}{\Delta\ln(r_1)} = -\frac{1}{G_s}\frac{\xi_i}{\xi_c}\frac{\Delta V_w}{\Delta V_{void}} \tag{4.42}$$

Because r_1 and r_2 represent soil suction ψ_1 and ψ_2, respectively, the left side of Eq. (4.42) can also be written as below.

$$\frac{\Delta\ln(r_2)}{\Delta\ln(r_1)} \cong \frac{\mathrm{d}\ln(\psi_2)}{\mathrm{d}\ln(\psi_1)} \tag{4.43}$$

The relationship below can be used since degree of saturation S is the ratio of volume of water to volume of soil voids.

$$\lim_{\Delta\to 0}\frac{\Delta V_{wi}}{\Delta V_{void}} = S_i' \tag{4.44}$$

where S_i is initial degree of saturation, S_i' denotes the derivative of initial degree of saturation.

A simplified form of relationship can be derived as below by substituting Eqs. (4.43) and (4.44) into (4.42).

$$\frac{\mathrm{d}\ln(\psi_2)}{\mathrm{d}\ln(\psi_1)} = -\frac{1}{G_s}\frac{\xi_i}{\xi_c}S_i' \tag{4.45}$$

Eq. (4.45) simply describes the effects of both initial stress state and water content on SWCCs.

Since soil suction represents soil potential Ψ, it means that both initial stress state and water content affect the variation of overall soil potential from reference state. This effect is imposed by altering initial degree of saturation of soils from its reference state (e.g., Wheeler et al., 2003; Tarantino, 2009; Gallipoli, 2012; Zhou et al., 2012a; Hu et al., 2013).

4.7 Conclusions

In this Chapter, a new model (i.e., Eqs. (4.11)) is proposed for predicting main wetting SWCC curve the from main drying curve. The wetting SWCC along with its hysteretic features were predicted for a variety of soils using simple equations based on the PoSD curve that were linked to the well-known SWCC fitting equations and a set of boundary conditions. Three methods for predicting scanning curves as well as the corresponding calibration processes are derived for coarse-grained soils (i.e., Eqs. (4.15), (4.17) and (4.19)). Comprehensive comparisons were provided using these equations, between the experimental results and the predicted SWCCs of both coarse-grained soils.

In addition, the SWCCs of fine-grained soils were successfully predicted taking account of the influence of stress state and soil structure associated with different initial water contents (i.e., Eqs. (4.31)). The multi-parametric influences for modelling SWCCs are also evaluated and discussed (i.e., Eq. (4.34)) and a modified SWCC model (i.e., Eq. (4.37)) is proposed based on van Genuchten equation.

The proposed equations can be used as tools for predicting various properties of unsaturated soils taking account of the influence of soil hysteresis and scanning curves. In addition, they can be incorporated into numerical models for analyzing the complex THMC behaviors of unsaturated soils.

4.8 Appendix: A generalized thermodynamics framework

In this Appendix, details related to the analytical methods are summarized based on the principles of thermodynamics and conservation laws. This framework is consistent with the continuum mechanics principles extending the independent stress state variables approach (e.g., Fredlund et al. 2012; Li and Vanapalli, 2021).

4.8.1 Background information and assumptions

4.8.1.1 Background information of the principles of thermodynamics

The expressions for internal energy *dU*, enthalpy *dH*, the Helmholtz free energy *dF*, and the Gibbs free energy *dG* are listed in Eqs. (A-1), (A-2), (A-3), and (A-4), respectively based on the principles of thermodynamics (e.g., Houlsby and Puzrin, 2000).

$$dU = -PdV + TdS^E + \sum \mu_k dN_k \quad \text{(A-1)}$$

$$dH = VdP + TdS^E + \sum \mu_k dN_k \quad \text{(A-2)}$$

$$dF = -PdV - S^E dT + \sum \mu_k dN_k \quad \text{(A-3)}$$

$$dG = VdP - S^E dT + \sum \mu_k dN_k \quad \text{(A-4)}$$

$$\mu_k = \mu_k^* + RT\ln(\gamma_k x_k) = \mu_k^* + RT\ln\left(\gamma_k \frac{N_k}{N}\right) \quad \text{(A-5)}$$

where V, P, S^E, T, and N are volume, pressure, entropy, temperature, and total number of substances, μ_k, μ_k^*, N_k, x_k, and γ_k are chemical potentials, standard chemical potentials, number of particles, mole fraction, and coefficient of activity of the k-th substance, respectively, and R is universal gas constant.

4.8.1.2 Assumptions used in the proposed method

The developed framework in this study is based on several assumptions that are summarized below.

(i) The compressibility of soil solids is not considered.

(ii) The components in soil pores cannot bear shear stress.

(iii) The spatial variations of porosity and degree of saturation are not considered.

(iv) Only dilute ideal solutions without volatility can be considered (e.g., *NaCl* in liquid water).

4.8.2 The expressions for work input *PdV*

The work input (e.g., Houlsby and Puzrin, 2000; Borja, 2006) for constant pressure P with respect to time can be expressed as Eq. (A-6).

$$\frac{dW}{Vdt} = \frac{-PdV}{Vdt} \quad \text{(A-6)}$$

In this study, the meanings of conjugate pairs (e.g., P and V) are extended to stress and strain to embrace the continuum mechanics principles.

4.8.2.1 Soil volume relationships

The volume relationships (e.g., Mitchell and Soga, 2005) between soil solids, soil pores, and the fraction of each component in soil pores are summarized in Eqs. (A-7), (A-8), and (A-9), respectively.

$$V = V_{solid} + V_{pore} = V(1-n) + Vn \tag{A-7}$$

$$\sum_{\alpha=1}^{m} S_\alpha = \frac{1}{V_{pore}} \sum_{\alpha=1}^{m} V_\alpha \equiv 1 \tag{A-8}$$

$$\sum_{\alpha=1}^{m} \theta_\alpha = \frac{\sum_{\alpha=1}^{m} V_\alpha}{V} = \frac{V_{pore}}{V} \tag{A-9}$$

where V_{solids}, and V_{pores} refer to volumes of soil solids and pores, respectively, n is porosity, and S_α, V_α, and θ_α refer to the degree of saturation, volume, and volumetric content of α-*th* component in soil pores, respectively.

4.8.2.2 Definitions of stress and strain tensors

To be compatible with geomechanics, the variables in thermodynamics are further expanded as following. The strain rate tensor and stress tensor (i.e., tension is positive) are defined following the sign convention in geotechnical engineering (Houlsby and Puzrin, 2000, Borja, 2006; Zhao et al. 2010; Xu et al. 2020) as shown in Eqs. (A-10), (A-11), (A-12). The left side of the three equations denote the thermodynamic variables, while the right side are extended to harbor convention of geomechanics.

$$P \rightarrow -\sigma_{ij} \tag{A-10}$$

$$\frac{dV}{Vdt} \rightarrow \dot{\varepsilon}_{ij} = \mathrm{div}\boldsymbol{v} \tag{A-11}$$

$$\frac{dV_\alpha}{Vdt} \rightarrow \dot{\varepsilon}_{ij}^{(\alpha)} = \mathrm{div}\boldsymbol{v}^{(\alpha)} \tag{A-12}$$

where $\boldsymbol{v}$ is velocity vector, div is divergence of velocity vector, and $\boldsymbol{\varepsilon}^{(\alpha)}$ and $\boldsymbol{v}^{(\alpha)}$ specifies the strain and velocity vector of a certain component in soils (i.e., the soil solids can be also expressed by Eq. (A-9)). The stress and strain tensors as shown in Eq. (A-9) along with the sign convention are widely used in geomechanics field (i.e., compression is set as positive).

The stress tensor (e.g., Borja, 2006) in Eq. (A-10) can be written as shown in Eq. (A-13) without considering contractile skin (i.e., surface tension) between distinct phases.

$$\sigma_{ij} = (1-n)s_{ij} + n\sum_{\alpha=1}^{m} S_\alpha \sigma_{ij}^{(\alpha)} \tag{A-13}$$

where s_{ij} refers to soil solid skeleton stress, and $\boldsymbol{\sigma}^{(\alpha)}$ is the stress tensor of α-*th* component in soil pores.

In this framework, all components except soil solids are treated as a part of soil pores.

4.8.2.3 The energy conservation

Eq. (A-14) can be obtained by substituting Eqs. (A-7), (A-8), and (A-13) into Eq. (A-6).

$$\frac{dW}{Vdt} = \frac{-PdV}{Vdt} = \left[(1-n)s_{ij} + n\sum_{\alpha=1}^{m} S_\alpha \sigma_{ij}^{(\alpha)}\right] \frac{d(V_{solid}+\sum_{\alpha=1}^{m} V_\alpha)}{Vdt} \tag{A-14}$$

The subsystem of work input W_α can be defined as summarized in Eq. (A-15).

$$\frac{dW_\alpha}{Vdt} = \left(\frac{V_\alpha}{V}\sigma_{ij}^{(\alpha)}\right)\frac{dV_\alpha}{Vdt} \tag{A-15}$$

In this subsystem α refers to soil solids or components in soil pores and the work output to subsystem β ($\alpha \neq \beta$) and work input from subsystem β can be written as Eq. (A-16).

$$\frac{dW_\alpha}{Vdt} = \left(\frac{V_\alpha}{V}\sigma_{ij}^{(\alpha)}\right)\frac{dV_\alpha}{Vdt} - \left(\frac{V_\alpha}{V}\sigma_{ij}^{(\alpha)}\right)\frac{dV_\beta}{Vdt} + \left(\frac{V_\beta}{V}\sigma_{ij}^{(\beta)}\right)\frac{dV_\alpha}{Vdt} \ (\alpha \neq \beta) \tag{A-16}$$

The work output from subsystem α equals to the work input to subsystem β, and vice versa based on the conservation of energy (e.g., Borja, 2006; Zhao et al. 2010; Xu et al. 2020), without considering the energy exchange with the environment. For subsystem β, the following Eq. (A-17) holds.

$$\frac{dW_\beta}{Vdt} = \left(\frac{V_\beta}{V}\sigma_{ij}^{(\beta)}\right)\frac{dV_\beta}{Vdt} - \left(\frac{V_\beta}{V}\sigma_{ij}^{(\beta)}\right)\frac{dV_\alpha}{Vdt} + \left(\frac{V_\alpha}{V}\sigma_{ij}^{(\alpha)}\right)\frac{dV_\beta}{Vdt} \ (\alpha \neq \beta) \tag{A-17}$$

Eq. (A-18) can be obtained by summing up all the work input and output for subsystem α.

$$\frac{dW_\alpha}{Vdt} = \left(\frac{V_\alpha}{V}\sigma_{ij}^{(\alpha)}\right)\frac{dV_\alpha}{Vdt} - \left(\frac{V_\alpha}{V}\sigma_{ij}^{(\alpha)}\right)\frac{d\left(\sum_{\beta=1}^{m} V_\beta\right)}{Vdt} + \frac{dV_\alpha}{Vdt}\sum_{\beta=1}^{m}\left(\frac{V_\beta}{V}\sigma_{ij}^{(\beta)}\right)(\alpha \neq \beta) \quad \text{(A-18)}$$

The total work input W equals to the sum up all subsystems W_α, extending this definition, Eq. (A-19) can be obtained.

$$\frac{dW}{Vdt} = \sum_{\alpha=1}^{m}\frac{dW_\alpha}{Vdt} = \frac{\sigma_{ij}dV}{Vdt} = \left(\frac{V_{solid}}{V}\sigma_{ij}^{(solid)}\right)\frac{dV_{solid}}{Vdt} + \sum_{\alpha=1}^{m}\left[\left(\frac{V_\alpha}{V}\sigma_{ij}^{(\alpha)}\right)\frac{dV_\alpha}{Vdt}\right] \quad \text{(A-19)}$$

Based on the above equation, relationships between total work input and the work done by each component are obtained. The form is of this equation is the same without energy supply (e.g., Borja, 2006) when dV_α / (Vdt) is expressed as the strain tensor of α-th component $\boldsymbol{\varepsilon}^{(\alpha)}$ (e.g., Eq. (A-12)). To be consistent, the relationships between system and subsystems are derived from the concepts of thermodynamics and energy conservation principles.

The following Eq. (A-20) can be obtained by substituting Eqs. (A-7), (A-10), (A-11), and (A-13) into Eq. (A-19).

$$\frac{dW}{Vdt} = \frac{PdV}{Vdt} = \sigma_{ij}\dot{\varepsilon}_{ij} = (1-n)s_{ij}\mathrm{div}\boldsymbol{v}^{(solid)} + n\sum_{\alpha=1}^{m}\left(S_\alpha\sigma_{ij}^{(\alpha)}\mathrm{div}\boldsymbol{v}^{(\alpha)}\right) = \sigma_{ij}\mathrm{div}\boldsymbol{v}^{(solid)} + n\sum_{\alpha=1}^{m}\left[S_\alpha\sigma_{ij}^{(\alpha)}\left(\mathrm{div}\boldsymbol{v}^{(\alpha)} - \mathrm{div}\boldsymbol{v}^{(solid)}\right)\right] \quad \text{(A-20)}$$

4.8.2.4 The mass conservation

The above Eq. (A-20) is further simplified such that the mass conservation is as shown in Eqs. (A-21) and (A-22) (e.g., Borja, 2006; Zhao et al. 2010; Xu et al. 2020).

$$\frac{d(V_\alpha\rho_\alpha)}{dt} + V_\alpha\rho_\alpha\mathrm{div}\boldsymbol{v}^{(\alpha)} = \zeta_\alpha \quad \text{(A-21a)}$$

$$\sum_{\alpha=1}^{m}\zeta_\alpha = 0 \quad \text{(A-21b)}$$

$$\rho_\alpha = \frac{m_\alpha}{V_\alpha} \quad \text{(A-22a)}$$

$$\rho = (1-n)\rho_{solid} + n\sum_{\alpha=1}^{m}S_\alpha\rho_\alpha \quad \text{(A-22b)}$$

where ρ_α and m_α are the density and mass of α-th component, respectively, ζ_α is the mass supply to component α from other components, ρ is the total density, and ρ_{solid} is the density of soil solids.

Eqs. (A-23) and (A-24) for soil solids and components in soil pores can be respectively obtained for unit soil mass, based on Eqs. (A-7), (A-8), and (A-9).

$$-\frac{dn}{dt} + (1-n)\mathrm{div}\boldsymbol{v}^{(solid)} = 0 \quad \text{(A-23)}$$

$$\theta_\alpha \frac{d\rho_\alpha}{\rho_\alpha dt} + S_\alpha \frac{dn}{dt} + n\frac{dS_\alpha}{dt} + \theta_\alpha \mathrm{div}\boldsymbol{v}^{(\alpha)} = \frac{\zeta_\alpha}{\rho_\alpha} \quad \text{(A-24)}$$

In Eq. (A-23), it should be noted that both the mass supply to soil solids from other components and the density change of soil solids are not considered (i.e., consistent with assumption (i) of the proposed approach).

4.8.2.5 The final expressions for work input PdV

Eq. (A-25) is a simplified relationship that can be derived by substituting Eqs. (A-23) and (A-24) into Eq. (A-20).

$$-\frac{PdV}{Vdt} = \sigma_{ij}\dot{\varepsilon}_{ij} = \left(\sigma_{ij} - \sum_{\alpha=1}^{m} S_\alpha \sigma_{ij}^{(\alpha)}\right)\dot{\varepsilon}_{ij}^{(solid)} - \sum_{\alpha=1}^{m}\left[\sigma_{ij}^{(\alpha)}\left(n\frac{dS_\alpha}{dt} + \theta_\alpha \frac{d\rho_\alpha}{\rho_\alpha dt} - \frac{\zeta_\alpha}{\rho_\alpha}\right)\right] \quad \text{(A-25)}$$

Eq. (A-25) constitutes of two parts on the right side. The first part of equation describes the stress in soil solids (i.e., effective stress $\boldsymbol{\sigma'}$) as shown in Eq. (A-26).

$$\boldsymbol{\sigma}' = \sigma_{ij} - \sum_{\alpha=1}^{m} S_\alpha \sigma_{ij}^{(\alpha)} \quad \text{(A-26a)}$$

$$\sum_{\alpha=1}^{m} S_\alpha \equiv 1 \quad \text{(A-26b)}$$

Eqs. (A-26) are written as continuous-form equations; however, evidence from the literature with respect to unsaturated soils behavior (e.g., Jennings and Burland, 1962; Bishop and Blight, 1963; Fredlund and Morgenstern, 1977; Vanapalli et al. 1996; Cunningham et al. 2003) suggests that the independent stress state variables approach is flexible and capable to capture the complex behavior of unsaturated soils. Therefore, Eqs. (A-26) are expressed in terms of independent stress state variables to describe the complex hydro-mechanical behavior of unsaturated soils (e.g., Garcia et al. 2010; Pouya et al. 2013; Qian et al. 2022; Li and Vanapalli et al. 2022a) that are consistent with continuum mechanics principles.

The above discussed philosophy of Eqs. (A-27) are also expressed in terms of independent

stress state variables by extending Eqs. (A-26). As suggested by Fredlund and Morgenstern (1977), various expressions of independent stress state variables are possible.

$$\left(\sigma_{ij}-\sigma_{ij}^{(\alpha)}\right),\left(\sigma_{ij}-\sigma_{ij}^{(\beta)}\right),\ldots,\left(\sigma_{ij}-\sigma_{ij}^{(m)}\right) \tag{A-27a}$$

$$\left(\sigma_{ij}-\sigma_{ij}^{(\alpha)}\right),\left(\sigma_{ij}^{(\beta)}-\sigma_{ij}^{(\alpha)}\right),\ldots,\left(\sigma_{ij}^{(m)}-\sigma_{ij}^{(\alpha)}\right) \tag{A-27b}$$

The second part of the right side in Eq. (A-25) is related to mass change of components in soil pores which is consistent with the conservation of mass. Here, assumption (ii) of the proposed approach is extended that no component in soil pores can bear shear stress is highlighted.

4.8.3 Expressions for work input *VdP*

The work input expression for *VdP* with respect to time can be expressed without considering heat exchange (e.g., Houlsby and Puzrin, 2000), as below.

$$\frac{dW}{Vdt}=\frac{VdP}{Vdt}=-\frac{d\sigma_{ij}}{dt}=-\frac{\partial\boldsymbol{\sigma}}{\partial x_j}\frac{dx_j}{dt}=-\frac{\partial\boldsymbol{\sigma}}{\partial x_j}v_j \tag{A-28}$$

In this relationship, only work input is considered extending similar discussions in the earlier section. More discussion related to conjugate pairs is summarized in the next section.

4.8.3.1 Linear momentum conservation

Eqs. (A-29) and (A-30) provide the linear momentum balance equations (e.g., Borja, 2006; Zhao et al. 2010; Xu et al. 2020) for soil solids and component in soils pores.

$$\nabla s_{ij}-\rho_{solid}g_i=\rho_{solid}\frac{dv_i^{(solid)}}{dt} \tag{A-29}$$

$$\nabla\sigma_{ij}^{(\alpha)}-\rho_\alpha g_i=\rho_\alpha\frac{dv_i^{(\alpha)}}{dt}+\zeta_\alpha v_i^{(\alpha)} \tag{A-30}$$

where g_i is acceleration due to gravity.

The linear momentum conservation of soil systems can be expressed as Eq. (A-31)) by summing up all components in unsaturated soils in Eqs. (A-13), (A-21), and (A-22).

$$\nabla\sigma_{ij} - \rho\left(g_i - \frac{dv_i}{dt}\right) = 0 \tag{A-31}$$

Eq. (A-31) is the total stress balance which is frequently used in continuum mechanics (e.g., Lei et al. 2016; Le Pense et al. 2016; Pouragha et al. 2021) when the influence of velocity $\boldsymbol{v}$ is not considered.

4.8.3.2 Linear angular momentum conservation

The two conclusions derived based on the mass conservation and the linear angular momentum conservation (e.g., Borja, 2006; Pouragha et al. 2021) are summarized below.

$$\sigma_{ij} = \sigma_{ji} \tag{A-32}$$

$$\mathrm{div}\sigma_{ij} = \nabla\sigma_{ij} \tag{A-33}$$

The gradients of stress tensor in Eqs. (A-28) and (A-31) can be written in divergence form by considering the conservation of linear angular momentum.

4.8.3.3 Final expressions for work input VdP

Eq. (A-34) can be derived by substituting Eqs. (A-13), (A-22), (A-29), and (A-33) into Eq. (A-28). However, in this equation the spatial variation of soil volume is neglected, which is consistent with assumption (iii) of this study.

$$-\frac{VdP}{Vdt} = \mathrm{div}(\sigma_{ij})v_j = \mathrm{div}\left((1-n)s_{ij} + n\sum_{\alpha=1}^{m} S_\alpha \sigma_{ij}^{(\alpha)}\right)v_j = \left[(1-n)\rho_{solid}g_i + (1-n)\rho_{solid}\frac{dv_i^{(solid)}}{dt}\right]v_j + n\sum_{\alpha=1}^{m} S_\alpha \mathrm{div}\sigma_{ij}^{(\alpha)}\, v_j = \left[\rho g_i + (1-n)\rho_{solid}\frac{dv_i^{(solid)}}{dt}\right]v_j + n\sum_{\alpha=1}^{m} S_\alpha\left(\mathrm{div}\sigma_{ij}^{(\alpha)} - \rho_\alpha g_i\right)v_j \tag{A-34}$$

The velocity vector $\boldsymbol{v}^{(\alpha)}$ can be defined using Eq. (A-35). Furthermore, Eq. (A-36) can be obtained by setting the velocity of soil solids $\boldsymbol{v}^{(solid)}$ as reference (e.g., constant).

$$v_j^{(\alpha)} = nS_\alpha v_j \tag{A-35}$$

$$-\frac{VdP}{Vdt} = \mathrm{div}(\sigma_{ij})\left(v_j - v_j^{(solid)}\right) = \rho g_i\left(v_j - v_j^{(solid)}\right) + \sum_{\alpha=1}^{m}\left[\left(\mathrm{div}\sigma_{ij}^{(\alpha)} - \rho_\alpha g_i\right)\left(v_j^{(\alpha)} -\right.\right.$$

$$v_j^{(solid)}\Big)\Big] \tag{A-36}$$

Eq. (A-37) can be derived by comparing Eq. (A-36) with Eq. (A-31).

$$-\frac{VdP}{Vdt} = \mathrm{div}(\sigma_{ij})\left(v_j - v_j^{(solid)}\right) - \rho g_i\left(v_j - v_j^{(solid)}\right) = -\rho\frac{dv_j}{dt}\left(v_j - v_j^{(solid)}\right) = \sum_{\alpha=1}^{m}\left[\left(\sigma_{ij,i}^{(\alpha)} - \rho_\alpha g_i\right)\left(v_j^{(\alpha)} - v_j^{(solid)}\right)\right] \tag{A-37}$$

Eq. (A-37) highlights the relationship of flow behavior within the thermodynamics framework.

Detailed comparisons with the available framework and verifications for the various models that are widely used in the literature are discussed in the next section.

4.8.4 Temperature and salts effects

Eq. (A-38) that is based on the second law of thermodynamics is valuable for explaining the temperature contribution (e.g., Houlsby and Puzrin, 2000; Borja, 2006).

$$TdS^E = TdS^{E,ir} + TdS^{E,re} \geq TdS^{E,re} = T\left(\frac{q_i}{T}\right)_{,i} \tag{A-38}$$

where $S^{E,ir}$ and $S^{E,re}$ are the entropy in irreversible and reversible processes, respectively, and q_i is the heat flux.

Eq. (A-38) states that the total entropy is equal to or greater than the entropy in reversible process. By introducing the dissipative heat (e.g., $D = TdS^{E,ir}$) for irreversible process, the dissipation function can be obtained (Houlsby and Puzrin, 2000).

In this section, the dissipation structure is not considered. However, another method based on the Maxwell relations is proposed as below.

$$\frac{TdS^E}{Vdt} = T\left(\frac{\partial S^E}{\partial V}\right)_T\frac{dV}{Vdt} + T\left(\frac{\partial S^E}{\partial T}\right)_V\frac{dT}{Vdt} = T\frac{\alpha_V}{K_V}\frac{dV}{Vdt} + C_V\frac{dT}{Vdt} \tag{A-39}$$

$$\frac{TdS^E}{Vdt} = T\left(\frac{\partial S^E}{\partial P}\right)_T\frac{dP}{Vdt} + T\left(\frac{\partial S^E}{\partial T}\right)_P\frac{dT}{Vdt} = -T\alpha_V V\frac{dP}{Vdt} + C_P\frac{dT}{Vdt} \tag{A-40}$$

where α_{VT} is the coefficient of thermal expansion, K_V is compressibility, and C_V and C_P are heat capacity at constant volume and pressure, respectively.

Eqs. (A-39) and (A-40) were obtained based on the Maxwell relations (more details in Appendix C).

The expressions for α_{VT} and K_V are listed in Eqs. (A-41a) and (A-41b), respectively.

$$\alpha_V = \frac{1}{V}\left(\frac{\partial V}{\partial T}\right)_P \tag{A-41a}$$

$$K_V = -\frac{1}{V}\left(\frac{\partial V}{\partial P}\right)_T = \frac{1}{V}\left(\frac{\partial V}{\partial \sigma_{ij}}\right)_T \tag{A-41b}$$

$$C_P \frac{dT}{Vdt} = C_P \frac{\partial T}{V\partial x_j}\frac{\partial x_j}{\partial t} = C_P \nabla T v_j = c_p^{(solid)} \nabla T v_j^{(solid)} + \sum_{\alpha=1}^{m} c_p^{(\alpha)} \nabla T v_j^{(\alpha)} \tag{A-41c}$$

where c_p refers to specific heat capacity with unit of [J·mol^{-1}K^{-1}]. As distinct components in unsaturated soils have different specific heat capacities c_P, based on definition of velocity vector $v^{(\alpha)}$ in Eq. (A-35), Eq. (A-41c) can be obtained.

Based on differential characteristics in the Maxwell relations (e.g., $1/(\partial x/\partial y) = \partial y/\partial x$), the following definition for thermal stress P_T can be obtained.

$$P_{ij}^T = T\frac{\alpha_V}{K_V} = T\frac{(\partial V/\partial T)_P}{-(\partial V/\partial P)_T} = T\frac{(\partial V/\partial T)_\sigma}{(\partial V/\partial \sigma_{ij})_T} = T\left(\frac{\partial \sigma_{ij}}{\partial V/V}\right)_T \left(\frac{\partial V/V}{\partial T}\right)_\sigma \tag{A-42}$$

As shown in Eq. (A-42), the sign notation for $\boldsymbol{P^T}$ follows the convention in geomechanics. Note the expressions of total stress tensor σ_{ij} in Eq. (A-13), the following Eq. (A-43) can be obtained.

$$P_{ij}^T = (1-n)T\left(\frac{\partial s_{ij}}{\partial V}\right)_T \left(\frac{\partial V}{\partial T}\right)_P + nT\sum_{\alpha=1}^{m} S_\alpha \left(\frac{\partial \sigma_{ij}^{(\alpha)}}{\partial V}\right)_T \left(\frac{\partial V}{\partial T}\right)_P = (1-n)P_{ij}^{T,solid} + n\sum_{\alpha=1}^{m} S_\alpha P_{ij}^{T,(\alpha)} \tag{A-43}$$

where $\boldsymbol{P^{T,solid}}$ and $\boldsymbol{P^{T,(\alpha)}}$ refer to thermal stress in soil solids and α-th component in soil pores, respectively.

Eq. (A-44) can be obtained by substituting Eq. (A-43) into Eq. (A-39).

$$\frac{TdS^E}{Vdt} = P_{ij}^T \frac{dV}{Vdt} + C_V \frac{dT}{Vdt} = \left((1-n)P_{ij}^{T,solid} + n\sum_{\alpha=1}^{m} S_\alpha P_{ij}^{T,(\alpha)}\right)\frac{dV}{Vdt} + C_V \frac{dT}{Vdt} \quad \text{(A-44)}$$

For conjugate variables μ_k and N_k, based on the assumption (iv)**,** only dilute ideal (liquid) water solution is considered (e.g., $\gamma_k = 1$ in Eq. (A-5)). This relationship is suitable for salts such as the *NaCl* and $CaCl_2$. For salts with high concentration or partially dissolved salts, more studies are required. Based on Eq. (A-5), the following Eq. (A-45) can be obtained for *k*-th solute.

$$\frac{\mu_k dN_k}{Vdt} = \frac{\mu_k^* + RT\ln\left(\frac{N_k}{N}\right)}{Vdt} dN_k = \left[\mu_k^* + RT\ln\left(\frac{c_k V_{lw}}{\frac{V_{lw}\rho_{lw}}{M_{lw}} + c_k V_{lw}}\right)\right]\frac{d(c_k V_{lw})}{Vdt} \cong \left[\mu_k^* + RT\ln\left(\frac{c_k V_{lw}}{V_{lw}\rho_{lw}/M_{lw}}\right)\right]\frac{d(c_k V_{lw})}{Vdt} = \left[\mu_k^* + RT\ln\left(\frac{c_k M_{lw}}{\rho_{lw}}\right)\right]\frac{V_{lw}dc_k}{Vdt} \quad \text{(A-45)}$$

where c_k is the concentration of *k*-th substance (solute) in liquid water, and M_{lw} is the molar mass of liquid water.

In Eq. (A-45), volume of liquid water (i.e., V_{lw}) is treated as a constant as it affects entire solutes rather than a specific solute. The effects of total number of (liquid) water molecular (i.e., volume of liquid water) on conjugate variables N_k and μ_k are evaluated as following.
Based on Eqs. (A-35) and (A-45), Eq. (A-5) can be written as Eqs. (A-46) for ideal dilute salt solutions as the solution can be divided into solutes (e.g., dissolved salts) and solvent (e.g., liquid water).

$$\frac{\sum \mu_k dN_k}{Vdt} = \sum\left[\mu_k^* + RT\ln\left(\frac{c_k M_{lw}}{\rho_{lw}}\right)\right]\frac{V_{lw}dc_k}{Vdt} + \frac{\mu_{lw}dN_{lw}}{Vdt} = \sum P_{\mu k}\frac{V_{lw}dc_k}{Vdt} + \frac{\left[\mu_{lw}^* + RT\ln\left(1-\frac{\sum c_k V_{lw}}{\rho_{lw}V_{lw}/M_{lw}+\sum c_k V_{lw}}\right)\right]\rho_{lw}dV_{lw}}{M_{lw}Vdt} \cong \sum P_{\mu k}\frac{V_{lw}dc_k}{Vdt} + \frac{\left[\mu_{lw}^* + RT\ln\left(1-\frac{\sum c_k V_{lw}}{\rho_{lw}V_{lw}/M_{lw}}\right)\right]\rho_{lw}dV_{lw}}{M_{lw}Vdt} \cong \sum P_{\mu k}\frac{V_{lw}dc_k}{Vdt} + \frac{\left(\mu_{lw}^* - RT\frac{\sum c_k V_{lw}}{\rho_{lw}V_{lw}/M_{lw}}\right)\rho_{lw}dV_{lw}}{M_{lw}Vdt} \quad \text{(A-46a)}$$

$$\frac{\sum \mu_k dN_k}{Vdt} = \sum\left[\mu_k^* + RT\ln\left(\frac{c_k M_{lw}}{\rho_{lw}}\right)\right]\frac{V_{lw}dc_k}{Vdt} + \frac{\mu_{lw}dN_{lw}}{Vdt} = \sum\left[\mu_k^* + RT\ln\left(\frac{c_k M_{lw}}{\rho_{lw}}\right)\right]\frac{V_{lw}dc_k}{Vdt} + \frac{\left(\mu_{lw}^* - RT\frac{\sum c_k V_{lw}}{\rho_{lw}V_{lw}/M_{lw}}\right)\rho_{lw}dV_{lw}}{M_{lw}Vdt} = \sum P_{\mu k}\frac{V_{lw}dc_k}{Vdt} + P_\mu\frac{dV_{lw}}{Vdt} = \sum P_{\mu k}\nabla c_k v_j^{(lw)} + P_\mu\frac{dV_{lw}}{Vdt} \quad \text{(A-46b)}$$

where P_μ and $P_{\mu k}$ refer to chemical potential of water and chemical potential of k-th solute, respectively. To derive the last term in Eq. (A-46a), Maclaurin series approximation near zero is adopted (i.e., ln (1 - x) ≈ -x, when x is near zero).

Two different roles of chemical solutions in liquid water can be highlighted based on Eq. (A-46b). The first role is related to the variation of salt concentration (i.e., the first term on the right side of Eq. (A-46b)); the second role is linked to (liquid) water volume change in unsaturated soils (i.e., the section term on the right side of Eq. (A-46b)).

Eq. (A-46b) can be separated for convenience into two distinct terms (i.e., Eq. (A-47) and Eq. (A-48)). In other words, the effects of solutes and solvent (liquid water) are separately evaluated by Eq. (A-47) and (A-48), respectively. It is convenient to cater distinct roles of conjugate pairs P and V, and T and S^E (e.g., distinct expressions for work input in the earlier two sections).

$$\frac{\sum \mu_k dN_k}{Vdt} = \sum \left[\mu_k^* + RT\ln\left(\frac{c_k M_{lw}}{\rho_{lw}}\right)\right]\frac{V_{lw} dc_k}{Vdt} = \sum P_{\mu k} \nabla c_k v_j^{(lw)} \quad \text{(A-47)}$$

$$\frac{\sum \mu_k dN_k}{Vdt} = \frac{\mu_{lw} dN_{lw}}{Vdt} = \frac{\left(\mu_{lw}^* - RT\frac{\sum c_k V_{lw}}{\rho_{lw} V_{lw}/M_{lw}}\right)\rho_{lw} dV_{lw}}{M_{lw} Vdt} = P_\mu \frac{dV_{lw}}{Vdt} \quad \text{(A-48)}$$

For temperature variation over time (i.e., the second term on the right side in Eqs. (A-3) and (A-4)), the following Eqs. (A-49) can be obtained by expressing the entropy from soil volume relations (e.g., Eq. (A-49a)).

$$S^E = S^{E(solid)} V_{solid} + \sum_{\alpha=1}^{m} S^{E(\alpha)} V_\alpha \quad \text{(A-49a)}$$

$$\frac{S^E dT}{Vdt} = \frac{S^E \partial T}{V \partial x_j}\frac{\partial x_j}{\partial t} = \frac{S^{E(solid)} V_{solid} \partial T}{V \partial x_j}\frac{\partial x_j}{\partial t} + \sum_{\alpha=1}^{m} \frac{S^{E(\alpha)} V_\alpha \partial T}{V \partial x_j}\frac{\partial x_j}{\partial t} = S^{E(solid)} \nabla T v_j^{(solid)} + \sum_{\alpha=1}^{m} S^{E(\alpha)} \nabla T v_j^{(\alpha)} \quad \text{(A-49b)}$$

where $S^{E(solid)}$ and $S^{E(\alpha)}$ refer to entropy of soil solids and α-th component in soil pores, respectively.

4.8.5 Final expressions for thermodynamic potentials

The generalized thermodynamic potentials can be built using the summarized information from earlier sections. In the present study, variables related to thermo-hydro-mechanical-chemo behaviors are incorporated into the proposed framework.

4.8.5.1 Final expression for internal energy

Eq. (A-50) can be obtained for internal energy by substituting Eqs. (A-10), (A-44) and (A-48) into Eq. (A-1).

$$\frac{dU(V,S^E,N_k)}{Vdt} = \frac{\sigma_{ij}dV}{Vdt} + \frac{TdS^E}{Vdt} + \frac{\sum \mu_k dN_k}{Vdt} = \left(\sigma_{ij} + P_{ij}^T\right)\frac{dV}{Vdt} + C_V\frac{dT}{Vdt} + P_\mu\frac{dV_{lw}}{Vdt} \tag{A-50}$$

Eqs. (A-51) and (A-52) can be obtained from Eq. (A-13) to define the stress tensor in energy $\boldsymbol{\sigma}^E$ concept.

$$\sigma_{ij}^E = (1-n)\left(s_{ij} + P_{ij}^{T,solid}\delta_{ij}\right) + n\sum_{\alpha=1}^{m} S_\alpha\left(\sigma_{ij}^{(\alpha)} + P_{ij}^{T,(\alpha)}\delta_{ij}\right) + nS_{lw}P_\mu\delta_{ij} \tag{A-51}$$

$$s_{ij}^E = s_{ij} + P_{ij}^{T,solid} \tag{A-52a}$$

$$\sigma_{ij}^{E(lw)} = \sigma_{ij}^{(lw)} + P^{T,(lw)}\delta_{ij} + P_\mu\delta_{ij} \tag{A-52b}$$

$$\sigma_{ij}^{E(\alpha)} = \sigma_{ij}^{(\alpha)} + P^{T,(\alpha)}\delta_{ij} \tag{A-52c}$$

where $\boldsymbol{s}^E$ and $\boldsymbol{\sigma}^{E(\alpha)}$ refer to stress tensor in energy concept for soil skeletons and α-th component in soil pores, respectively, and δ_{ij} is Kronecker delta ($\delta_{ij} = 1$ for $i = j$; $\delta_{ij} = 0$ for $i \neq j$).

Eq. (A-53) can be obtained by substituting Eqs. (A-52) into Eq. (A-51).

$$\sigma_{ij}^E = (1-n)s_{ij}^E + n\sum_{\alpha=1}^{m} S_\alpha\sigma_{ij}^{E(\alpha)} \tag{A-53}$$

Based on Eq. (A-53), Eq. (A-50) is written in a different form, i.e., Eq. (A-54).

$$\frac{dU}{Vdt} = \frac{\sigma_{ij}dV}{Vdt} + \frac{TdS^E}{Vdt} + \frac{\sum \mu_k dN_k}{Vdt} = \sigma_{ij}^E\frac{dV}{Vdt} + C_V\frac{dT}{Vdt} \tag{A-54}$$

The liquid water density can be written as Eq. (A-55) when chemical potential is expressed as

part of water pressure (e.g., Eq. (A-52b)).

$$\rho_{lw} = \frac{m_{lw}+\sum M_k N_k}{V_{lw}+\sum M_k N_k/\rho_k} \cong \frac{m_{lw}+\sum M_k N_k}{V_{lw}} \quad \text{(A-55)}$$

where M_k is the molar mass of k-th substance.

Eq. (A-56) can be obtained in a similar manner to solve Eq. (A-30).

$$\frac{dU}{Vdt} = \sigma_{ij}^{E}\frac{dV}{Vdt} + C_V\frac{dT}{Vdt} = \left(\sigma_{ij}^{E} - \sum_{\alpha=1}^{m} S_\alpha \sigma_{ij}^{E(\alpha)}\right)\dot{\varepsilon}_{ij}^{(solid)} - \sum_{\alpha=1}^{m}\left[\sigma_{ij}^{E(\alpha)}\left(n\frac{dS_\alpha}{dt} + \theta_\alpha\frac{d\rho_\alpha}{\rho_\alpha dt} - \frac{\zeta_\alpha}{\rho_\alpha}\right)\right] + C_V\frac{dT}{Vdt} \quad \text{(A-56)}$$

Eq. (A-56) summarizes the stress tensors based on energy concepts that are discussed in various equations (i.e., Eqs. (A-51), (A-52), (A-53), and (A-55)).

4.8.5.2 Final expression for enthalpy

The enthalpy relationship over time can be expressed as Eq. (A-57) by substituting Eqs. (A-40), (A-41c), (A-47), and (A-49b) into Eq. (A-2).

$$\frac{dH(P,S^E,N_k)}{Vdt} = \frac{VdP}{Vdt} + \frac{TdS^E}{Vdt} + \frac{\sum \mu_k dN_k}{Vdt} = \frac{(1-T\alpha_V)VdP}{Vdt} + C_P\frac{dT}{Vdt} + \sum P_{\mu k}\nabla c_k v_j^{(lw)} = \frac{(1-T\alpha_V)VdP}{Vdt} + \left(c_p^{(solid)}\nabla T v_j^{(solid)} + \sum_{\alpha=1}^{m} c_p^{(\alpha)}\nabla T v_j^{(\alpha)}\right) + \sum P_{\mu k}\nabla c_k v_j^{(lw)} \quad \text{(A-57)}$$

Eq. (A-58) for enthalpy can be obtained by substituting Eq. (A-37) into above Eq. (A-57) and set the velocity of soil solids $\boldsymbol{v}^{(solid)}$ as reference term.

$$\frac{dH}{Vdt} = -\frac{(1-T\alpha_V)d\sigma_{ij}}{dt} + \frac{TdS^E}{Vdt} + \frac{\sum \mu_k dN_k}{Vdt} = \rho\frac{(1-T\alpha_V)dv_j}{dt}\left(v_j - v_j^{(solid)}\right) + \sum_{\alpha=1}^{m} c_p^{(\alpha)}\nabla T\left(v_j^{(\alpha)} - v_j^{(solid)}\right) + \sum P_{\mu k}\nabla c_k\left(v_j^{(lw)} - v_j^{(solid)}\right) = -(1-T\alpha_V)\sum_{\alpha=1}^{m}\left[\left(\sigma_{ij,i}^{(\alpha)} - \rho_\alpha g_i\right)\left(v_j^{(\alpha)} - v_j^{(solid)}\right)\right] + \sum_{\alpha=1}^{m} c_p^{(\alpha)}\nabla T\left(v_j^{(\alpha)} - v_j^{(solid)}\right) + \sum P_{\mu k}\nabla c_k\left(v_j^{(lw)} - v_j^{(solid)}\right) \quad \text{(A-58)}$$

4.8.5.3 Final expression for the Helmholtz free energy

The Helmholtz free energy relationship (i.e., Eq. (A-59)) can be obtained by substituting Eqs. (A-10), and (A-48) into Eq. (A-3).

$$\frac{dF(V,T,N_k)}{Vdt} = \frac{-PdV}{Vdt} - \frac{S^E dT}{Vdt} + \frac{\sum \mu_k dN_k}{Vdt} = \frac{\sigma_{ij} dV}{Vdt} - \frac{S^E dT}{Vdt} + P_\mu \frac{dV_{lw}}{Vdt} \quad \text{(A-59)}$$

The stress tensor for liquid water and total stress tensor in energy concept (i.e., Eq. (A-60a) and (A-60b)) can be defined similar to Eq. (A-52b).

$$\sigma_{ij}^{E(lw)} = \sigma_{ij}^{(lw)} + P_\mu \delta_{ij} \quad \text{(A-60a)}$$

$$\sigma_{ij}^{E} = (1-n)s_{ij} + nS_\alpha \sigma_{ij}^{(\alpha)} + nS_{lw}\sigma_{ij}^{E(lw)} \quad \text{(A-60b)}$$

It should be noted that only stress tensor for liquid water is expressed in the energy concept in Eq. (A-60b) in comparison with Eq. (A-13). In other words, except for the term liquid water, other terms (e.g., solid skeleton stress and other components in soil pores are consistent with the conventional definition in Eq. (A-13)). Extending the above philosophy, Eq. (A-61) is obtained that is consistent with Eq. (A-30).

$$\frac{dF}{Vdt} = \left(\sigma_{ij}^{E} - \sum_{\alpha=1}^{m} S_\alpha \sigma_{ij}^{E(\alpha)}\right)\dot{\varepsilon}_{ij}^{(solid)} - \sum_{\alpha=1}^{m}\left[\sigma_{ij}^{E(\alpha)}\left(n\frac{dS_\alpha}{dt} + \theta_\alpha \frac{d\rho_\alpha}{\rho_\alpha dt} - \frac{\zeta_\alpha}{\rho_\alpha}\right)\right] - \frac{S^E dT}{Vdt} \quad \text{(A-61)}$$

4.8.5.4 Final expression for the Gibbs free energy

The Gibbs free energy with respect to time can be obtained as Eq. (A-62) by setting velocity of soil solids as reference by substituting Eqs. (A-37), (A-47), and (A-49b) into Eq. (A-4). It should be noted that volume is considered as constant in the Gibbs free energy.

$$\frac{dG(P,T,N_k)}{Vdt} = \frac{VdP}{Vdt} - \frac{S^E dT}{Vdt} + \frac{\sum \mu_k dN_k}{Vdt} = -\frac{d\sigma_{ij}}{dt} - \frac{S^E dT}{Vdt} + \sum P_{\mu k}\nabla c_k v_j^{(lw)} = -\sum_{\alpha=1}^{m}\left[\left(\sigma_{ij,i}^{(\alpha)} - \rho_\alpha g_i + S^{E(\alpha)}\nabla T\right)\left(v_j^{(\alpha)} - v_j^{(solid)}\right)\right] + \sum P_{\mu k}\nabla c_k\left(v_j^{(lw)} - v_j^{(solid)}\right) \quad \text{(A-62)}$$

4.8.5.5 Some simplified expressions

Eq. (A-63) can be obtained for internal energy at a constant temperature, based on Eq. (A-56).

$$\frac{dU}{Vdt} = \sigma_{ij}^{E}\frac{dV}{Vdt} + C_V\frac{dT}{Vdt} = \left(\sigma_{ij}^{E} - \sum_{\alpha=1}^{m} S_\alpha \sigma_{ij}^{E(\alpha)}\right)\dot{\varepsilon}_{ij}^{(solid)} - \sum_{\alpha=1}^{m}\left[\sigma_{ij}^{E(\alpha)}\left(n\frac{dS_\alpha}{dt} + \theta_\alpha\frac{d\rho_\alpha}{\rho_\alpha dt} - \frac{\zeta_\alpha}{\rho_\alpha}\right)\right] \quad \text{(A-63)}$$

Similarly, for Helmholtz free energy, a relationship can be obtained as Eq. (A-64) by setting temperature as constant.

$$\frac{dF}{Vdt} = \left(\sigma_{ij}^{E} - \sum_{\alpha=1}^{m} S_\alpha \sigma_{ij}^{E(\alpha)}\right)\dot{\varepsilon}_{ij}^{(solid)} - \sum_{\alpha=1}^{m}\left[\sigma_{ij}^{E(\alpha)}\left(n\frac{dS_\alpha}{dt} + \theta_\alpha \frac{d\rho_\alpha}{\rho_\alpha dt} - \frac{\zeta_\alpha}{\rho_\alpha}\right)\right] \quad \text{(A-64)}$$

In summary, Eq. (A-64) is a simplified form for the final expression for the Helmholtz free energy. The four fundamental thermodynamic potentials (i.e., Eqs. (A-58), (A-62), (A-63) and (A-64)) are summarized in Table A.1.

4.8.6 Verification

This section consists of three main parts; the first part highlights the relationships with available frameworks in the literature; the second part provides validations with the traditional models for both saturated and unsaturated soils; while the third part presents a rational explanation related to dissipative function based on the proposed framework.

Based on Eqs. (A-41), (A-42), (A-48), (A-51), (A-52), and (A-63), the internal energy at constant (high) temperature and salt concentration is summarized as Eqs. (A-65) for unsaturated soils.

$$\frac{dU}{Vdt} = \left(\sigma_{ij}^{E} - S_{\alpha ir}\sigma_{ij}^{E(\alpha ir)} - S_{lw}\sigma_{ij}^{E(lw)}\right)\dot{\varepsilon}_{ij}^{(solid)} - \left[\sigma_{ij}^{E(\alpha ir)}\left(n\frac{dS_{\alpha ir}}{dt} + \theta_{air}\frac{d\rho_{\alpha ir}}{\rho_{\alpha ir}dt} - \frac{\zeta_{\alpha ir}}{\rho_{\alpha ir}}\right) + \sigma_{ij}^{E(lw)}\left(n\frac{dS_{lw}}{dt} + \theta_{lw}\frac{d\rho_{lw}}{\rho_{lw}dt} - \frac{\zeta_{lw}}{\rho_{lw}}\right)\right] \quad \text{(A-65a)}$$

$$\sigma_{ij}^{E} = (1-n)s_{ij}^{E} + nS_{\alpha ir}\sigma_{ij}^{E(\alpha ir)} + nS_{lw}\sigma_{ij}^{E(lw)} + nS_{lw}P_\mu\delta_{ij} \quad \text{(A-65b)}$$

$$s_{ij}^{E} = s_{ij} + P^{T,(solid)}\delta_{ij} \quad \text{(A-65c)}$$

$$\sigma_{ij}^{E(\alpha ir)} = \sigma_{ij}^{(\alpha ir)} + P^{T,(air)}\delta_{ij} \quad \text{(A-65d)}$$

$$\sigma_{ij}^{E(lw)} = \sigma_{ij}^{(lw)} + P^{T,(lw)}\delta_{ij} + P_\mu\delta_{ij} \quad \text{(A-65e)}$$

$$P_T = T\frac{\alpha_V}{K_V} = T\frac{(\partial V/\partial T)_P}{(\partial V/\partial\sigma_{ij})_T} = T\left(\frac{\partial\sigma_{ij}}{\partial V/V}\right)_T\left(\frac{\partial V/V}{\partial T}\right)_\sigma \quad \text{(A-65f)}$$

$$P_\mu = \frac{\left(\mu_{lw}^{*} - RT\frac{\sum c_k V_{lw}}{\rho_{lw}V_{lw}/M_{lw}}\right)\rho_{lw}}{M_{lw}} \quad \text{(A-65g)}$$

Eqs. (A-65) are further simplified into conventional work input form *PdV* (i.e., Eq. (A-25)) when temperature and saline effects are not of concern.

Table A.1 The summary of the generalized THMC expressions based on thermodynamics principles and related definitions.

Thermodynamic potentials and term definitions	The generalized THMC expressions in thermodynamics	Note
Internal energy (*dU*)	$\frac{dU}{Vdt} = \left(\sigma_{ij}^{E} - \sum_{\alpha=1}^{m} S_\alpha \sigma_{ij}^{E(\alpha)}\right)\dot{\varepsilon}_{ij}^{(solid)} - \sum_{\alpha=1}^{m}\left[\sigma_{ij}^{E(\alpha)}\left(n\frac{dS_\alpha}{dt} + \theta_\alpha \frac{d\rho_\alpha}{\rho_\alpha dt} - \frac{\zeta_\alpha}{\rho_\alpha}\right)\right]$	The definition of $\boldsymbol{\sigma^E}$ is listed below.
Enthalpy (*dH*)	$\frac{dH}{Vdt} = -(1 - T\alpha_V)\sum_{\alpha=1}^{m}\left[\left(\sigma_{ij,i}^{(\alpha)} - \rho_\alpha g_i\right)\left(v_j^{(\alpha)} - v_j^{(solid)}\right)\right] + \sum_{\alpha=1}^{m} c_p^{(\alpha)}\nabla T\left(v_j^{(\alpha)} - v_j^{(solid)}\right) + \sum P_{\mu k}\nabla c_k\left(v_j^{(lw)} - v_j^{(solid)}\right)$	c_p is specific heat capacity and the definition of α_V is listed below.
The Helmholtz free energy (*dF*)	$\frac{dF}{Vdt} = \left(\sigma_{ij}^{E} - \sum_{\alpha=1}^{m} S_\alpha \sigma_{ij}^{E(\alpha)}\right)\dot{\varepsilon}_{ij}^{(solid)} - \sum_{\alpha=1}^{m}\left[\sigma_{ij}^{E(\alpha)}\left(n\frac{dS_\alpha}{dt} + \theta_\alpha \frac{d\rho_\alpha}{\rho_\alpha dt} - \frac{\zeta_\alpha}{\rho_\alpha}\right)\right]$	The definition of σ^E is different from that in internal energy.
The Gibbs free energy (*dG*)	$\frac{dG}{Vdt} = -\sum_{\alpha=1}^{m}\left[\left(\sigma_{ij,i}^{(\alpha)} - \rho_\alpha g_i + S^{E(\alpha)}\nabla T\right)\left(v_j^{(\alpha)} - v_j^{(solid)}\right)\right] + \sum P_{\mu k}\nabla c_k\left(v_j^{(lw)} - v_j^{(solid)}\right)$	S^E is specific entropy.

σ^E in internal energy

$$\begin{cases} \sigma_{ij}^{E} = (1-n)\left(s_{ij} + P_T^{solid}\delta_{ij}\right) + n\sum_{\alpha=1}^{m} S_\alpha\left(\sigma_{ij}^{(\alpha)} + P_T^{(\alpha)}\delta_{ij}\right) + nS_{lw}P_\mu\delta_{ij} \\ s_{ij}^{E} = s_{ij} + P_{ij}^{T,solid} \\ \sigma_{ij}^{E(lw)} = \sigma_{ij}^{(lw)} + P^{T,(lw)}\delta_{ij} + P_\mu\delta_{ij} \\ \sigma_{ij}^{E(\alpha)} = \sigma_{ij}^{(\alpha)} + P^{T,(\alpha)}\delta_{ij} \\ P_T = T\dfrac{\alpha_V}{K_V} = T\left(\dfrac{\partial\sigma_{ij}}{\partial V/V}\right)_T\left(\dfrac{\partial V/V}{\partial T}\right)_\sigma \\ \alpha_V = \dfrac{1}{V}\left(\dfrac{\partial V}{\partial T}\right)_P \\ K_V = \dfrac{1}{V}\left(\dfrac{\partial V}{\partial \sigma_{ij}}\right)_T \\ P_\mu = \dfrac{\left(\mu_{lw}^* - RT\dfrac{\sum c_k V_{lw}}{\rho_{lw}V_{lw}/M_{lw}}\right)\rho_{lw}}{M_{lw}} \\ \rho_{lw} = \dfrac{m_{lw} + \sum M_k N_k}{V_{lw}} \end{cases}$$

$P_{\mu k}$ in enthalpy and the Gibbs free energy

$$P_{\mu k} = \mu_k^* + RT\ln\left(\frac{c_k M_{lw}}{\rho_{lw}}\right)$$

σ^E in the Helmholtz free energy

$$\begin{cases} \sigma_{ij}^{E} = (1-n)s_{ij} + nS_\alpha\sigma_{ij}^{(\alpha)} + nS_{lw}\sigma_{ij}^{E(lw)} \\ \sigma_{ij}^{E(lw)} = \sigma_{ij}^{(lw)} + P_\mu\delta_{ij} \end{cases}$$

4.8.6.1 Comparisons with other frameworks in the literature

The key conclusions based on the proposed generalized framework (i.e., the Gibbs and the Helmholtz free energy) in Eqs. (A-62) and (A-64) without considering temperature and saline effects in the study are summarized in the following Eqs. (A-66a) and (A-66b), respectively.

$$\frac{dG}{Vdt} = \rho \frac{dv_j}{dt}\left(v_j - v_j^{(solid)}\right) = -\sum_{\alpha=1}^{m}\left[\left(\sigma_{ij,i}^{(\alpha)} - \rho_\alpha g_i\right)\left(v_j^{(\alpha)} - v_j^{(solid)}\right)\right] \quad \text{(A-66a)}$$

$$\frac{dF}{Vdt} = \sigma_{ij}\dot{\varepsilon}_{ij} = \left(\sigma_{ij} - \sum_{\alpha=1}^{m} S_\alpha \sigma_{ij}^{(\alpha)}\right)\dot{\varepsilon}_{ij}^{(solid)} - \sum_{\alpha=1}^{m}\left[\sigma_{ij}^{(\alpha)}\left(n\frac{dS_\alpha}{dt} + \theta_\alpha \frac{d\rho_\alpha}{\rho_\alpha dt} - \frac{\zeta_\alpha}{\rho_\alpha}\right)\right] \quad \text{(A-66b)}$$

The current study highlights two processes (i.e., Eqs. (A-66)) in thermodynamics by comparing with the work input method in the literature (Houlsby, 1997). Detailed comparison reveals that these two processes are $\partial(PV) / \partial t$ relationships. A negative sign notation is extended based on the Legendre transformation (Houlsby and Puzrin, 2000) for these relationships.

Close examination of Eq. (A-66b) with the succinctly summarized method proposed by Borja (2006) suggest they are the same except for the difference in linear elastic assumption in treating variation of densities.

However, Eq. (A-66a) proposed in the present study is based on thermodynamics and conservation laws. It is of interest to highlight that Eq. (A-66a) is strongly related to the flow behavior of soils. For this reason, this process is valuable in understanding the hydro-mechanical behaviors of soils (e.g., Garcia et al. 2010; Fredlund et al. 2012; Pouya et al. 2013; Li and Vanapalli, 2022b; Qian et al. 2022).

In summary, the generalized framework proposed in the present study highlights two distinct processes in geotechnical engineering within thermodynamics framework as summarized in Eqs. (A-58), (A-62), (A-63) and (A-64) (see Table A.1): one is related to the extended hydro-mechanical behavior of soils (the variation of degree of saturation and density and mass exchange are also included), while the other highlights the flow behaviors (including heat and mass transports).

4.8.6.2 Comparisons with the classical models for saturated and unsaturated soils

The generality of the proposed framework is also validated by drawing theoretical deductions

of several classical forms from the literature for both saturated and unsaturated soils. In addition, extensions to explain unsaturated frozen soils are succinctly discussed based on the independent stress state variables, which is consistent with explaining unsaturated unfrozen soils behaviors proposed by Fredlund and Morgenstern (1977). Finally, the similarities and differences between the analytical relationships proposed in this study with other models from the literature are also discussed and summarized.

Most verifications are provided using Eqs. (A-66), or more specifically, the various forms of equations summarized in Eqs. (A-67) and (A-68) that facilities in providing clear explanation without considering temperature effects. The symbols $\boldsymbol{\sigma}^{(\alpha)}$ in expressing pore pressures are replaced by $\boldsymbol{P}^{(\alpha)}$ to follow the conventions in the literature. In other words, Eqs. (A-67) can be regarded as a general equation that considers pore- air and water pressures and osmotic suction induced by salts solution.

$$\boldsymbol{\sigma}' = \boldsymbol{\sigma} - S_{lw}\boldsymbol{\sigma}^{E(lw)} - S_{air}\boldsymbol{P}^{air} \tag{A-67a}$$

$$S_{lw} + S_{air} = 1 \tag{A-67b}$$

$$\boldsymbol{\sigma}^{E(lw)} = \boldsymbol{P}^{lw} + \boldsymbol{P}_{\mu} \tag{A-67c}$$

Eq. (A-68) summarized below is one set of frequently used independent stress state variables based on Eqs. (A-67).

$$\left(\boldsymbol{\sigma} - \boldsymbol{P}^{air}\right), \left(\boldsymbol{P}^{air} - \boldsymbol{\sigma}^{E(lw)}\right) \tag{A-68}$$

The choice of stress state variables in Eq. (A-68) are flexible and dependent on the scenarios that arise in engineering practice (Fredlund and Morgenstern, 1977).

4.8.6.2.1 Discussions on salt solution effects

One of the equations that considers osmotic suction into account is proposed by Rao and Thyagaraj (2007) as shown in Eq. (A-69).

$$\boldsymbol{\sigma}' = \boldsymbol{\sigma} - \boldsymbol{P}^{lw} + \alpha_R\left(\boldsymbol{P}_{\mu f} - \boldsymbol{P}_{\mu 0}\right) = \sigma_{ij} - P^{lw}\delta_{ij} + \alpha_R(i_{vh}c_k RT)\delta_{ij} \tag{A-69}$$

where $\boldsymbol{P}_{\mu f}$ and $\boldsymbol{P}_{\mu 0}$ are final and initial osmotic suctions, respectively, α_R is a model parameter,

and i_{vh} is Van't Hoff factor. In Eq. (A-69), concentration c_k specifies the concentration of salts (e.g., Rao and Shivananda, 2005). Eq. (A-69) can be derived from Eqs. (A-67) as shown below.

$$\boldsymbol{\sigma}' = \boldsymbol{\sigma} - \boldsymbol{P}^{lw} - \boldsymbol{P}_{\mu} = \boldsymbol{\sigma} - \boldsymbol{P}^{lw} - \left(\boldsymbol{P}_{\mu f} - \boldsymbol{P}_{\mu 0}\right) = \sigma_{ij} - P^{lw}\delta_{ij} - \left[\frac{\left(\mu_{lw}^{*} - RT\frac{\sum c_k V_{lw}}{\rho_{lw} V_{lw}/M_{lw}}\right)\rho_{lw}}{M_{lw}} - \frac{\mu_{lw}^{*}\rho_{lw}}{M_{lw}}\right]\delta_{ij} = \sigma_{ij} - P^{lw}\delta_{ij} + (RT\sum c_k)\delta_{ij} \quad \text{(A-70)}$$

In Eq. (A-69), model parameter α_R is unity and Van't Hoff factor equals to two for ideal dilute sodium chloride (*NaCl*) solution (i.e., one molar sodium chloride salts are ideally dissolved into two molar ions) based on the assumption (iv) used in this study. Eq. (A-69) is the same as Eq. (A-70) while Eq. (A-70) is expressed as the sum of dissolved substances (ions) in the last term.

4.8.6.3 Discussion on dissipation function

Eq. (A-71), which is a dissipation function D can be written based on research studies summarized in the literature (e.g., Collins and Houlsby, 1997; Houlsby and Puzrin, 2000).

$$D \equiv T\frac{dS^{E,ir}}{dt} = \chi_{ij}^{D}\frac{d\alpha_{ij}^{D}}{dt} \quad \text{(A-71)}$$

where $\boldsymbol{\chi}^{\boldsymbol{D}}$ is a stress-like variable and $\boldsymbol{\alpha}^{\boldsymbol{D}}$ is a strain-like variable (e.g., Collins and Houlsby, 1997; Houlsby and Puzrin, 2000).

Based on Eqs. (A-11), (A-39), (A-42), and (A-50), without considering chemical solution, the following Eqs. (A-72) can be obtained.

$$\frac{dU}{Vdt} = \frac{\sigma_{ij}dV}{Vdt} + \frac{TdS^{E}}{Vdt} = \frac{\sigma_{ij}dV}{Vdt} + \left[T\left(\frac{\partial S^{E}}{\partial V}\right)_{T}\frac{dV}{Vdt} + T\left(\frac{\partial S^{E}}{\partial T}\right)_{V}\frac{dT}{Vdt}\right] = \frac{\sigma_{ij}dV}{Vdt} + \left[T\frac{\alpha_V}{K_V}\frac{dV}{Vdt} + C_V\frac{dT}{Vdt}\right] = \frac{\sigma_{ij}dV}{Vdt} + \left[P_{ij}^{T}\frac{dV}{Vdt} + C_V\frac{dT}{Vdt}\right] = \left(\sigma_{ij} + P_{ij}^{T}\right)\frac{d\varepsilon_{ij}}{dt} + C_V\frac{dT}{Vdt} \quad \text{(A-72a)}$$

$$P_{ij}^{T} = T\frac{\alpha_V}{K_V} = T\frac{(\partial V/\partial T)_P}{-(\partial V/\partial P)_T} = T\left(\frac{\partial \sigma_{ij}}{\partial V/V}\right)_{T}\left(\frac{\partial V/V}{\partial T}\right)_{\sigma} \quad \text{(A-72b)}$$

Note $\boldsymbol{P}^{\boldsymbol{T}}$ in Eq. (A-72b) is derived from the second term of internal energy (i.e., TdS^{E}) based on the Maxwell relationships (see Appendix B). By analogy the derivation process in Eq. (A-72a)

that is based on the entropy S^E definition (i.e., reversible and irreversible parts in Eq. (A-38)), the second term (i.e., TdS^E) in Eq. (A-72a) can be expressed as Eq. (A-73a).

$$\frac{TdS^E}{Vdt} = \frac{TdS^{E,ir}}{Vdt} + \frac{TdS^{E,re}}{Vdt} = \left[T\left(\frac{\partial S^{E,ir}}{\partial V}\right)_T \frac{dV}{Vdt} + T\left(\frac{\partial S^{E,ir}}{\partial T}\right)_V \frac{dT}{Vdt}\right] + \left[T\left(\frac{\partial S^{E,re}}{\partial V}\right)_T \frac{dV}{Vdt} + T\left(\frac{\partial S^{E,re}}{\partial T}\right)_V \frac{dT}{Vdt}\right] = \left[P_{ij}^{T,ir}\frac{dV}{Vdt} + C_V^{ir}\frac{dT}{Vdt}\right] + \left[P_{ij}^{T,re}\frac{dV}{Vdt} + C_V^{re}\frac{dT}{Vdt}\right] \quad \text{(A-73a)}$$

Extending Eq. (A-72b), Eq. (A-73a) can be expressed as Eq. (A-73b).

$$P_{ij}^T = P_{ij}^{T,ir} + P_{ij}^{T,re} = T\left(\frac{\partial \sigma_{ij}^{ir}}{\partial V/V}\right)_T \left(\frac{\partial V/V}{\partial T}\right)_\sigma + T\left(\frac{\partial \sigma_{ij}^{re}}{\partial V/V}\right)_T \left(\frac{\partial V/V}{\partial T}\right)_\sigma \quad \text{(A-73b)}$$

where superscript *-ir* and *-re* denote irreversible and reversible parts, respectively. Based on the energy conservation (i.e., the total work input equals to the sum of work input into each subsystem) in Eq. (A-19), Eq. (A-73a) for irreversible and reversible parts should be further written as following Eq. (A-74).

$$\frac{dW}{Vdt} = \sum_{\alpha=1}^{m} \frac{dW_\alpha}{Vdt} = P_{ij}^{T,ir}\frac{dV^{ir}}{Vdt} + P_{ij}^{T,re}\frac{dV^{re}}{Vdt} = P_{ij}^{T,ir}\frac{d\varepsilon_{ij}^{ir}}{Vdt} + P_{ij}^{T,re}\frac{d\varepsilon_{ij}^{re}}{Vdt} \quad \text{(A-74)}$$

The dissipation function in Eq. (A-71) can be expressed as Eq. (A-75) based on Eqs. (A-73) and (A-74).

$$D \equiv T\frac{dS^{E,ir}}{dt} = \chi_{ij}^D \frac{d\alpha_{ij}^D}{dt} = T\left(\frac{\partial S^{E,ir}}{\partial V}\right)_T \frac{dV^{ir}}{Vdt} = \left[T\left(\frac{\partial \sigma_{ij}^{ir}}{\partial V/V}\right)_T \left(\frac{\partial V/V}{\partial T}\right)_\sigma\right]\frac{dV^{ir}}{Vdt} = P_{ij}^{T,ir}\frac{d\varepsilon_{ij}^{ir}}{dt} \quad \text{(A-75)}$$

In the last term of Eq. (A-75), the irreversible strain $\boldsymbol{\varepsilon}^{ir}$ induced by irreversible stress shall be highlighted to follow the energy conservation in Eq. (A-19). Based on Eq. (A-75), the stress-like term $\boldsymbol{\chi D}$ in dissipation function can be explained based on the framework proposed in this study. In addition, friction in geomaterials has a strong contribution towards irreversible stress during isothermal process.

4.8.7 Applications for unsaturated soils

4.8.7.1 Isotropic compression under constant soil suction

The hydro-mechanical behaviors of unsaturated soils are of significant interest in the field of geotechnical engineering. Various experimental studies were undertaken in the literature for better understanding the coupled deformation and flow behaviors of unsaturated soils. For example, Sun et al. 2007b and 2007c have performed classical experimental tests with different initial void ratios under isotropic compression.

In the experimental procedures while performing tests on unsaturated soil specimens, soil suction ($\psi = P_{air} - P_{lw}$) is typically kept constant, while gradually increasing net mean loadings. Experimental results and model simulations (e.g., Sun et al. 2007b and 2007c; Sheng and Zhou, 2011) suggest that the increment of water content is not in accordance with volume change of unsaturated soils. The developed framework in the present study is extended for better understanding the mechanisms of isotropic compression tests with various void ratios in unsaturated soils.

The internal energy relationship without considering temperature and salt solution can be reduced into Eq. (A-76) based on Eq. (A-65) for unsaturated soils that are subjected to isotropic loadings (i.e., without shearing stress).

$$\frac{dU}{Vdt} = \left(p - u^{(air)}\right)\dot{\varepsilon}_V^{(solid)} + \left(u^{(air)} - u^{(lw)}\right)\left(S_{lw}\dot{\varepsilon}_V^{(solid)} + n\frac{dS_{lw}}{dt}\right) \quad \text{(A-76)}$$

where σ_v and ε_v mean stress and volumetric strain, respectively extending scalar form for isotropic compression loading condition. In addition, in the above equation, both density and mass changes are not considered.

Eq. (A-76) suggests that the soil suction ($\psi = P_{air} - P_{lw}$) is related to both volume and water content changes of unsaturated soils. However, under isotropic compression tests, the change of soil suction is always zero (i.e., $d\psi \equiv 0$). The second part on the right side of Eq. (A-76), suggests the internal energy is dependent on the variation of water content. From the above analyses and discussions, Eq. (A-77) is valid for isotropic compression tests with constant soil suction.

$$d\psi = d\psi(\text{soil volume reduce}) + d\psi(\text{water content rise}) \equiv 0 \quad \text{(A-77)}$$

Eq. (A-77) provides a fundamental explanation of the water content changes associated with soil suction or water content dependent hydro-mechanical behaviors of soil subjected to isotropic loadings from experimental studies under constant soil suction conditions.

The soil suction increment caused by the volume contraction of soils can be evaluated using Eq. (A-79) based on the classical definition from the Capillary law as shown in Eq. (A-78),

$$\psi = \frac{\gamma_{aw}}{r_d} \quad \text{(A-78)}$$

$$\frac{d\psi}{\psi} = -\frac{1}{r_d} dr_d = -\frac{1}{h(V_{pore})} dV_{pore} = -\frac{1}{h(e)} de \quad \text{(A-79)}$$

where γ_{aw} is air-water interfacial energy in unsaturated soils, r_d is the pore radius, and void ratio $e = V_{pore} / V_{solid}$.

In this relationship, the volume of soil solids is set as constant (e.g., unity). By introducing various relationships between the soil volume and pore radii, the links between the variation of soil suction that is induced from soil volume change can be found (e.g., Hu et al. 2013; Li and Vanapalli et al. 2022b).

Relationships of Eqs. (A-80) can be used extending the above philosophy.

$$\frac{d\psi}{\psi} = -\xi_s \frac{de}{e_0} \quad \text{(A-80a)}$$

$$\frac{\psi}{\psi_0} = \exp\left(-\xi_s \frac{e-e_0}{e_0}\right) \quad \text{(A-80b)}$$

where e_0 is the initial void ratio, and ξ_s is a model parameter.

The widely accepted equations in isotropic compression tests (e.g., Alonso et al. 1990; Sheng and Zhou, 2011; Lei et al. 2016; Le Pense et al. 2016) for elastic regime and elastoplastic response are listed in Eqs. (A-81a) and (A-81b), respectively.

$$d\varepsilon_v = k_p \frac{dp}{p+\psi_0} + k_s \frac{d\psi}{p_0+\psi} \quad \text{(A-81a)}$$

$$d\varepsilon_v = \lambda_p \frac{dp}{p+\psi_0} + \lambda_s \frac{d\psi}{p_0+\psi} \quad \text{(A-81b)}$$

where k_p, k_s, λ_p and λ_s are model parameters, ψ_0 is the initial soil suction, and p_0 is the mean pressure at reference state. Based on Eqs. (A-80a) and (A-81), the Eq. (A-82) is suggested that can be used to calculate the volumetric deformation for unsaturated soils with distinct initial void ratio.

$$d\varepsilon_v = \lambda_p \frac{dp}{p+\psi_0} + \lambda_s \frac{d\psi}{p_0+\psi} \cong \lambda_p \frac{dp}{p+\psi_0} - \xi_s \lambda_s \frac{de}{e_0} = \lambda_p (1+\xi_s \lambda_s) \frac{dp}{p+\psi_0} = \lambda_p (1+\xi_{s0}) \frac{dp}{p+\psi_0} \quad \text{(A-82)}$$

where ξ_{s0} is a model parameter.

As shown in Eq. (A-82), the parameter ξ_{s0} is dependent with compression behaviors of unsaturated soils under soil (matric) suction. This relationship also suggests that for different initial void ratios, the compression behaviors under mechanical loadings are distinct even at constant soil suction (e.g., Alonso et al. 1990; Lei et al. 2016; Le Pense et al. 2016).
Eq. (A-83) is suggested to compute volumetric strain under isotropic mechanical loadings at constant soil suction assuming elastoplastic response for various initial states (e.g., distinct initial void ratios).

$$d\varepsilon_v = \begin{cases} k_p \frac{dp}{p+\psi_0}, p \le p_{y0} \\ \left[\lambda_p \exp\left(-\xi_{s1} \frac{e_{ref}-e_0}{e_{ref}}\right)\right] \frac{dp}{p+\psi_0}, p > p_{y0} \end{cases} \quad \text{(A-83)}$$

where p_{y0} is the preconsolidation pressure, ξ_{s1} is a model parameter and e_{ref} is the initial void ratio at reference state. As can be seen in Eq. (A-83), prior to preconsolidation pressure p_{y0}, only elastic response is observed, while after preconsolidation pressure p_{y0}, elastoplastic response is highlighted. The parameter λ_p is strongly related to the variation of soil suction (e.g., Alonso et al., 1990; Sheng and Zhou, 2011), as soil suction is kept as constant in the test, the parameter is set as a constant value.

Eq. (A-84) is the BC model (Brooks and Corey, 1964) that can be extended for the soil suction reduction caused by the water content rise.

$$\frac{S_{lw}}{S_{lw,0}} = \left(\frac{\psi}{\psi_0}\right)^{-\lambda_{bc}} \quad \text{(A-84)}$$

where λ_{bc} is a model parameter in BC model, and $S_{lw,0}$ is the degree of saturation at initial state. Eq. (A-85a) can be obtained by substituting Eq. (A-80b) into Eq. (A-84).

As shown in Eqs. (A-80), soil volume contraction will result in soil suction increase. Based on Eq. (A-77), the water content rise process is possible to compensate for the soil suction rise induced from mechanical compression.

$$\frac{S_{lw}}{S_{lw,0}} = \exp\left(\xi_s \lambda_{bc} \frac{e-e_0}{e_0}\right) \quad \text{(A-85a)}$$

A negative sign on the right side of Eq. (A-85b) is introduced in comparison with Eq. (A-85a) to describe the water content rise process.

$$\frac{S_{lw}}{S_{lw,0}} = \exp\left(-\xi_s \lambda_{bc} \frac{e-e_0}{e_0}\right) = \exp\left(\frac{1+e_0}{e_0} \xi_s \lambda_{bc} \frac{e_0-e}{1+e_0}\right) = \exp\left(\frac{1+e_0}{e_0} \xi_s \lambda_{bc} \varepsilon_v\right) = \exp\left(\frac{1+e_0}{e_0} \xi_{s2} \varepsilon_v\right)$$
(A-85b)

where ξ_{s2} is a model parameter.

It should be noted that this is the water rise process that contributes to a decrease in soil suction as revealed by Eq. (A-77). Based on Eqs. (A-82) and (A-85b), the overall increase of degree of saturation of water (i.e., the sum of soil volume contraction and water content rise) can be written as Eq. (A-86).

$$S_{lw} = S_{lw,o} \frac{S_{lw}/V}{S_{lw,o}/V_0} = S_{lw,o} \frac{S_{lw}}{S_{lw,0}} \frac{V_0}{V} = S_{lw,o} \exp\left(\frac{1+e_0}{e_0} \xi_{s2} \varepsilon_v\right) / (1 - \varepsilon_v) \quad \text{(A-86)}$$

Based on Eqs. (A-83) and (A-86), the volumetric deformation and water content rise under isotropic loadings can be predicted. The elastoplastic response of degree of saturation corresponding to soil suction is not considered as soil suction is kept as constant in the test. The model performance using the experimental results (ψ_0 =147 kPa) in the literature (e.g., Sun et al. 2007b and 2007c) are highlighted in Figure A-1. The preconsolidation pressure p_{y0} is set

as 50 kPa for all cases. And the model values for parameters k_p, λ_p, ξ_{s1}, and ξ_{s2} are 0.06, 0.20, 3.92, and 0.22, respectively.

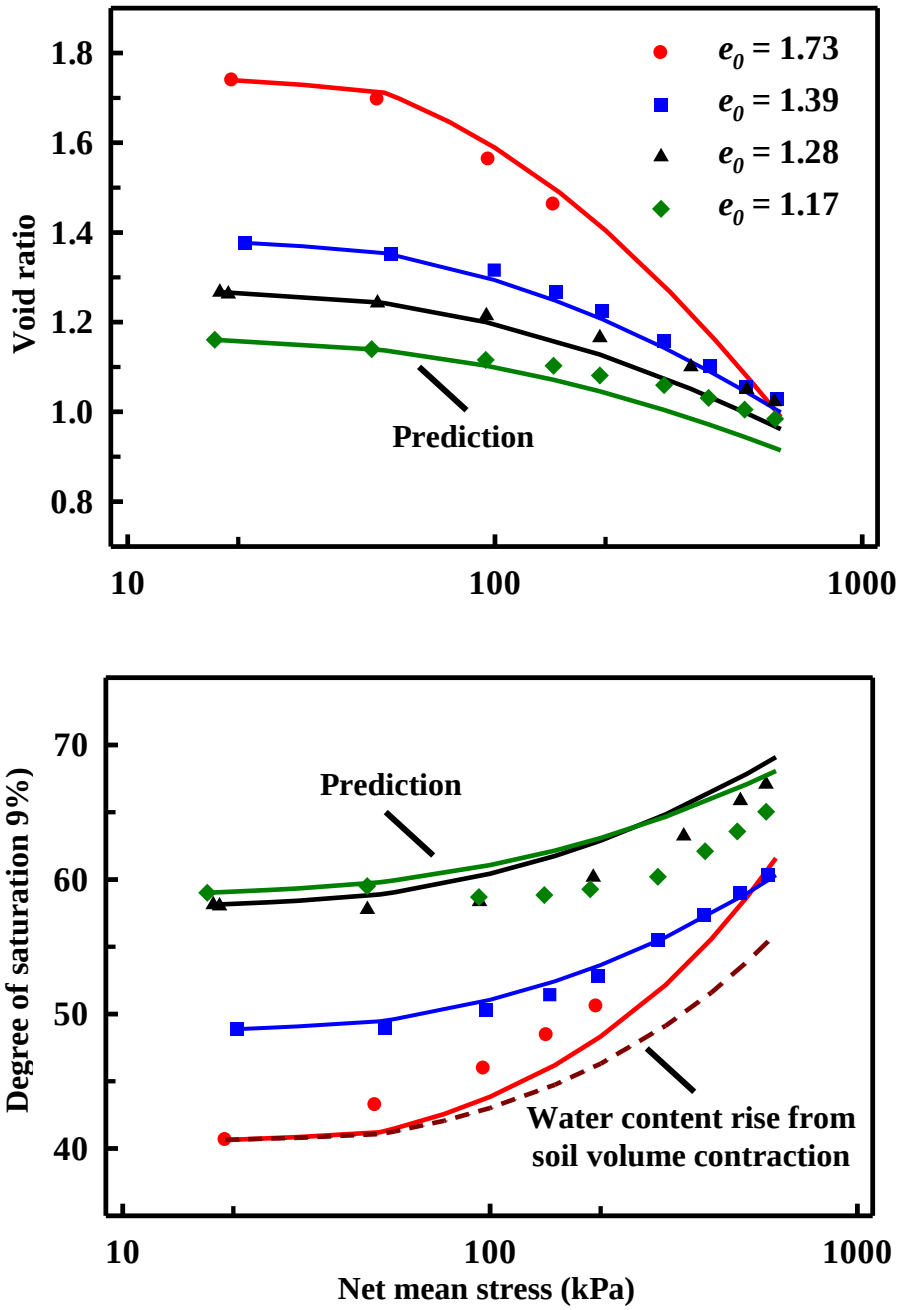

(a) Water content variation

Note: Experimental dots are gathered from Sun et al. 2007b and 2007c. Solid lines are prediction results.

Figure A-1 Prediction on isotropic compression tests at constant soil suction.

4.8.8 Discussion

Eqs. (A-67) are a set of generalized equations for solid skeleton stress loading on soil solids expressed in a continuum form. However, continuum form equation is not suitable to model complex hydro-mechanical behaviors of unsaturated soils as revealed by experimental results evidence in the literature (e.g., Wheeler & Sivakumar, 1995; Cunningham et al., 2003). In this study, the flexibility and generality of Eq. (A-68) is highlighted.

Eq. (A-68) is expressed in terms of independent stress state variables (e.g., Fredlund et al. 2012; Yang and Vanapalli, 2023) that can be used for reasonable interpretation of the complex hydro-mechanical behaviors of unsaturated soils. Different combinations of three independent stress state variables can be used for quantitative evaluation (Fredlund and Morgenstern, 1977).

4.9 Appendix B

Based on the symmetry of second derivatives and thermodynamic potentials, the following commonly used Maxwell relations are highlighted.

$$\left(\frac{\partial y}{\partial x}\right)_z = 1/\left(\frac{\partial x}{\partial y}\right)_z \tag{B-1}$$

$$-\frac{\partial^2 F}{\partial V \partial T} = \left(\frac{\partial S^E}{\partial V}\right)_T = \left(\frac{\partial P}{\partial T}\right)_V = \frac{\alpha_V}{K_V} \tag{B-2}$$

$$\frac{\partial^2 G}{\partial T \partial P} = -\left(\frac{\partial S^E}{\partial P}\right)_T = \left(\frac{\partial V}{\partial T}\right)_P = \alpha_V V \tag{B-3}$$

4.10 Notation

c_k	the concentration of k-th substance (solute) in liquid water
c_p	specific heat capacity
C_V and C_P	heat capacity at constant volume and pressure, respectively
e_0	initial void ratio
e_{ij}	deviatoric strain
e_{ref}	initial void ratio at reference state
f^{lw}, f^{air}, f^{ice}	average velocities of pore-liquid-water, pore-air, and pore-ice, respectively
g_i	acceleration of gravity
i_{vh}	Van't Hoff factor
$\boldsymbol{I}$	identity tensor of second order
k_p and k_s	model parameters

K_α	bulk modulus
K_V	compressibility
L_a	latent heat of fusion of ice
M_k	molar mass of k-th substance
M_{lw}	molar mass of liquid water
n	soil porosity
p_{y0}	preconsolidation pressure
$\boldsymbol{P}^{T,solid}$, $\boldsymbol{P}^{T,(\alpha)}$	thermal stress in soil solids and α-th component in soil pores, respectively
P_μ and $P_{\mu k}$	chemical potential of water and chemical potential of k-th solute, respectively
$\boldsymbol{P}_{\mu f}$ and $\boldsymbol{P}_{\mu 0}$	final and initial osmotic suctions, respectively
R	universal gas constant
r_d	the pore radius
$\boldsymbol{s}$	soil solid skeleton stress
$\boldsymbol{s}^E$ and $\boldsymbol{\sigma}^{E(\alpha)}$	stress tensor in energy concept for soil skeletons and α-th component in soil pores, respectively
S_{lw}, S_{air}, S_{ice}	degree of saturations for pore-liquid-water, pore-air, and pore-ice, respectively
$S_{lw,0}$	degree of saturation at initial state
S_r	residual degree of saturation
S_α, V_α, θ_α	degree of saturation, volume, and volumetric content of α-th component in soil pores, respectively
S^E, T	entropy, and temperature, respectively
$S^{E,ir}$ and $S^{E,re}$	entropy in irreversible and reversible processes, respectively
$S^{E(solid)}$, $S^{E(\alpha)}$	entropy of soil solids and α-th component in soil pores, respectively
t	time
T	temperature
T_0	freezing point of free water
T_{ij}	surface tension
q_i	the heat flux
u^{lw}, u^{air}	pore-water (liquid), and pore-air pressures, respectively
V, P	volume, and pressure, respectively
V_{solids}, V_{pores}	volumes of soil solids and pores, respectively
x_k, and γ_k	mole fraction, and coefficient of activity of the k-th substance, respectively
α_k, α_1, α_2	parameters of effective stress equation
α_{12}, α_{34}	parameters of effective stress equation

$\boldsymbol{\alpha^D}$	strain-like variable in dissipation function
α_R	model parameter
α_{VT}	coefficient of thermal expansion
γ_{aw}	air-water interfacial energy in unsaturated soils
$\boldsymbol{\delta} = \delta_{ij}$	Kronecker delta
$\boldsymbol{\varepsilon}^{(\alpha)}$, $\boldsymbol{v}^{(\alpha)}$	the strain and velocity vector of α-th component, respectively
ε_v	volumetric strain
ζ_α	the mass supply to component α from other components
θ_{lw}, θ_{air}	volumetric fractions for pore-liquid-water, and pore-air, respectively
θ_{ice}	volumetric fractions for pore-ice
λ	model variable for frozen soils
λ_{bc}	model parameter in BC model (Brooks and Corey, 1964)
λ_p, λ_s, λ_{sp}	model parameters
μ_k and N_k	chemical potentials, and the number of particles of the k-th substance, respectively
ξ	model parameter for effective stress of unsaturated soils
ξ_{s0}, ξ_{s1}, ξ_{s2}	model parameters
ρ	the total density
ρ_α, m_α	the density and mass of α-th component, respectively
ρ_{solid}	the density of soil solids
$\boldsymbol{\sigma}$	total stress tensor
σ_v, ε_v	mean stress and volumetric strain in scalar, respectively
σ_{v0}	mean pressure at initial state in scalar
$\boldsymbol{\sigma'}$	effective stress tensor
$\boldsymbol{\sigma}^{(\alpha)}$	the stress tensor of α-th component
$\boldsymbol{v}$	velocity vector
χ	model parameter in Bishop expression for effective stress
χ_{12}, χ_{34}	parameters of effective stress equation
$\boldsymbol{\chi^D}$	stress-like variable in dissipation function
ψ	soil suction
ψ_0, e_0	initial soil suction and initial void ratio, respectively

CHAPTER 5

Equations for Soil Freezing Characteristics Curves Based on the Thermodynamics Principles

5.1. Introduction

The soil-water characteristics curve (SWCC) is widely used as a tool for explaining the behavior of unsaturated soils that are in a state of unfrozen condition (e.g., Parlange, 1976; Fredlund et al., 1994; Vanapalli et al., 1999; Khosravi and McCartney, 2012; Li and Vanapalli, 2021). The relationship between either volumetric or gravimetric water content or degree of saturation and soil suction is widely known as the SWCC. This relationship is also referred to as the soil-moisture curve or soil-water retention curve in the literature (e.g., Fredlund and Rahardjo, 1993). Several SWCC models have been successfully developed and used for predicting the non-linear hydro-mechanical behavior of unfrozen unsaturated soils (e.g., Mualem, 1976; Nemes et al., 2001; Chin et al., 2010; Zhai et al., 2017; Li and Vanapalli, 2022a).

The THMC behavior of soils are significantly influenced by both the freeze-thaw and wet-dry cycles (e.g., Barbour and Yang, 1993; Hansson et al., 2004; Langman et al., 2017; Zhou et al., 2019; Li and Vanapalli, 2022b). In frozen soils, the pore-water can exist in a partial or in a fully frozen state (e.g., Drotz et al., 2009; Li et al., 2012; Vugmeyster et al., 2017; Fu et al., 2018; He et al., 2021). The initial freezing point of water within the soils is lower than the fusion point of pure water due to certain factors such as the high pore pressures (Koopmans and Miller, 1966; Banin and Anderson, 1974; Black and Tice, 1989; Ren and Vanapalli, 2019). The relationship between the unfrozen water content and temperature which is referred to as the soil freezing characteristic curve (SFCC) is used for understanding, interpreting and predicting the behavior of frozen unsaturated soils with temperatures lower than 0 °C (e.g., Kurylyk and Watanabe, 2013; Hu et al., 2020; Teng et al., 2020; Xiao et al., 2022).

The contents of this chapter are published in Geoderma Journal.
Li, Y., and Vanapalli, S. K. (2023). Equations for Soil Freezing Characteristics Curves Based on the Thermodynamics Principles. Geoderma, 439: 116644. doi: 10.1016/j.geoderma.2023.116644.

In recent decades, several approaches have been used for modeling SFCC behavior in the literature (Coussy, 2005; Kurylyk and Watanabe, 2013; Zhang and Lu, 2021). One of the approaches is based on semi-empirical or empirical methods (e.g., Black and Tice, 1989; Kozlowski, 2007); the other approach is based on exploiting the SFCC similarities with the SWCC (e.g., Watanabe and Mizoguchi, 2002; Liu and Yu, 2013; Wang et al., 2017; Bai et al., 2018; Chai et al., 2018; Zhou et al., 2018; Teng et al., 2020; Wan and Yang, 2020; Jin et al., 2020; Teng et al., 2021; Kong et al., 2022). Figure 5.1 highlights the similarities between the SFCCs and SWCCs; however, the physical meanings of model parameters and the relationships between the SFCCs and SWCCs based on a consistent theoretical framework require further discussion.

In this study, rigorous SFCC models are proposed extending the principles of thermodynamics highlighting relationships between the cryogenic pressure and temperature. The proposed SFCC models were also linked to the widely used SWCC models in the literature. The complex hysteretic behaviors are also explained using the proposed SFCC models. In addition, different zones in the SFCC are clearly distinguished and the influential factors (i.e., salinity, and initial water content effects) on the SFCC behavior are quantitively analyzed and discussed. In simple terms, the proposed models in this Chapter are valuable in rigorous understanding and in the prediction of the THMC behaviors of frozen unsaturated soils.

5.2. Soil Freezing Characteristic Curve (SFCC) models

5.2.1 Background information

Of the various SWCC models available in the literature, Brooks and Corey model (BC model, Brooks and Corey, 1964), van Genuchten model (VG model, van Genuchten, 1980), and Fredlund and Xing model (FX model, Fredlund and Xing, 1994) are well-known; these equations are shown respectively as Eqs. (5.1), (5.2), and (5.3) below.

$$\frac{S_{lw}-S_{res}}{S_{sat}-S_{res}} = \frac{1}{(\psi/\psi_{AEV})^{\lambda_{bc}}} \tag{5.1}$$

$$\frac{S_{lw}-S_{res}}{S_{sat}-S_{res}} = \frac{1}{\left[1+(a_{vg}\psi)^{n_{vg}}\right]^{m_{vg}}} \tag{5.2}$$

$$\frac{S_{lw}}{S_{sat}} = \left[1-\frac{\ln[1+(\psi/\psi_{res})]}{\ln[1+(10^6/\psi_{res})]}\right]\frac{1}{\left\{\ln\left[\exp(1)+(\psi/a_{fx})^{n_{fx}}\right]\right\}^{m_{fx}}} \tag{5.3}$$

where ln () and exp () are logarithmic and exponential functions, respectively, S_{lw} is degree of saturation, S_{sat} and S_{res} are respectively saturated and residual degree of saturation, ψ is soil suction, ψ_{AEV} is air-entry value, λ_{bc} is model parameter in BC model, a_{vg}, n_{vg}, and m_{vg} are model parameters in VG model, a_{fx}, n_{fx}, and m_{fx} are model parameters in FX model, respectively.

The above SWCC models (i.e., Eqs. (5.1), (5.2), and (5.3)) are widely used in the agriculture, soil science, water resources, geotechnical and geo-environmental engineering fields for predicting various hydro-mechanical properties of unfrozen unsaturated soils (e.g., van Genuchten, 1980; Fredlund et al. 1994; Vanapalli et al., 1996; Lu et al., 2010; Vereecken et al., 2016; Yang and Vanapalli, 2020).

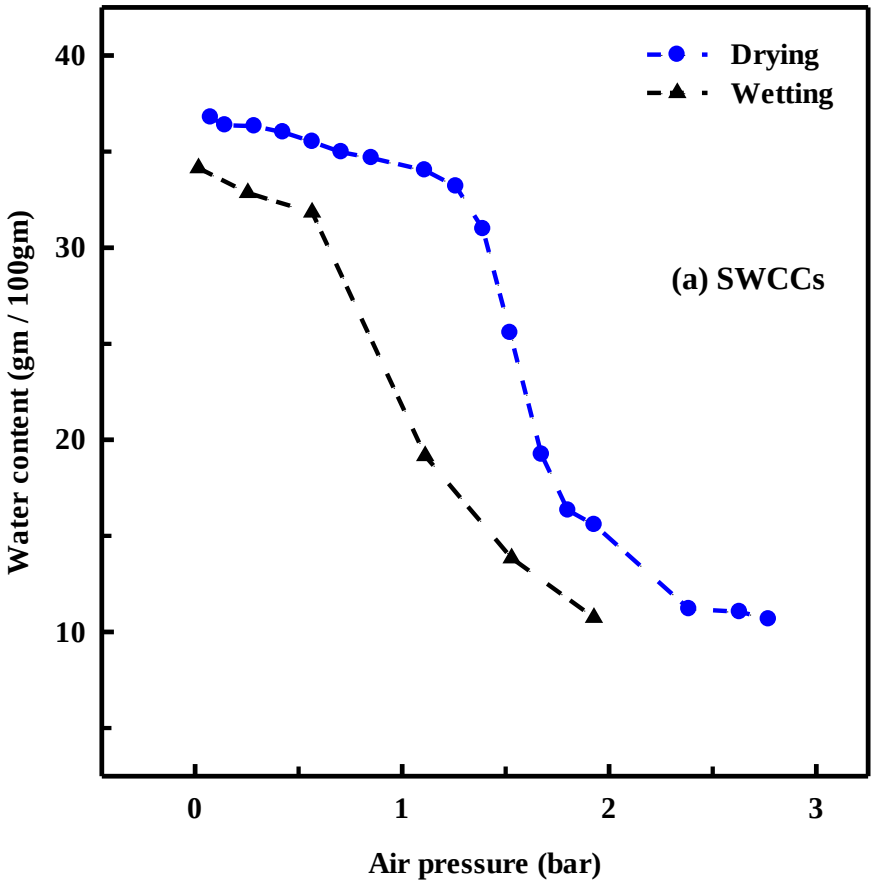

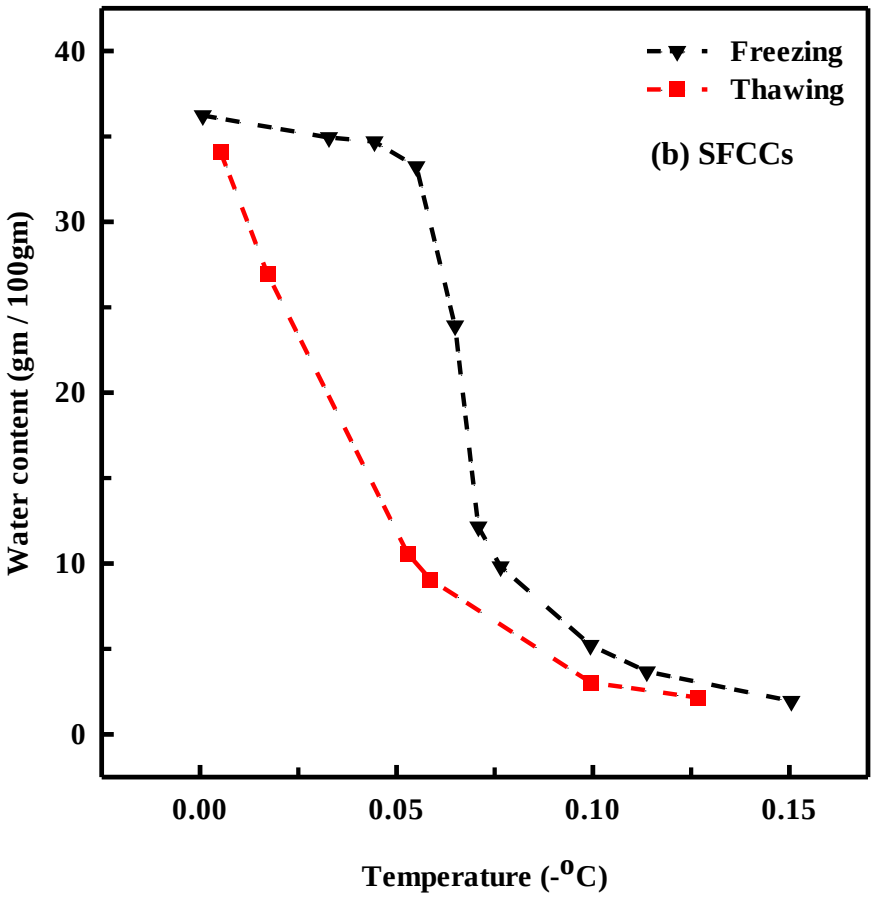

Note: Data is gathered from Koopmans & Miller (1966).

Figure 5.1 Typical SWCCs and SFCCs with hysteresis.

Several SFCC models are available in the literature that are expressed as relationships between pore radius, the cryogenic pressure, and temperature (e.g., Koopmans and Miller, 1966; Dash et al., 2006; Drotz et al., 2009; Enninful et al., 2020). These key relationships are summarized below.

$$(P_{ice} - P_{lw}) = \frac{\gamma_{wa}}{\gamma_{iw}}(P_{air} - P_{lw}) = \frac{1}{\lambda_{km}}(P_{air} - P_{lw}), 1.0 \leq \frac{1}{\lambda_{km}} \leq 2.2 \quad (5.4)$$

$$\frac{T_{f0} - T}{T_{f0}} = \frac{\gamma_{iw}}{L_A \rho_{ice} r} \quad (5.5)$$

where P_{ice}, P_{lw} and P_{air} are ice, water and air pressures, respectively, γ_{iw} and γ_{wa} are the ice-liquid water and water and air interfacial free energies, respectively, λ_{km} is the ratio of the

interfacial energies, T_{f0} is initial freezing point, L_A is the specific latent heat (334 kJ / kg), ρ_{ice} is density of ice (0.92 g / mL), and r is the pore radius.

SFCC models are typically proposed in the literature by extending pore size distribution functions (Watanabe and Mizoguchi, 2002; Liu and Yu, 2013; Bai et al., 2018; Zhou et al., 2018; Teng et al., 2020; Wan and Yang, 2020). In the present study a different approach that is based on fundamentals of thermodynamics principles is used for developing the SFCC models. Such approaches can be used for providing well-defined and novel explanations related to the THMC behavior of frozen unsaturated soils.

5.2.2 Basic relationships

5.2.2.1 Basic relationships from thermodynamics

The differential form expression of Gibbs free energy (i.e., dG) based on the first law of thermodynamics (Denbigh, 1981) can be expressed as below.

$$dG = VdP - S^E dT + \sum_{i=1}^{k} \mu_i dN_i \tag{5.6}$$

where V, P, S^E, and T are volume, pressure, entropy, and temperature, respectively, μ_i and N_i are chemical potential and the number of particles of the i-th substance, respectively. More details with respect to this relationship are summarized in Appendix A of this Chapter.

Eq. (5.7) can be obtained for a given temperature (below 273.15 K), when the pore liquid water and pore ice in unsaturated frozen soils reaches an equilibrium condition (e.g., dG (pore-water) = dG (pore-ice)).

$$V_{lw} dP_{lw} - S_{lw}^E dT = V_{ice} dP_{ice} - S_{ice}^E dT \tag{5.7}$$

where the subscripts *lw* and *ice* refer to variables for pore liquid water and pore ice, respectively.

The infinitesimal change of entropy equals infinitesimal heat transfer associated with temperature changes based on the second law of thermodynamics. The relationship at equilibrium conditions during this reversible process can be expressed as Eq. (5.8).

$$dS^E \equiv \frac{\delta Q_{rev}}{T} \tag{5.8}$$

where Q_{rev} is the heat absorption in reversible process with unit of kJ.

The difference of entropy change between ice and water with certain mass m can be expressed as Eq. (5.9) that is summarized below.

$$S_{ice}^E - S_{lw}^E = -\frac{L_A m}{T} \tag{5.9}$$

where m is mass (unit is kg), and the unit of specific latent heat, unit of L_A is kJ / kg.

The well-known Clausius-Clapeyron relationship (Denbigh, 1981) between the temperature and pressure can be obtained by substituting Eq. (5.9) into Eq. (5.7) as given below.

$$\frac{dP}{dT} = \frac{L_A m}{T\Delta V} = \frac{L_A}{T\Delta v} \tag{5.10}$$

where ΔV and Δv are volume and specific volume difference in phase change, respectively.

Eq. (5.10) suggests that the freezing point (temperature) is strongly dependent on the pressure. The relationship between the temperature and unfrozen water content (i.e., soil freezing characteristics curve (SFCC)) can be used as a tool for interpreting unsaturated unfrozen/frozen soils behaviors. To derive this relation, the Legendre transformation (or using the Helmholtz free energy) can be applied (Denbigh, 1981; Houlsby and Puzrin, 2000; Coussy, 2005) to Eq. (5.7) to obtain Eq. (5.11).

$$-P_{lw}dV_{lw} - S_{lw}^E dT = -P_{ice}dV_{ice} - S_{ice}^E dT \tag{5.11}$$

The volume of pore liquid water, V_{lw} and pore ice, V_{ice} of unit soil in Eq. (5.11) can be expressed by the degree of saturation of liquid water and unfrozen water content, respectively, as shown in Eqs. (5.12).

$$V_{lw} = nS_{lw,0}S_{ufw} \tag{5.12a}$$

$$V_{ice} = \frac{\rho_{lw}}{\rho_{ice}}\left(V_{lw,0} - V_{lw}\right) = n\frac{\rho_{lw}}{\rho_{ice}}S_{lw,0}\left(1 - S_{ufw}\right) \tag{5.12b}$$

where S_{ufw} is unfrozen water content, n is porosity of soils, ρ_{lw} is density of pore liquid water (1.00 g / mL, densities are set as constants for simplicity), respectively, and $V_{lw,0}$ and $S_{lw,0}$ are initial volume and initial degree of saturation of water before freezing, respectively.

The specific latent heat, L_A is expressed as energy per unit mass (e.g., Eq. (5.9)), the absorbed or released energy also varies with the mass of ice content or the unfrozen water content, as shown in Eqs. (5.13) for freezing and thawing processes, respectively.

$$S_{ice}^E - S_{lw}^E = -\frac{L_A}{T}\rho_{ice}nS_{lw,0}\left(1 - S_{ufw}\right) \tag{5.13a}$$

$$S_{ice}^E - S_{lw}^E = -\frac{L_A}{T}\rho_{lw}nS_{lw,0}S_{ufw} \tag{5.13b}$$

Eqs. (5.14) can be obtained for freezing and thawing processes by substituting Eqs. (5.12), (5.13a) and (5.13b) into Eq. (5.11), respectively.

$$\left(\frac{\rho_{lw}}{\rho_{ice}}P_{ice} + P_{lw}\right)dS_{ufw} = -\frac{L_A}{T}\rho_{ice}\left(1 - S_{ufw}\right)dT \tag{5.14a}$$

$$\left(\frac{\rho_{lw}}{\rho_{ice}}P_{ice} + P_{lw}\right)dS_{ufw} = -\frac{L_A}{T}\rho_{lw}S_{ufw}dT \tag{5.14b}$$

Eqs. (5.14) are the basic relationships between the temperature T and unfrozen water content S_{ufw}. The specific latent heat, L_A, densities of pore liquid water, ρ_{lw} and pore ice ρ_{ice} typically have constant values. However, variables which include P_{ice}, and P_{lw} that are highly dependent on temperature are summarized as Eqs. (5.15).

$$d\left(\frac{\rho_{lw}}{\rho_{ice}}P_{ice} + P_{lw}\right) = \frac{\rho_{lw}}{\rho_{ice}}\left(\frac{\partial P_{ice}}{\partial T}\right)_{P_{lw}}dT + \left(\frac{\partial P_{lw}}{\partial T}\right)_{P_{ice}}dT \tag{5.15a}$$

$$\left(\frac{\rho_{lw}}{\rho_{ice}}P_{ice} + P_{lw}\right) = \left(\frac{\rho_{lw}}{\rho_{ice}}P_{ice} + P_{lw}\right)_{T_{f0}} - \int_T^{T_{f0}}\left[\frac{\rho_{lw}}{\rho_{ice}}\left(\frac{\partial P_{ice}}{\partial T}\right)_{P_{lw}} + \left(\frac{\partial P_{lw}}{\partial T}\right)_{P_{ice}}\right]dT = P_{lw,0} - \int_T^{T_{f0}}\left[\frac{\rho_{lw}}{\rho_{ice}}\left(\frac{\partial P_{ice}}{\partial T}\right)_{P_{lw}} + \left(\frac{\partial P_{lw}}{\partial T}\right)_{P_{ice}}\right]dT \tag{5.15b}$$

where $P_{lw,0}$ is the pore liquid water pressure at initial freezing point (e.g., T_{f0}).

Various relations can be built based on Eq. (5.15b) for both the pore-ice pressure $\underline{P_{ice}}$ and pore-water pressure P_{lw} with respect to temperature T. The distinct relations between the pore-pressure and temperature can be used to build distinct relationships between the unfrozen water content, S_{ufw} and the temperature T based on Eqs. (5.15).

A simple linear relationship as shown in Eq. (5.16) is highlighted among various relations for Eqs. (5.15). The derivation process of this relationship is available in Appendix B.

$$\left(\frac{\rho_{lw}}{\rho_{ice}}P_{ice}+P_{lw}\right)=-A-B(L_A\rho_{lw})\frac{(T_{f0}-T)}{T_{f0}} \tag{5.16}$$

where T_{f0} is initial freezing point, and A and B are positive model parameters. The physical meanings of parameters A and B are listed in Eqs. (5.17).

$$A=\left(\left|P_{lw,0}\right|\right)\Big|_{T\to T_{f0+}} \tag{5.17a}$$

$$B=\left[\left(1+\frac{\rho_{lw}}{\rho_{ice}}\right)\frac{\gamma_{iw}}{\gamma_{wa}}-\frac{\rho_{lw}}{\rho_{ice}}\right], 0<B\leq 1.0 \tag{5.17b}$$

In Eqs. (5.17), parameter A is an absolute value of initial pore-water pressure prior to freezing, while parameter B represents the pore ice pressure (together with pore-water pressure as shown in Eqs. (5.15) and (5.16) and Appendix B) variations with respect to temperature. The relation in Eq. (5.16) is consistent with the experimental results in frozen unsaturated soils (e.g., Koopmans and Miller, 1966; Zhang et al., 2016; Zhang et al., 2018). More details with respect to Eqs. (5.17) are discussed in Appendix B of this Chapter.

By substituting Eq. (5.16) into Eq. (5.14b), Eq. (5.18) can be obtained for explaining the thawing process.

$$\frac{dS_{ufw}}{S_{ufw}}=\frac{L_A\rho_{lw}}{T[A+B(T_{f0}-T)]}dT \tag{5.18}$$

The relationship between the temperature and unfrozen water content can be obtained by integrating Eq. (5.18). To simplify the model, the revised relations between pressure and temperature are proposed as following Eq. (5.19).

$$\left(\frac{\rho_{lw}}{\rho_{ice}}P_{ice}+P_{lw}\right)=-\frac{AT_{f0}}{T}-\frac{BT_{f0}}{T}(L_A\rho_{lw})\frac{(T_{f0}-T)}{T_{f0}} \tag{5.19}$$

The units for parameters *A* and *B* are [Pa] and dimensionless [-], respectively.

5.2.2.2 Soil thawing curve

By substituting Eq. (5.19) into Eq. (5.14b), Eqs. (5.20) in differential and integral forms can be obtained, respectively.

$$\frac{dS_{ufw}}{S_{ufw}}=\frac{L_A\rho_{lw}}{AT_{f0}+BT_{f0}(L_A\rho_{lw})\frac{(T_{f0}-T)}{T_{f0}}}dT \tag{5.20a}$$

$$\int_{S_{ufw}}^{1}\frac{dS_{ufw}}{S_{ufw}}=\int_{T}^{T_{f0}}\frac{L_A\rho_{lw}}{AT_{f0}+BT_{f0}(L_A\rho_{lw})\frac{(T_{f0}-T)}{T_{f0}}}dT \tag{5.20b}$$

Eq. (5.21) can be obtained by integrating Eq. (5.20b); this is similar in form of VG equation with clear physical meanings for the model parameters *A* and *B*.

$$S_{ufw}=\frac{1}{\left[1+\frac{B}{A}L_A\rho_{lw}\left(\frac{T_{f0}-T}{T_{f0}}\right)\right]^{\frac{1}{B}}} \tag{5.21}$$

The detailed expressions for parameters *A* and *B* in Eqs. (5.17) are available in Appendix B. Eq. (5.21) describes the well-defined relationship between the unfrozen water content, S_{ufw} and temperature *T*. However, the residual unfrozen water content is typically obtained from experimental results of the SFCC (e.g., Ren and Vanapalli, 2019; Teng et al., 2020). Eq. (5.21) can be expressed as Eq. (5.22) to highlight the role of residual unfrozen water.

$$\frac{S_{ufw}-S_{res}}{S_{sat}-S_{res}}=\frac{1}{\left[1+\frac{B}{A_{lv}}\left(\frac{L_A\rho_{lw}}{P_{atm}}\right)\left(\frac{T_{f0}-T}{T_{f0}}\right)\right]^{\frac{1}{B}}} \tag{5.22}$$

where S_{res} specifies residual degree of saturation of unfrozen water in the SFCC models, P_{atm} is the standard atmosphere pressure (101.325 kPa or 1.01 bar), and A_{lv} is the ratio of initial pore water pressure over the standard atmosphere pressure, P_{atm}.

Parameter A_{lv} is introduced into the model calibration such that the units of both parameters *A* and *B* are dimensionless. Eq. (5.22) can be used as a tool for calibration purposes of the SFCC for thawing process providing clear explanations of each of the parameters based on the principles of thermodynamics.

5.2.2.3 Soil freezing curve

A mathematical model for explaining the freezing process of SFCC can be obtained by substituting Eq. (5.19) into Eq. (5.14a), as shown below as Eqs. (5.23).

$$\frac{dS_{ufw}}{1-S_{ufw}} = \frac{L_A\rho_{ice}}{AT_{f0}+BT_{f0}(L_A\rho_{lw})\frac{\left(T_{f0}-T\right)}{T_{f0}}}dT \tag{5.23a}$$

$$\int_{S_{ufw}}^{S_{res}} \frac{dS_{ufw}}{1-S_{ufw}} = \int_{T}^{T_{ff0}} \frac{L_A\rho_{ice}}{AT_{f0}+BT_{f0}(L_A\rho_{lw})\frac{\left(T_{f0}-T\right)}{T_{f0}}}dT \tag{5.23b}$$

where T_{ff0} is the freezing temperature at residual degree of saturation S_{res}. Eq. (5.23b) is integral from residual stage to avoid zero in calculation. Eq. (5.24) can be obtained from (5.23b).

$$\frac{S_{ufw}-S_{res}}{1-S_{res}} = 1-\left[\frac{1+\frac{B}{A}(L_A\rho_{lw})\frac{\left(T_{f0}-T\right)}{T_{f0}}}{1+\frac{B}{A}(L_A\rho_{lw})\frac{\left(T_{f0}-T_{ff0}\right)}{T_{f0}}}\right]^{\rho_{ice}/(B\rho_{lw})} \approx \frac{1}{1+\left[\frac{1+\frac{B}{A}(L_A\rho_{lw})\frac{\left(T_{f0}-T\right)}{T_{f0}}}{1+\frac{B}{A}(L_A\rho_{lw})\frac{\left(T_{f0}-T_{ff0}\right)}{T_{f0}}}\right]^{\rho_{ice}/(B\rho_{lw})}} \tag{5.24}$$

A close comparison of Eq. (5.20b) and Eq. (5.23b) highlights that these two equations are similar. While Eq. (5.24) and Eq. (5.22) highlight distinct models for the freezing and thawing processes, respectively. It is inconvenient to use two different expressions for the SFCC related to freezing and thawing processes. For this reason, a simplified model (i.e., Eq. (5.25)) to keep a similar form to Eq. (5.22) is suggested for modeling the soil freezing curve.

$$\frac{S_{ufw}-S_{res}}{S_{sat}-S_{res}} = \frac{1}{\left[1+\frac{B}{A_{lv}}\left(\frac{L_A\rho_{lw}}{P_{atm}}\right)\left(\frac{T_{f0}-T}{T_{f0}}\right)\right]^{\frac{\rho_{ice}}{B\rho_{lw}}}} \tag{5.25}$$

On the right side of Eq. (5.24), Taylor series approximation is used. Eq. (5.25) can be regarded as a simplified model to avoid some constants in Eq. (5.24). The influence of parameters on the model performance, and model results for thawing and freezing processes are respectively presented in Figures 5.2, 5.3, and 5.4. More details related to these figures (i.e., Figures 5.2, 5.3, and 5.4) are discussed in a later section.

5.2.3 Various distinguishable zones in SFCCs

5.2.3.1 Explanatory model for hysteretic effect in SFCCs

There are various factors that influence the hysteresis (Kurylyk and Watanabe, 2013) characteristics between the soil freezing curve and the soil thawing curve (i.e., two branches of the SFCC). These factors include (i) supercooling effect; (ii) effect of electrolytes; (iii) pore structure change during freezing and thawing cycles (Kurylyk and Watanabe, 2013; Ren and Vanapalli, 2019). The hysteretic effects can be well explained using the proposed models (i.e., Eqs. (5.22) and (5.25)) based on thermodynamics principles.

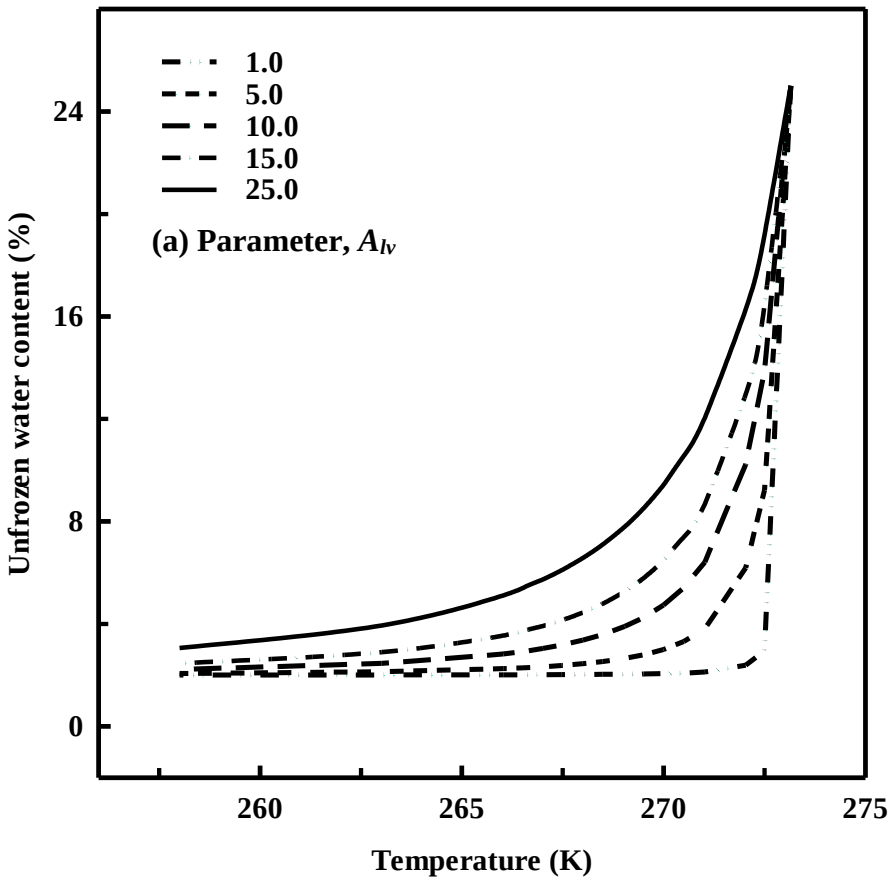

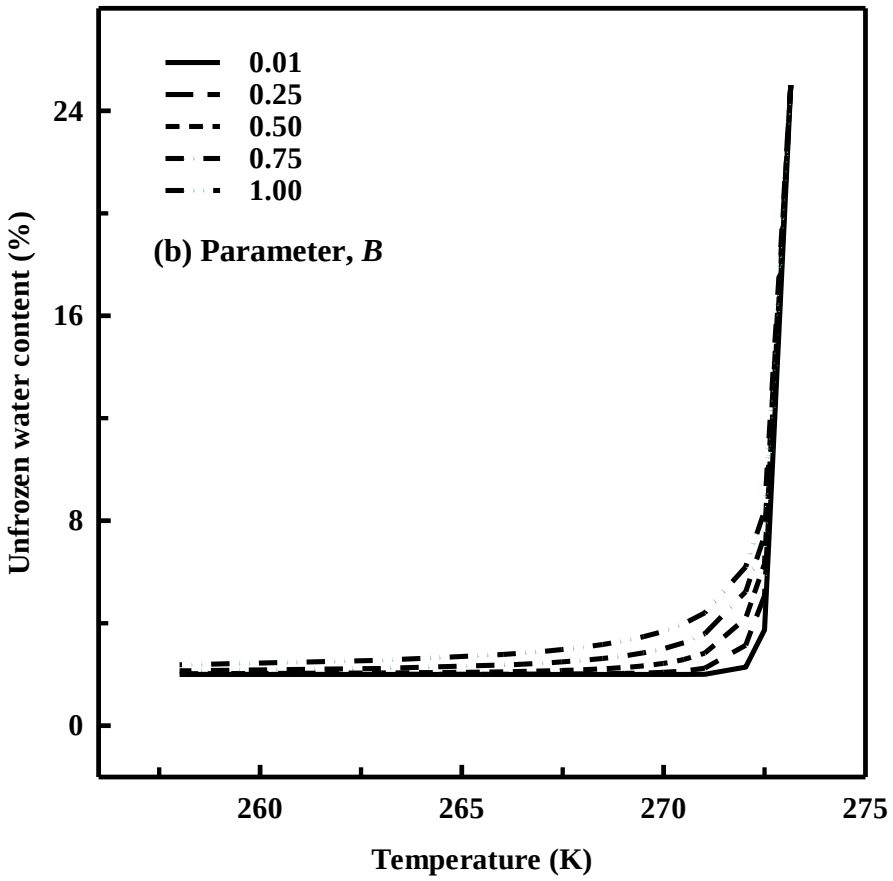

Note: The curves are obtained based on Eq. (5.22).

Figure 5.2 Influence of various parameters based on the proposed SFCC model.

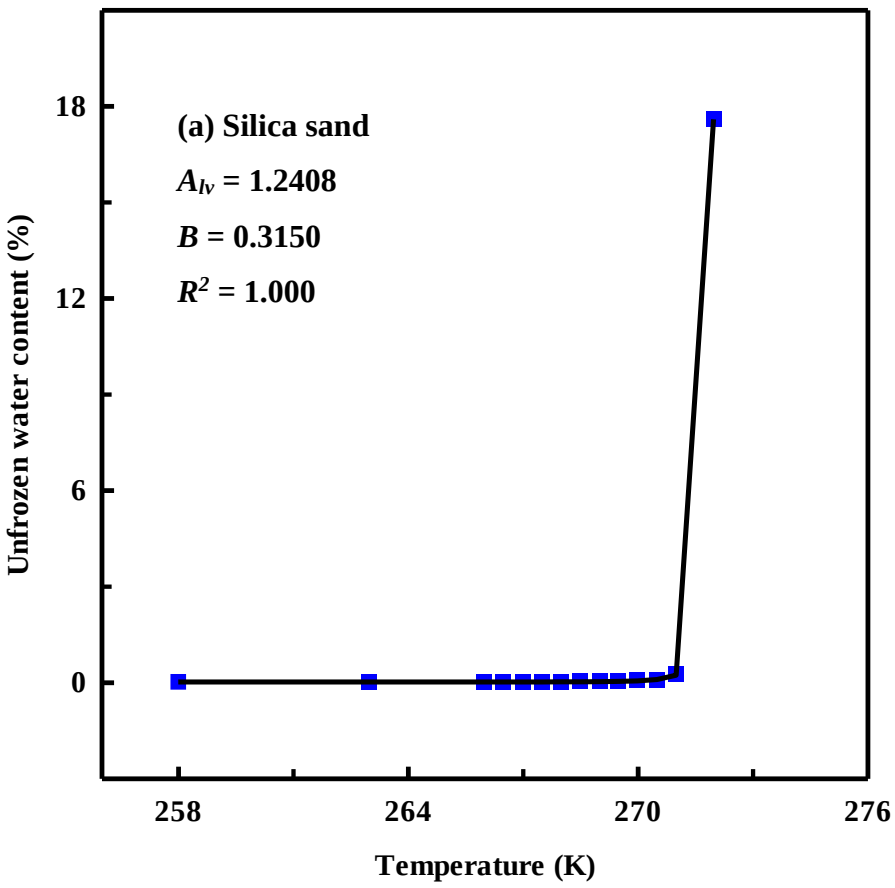
(a) Silica sand
A_{lv} = 1.2408
B = 0.3150
R^2 = 1.000
Unfrozen water content (%)
Temperature (K)
0
6
12
18
258
264
270
276

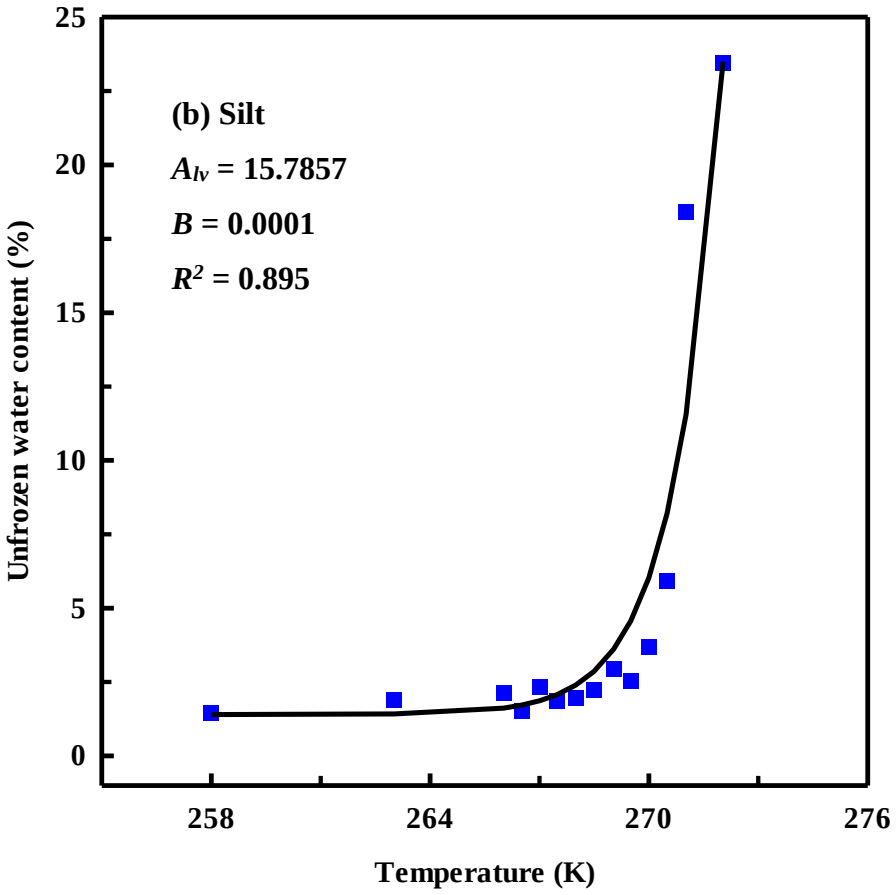
(b) Silt
A_{lv} = 15.7857
B = 0.0001
R^2 = 0.895
Unfrozen water content (%)
Temperature (K)
0
5
10
15
20
25
258
264
270
276

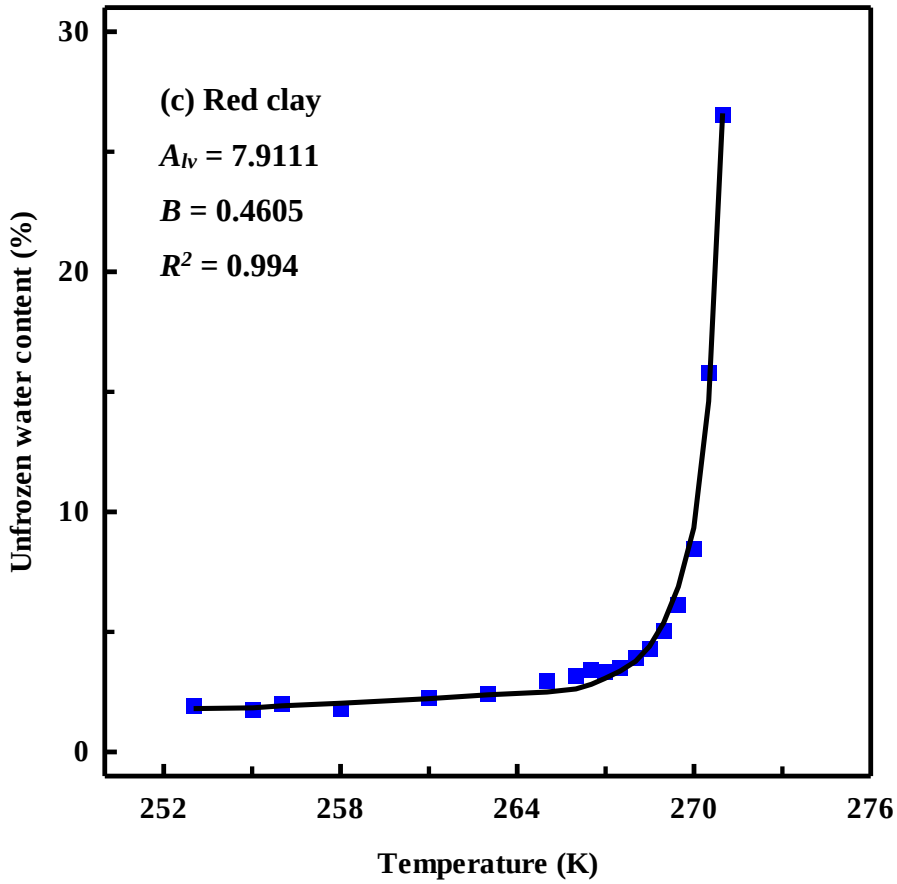

Note: Figures (a), (b), and (c) are silica sand, silt, and red clay, respectively. The model prediction based on Eq. (5.22) is shown as a continuous line. Experimental data shown as symbols is collected from Teng et al. (2020).

Figure 5.3 Model performance for the soil thawing curves.

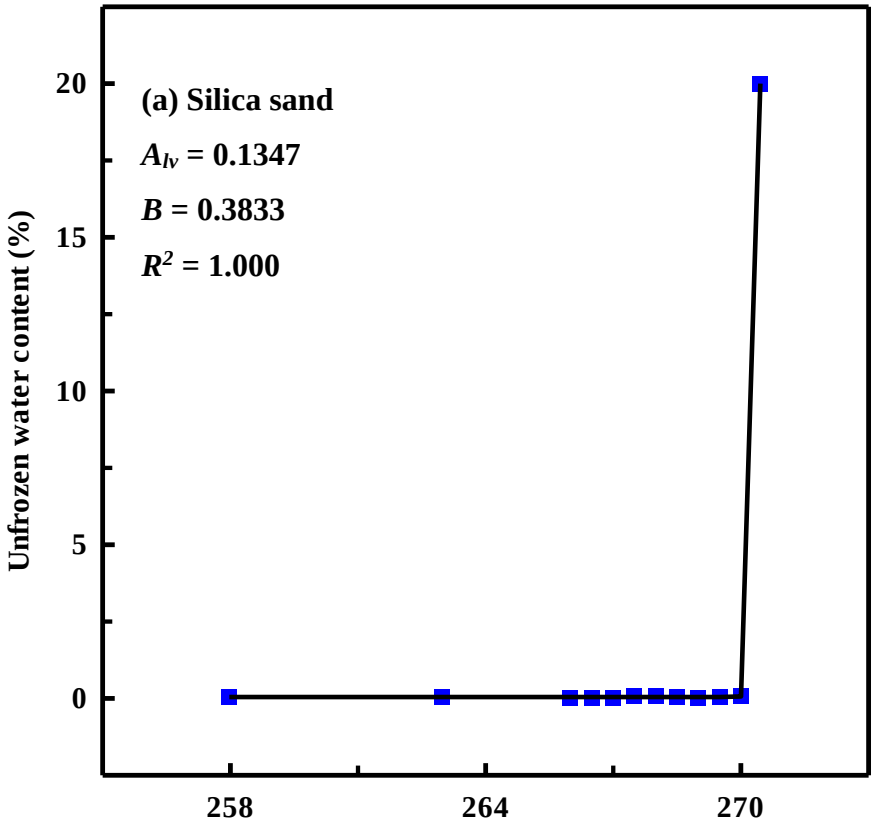
(a) Silica sand
A_{lv} = 0.1347
B = 0.3833
R^2 = 1.000
Unfrozen water content (%)
0
5
10
15
20
258
264
270

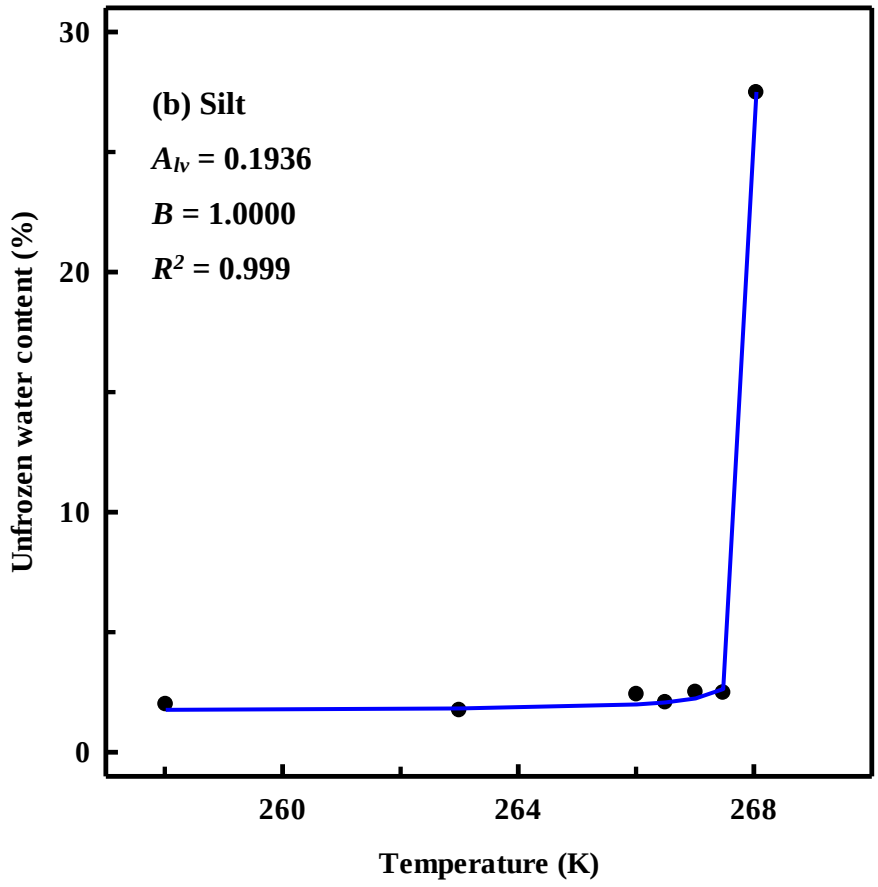
(b) Silt
A_{lv} = 0.1936
B = 1.0000
R^2 = 0.999
Unfrozen water content (%)
0
10
20
30
260
264
268
Temperature (K)

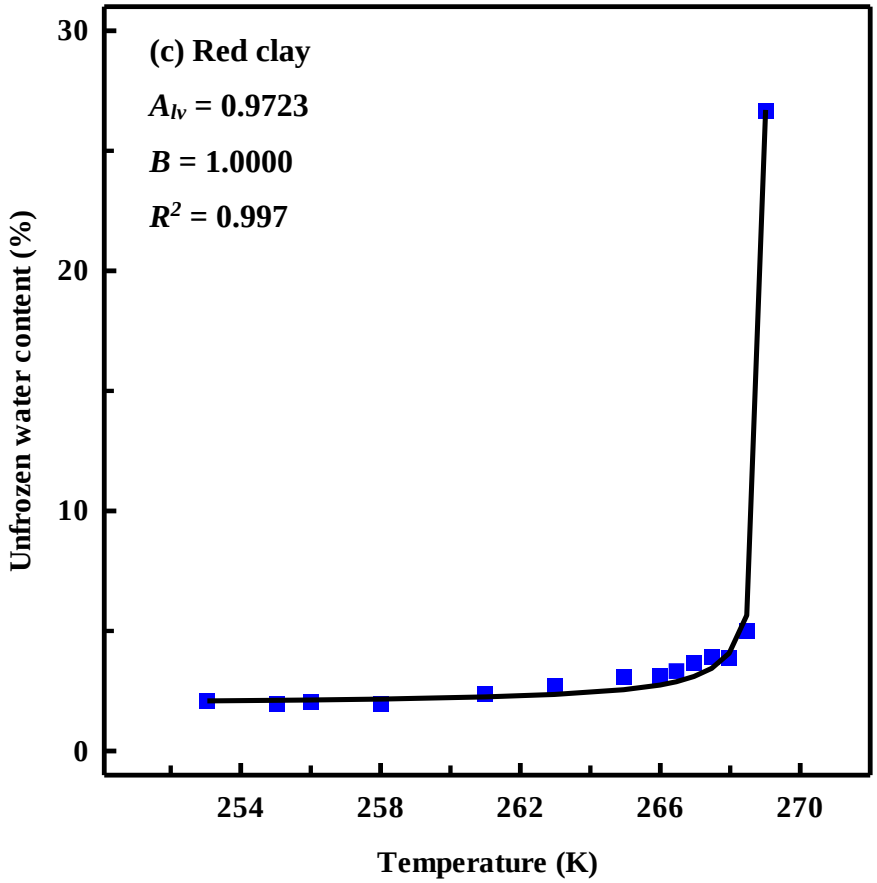

Note: Figures (a), (b), and (c) are silica sand, silt, and red clay, respectively. The model prediction based on Eq. (5.25) is shown as a continuous line. Experimental data shown as symbols is collected from Teng et al. (2020).

Figure 5.4 Model performance for the soil freezing curves.

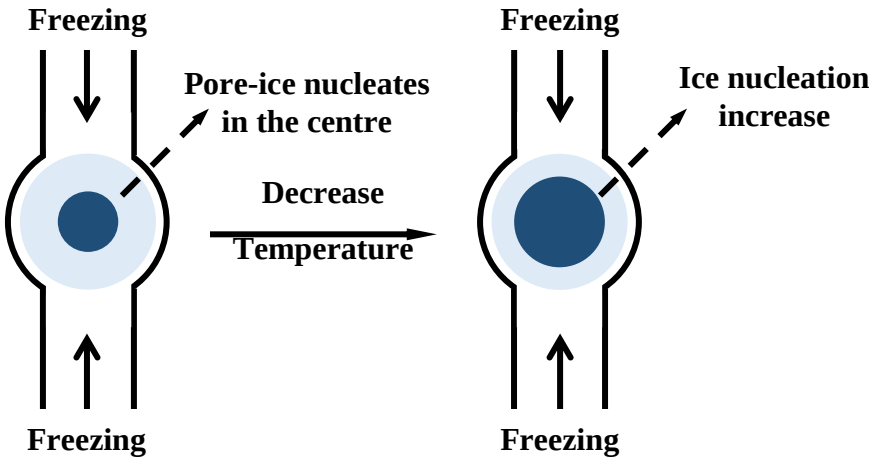

(a) Freezing process

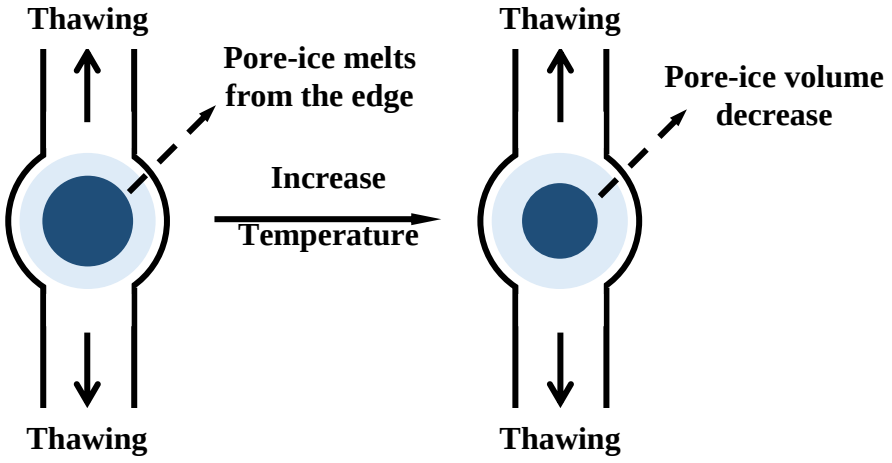

(b) Thawing process

Figure 5.5 Conceptual model for freezing and thawing processes.

Eqs. (5.26) are the equations derived in previous section for soil thawing curve and soil freezing curve, respectively. Eq. (5.27) is the summarized relationship for these two equations, which is summarized below.

$$\begin{cases} \frac{S_{ufw}-S_{res}}{S_{sat}-S_{res}} = \frac{1}{\left[1+\frac{B}{A_{lv}}\left(\frac{L_A\rho_{lw}}{P_{atm}}\right)\left(\frac{T_{f0}-T}{T_{f0}}\right)\right]^{\frac{1}{B}}}, thawing \\ \frac{S_{ufw}-S_{res}}{S_{sat}-S_{res}} = \frac{1}{\left[1+\frac{B}{A_{lv}}\left(\frac{L_A\rho_{lw}}{P_{atm}}\right)\left(\frac{T_{f0}-T}{T_{f0}}\right)\right]^{\frac{\rho_{ice}}{B\rho_{lw}}}}, freezing \\ A_{lv} = \left(\left|\frac{P_{lw,0}}{P_{atm}}\right|\right)\Big|_{T\to T_{f0+}} \\ B = \left[\left(1+\frac{\rho_{lw}}{\rho_{ice}}\right)\frac{\gamma_{iw}}{\gamma_{wa}} - \frac{\rho_{lw}}{\rho_{ice}}\right], 0 < B \le 1.0 \end{cases} \quad (5.26)$$

$$\frac{dS_{ufw}}{S_{ufw}} = -\frac{1}{P(T)}\frac{dT}{T}, P(T) \le 0 \quad (5.27)$$

As discussed in Appendix B, parameter A (or A_{lv}) is the initial water pressure near the freezing point while parameter B is the pressure (i.e., pore- water and ice pressures) variation along with temperature. In Eq. (27), $P(T)$ is function indicates the pressure variation along with temperature. It should be less than 273 K to ensure the model is consistent with experimental results of the SFCC. As temperature decreases, the pore-ice amount increases; however, the temperature must be low enough (lower than 273 K) for satisfying the criterion of ice nucleation, as the pore-ice nucleates in the center of pore-water as shown in Figure 5.5 (a).

However, during the thawing process, as temperature rises, the pore-ice melts into pore-water from the edge and the pore-ice in the pore center remains frozen as shown in Figure 5.5 (b).

In summary, the direction of the freezing and the thawing processes of pore-ice is distinct (i.e., the pore-ice formation process starts from the pore center, while the thawing process begins from the pore edge). More details are discussed in a later section providing numerical evidence using the published results from the literature.

5.2.3.2 Various zones in the soil freezing curve

Various zones in the soil freezing curve (freezing branch of the SFCC) can be determined based on Eqs. (5.24) and (5.25), as shown in Figure 5.6 (a). The first zone is the liquid water stage (zone (i)). This stage can be regarded as the specific latent heat zone equal zero, where water is not frozen prior to the freezing point of pure water (e.g., 273.15 K).

The second stage is the ice nucleation zone (i.e., zone (ii)) that arises as temperature further decreases. This zone can be postulated to start from the freezing point of pure water (e.g., 273.15 K). In this zone, the heat (energy) is released from the pore-water until the temperature is low enough for ice nucleation. In this process, there is only a limited amount of water that is frozen into ice at the end of the stage as ice nucleates. As ice forms after this stage, the specific latent heat, L_A is non-zero at the end of the stage.

The third stage is the zone for freezing process in macropores (i.e., zone (iii)). In this zone, a significant amount of pore-water is frozen into pore-ice. The last stage is the zone of freezing in micropores (i.e., zone (iv)). In this zone, pore-water in micropores is gradually frozen into pore-ice, and only a small amount of water remains as liquid phase. The intersection point between zone (iii) and zone (iv) is regarded as the freezing point for residual water. This point can be determined using a graphical construction or a computational method that is widely used for estimating the residual water content from SWCC (Vanapalli et al., 1998) as shown in Figure 5.6 (a).

5.2.3.3 Various zones in the soil thawing curve

Figure 5.6 (b) highlights three zones related to soil thawing curve based on Eq. (5.22). As temperature increases, the first stage (i.e., zone (i)) arises during the thawing process that

influences the residual water content. A small amount of ice stored in the micropores melts into water in this zone. The next stage is the zone for thawing process in the macropores (zone (ii)). In this zone, when most of pore-ice melts, a sharp increase in soil thawing curve can be observed. The intersection point between zone (i) and zone (ii) can be referred to as the thawing point for macropores. This point can be determined either by graphical construction or computational method as described in Vanapalli et al. (1998), which is also shown in Figure 5.6 (b). The third stage is the zone that is related to the water that is available in the liquid phase. In this stage, the volume of liquid water varies as temperature increases. As discussed earlier, this is a stage where specific latent heat is zero (i.e., no ice melts).

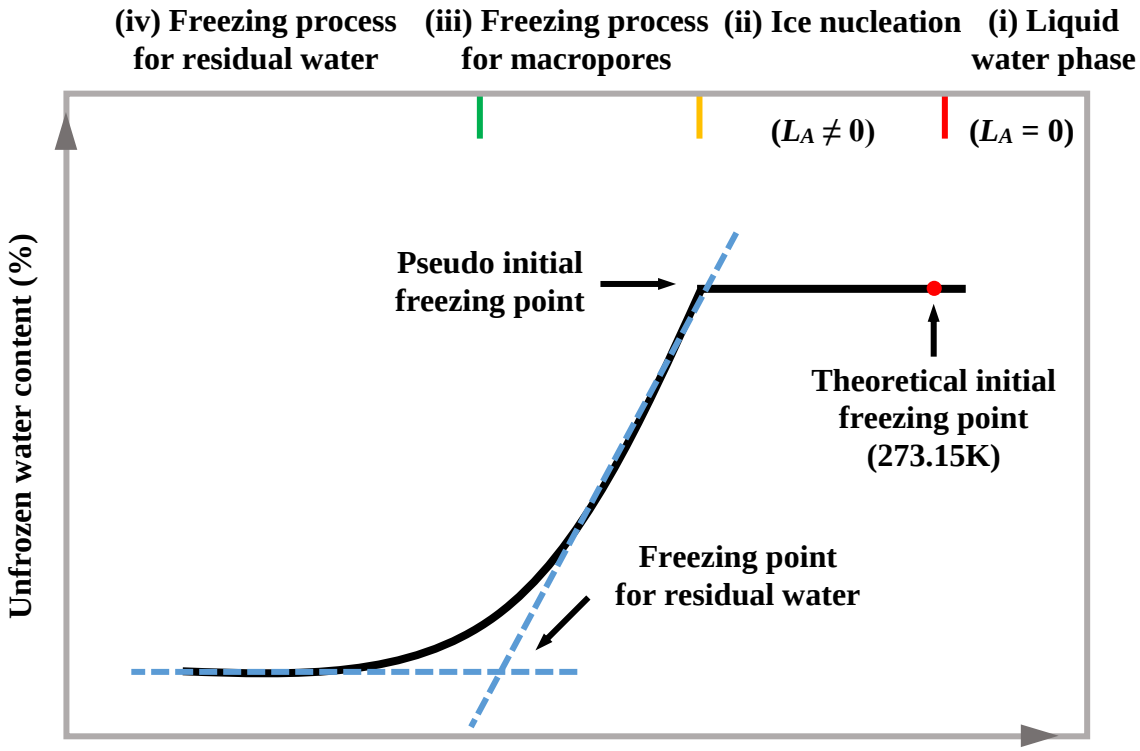

(a) Soil freezing curve

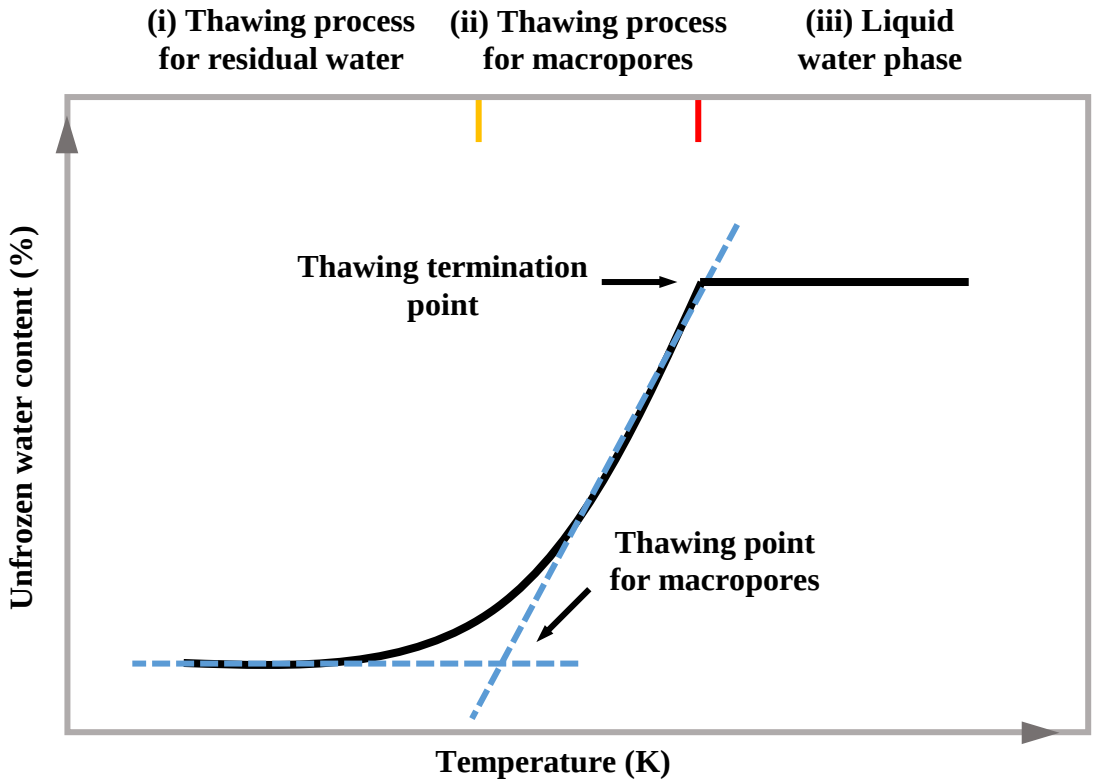

(b) Soil thawing curve

Figure 5.6 Distinguished zones in the soil freezing and thawing curves.

5.2.3.4 Model calibration and evaluation indicators

In this study, the zones that go through significant variation of unfrozen water content are modeled (e.g., zones (iii) and (iv) in the soil freezing curve and zones (i) and (ii) in soil thawing curve) (see Figure 5.6 (a)). The initial freezing point including initial freezing temperature and water content is set as already known point in this study. The parameters in Eqs. (5.22) and (5.25) are determined by the least-square method (Fredlund and Xing, 1994) as shown in Eq. (5.28) (i.e., by minimizing the objective function *O*). In addition, Eq. (5.29) is highlighted for model comparison and evaluation purposes.

$$O = \sum_{i=1}^{N}(S_{obv} - S_{cal})^2 \tag{5.28}$$

$$R^2 = \frac{\left[\sum_{i=1}^{N}(S_{obv}-\bar{S}_{obv})(S_{cal}-\bar{S}_{cal})\right]^2}{\sum_{i=1}^{N}(S_{obv}-\bar{S}_{obv})^2 \sum_{i=1}^{N}(S_{cal}-\bar{S}_{cal})^2} \tag{5.29}$$

where S_{obv} and S_{cal} are the observed and the calculated degree of saturations within unfrozen water content, respectively, and $\bar{S}_{obv}$ and $\bar{S}_{cal}$ are the average values of the observed and the

calculated degree of saturations (of unfrozen water content), respectively.

5.2.4 Experimental and numerical evidence related to the proposed SFCC models

5.2.4.1 Experimental evidence for the basic assumption

One key assumption is inherently included within Eqs. (5.16) and (5.19). This assumption suggests that the pore- water and ice pressures follow a negative linear relationship with the temperature. It is reasonable to set a negative pressure value for parameter *A* in Eqs. (5.16) and (5.19), as it relates to initial (water) pressure.

The parameter *B* in Eqs. (5.16) and (5.19) is related to the pore pressure (i.e., pore- water and ice pressures) change with temperature. The theoretical derivation and definition for parameter *B* can be found in Appendix B. For experimental verification, a close to negative linear relationship (downward trend) between pore-water pressure and temperature (lower than 273.15 K) can be found in the literature (Zhang et al., 2016; Zhang et al., 2018). A negative linear relationship in Eqs. (5.16) and (5.19) is justified based on derivation of Eqs. (5.16) and (5.17) summarized in Appendix B and from the experimental evidence in the literature (Zhang et al., 2016; Zhang et al., 2018).

5.2.4.2 Numerical evidence related to distinct zones

Some investigators in the literature (e.g., Matsumoto et al., 2002) have proposed molecular dynamics simulation approach for explaining ice formation process (i.e., ice nucleation and its growth). Several stages can be summarized from the molecular simulation results which include ice nucleation that is related to the development of long-lived hydrogen bonds; and rapid crystallization that arises due to slow shape and size changes of initial nucleus.

The distinct zones (stages) in a SFCC can be well explained based on the summarized freezing process relationships (i.e., Eqs. (5.26)) and molecular simulation results from the literature (e.g., Matsumoto et al., 2002). For example, the freezing stage (ii) in Figure 5.6 (a) can be attributed to the hydrogen bonds development for ice nucleation at microscopic level. As the ice nucleation process is strongly related to the release of energy, the best understanding of macroscopic changes can be related to the changes of specific latent heat, L_A during this process (i.e., the value of specific latent heat changes from zero to non-zero (e.g., 334 kJ / kg in this stage). The changes related to the specific latent heat, L_A are not of concern during the thawing process, which is consistent with Eq. (5.22). This is because thawing is associated only with an

increase temperature from a lower to a higher value in frozen soils.

5.2.4.3 Relationships with other models in the literature

The focus of many studies in the literature during the last two decades is linked to pressure and volume relationships (e.g., Watanabe and Mizoguchi, 2002; Liu and Yu, 2013; Wang et al., 2017; Bai et al., 2018; Chai et al., 2018; Zhou et al., 2018; Teng et al., 2020; Wan and Yang, 2020; Jin et al., 2020; Teng et al., 2021; Kong et al., 2022). The variation of temperature is connected to interfacial surfaces between liquid water and ice using the Gibbs-Thomson equation (see Eq. (5.5)). The relationship between the unfrozen water content and temperature can be explained based in Eq. (5.5) with the aid of suitable pore size distribution function from SWCC models (i.e., Eqs. (5.1), (5.2), and (5.3)).

In the proposed model, as shown in Eqs. (5.26), the form of the equation is similar to VG model (e.g., Eq. (5.2)) with parameter $n_{vg} \equiv 1$. The physical meanings related to the proposed model are also summarized in Eqs. (5.26). More details are summarized in the results and discussion section.

The philosophy of the current research is not directed towards developing a model that matches a certain pore size distribution function but towards proposing a valid theoretical framework. It is well known the pressure P and volume V are conjugate variables in thermodynamics (Houlsby and Puzrin, 2000). To solve the relationship between pressure, volume, and temperature (e.g., $P\ dV = f\ (T)\ dT$), the pore size distribution function is extended using the established relationships in the literature (i.e., the links between volume V and pressure P (i.e., $V = g(P)$ or $P = g^{-1}(V)$). In the present study, pressure P is directly linked to temperature (i.e., $P = h(T)$). In other words, the focus of current research is directed towards a new approach to address conjugate variables; namely, pressure P and volume V within the framework of thermodynamics for addressing problems related to frozen soils using the SFCC as a tool.

5.3 Factors influencing the behaviors of SFCCs

The SFCCs behaviors are significantly influenced by several factors; namely, salt concentration (i.e., salinity), initial water content, and initial stress state (e.g., Kurylyk and Watanabe, 2013; Zhou et al., 2018; Teng et al., 2020; Wan and Yang, 2020). The effects associated with salinity and initial water content are discussed using the SFCC models derived in the earlier sections.

5.3.1 Salinity effects

The salinity effects on the SFCC behavior can be evaluated using Eqs. (5.30) by adding terms related to mass change extending thermodynamics principles (Denbigh, 1981).

$$-P_{lw}dV_{lw} - S_{lw}^{E}dT + \sum_{i=1}^{k}\mu_i dN_i = -P_{ice}dV_{ice} - S_{ice}^{E}dT + \sum_{i=1}^{k}\mu_i dN_i \quad (5.30a)$$

$$\mu_i = \mu_i^* + RT\ln c_i = \mu_i^* + RT\ln\left(\frac{N_i}{N}\right) \quad (5.30b)$$

where N is total number of substances, c_i are the concentration of the i-th substances, respectively, R is universal gas constant (8.31 J / (K · mol)), and μ_i* is standard chemical potential (unit: J / mol) and it is the function of temperature and pressure.

Eq. (5.31) can be derived from Eq. (5.30a) by applying Legendre transformation (summarized in Appendix A). This relationship is widely referred to as the grand potential or Landau potential from the literature (Denbigh, 1981).

$$-P_{lw}dV_{lw} - S_{lw}^{E}dT - N_{lw}d\mu_{lw} - N_{salt}d\mu_{salt} = -P_{ice}dV_{ice} - S_{ice}^{E}dT - N_{ice}d\mu_{ice} \quad (5.31)$$

The variation of standard potential of the liquid water and ice potential is approximately equivalent to the standard chemical potential for dilute solutions as shown below.

$$\mu_{lw} = \mu_{lw}^* + RTln(x_{lw}) \cong \mu_{lw}^* \quad (5.32a)$$

$$\mu_{ice} = \mu_{ice}^* + RTln(x_{ice}) = \mu_{ice}^* \quad (5.32b)$$

Eqs. (32) are generally used for dilute solutions, in which the mass of salt is significantly low compared to the amount of solution (i.e., the concentration of sodium chloride solution is typically below 3 or 4 mol / L to ensure model accuracy). If the standard chemical potential can be regarded as constant, the left side in Eq. (5.31) can be simplified into Eq. (5.33).

$$-P_{lw}dV_{lw} - S_{lw}^{E}dT - N_{salt}d\left(RT\ln\left(\frac{N_{salt}}{N_{lw}+N_{salt}}\right)\right) \cong -P_{lw}dV_{lw} - S_{lw}^{E}dT -$$

$$N_{salt}d\left(RT\ln\left(\frac{N_{salt}}{V_{lw}\rho_{lw}/M_{lw}}\right)\right) = -P_{lw}dV_{lw} - S_{lw}^{E}dT - RN_{salt}\ln\left(\frac{N_{salt}M_{lw}}{V_{lw}\rho_{lw}}\right)dT + \frac{RTN_{salt}}{V_{lw}}dV_{lw}$$

(5.33)

where M_{lw} is the molar mass of water (e.g., 18 g / mol). Eq. (5.34) summarized below can be obtained by substituting Eqs. (5.32), and (5.33) into Eq. (5.31).

$$-P_{lw}dV_{lw} - S_{lw}^{E}dT - RN_{salt}\ln\left(\frac{M_{lw}N_{salt}}{V_{lw}\rho_{lw}}\right)dT + \frac{RTN_{salt}}{V_{lw}}dV_{lw} = -P_{ice}dV_{ice} - S_{ice}^{E}dT \quad (5.34)$$

The amount of salt (NaCl) can be expressed by its concentration in an ideal dilute solution as shown in Eq. (5.35). In this study, only dilute salt (NaCl) solution is considered, the salt precipitation affect in freezing process deserves further consideration (Xiao et al., 2020).

$$N_{NaCl} = 2nS_{lw,0}c_{NaCl} \quad (5.35)$$

where c_{NaCl} is the concentration of NaCl in solution prior to freezing (unit is mol / L).

Eq. (5.36) can be derived for explaining thawing process by substituting Eqs. (5.12), (5.13b), (5.17), (5.19) and (5.35) into above Eq. (5.34).

$$\frac{dS_{ufw}}{S_{ufw}} = \frac{\frac{L_A\rho_{lw}}{AT_{f0}} + \frac{RT}{AT_{f0}}\left(\frac{2c_{NaCl}}{S_{ufw}}\right)\ln\left(\frac{M_{lw}2c_{NaCl}}{\rho_{lw}\ S_{ufw}}\right)}{\left[1+\frac{B}{A}(L_A\rho_{lw})\frac{(T_{f0}-T)}{T_{f0}}\right] + \frac{RT^2}{AT_{f0}}\left(\frac{2c_{NaCl}}{S_{ufw}}\right)}dT \quad (5.36)$$

Eq. (5.36) is the same as Eq. (5.20a) when the salt concentration equals zero. Eq. (5.36) can be expressed in slightly modified form as Eq. (5.37) to simplify model calibration for parameter A, by adding the standard atmosphere pressure, P_{atm} (i.e., 101.325 kPa or 1.01 Bar).

$$\frac{dS_{ufw}}{S_{ufw}} = \frac{\frac{1}{A_{lv}T_{f0}}\left(\frac{L_A\rho_{lw}}{P_{atm}}\right) + \frac{T}{A_{lv}T_{f0}}\left(\frac{R}{P_{atm}}\right)\left(\frac{2c_{NaCl}}{S_{ufw}}\right)\ln\left(\frac{M_{lw}2c_{NaCl}}{\rho_{lw}\ S_{ufw}}\right)}{\left[1+\frac{B}{A_{lv}}\left(\frac{L_A\rho_{lw}}{P_{atm}}\right)\frac{(T_{f0}-T)}{T_{f0}}\right] + \frac{T^2}{A_{lv}T_{f0}}\left(\frac{R}{P_{atm}}\right)\left(\frac{2c_{NaCl}}{S_{ufw}}\right)}dT \quad (5.37)$$

As shown in Eq. (5.22) and Eq. (5.25), similar equations for both soil freezing and thawing curves are used. For simplicity purposes, the salinity effects on both soil freezing and thawing curves are modeled using Eq. (5.37) by adjusting parameters values. Eq. (5.37) can be numerically solved with suitable initial conditions (e.g., initial freezing temperature and initial water content).

5.3.2 Initial water content effects

The initial water content has a significant effect on both the soil freezing and soil thawing curves as shown in the SFCC models (i.e., Eqs. (5.26)). This effect can be evaluated by changing model parameters values (e.g., initial water content is directly related to initial pore-water pressure as discussed in Vanapalli et al., 1999). Eq. (5.17a) proposed in this study can take account of the influence of pore-water pressure. The relationships between model parameters A or A_{lv} (shown in Eqs. (5.26)) and initial pore water pressure can be summarized as Eq. (5.38).

$$\frac{A}{P_{atm}} = A_{lv} = \left(\left|\frac{P_{lw,0}}{P_{atm}}\right|\right)\Big|_{T\to T_{f0+}} \tag{5.38}$$

The following Eq. (5.39) can be built based on the BC model (i.e., Eq. (5.1)) by neglecting pore-air pressure.

$$\left(\frac{w_{lw,0}-w_{res}}{w_{lw,ref}-w_{res}}\right)^{1/\lambda_{bc}} \cong \frac{P_{lw,ref}}{P_{lw,0}} \tag{5.39}$$

where $w_{lw,ref}$ and $P_{lw,ref}$ are the initial water content and pore-water pressure at reference state, respectively, and $w_{lw,0}$ is the initial water content at initial pore-water pressure $P_{lw,0}$.
Along similar lines, Eq. (5.2) (i.e., VG model, van Genuchten, 1980) and Eq. (5.3) (i.e., FX model, Fredlund and Xing, 1994) can be respectively used for developing relationships similar to Eq. (5.39).

Eq. (5.40) is an approximate form that can be used for soils in which the residual water content is negligible.

$$\left(\frac{w_{lw,0}}{w_{lw,ref}}\right)^{1/\lambda_{bc}} = \frac{P_{lw,ref}}{P_{lw,0}} \tag{5.40}$$

where ξ_{ini} is a model parameter ($\xi_{ini} \approx 1 / \lambda_{BC}$). Eqs. (5.41) can be obtained for evaluating initial water content effects on the SFCC behavior by substituting Eq. (5.40) into Eq. (5.38).

$$A = A_{ref}\left(\frac{w_{lw,ref}}{w_{lw,0}}\right)^{\xi_{ini}} \tag{5.41a}$$

$$A_{lv} = A_{lv,ref}\left(\frac{w_{lw,ref}}{w_{lw,0}}\right)^{\xi_{ini}} \tag{5.41b}$$

where A_{ref} and $A_{lv,ref}$ are respectively A and A_{lv} values in reference state at initial water content, $w_{lw,ref}$.

5.4. Results and discussion

Figure 5.2 presents the model variation associated with different model parameters in Eq. (5.22). As shown in Figure 5.2 (a), parameter A_{lv} alters model shapes contributing to variations in slopes of the SFCCs without any change in the residual water content. However, as shown in Figure 5.2 (b), curve shapes and residual water contents are both affected by various values of parameter B. The distinct characteristics of the model parameters ensure that the proposed relationships are capable of modeling different types of soils.

Figure 5.3 shows model performance of thawing curves based on Eq. (5.25) for three different soils. As listed in Table 5.1, the physical value (i.e., $L_A\rho_{lw} / P_{atm} \approx 3296.3237$) is used for all cases discussed in the figure. The experimental results for two soils (i.e., Figures 5.3 (a) and (c)) are well predicted by the model. Figure 5.3 (b) summarizes results for silt; although R^2 value is not high (i.e., 0.895), the shape of the curve is well captured for this soil. The summarized results in Figure 5.3 suggest that Eq. (5.17) is rigorous and is capable of modeling soil thawing curves.

Figure 5.4 highlights the performance of modeling SFCC using the proposed Eq. (5.25). The experimental data for different soils (i.e., silica sand, silt, and red clay) is reliably described by the model. The R^2 values for all soils are greater than 0.99 highlighting this point. The results summarized in Figure 5.4 for different soils suggest that Eq. (5.25) can be used in rigorous modeling the SFCC behavior. This study focuses on SFCCs, while the overall framework for frozen unsaturated soils using work input method (Houlsby, 1997) and thermodynamic framework (Borja, 2006) can be found in Appendix C and D, respectively.

Table 5.1 Physical meanings of parameters in proposed models.

Eq. #	Equations	Para meter	Unit	Physical meanings	Note
Eq. (5.22)	$\frac{S_{ufw}-S_{res}}{S_{sat}-S_{res}}=\frac{1}{\left[1+\frac{B}{A_{lv}}\left(\frac{L_A\rho_{lw}}{P_{atm}}\right)\left(\frac{T_{f0}-T}{T_{f0}}\right)\right]^{\frac{1}{B}}}$	A_{lv}	-	$A_{lv}=\left(\left\lvert\frac{P_{lw,0}}{P_{atm}}\right\rvert\right)\Big\rvert_{T\to T_{f0}+}$	Parameter A_{lv} is the ratio of initial pore water pressure over standard atmosphere pressure when temperature T approaches to initial freezing temperature T_{f0} based on Eqs. (5.26).
Eq. (5.25)	$\frac{S_{ufw}-S_{res}}{S_{sat}-S_{res}}=\frac{1}{\left[1+\frac{B}{A_{lv}}\left(\frac{L_A\rho_{lw}}{P_{atm}}\right)\left(\frac{T_{f0}-T}{T_{f0}}\right)\right]^{\frac{\rho_{ice}}{B\rho_{lw}}}}$	B_{lv}	-	$B=\left[\left(1+\frac{\rho_{lw}}{\rho_{ice}}\right)\frac{\gamma_{iw}}{\gamma_{wa}}-\frac{\rho_{lw}}{\rho_{ice}}\right],0<B\leq 1.0$	Parameter B is ratio of interfacial free energies between ice-liquid water over water and air in Eqs. (5.26).
Eq. (5.37)	$\frac{dS_{ufw}}{S_{ufw}}=\frac{\frac{1}{A_{lv}T_{f0}}\left(\frac{L_A\rho_{lw}}{P_{atm}}\right)+\frac{T}{A_{lv}T_{f0}}\left(\frac{R}{P_{atm}}\right)\left(\frac{2c_{NaCl}}{S_{ufw}}\right)\ln\left(\frac{M_{lw}}{\rho_{lw}}\frac{2c_{NaCl}}{S_{ufw}}\right)}{\left[1+\frac{B}{A_{lv}}\left(\frac{L_A\rho_{lw}}{P_{atm}}\right)\frac{\left(T_{f0}-T\right)}{T_{f0}}\right]+\frac{T^2}{A_{lv}T_{f0}}\left(\frac{R}{P_{atm}}\right)\left(\frac{2c_{NaCl}}{S_{ufw}}\right)}dT$				
Eq. (5.41b)	$A_{lv}=A_{lv,ref}\left(\frac{w_{lw,ref}}{w_{lw,0}}\right)^{\xi_{ini}}$	ξ_{ini}	-	$\xi_{ini}=\frac{1}{\lambda_{BC}}$	λ_{BC} is dimensionless model parameter in BC model for SWCC (Eq. (5.1)).

Eqs. (5.26) summarizes the thermodynamics relationship between the unfrozen water content and temperature. This relationship can be used not only in the prediction of variations considering the changes in ice volume and temperature but also in the rational understanding of the frozen soils behavior. For example, Figure 5.6 (a) highlights the hysteretic effect on the soil freezing curve. This is a simple and novel approach for interpreting and modeling the variations of volume of frozen and unfrozen pore-water with respect to temperatures lower than zero degrees Celsius.

Figures 5.6 (a) and (b) summarize the various zones in the soil freezing and thawing curves. The different zones in these curves can be attributed to the complex behaviors of liquid water freezing as discussed earlier (see Section 2.3); only salient features of these curves are modeled and highlighted (with the aid of Eqs. (5.22) and (5.25)). The density changes associated with freezing and other factors are not discussed. These behaviors are beyond the scope of present study. In addition, Eqs. (5.22) and (5.25) developed in this study do not take account to describe water density change prior to freezing.

Figures 5.7 and 5.8 highlight model results for predicting the SFCCs with various salt concentrations based on Eq. (5.37). The values for parameters A_{lv} and B (i.e., 15.4837, and 0.0010,) respectively are used in the Figures As this study focuses more on soil freezing and thawing curves rather than initial freezing points, the initial freezing temperature is assumed linear downward with an increase in salt concentration (i.e., $T_{f0} = 273.15 - 2K_T c_{NaCl}$, ($K_T = 2.25$ $K \cdot mol^{-1}$)). The initial freezing temperatures for salt concentrations of 0.0, 0.8547, 1.7094, 2.5641, and 3.4188 (mol / L) are set as 273.15, 269.30, 265.46, 261.61, and 257.77 K, respectively (Zhou et al., 2018; Wan and Yang, 2020). The saturated and residual water contents are set as 18.0 and 2.9 (kg / 100kg), respectively, and are applied to all curves. As shown in Figure 5.7, the salinity effects on soil freezing curve are reasonably described by the model. The results summarized in Figure 5.7 suggest that the shapes of SFCCs are influenced by different salinity concentrations, which are consistent with Eq. (5.37).

Figures 5.9 and 5.10 summarize the results using the proposed model (i.e., Eq. (5.41b)) to evaluate the influence of initial water content effects on the SFCCs. The effect of initial water content effects for this soil is evaluated via parameter A_{lv} in Eq. (5.41b). The curve shapes for various initial water contents are reasonably described by the model. As shown in experimental

and numerical results summarized in Figure 5.9, the residual water contents vary with a decrease in the soil initial water contents. This behavior can also be explained by Clausius-Clapeyron relation (i.e., Eq. (5.10)). This relationship suggests that more energy (i.e., lower temperature) is necessary to freeze the pore-water under high pore pressure, (i.e., lower initial water content).

The initial water content and salt concentration have coupled effects on the SFCC behavior based on Eq. (5.37). The parameter A_{lv} is strongly related to initial water content (see Eqs. (5.41)) that has a coupled relation with the salt concentrations. However, modeling discussions related to the coupling effects of initial water content and salinity concentration on the SFCCs is not undertaken in this study due to the limited data. In other words, more studies in this direction are required in the future. The physical meanings and values of each parameter in the proposed SFCC models are summarized in Table 5.1, and the model calibration processes are shown in Figure 5.11.

Eqs. (5.42) summarize the transformations between the proposed model (i.e., Eq. (5.26) and the well-known VG model (i.e., Eq. (5.2)).

$$\text{(VG model)}\ \frac{S_{lw}-S_{res}}{S_{sat}-S_{res}}=\frac{1}{\left[1+(a_{vg}\psi)^{n_{vg}}\right]^{m_{vg}}}$$

$$\text{(Proposed models)}\begin{cases}\dfrac{S_{ufw}-S_{res}}{S_{sat}-S_{res}}=\dfrac{1}{\left[1+\frac{B}{A_{lv}}\left(\frac{L_A\rho_{lw}}{P_{atm}}\right)\left(\frac{T_{f0}-T}{T_{f0}}\right)\right]^{\frac{1}{B}}},thawing\\ \dfrac{S_{ufw}-S_{res}}{S_{sat}-S_{res}}=\dfrac{1}{\left[1+\frac{B}{A_{lv}}\left(\frac{L_A\rho_{lw}}{P_{atm}}\right)\left(\frac{T_{f0}-T}{T_{f0}}\right)\right]^{\frac{\rho_{ice}}{B\rho_{lw}}}},freezing\\ A_{lv}=\left(\left|\frac{P_{lw,0}}{P_{atm}}\right|\right)\Big|_{T\to T_{f0+}}\\ B=\left[\left(1+\frac{\rho_{lw}}{\rho_{ice}}\right)\frac{\gamma_{iw}}{\gamma_{wa}}-\frac{\rho_{lw}}{\rho_{ice}}\right],0<B\le 1.0\end{cases}$$

$$\text{(Links)}\begin{cases}n_{vg}\equiv 1\\ m_{vg}=\begin{cases}\frac{1}{B},thawing\\ \frac{\rho_{ice}}{B\rho_{lw}},freezing\end{cases}\\ \psi=(L_A\rho_{lw})\left(\frac{T_{f0}-T}{T_{f0}}\right)\\ a_{vg}=\frac{B}{A_{lv}P_{atm}}\end{cases}\qquad(5.42)$$

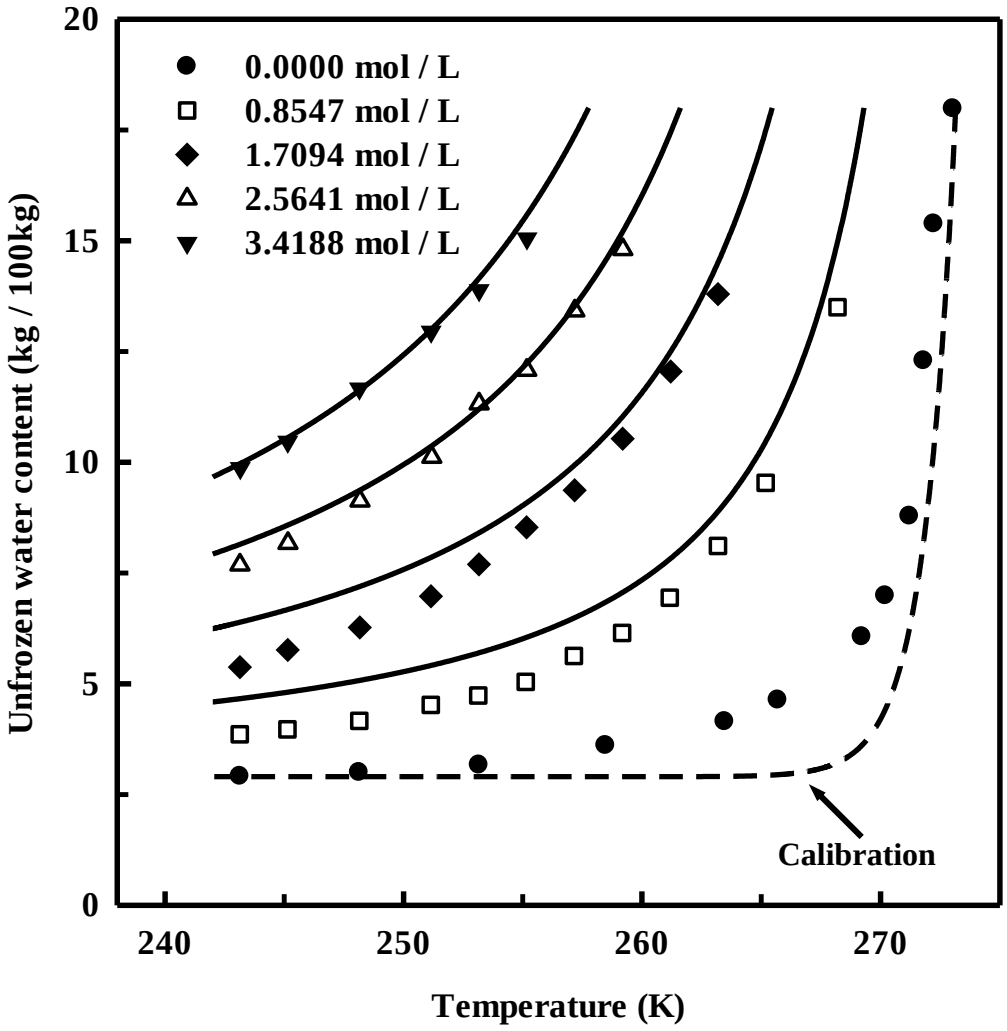

Note: The continuous lines are predicted soil freezing curve for various salt concentrations. Parameters values for A_{lv}, and B are 15.4837, and 0.0010, respectively based on Eq. (5.37). Experimental data is collected from Wan & Yang (2020).

Figure 5.7 SFCCs predictions considering the salinity effects.

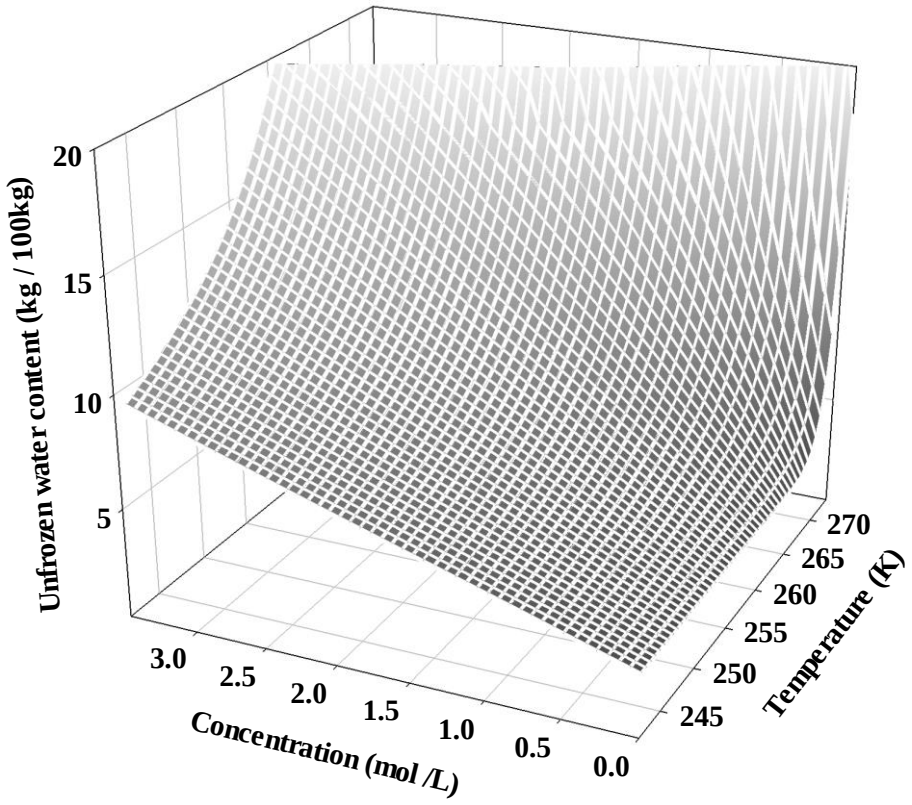

Figure 5.8 Salinity effects on the SFCC expressed as a 3D surface.

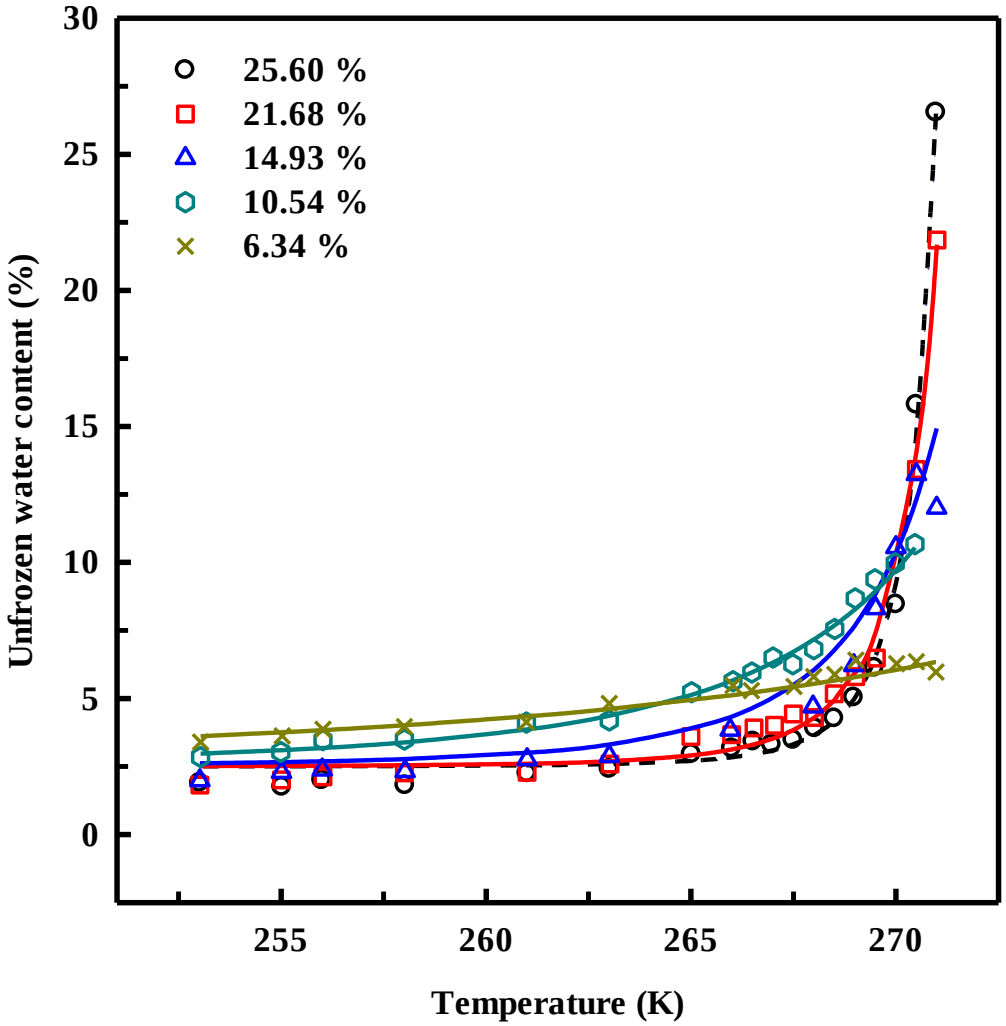

Note: The solid lines are predicted soil thawing curve for the different initial water contents shown as inset in the figure. Parameters values for $A_{lv,ref}$, B, and ξ_{ini} are 7.9556, 0.2489, and 2.1078, respectively. Experimental data shown as symbols is collected from Teng et al. (2020).

Figure 5.9 SFCCs predictions considering influence of different initial water contents.

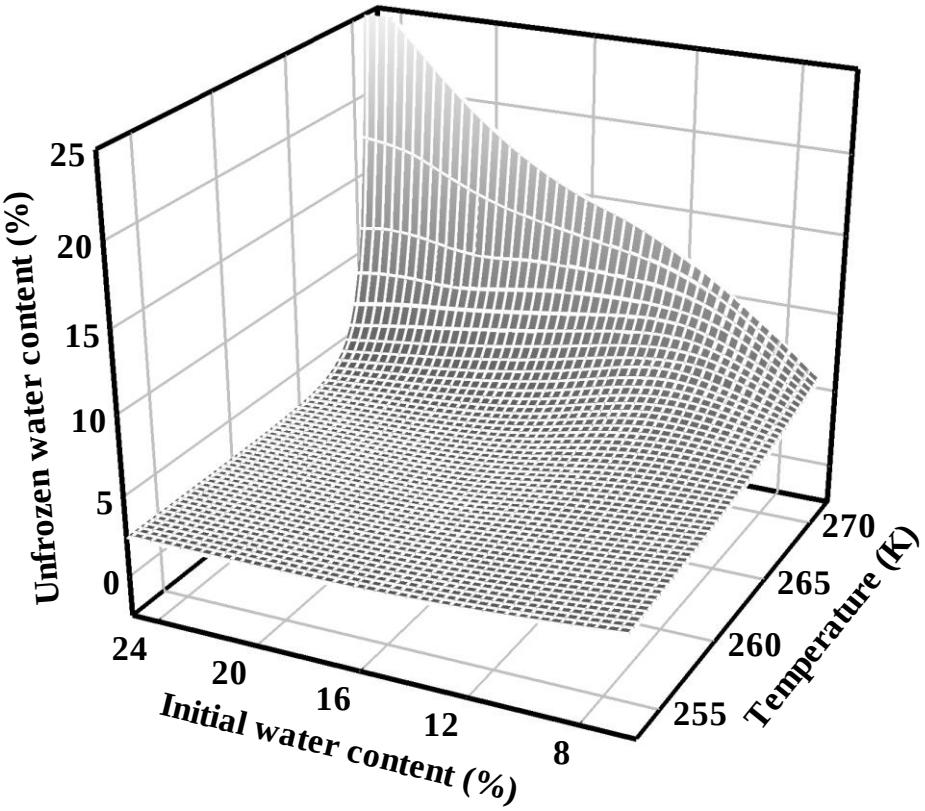

Figure 5.10 3D SFCC surface considering the different initial water content effects.

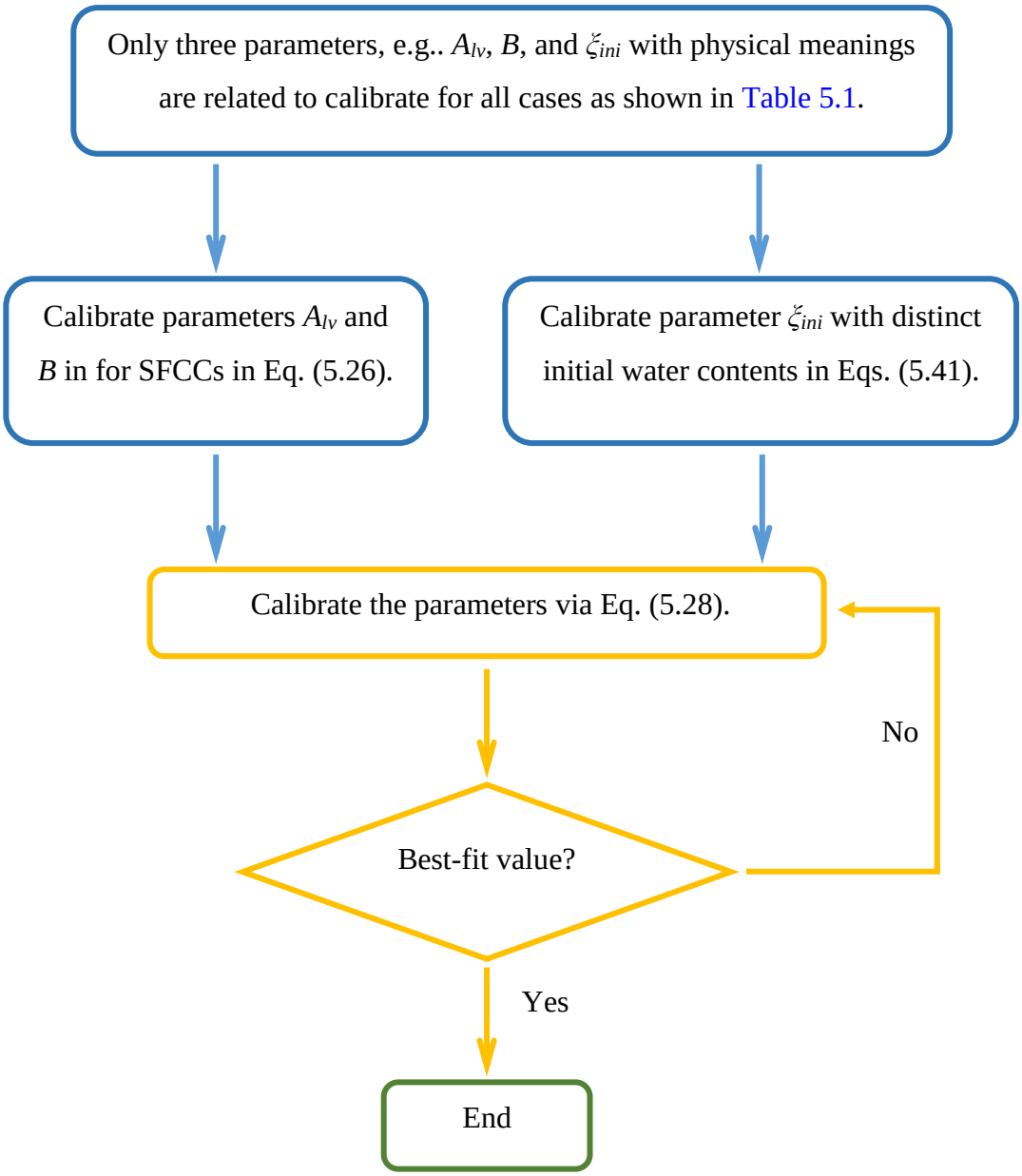

Figure 5.11 Calibration processes for SFCC models.

5.5 Conclusions

In this Chapter, novel equations for SFCCs (i.e., Eqs. (5.22) and (5.25)) are derived for modeling the THMC behaviors of unsaturated frozen soils. Each of the parameters in these models are well-defined and have physical meaning (e.g., Eqs. (5.26)) that can be explained using thermodynamics principles. The proposed models were validated using the published experimental results from the literature starting from the initial freezing point. In a simplified form, the physical meanings, and the selections of the proposed SFCC models for various scenarios are summarized in Table 5.1.

The hysteretic effects that influence the SFCC behavior are reasonably explained by the proposed pore water/ice volume and temperature relationship (i.e., Eqs. (5.26)). The distinguished zones in two branches of SFCCs (e.g., soil freezing and thawing curves) are comprehensively characterized with detailed explanation using the proposed models.

The salinity and initial water content effects on the SFCCs are also incorporated into the proposed models (i.e., Eqs. (5.37) and (5.41)). The proposed SFCC model is also capable of providing direct links with the available SWCC model in the literature as shown in Eq. (5.42). The models proposed in this study are valuable tools for modeling the influence of complex THMC behaviors of unsaturated soils extending thermodynamics principles.

To better understand SFCCs, more validations are necessary based on a large volume dataset. In addition, salt precipitation at low unfrozen water content, and soil structure effects on the proposed models need further study.

5.6 Appendix A

In physics, the Legendre transformation can be used to convert one variable (i.e., pressure, temperature, and number of particles into conjugate variables (i.e., volume, entropy, and chemical potential, respectively) (Denbigh, 1981; Houlsby and Puzrin, 2000). Based on the Legendre transformation, various thermodynamic potentials can be expressed in a differential equation form as follows.

$$dG = VdP - S^E dT + \sum_{i=1}^{k} \mu_i dN_i \quad \text{(A-1)}$$

$$dF = -PdV - S^E dT + \sum_{i=1}^{k} \mu_i dN_i \quad \text{(A-2)}$$

$$dH = VdP + TdS^E + \sum_{i=1}^{k} \mu_i dN_i \quad \text{(A-3)}$$

$$dU = -PdV + TdS^E + \sum_{i=1}^{k} \mu_i dN_i \quad \text{(A-4)}$$

$$d\Phi_G = -PdV - S^E dT - \sum_{i=1}^{k} N_i d\mu_i \quad \text{(A-5)}$$

where G, F, H, U, and Φ_G are Gibbs free energy, Helmholtz free energy, enthalpy, internal energy, the grand potential, respectively.

5.7 Appendix B

Eq. (5.4) can be written as Eq. (B-1) by neglecting pore-air pressure P_{air} at saturation condition.

$$\begin{cases} P_{ice} = \left(1 - \frac{1}{\lambda_{km}}\right) P_{lw}, 1.0 \le \frac{1}{\lambda_{km}} \le 2.2 \\ \frac{1}{\lambda_{km}} = \frac{\gamma_{wa}}{\gamma_{iw}} \end{cases} \quad \text{(B-1)}$$

The relations between cryogenic pressure (i.e., (P_{ice} - P_{lw})) and pore radius r can be expressed as Eq. (B-2) which is well-known in the literature (e.g. Koopmans and Miller, 1966; Liu and Yu, 2013).

$$(P_{ice} - P_{lw}) = \frac{\gamma_{iw}}{r} \quad \text{(B-2)}$$

The following Eqs. (B-3) and (B-4) can be obtained by substituting Eq. (B-1) into Eq. (B-2).

$$\left(-\frac{1}{\lambda_{km}}\right) P_{lw} = \frac{\gamma_{iw}}{r} \quad \text{(B-3)}$$

$$\left(\frac{-1}{\lambda_{km}-1}\right) P_{ice} = \frac{\gamma_{iw}}{r} \quad \text{(B-4)}$$

The following Eqs. (B-5) and (B-6) can be obtained by substituting Eqs. (B-3) and (B-4) into Eq. (5).

$$P_{lw} = -(\lambda_{km})(L_A \rho_{ice}) \frac{T_{f0} - T}{T_{f0}} \quad \text{(B-5)}$$

$$\frac{\rho_{lw}}{\rho_{ice}} P_{ice} = -(\lambda_{km} - 1) \frac{\rho_{lw}}{\rho_{ice}} (L_A \rho_{ice}) \frac{T_{f0} - T}{T_{f0}} \quad \text{(B-6)}$$

The following Eq. (B-7) can be obtained by summing up Eqs. (B-5) and (B-6).

$$\left(\frac{\rho_{lw}}{\rho_{ice}}P_{ice}+P_{lw}\right)=-\left[(\lambda_{km}-1)\frac{\rho_{lw}}{\rho_{ice}}+\lambda_{km}\right](L_A\rho_{lw})\frac{T_{f0}-T}{T_{f0}},1.0\leq\frac{1}{\lambda_{km}}\leq 2.2 \quad \text{(B-7)}$$

The empirical relationship $1.0 \leq (1/\lambda_{km}) \leq 2.2$ that is developed based on limited experiments (Koopmans and Miller, 1966), it might be slightly lower than zero when it reaches the lower bound. A more rigorous relation is feasible which is shown below as Eq. (B-8).

$$B=\left[\left(1+\frac{\rho_{lw}}{\rho_{ice}}\right)\frac{\gamma_{iw}}{\gamma_{wa}}-\frac{\rho_{lw}}{\rho_{ice}}\right],0<B\leq 1.0 \quad \text{(B-8)}$$

Eq. (B-9) that is built to take account of variation of pore- water and ice pressures along with temperature using Eq. (B-7), by adding the initial pore water pressure $P_{lw,0}$ (lower than zero in unsaturated soils) prior to the initial freezing point T_{f0}.

$$\left(\frac{\rho_{lw}}{\rho_{ice}}P_{ice}+P_{lw}\right)+P_{lw,0}=-A-\left[\left(1+\frac{\rho_{lw}}{\rho_{ice}}\right)\frac{\gamma_{iw}}{\gamma_{wa}}-\frac{\rho_{lw}}{\rho_{ice}}\right](L_A\rho_{lw})\frac{T_{f0}-T}{T_{f0}} \quad \text{(B-9)}$$

where parameter A is the value of initial pore water pressure when temperature T approaches to initial freezing temperature T_{f0}.

The following Eq. (B-10) is obtained by replacing variables in Eq. (B-9) by non-negative parameters A and B.

$$\begin{cases}\left(\frac{\rho_{lw}}{\rho_{ice}}P_{ice}+P_{lw}\right)=-A-B(L_A\rho_{lw})\frac{T_{f0}-T}{T_{f0}}\\ A=\left(\left|P_{lw,0}\right|\right)\big|_{T\to T_{f0+}}\\ B=\left[\left(1+\frac{\rho_{lw}}{\rho_{ice}}\right)\frac{\gamma_{iw}}{\gamma_{wa}}-\frac{\rho_{lw}}{\rho_{ice}}\right],0<B\leq 1.0\end{cases} \quad \text{(B-10)}$$

It is important to note that initial pore-water pressure must be negative, as the equations are derived from ratios of surface tension between pore- air and water over the surface tension between pore- liquid water and ice. Eqs. (B-10) exactly is the Eq. (5.16) with clear physical meanings.

5.8 Appendix C

The original framework proposed by Houlsby (1997) is extended in this appendix using pore-ice, liquid water, and ice as example. In the appendix, ice is considered as an additional (solid) part despite the presence of pore- air and water inside soil pores. The subscripts -$_{lw}$, -$_{air}$, and -$_{ice}$ are used to represent pore-liquid-water, pore-air, and pore-ice, respectively in this Appendix. If the average stress for soil solids is expressed as s_{ij}, the total stress in unsaturated frozen soils can be expressed using the following relationship.

$$\sigma_{ij} = (1-n)s_{ij} + n\left(S_{lw}u^{lw} + S_{air}u^{air}\right)\delta_{ij} + nS_{ice}P_{ij}^{ice} + T_{ij} \tag{C-1}$$

where T_{ij} is surface tension. The surface tension for unsaturated frozen soils includes two parts, (i.e., the interface forces between soil solids, pore-liquid-water, and pore-air, and the forces acting on the interface between pore-ice, pore-liquid-water, and pore-air).

The total density ρ can be written as below.

$$\rho = (1-n)\rho_s + n(S_{lw}\rho_{lw} + S_{air}\rho_{air} + S_{ice}\rho_{ice}) \tag{C-2}$$

where ρ_s, ρ_{lw}, ρ_{air}, and ρ_{ice} are densities of soil solids, pore-liquid-water, pore-air, and pore-ice, respectively. As suggested by Houlsby (1997), the strain rate is defined as below.

$$\dot{\varepsilon}_{ij} = -v_{(j,i)} \tag{C-3}$$

where v_i is the velocity vector of soil solids, a comma notation means differentiation over a spatial coordinate x_j (i.e., $v_{i,j} = \partial v_i / \partial x_j$, and $t_{(ij)}$ indicates the symmetric part of tensor t_{ij}). Based on conventional practice in geotechnical engineering, compression is set as positive.

The total stress equilibrium is required for a static system as listed below.

$$-\sigma_{ij,j} + \rho g_i = 0 \tag{C-4}$$

where g_i is the gravitational accelerator expressed by vector, and Einstein summation over a

repeated index is adopted.

The power input for the soils with volume V and a bounding area A is the sum of power input at boundary and the power done inside soils (i.e., the power associated with gravitational forces).

$$\int_V W dV = -\int_A \left[n\left(S_{lw}u^{lw}f_i^{lw} + S_{air}u^{air}f_i^{air}\right)\delta_{ij} + nS_{ice}P_{ij}^{ice}f_i^{ice} + (1-n)s_{ij}v_i + T_{ij}v_i^c\right]n_j dA + \int_V \left[n\left(S_{lw}\rho_{lw}f_i^{lw} + S_{air}\rho_{air}f_i^{air} + S_{ice}\rho_{ice}f_i^{ice}\right) + (1-n)\rho_s v_i\right]g_i dV \quad \text{(C-5)}$$

where f^{lw}, f^{air}, and f^{ice} are average velocities of pore-liquid-water, pore-air, and pore-ice, respectively.

Eq. (C-6) can be obtained by substituting Eqs. (C-1) and (C-2) into Eq. (C-5), which is given below.

$$\int_V W dV = -\int_A \left\{n\left[S_{lw}u^{lw}(f_i^{lw} - v_i) + S_{air}u^{air}(f_i^{air} - v_i)\right]\delta_{ij} + nS_{ice}P_{ij}^{ice}(f_i^{ice} - v_i) + \sigma_{ij}v_i + T_{ij}(v_i^c - v_i)\right\}n_j dA + \int_V \left\{n\left[S_{lw}\rho_{lw}(f_i^{lw} - v_i) + S_{air}\rho_{air}(f_i^{air} - v_i) + S_{ice}\rho_{ice}(f_i^{ice} - v_i)\right] + \rho v_i\right\}g_i dV \quad \text{(C-6)}$$

Eq. (C-7) can be derived by applying the Gauss divergence theorem (i.e., $\int_A y n_i dA = \int_V y_{,i} dV$).

$$\int_V W dV = \int_V - \left\{n\left[S_{lw}u^{lw}(f_i^{lw} - v_i) + S_{air}u^{air}(f_i^{air} - v_i)\right]\delta_{ij} + nS_{ice}P_{ij}^{ice}(f_i^{ice} - v_i) + \sigma_{ij}v_i + T_{ij}(v_i^c - v_i)\right\}_{,j} + n\left[S_{lw}\rho_{lw}(f_i^{lw} - v_i) + S_{air}\rho_{air}(f_i^{air} - v_i) + S_{ice}\rho_{ice}(f_i^{ice} - v_i)\right]g_i + \rho v_i g_i dV \quad \text{(C-7)}$$

For the term associated with surface tension, T_{ij} in Eq. (C-7), the forces acting on the interfaces will be equal if the system is in an equilibrium condition. If the system has mass exchange with external environment, v^c - v = 0 can be assumed, provided the interfaces have no power input to the system. The arbitrary volume V, the integral on both sides of Eq. (C-7) should therefore be equal. Expanding Eq. (C-7) leads to the following Eq. (C-8).

$$W = -\{n[S_{lw}u_{,j}^{lw}(f_j^{lw} - v_j) + S_{lw}u^{lw}\delta_{ij}(f_{j,j}^{lw} - v_{j,j}) + S_{air}u_{,j}^{air}(f_j^{air} - v_j) + S_{air}u^{air}\delta_{ij}(f_{j,j}^{air} - v_{j,j})] + S_{ice}P_{ij,j}^{ice}(f_i^{ice} - v_i) + S_{ice}P_{ij}^{ice}(f_{i,j}^{ice} - v_{i,j}) + \sigma_{ij,j}v_i + \sigma_{ij}v_{i,j}\} + n[S_{lw}\rho_{lw}(f_i^{lw} - v_i) + S_{air}\rho_{air}(f_i^{air} - v_i) + S_{ice}\rho_{ice}(f_i^{ice} - v_i)]g_i + \rho v_i g_i \quad \text{(C-8)}$$

For a quasi-static system (i.e., in which the flow of pore-liquid-water, pore-air, and pore-ice is negligible), the total stress equilibrium (i.e., Eq. (C-4)) can be applied to Eq. (C-8).

The following Eq. (C-9) can be derived extending these criteria.

$$W = -\{n[S_{lw}u_{,j}^{lw}(f_j^{lw} - v_j) + S_{lw}u^{lw}\delta_{ij}(f_{j,j}^{lw} - v_{j,j}) + S_{air}u_{,j}^{air}(f_j^{air} - v_j) + S_{air}u^{air}\delta_{ij}(f_{j,j}^{air} - v_{j,j})] + S_{ice}P_{ij,j}^{ice}(f_i^{ice} - v_i) + S_{ice}P_{ij}^{ice}(f_{i,j}^{ice} - v_{i,j}) + \sigma_{ij}v_{i,j}\} + n[S_{lw}\rho_{lw}(f_i^{lw} - v_i) + S_{air}\rho_{air}(f_i^{air} - v_i) + S_{ice}\rho_{ice}(f_i^{ice} - v_i)]g_i \quad \text{(C-9)}$$

A suitable definition for the compressibility of each phase is expressed below.

$$\int_A \rho_s(1-n)v_i n_i dA = -\int_V \frac{\partial}{\partial t}(\rho_s(1-n))dV \quad \text{(C-10)}$$

$$\int_A \rho_{lw} n S_{lw} f_i^{lw} n_i dA = -\int_V \frac{\partial}{\partial t}(\rho_{lw} n S_{lw})dV \quad \text{(C-11)}$$

$$\int_A \rho_{air} n S_{air} f_i^{air} n_i dA = -\int_V \frac{\partial}{\partial t}(\rho_{air} n S_{air})dV \quad \text{(C-12)}$$

The following relationships that are consistent with Houlsby (1997) can be derived by applying Gauss divergence theorem to the left sides of above equations.

$$v_{i,i} = \frac{\dot{n}}{1-n} \quad \text{(C-13)}$$

$$f_{i,i}^{lw} = -\frac{\dot{\rho}_{lw}}{\rho_{lw}} - \frac{\dot{n}}{n} - \frac{\dot{S}_{lw}}{S_{lw}} \quad \text{(C-14)}$$

$$f_{i,i}^{air} = -\frac{\dot{\rho}_{air}}{\rho_{air}} - \frac{\dot{n}}{n} - \frac{\dot{S}_{air}}{S_{air}} \quad \text{(C-15)}$$

where $v_{i,i} = -\dot{\varepsilon}_{ii}$, $\dot{\varepsilon}_{ii} = \delta_{ij}\dot{\varepsilon}_v$. Here, $\dot{\varepsilon}_{ii}$ specifies to each element in the tensor rather than summation over repeated index, and $\dot{\varepsilon}_v$is the rate of volumetric strain (ε_v is a scalar).

The definition of $\dot{\varepsilon}_{ii}$ is slightly different from traditional notation for convenience in

computations. In Eq. (C-14), the density of liquid water is set as a variable due to the variation of temperature in unsaturated frozen soils. By substituting the three equations in Eqs. (C-13), (C-14), and (C-15) into Eq. (C-9), the following Eq. (C-16) can be obtained.

$$W = -n\left[S_{lw}\left(u_{,j}^{lw} - \rho_{lw}g_i\right)\left(f_j^{lw} - v_j\right) + S_{air}\left(u_{,j}^{air} - \rho_{ice}g_i\right)\left(f_j^{air} - v_j\right)\right] + n\left(S_{lw}u^{lw}\delta_{ij}\frac{\dot{\rho}_{lw}}{\rho_{lw}} + S_{air}u^{air}\delta_{ij}\frac{\dot{\rho}_{air}}{\rho_{air}}\right) + n\left(\dot{S}_{lw}u^{lw}\delta_{ij} + \dot{S}_{air}u^{air}\delta_{ij}\right) - \left(S_{lw}u^{lw}\delta_{ij} + S_{air}u^{air}\delta_{ij}\right)\dot{\varepsilon}_{jj} + \sigma_{ij}\dot{\varepsilon}_{ij} - nS_{ice}\left[\left(P_{ij,j}^{ice} - \rho_{ice}g_i\right)\left(f_i^{ice} - v_i\right)\right] - nS_{ice}P_{ij}^{ice}\left(f_{i,j}^{ice} - v_{i,j}\right) \quad \text{(C-16)}$$

Eq. (C-17) can be applied for unsaturated frozen soils; however, the last three terms need careful evaluation. To estimate the role of the last term in Eq. (C-16), let us consider the compressibility of pore-ice, first. Similar to Eqs. (C-14) and (C-15), if the rate of pore-ice flow outside the volume is equal to the rate of variation of pore-ice, the following Eq. (C-17) can be established.

$$\int_A \rho_{ice}nS_{ice}f_i^{ice}n_j dA = -\int_V \frac{\partial}{\partial t}(\rho_{ice}nS_{ice})dV \quad \text{(C-17)}$$

Eq. (C-18) can be derived by applying the Gauss divergence theorem to the left side of Eq. (C-17).

$$f_{i,j}^{ice} = -\frac{\dot{\rho}_{ice}}{\rho_{ice}} - \frac{\dot{n}}{n} - \frac{\dot{S}_{ice}}{S_{ice}} \quad \text{(C-18)}$$

Eq. (C-19) can be obtained by substituting Eq. (C-18) into Eq. (C-17).

$$nS_{ice}P_{ij}^{ice}\left(f_{i,j}^{ice} - v_{i,j}\right) = -P_{ij}^{ice}\left(nS_{ice}\frac{\dot{\rho}_{ice}}{\rho_{ice}} + S_{ice}\dot{n} + n\dot{S}_{ice} + nS_{ice}v_{i,j}\right) \quad \text{(C-19)}$$

Eq. (C-20) can be derived by substituting Eqs. (C-3) and (C-13) into Eq. (C-19).

$$nS_{ice}P_{ij}^{ice}\left(f_{i,j}^{ice} - v_{i,j}\right) = -P_{ij}^{ice}\left(nS_{ice}\frac{\dot{\rho}_{ice}}{\rho_{ice}} - (1-n)S_{ice}\dot{\varepsilon}_{ii} + n\dot{S}_{ice} - nS_{ice}\dot{\varepsilon}_{ij}\right) = -P_{ij}^{ice}\left[nS_{ice}\frac{\dot{\rho}_{ice}}{\rho_{ice}} - S_{ice}\dot{\varepsilon}_{ii} - nS_{ice}\left(\dot{\varepsilon}_{ij} - \dot{\varepsilon}_{ii}\right) + n\dot{S}_{ice}\right] \quad \text{(C-20)}$$

By substituting Eq. (C-20) into Eq. (C-16) and rearranging Eq. (C-16), Eq. (C-21) can be

obtained.

$$W = -n\left[S_{lw}\left(u_{,j}^{lw} - \rho_{lw}g_i\right)\left(f_j^{lw} - v_j\right) + S_{air}\left(u_{,j}^{air} - \rho_{ice}g_i\right)\left(f_j^{air} - v_j\right) + S_{ice}\left(P_{ij,j}^{ice} - \rho_{ice}g_i\right)\left(f_i^{ice} - v_i\right)\right] + n\left(S_{lw}u^{lw}\delta_{ij}\frac{\dot{\rho}_{lw}}{\rho_{lw}} + S_{air}u^{air}\delta_{ij}\frac{\dot{\rho}_{air}}{\rho_{air}} + S_{ice}P_{ij}^{ice}\frac{\dot{\rho}_{ice}}{\rho_{ice}}\right) + n\left(\dot{S}_{lw}u^{lw}\delta_{ij} + \dot{S}_{air}u^{air}\delta_{ij} + \dot{S}_{ice}P_{ij}^{ice}\right) - \left(S_{lw}u^{lw}\delta_{ij} + S_{air}u^{air}\delta_{ij} + S_{ice}P_{ij}^{ice}\right)\dot{\varepsilon}_{jj} + \sigma_{ij}\dot{\varepsilon}_{ij} - nS_{ice}P_{ij}^{ice}\left(\dot{\varepsilon}_{ij} - \dot{\varepsilon}_{jj}\right) \quad \text{(C-21)}$$

Eq. (C-21) can be written in four parts, namely, $W = W_1 + W_2 + W_3 + W_4$. The four different parts are expressed below.

$$W_1 = -n\left[S_{lw}\left(u_{,j}^{lw} - \rho_{lw}g_i\right)\left(f_j^{lw} - v_j\right) + S_{air}\left(u_{,j}^{air} - \rho_{ice}g_i\right)\left(f_j^{air} - v_j\right) + S_{ice}\left(P_{ij,j}^{ice} - \rho_{ice}g_i\right)\left(f_i^{ice} - v_i\right)\right] \quad \text{(C-22)}$$

$$W_2 = n\left(S_{lw}u^{lw}\delta_{ij}\frac{\dot{\rho}_{lw}}{\rho_{lw}} + S_{air}u^{air}\delta_{ij}\frac{\dot{\rho}_{air}}{\rho_{air}} + S_{ice}P_{ij}^{ice}\frac{\dot{\rho}_{ice}}{\rho_{ice}}\right) \quad \text{(C-23)}$$

$$W_3 = n\left(\dot{S}_{lw}u^{lw}\delta_{ij} + \dot{S}_{air}u^{air}\delta_{ij} + \dot{S}_{ice}P_{ij}^{ice}\right) \quad \text{(C-24)}$$

$$W_4 = -\left(S_{lw}u^{lw}\delta_{ij} + S_{air}u^{air}\delta_{ij} + S_{ice}P_{ij}^{ice}\right)\dot{\varepsilon}_{jj} + \sigma_{ij}\dot{\varepsilon}_{ij} - nS_{ice}P_{ij}^{ice}\left(\dot{\varepsilon}_{ij} - \dot{\varepsilon}_{jj}\right) \quad \text{(C-25)}$$

The meaning of the first three parts of the equation is well defined. However, the fourth part needs further discussion, which is provided with the aid of other equations. This is achieved by rewriting Eq. (C-25) in the form as shown in Eq. (C-26).

$$W_4 = -\left(S_{lw}u^{lw}\delta_{ij} + S_{air}u^{air}\delta_{ij} + S_{ice}P_{ij}^{ice}\right)\dot{\varepsilon}_{jj} + \sigma_{ij}\left(\dot{\varepsilon}_{ij} - \dot{\varepsilon}_{jj} + \dot{\varepsilon}_{jj}\right) - nS_{ice}P_{ij}^{ice}\left(\dot{\varepsilon}_{ij} - \dot{\varepsilon}_{jj}\right) \quad \text{(C-26)}$$

Eq. (C-27) can be obtained by rearranging Eq. (C-26), which is given below.

$$W_4 = \left[\sigma_{ij} - \left(S_{lw}u^{lw}\delta_{ij} + S_{air}u^{air}\delta_{ij} + S_{ice}P_{ij}^{ice}\right)\right]\dot{\varepsilon}_{jj} + \left(\sigma_{ij} - nS_{ice}P_{ij}^{ice}\right)\left(\dot{\varepsilon}_{ij} - \dot{\varepsilon}_{jj}\right) \quad \text{(C-27)}$$

Based on Eq. (C-27), the effective stress $\boldsymbol{\sigma}'$ can be written as Eq. (C-28).

$$\sigma_{ij}' = \sigma_{ij} - \left(nS_{ice}P_{ij}^{ice}\right)_{i\neq j} - \left(S_{lw}u^{lw}\delta_{ij} + S_{air}u^{air}\delta_{ij} + S_{ice}P_{ij}^{ice}\right)_{i=j} \quad \text{(C-28)}$$

Eq. (C-29) can be obtained, by taking account of the deviatoric stress acting on pore-ice as a part of soil solids.

$$\sigma'_{ij} = \sigma_{ij} - \left(S_{lw}u^{lw}\delta_{ij} + S_{air}u^{air}\delta_{ij} + S_{ice}P_{ij}^{ice}\right) \quad \text{(C-29)}$$

Further, if the stress (deviatoric and isotropic stresses) acting on pore-ice is included as a part of soil solids, Eq. (C-30) can be obtained.

$$\sigma'_{ij} = \sigma_{ij} - \left(S_{lw}u^{lw} + S_{air}u^{air}\right)\delta_{ij} \quad \text{(C-30)}$$

Studies by several researchers suggest equations that are similar in form as Eq. (C-30) have limitations in explaining the behavior of unsaturated soils (Jennings and Burland, 1962; Bishop and Blight, 1963; Fredlund & Morgenstern, 1977). However, this limitation can be alleviated by extending the independent stress state variables approach.

5.9 Appendix D

The total stress $\boldsymbol{\sigma}$ can be defined as the summation of stresses of each part (i.e., $\boldsymbol{\sigma}_a$ in Eq. (D-1)).

$$\boldsymbol{\sigma} = \sum_{\alpha=sp,lw,air,ice} \theta_\alpha \boldsymbol{\sigma}_\alpha \quad \text{(D-1)}$$

The relationships between fluid stresses and the corresponding fluid pressures $\boldsymbol{P}_\alpha$ ($\alpha = lw, air$) for pore-liquid water and pore-air are listed in Eq. (D-2).

$$\boldsymbol{\sigma}_\alpha = P_\alpha \boldsymbol{\delta} \quad (\alpha = lw, air) \quad \text{(D-2)}$$

Similarly, the total density ρ can be written as sum of densities for each component as shown in following Eq. (D-3).

$$\rho = \sum_{\alpha=sp,lw,air,ice} \theta_\alpha \rho_\alpha \quad \text{(D-3)}$$

The mass balance for single phase can be written as Eqs. (D-4).

$$\frac{d}{dt}(\theta_\alpha \rho_\alpha) + \theta_\alpha \rho_\alpha \mathrm{div}\boldsymbol{v}_\alpha = \zeta_\alpha \quad (\alpha = sp, lw, air, ice) \quad \text{(D-4)}$$

where t is time, div is divergence of velocity vector $\boldsymbol{v}_\alpha$, and ζ_α is the mass supply to phase α from other phases. Eq. (D-5) holds for mass conservation of the soil system by neglecting the mass exchange from soil solid grains (i.e., $\zeta_{sp} = 0$).

$$\sum_{\alpha=lw,air,ice} \zeta_\alpha \equiv 0 \tag{D-5}$$

The bulk modulus K_α for phase α can be defined as Eq. (D-6)

$$K_\alpha = \rho_\alpha \frac{dP_\alpha}{d\rho_\alpha} \quad (\alpha = sp, lw, air, ice) \tag{D-6}$$

where P_α refers to as isotropic pressure value (scalar) for each phase.

Eq. (D-7) can be obtained by substituting Eq. (D-6) into Eq. (D-4).

$$\frac{d\theta_\alpha}{dt} + \frac{\theta_\alpha}{K_\alpha}\frac{dP_\alpha}{dt} + \theta_\alpha \mathrm{div}\left(\boldsymbol{v}_\alpha - \boldsymbol{v}_{sp}\right) + \theta_\alpha \mathrm{div}\left(\boldsymbol{v}_{sp}\right) = \frac{\zeta_\alpha}{\rho_\alpha} \quad (\alpha = sp, lw, air, ice) \tag{D-7}$$

Here, $\zeta_{sp} = 0$ as mentioned in Eq. (D-5). The work input to the unsaturated frozen soil can be written as following Eq. (D-8).

$$W = \sum \mathrm{tr}(\boldsymbol{\sigma}_\alpha \cdot \mathrm{grad}\, \boldsymbol{v}_\alpha) = \mathrm{tr}\left(\theta_{sp}\boldsymbol{\sigma}_{sp} \cdot \mathrm{grad}\, \boldsymbol{v}_{sp}\right) + \mathrm{tr}(\theta_{lw}\boldsymbol{\sigma}_{lw} \cdot \mathrm{grad}\, \boldsymbol{v}_{lw}) + \mathrm{tr}(\theta_{\alpha ir}\boldsymbol{\sigma}_{air} \cdot \mathrm{grad}\, \boldsymbol{v}_{air}) + \mathrm{tr}(\theta_{ice}\boldsymbol{\sigma}_{ice} \cdot \mathrm{grad}\, \boldsymbol{v}_{ice}) = \mathrm{tr}\left((\boldsymbol{\sigma} - \theta_{lw}\boldsymbol{\sigma}_{lw} - \theta_{\alpha ir}\boldsymbol{\sigma}_{air} - \theta_{ice}\boldsymbol{\sigma}_{ice}) \cdot \mathrm{grad}\, \boldsymbol{v}_{sp}\right) + \mathrm{tr}(\theta_{lw}\boldsymbol{\sigma}_{lw} \cdot \mathrm{grad}\, \boldsymbol{v}_{lw}) + \mathrm{tr}(\theta_{\alpha ir}\boldsymbol{\sigma}_{air} \cdot \mathrm{grad}\, \boldsymbol{v}_{air}) + \mathrm{tr}(\theta_{ice}\boldsymbol{\sigma}_{ice} \cdot \mathrm{grad}\, \boldsymbol{v}_{ice}) \tag{D-8}$$

The term, $\boldsymbol{\sigma}_{ice}$ which is defined as stress acting on pore-ice has two components in comparison of fluid pressures (pore-liquid water and -air) as shown in Eq. (D-9)

$$\boldsymbol{\sigma}_{ice} = \boldsymbol{q}_{ice} + P_{ice}\boldsymbol{\delta} \tag{D-9}$$

where $\boldsymbol{q}_{ice}$ is deviatoric stress loaded by pore ice. By substituting Eqs. (D-2) and (D-9) into Eq. (D-8), the following Eq. (D-10) can be obtained.

$$W = \mathrm{tr}\left((\boldsymbol{\sigma} - \theta_{ice}\boldsymbol{q}_{ice}) \cdot \mathrm{grad}\, \boldsymbol{v}_{sp}\right) + \mathrm{tr}\left(\theta_{lw}P_{lw}\boldsymbol{\delta} \cdot \mathrm{grad}\left(\boldsymbol{v}_{lw} - \boldsymbol{v}_{sp}\right)\right) + \mathrm{tr}\left(\theta_{air}P_{air}\boldsymbol{\delta} \cdot \mathrm{grad}\left(\boldsymbol{v}_{air} - \boldsymbol{v}_{sp}\right)\right) + \mathrm{tr}\left(\theta_{ice}P_{ice}\boldsymbol{\delta} \cdot \mathrm{grad}\left(\boldsymbol{v}_{ice} - \boldsymbol{v}_{sp}\right)\right) \quad \text{(D-10)}$$

Note $\theta_\alpha P_\alpha$ (α = liquid water, air, ice) is scalar and with Eq. (D-11), the above equation can be simplified as Eq. (D-12).

$$\mathrm{tr}(\mathrm{grad}\,(\boldsymbol{v}_\alpha) \cdot \boldsymbol{\delta}\,) = \mathrm{div}\,(\boldsymbol{v}_\alpha) \quad \text{(D-11)}$$

$$W = \mathrm{tr}\left((\boldsymbol{\sigma} - \theta_{ice}\boldsymbol{q}_{ice}) \cdot \mathrm{grad}\, \boldsymbol{v}_{sp}\right) + \theta_{lw}P_{lw}\,\mathrm{div}\left(\boldsymbol{v}_{lw} - \boldsymbol{v}_{sp}\right) + \theta_{air}P_{air}\mathrm{div}\left(\boldsymbol{v}_{air} - \boldsymbol{v}_{sp}\right) + \theta_{ice}P_{ice}\mathrm{div}\left(\boldsymbol{v}_{ice} - \boldsymbol{v}_{sp}\right) \quad \text{(D-12)}$$

Eq. (D-13) can be obtained by substituting Eq. (D-7) into Eq. (D-12).

$$W = \mathrm{tr}\left((\boldsymbol{\sigma} - \theta_{ice}\boldsymbol{q}_{ice}) \cdot \mathrm{grad}\, \boldsymbol{v}_{sp}\right) + \left[P_{lw}\frac{\zeta_{lw}}{\rho_{lw}} - P_{lw}\theta_{lw}\mathrm{div}(\boldsymbol{v}_{sp}) - P_{lw}\frac{d\theta_{lw}}{dt} - P_{lw}\frac{\theta_{lw}}{K_{lw}}\frac{dP_{lw}}{dt}\right] + \left[P_{air}\frac{\zeta_{air}}{\rho_{air}} - P_{air}\theta_{air}\mathrm{div}(\boldsymbol{v}_{sp}) - P_{air}\frac{d\theta_{air}}{dt} - P_{air}\frac{\theta_{air}}{K_{air}}\frac{dP_{air}}{dt}\right] + \left[P_{ice}\frac{\zeta_{ice}}{\rho_{ice}} - P_{ice}\theta_{ice}\mathrm{div}(\boldsymbol{v}_{sp}) - P_{ice}\frac{d\theta_{ice}}{dt} - P_{ice}\frac{\theta_{ice}}{K_{ice}}\frac{dP_{ice}}{dt}\right] \quad \text{(D-13)}$$

Eq. (D-13) can be rearranged as a sum of four parts as shown in Eq. (D-14).

$$W = \sum_{i=1}^{5} W_i = \begin{cases} W_1 = \mathrm{tr}\left((\boldsymbol{\sigma} - \theta_{ice}\boldsymbol{q}_{ice}) \cdot \mathrm{grad}\, \boldsymbol{v}_{sp}\right) \\ W_2 = -P_{lw}\frac{\theta_{lw}}{K_{lw}}\frac{dP_{lw}}{dt} - P_{air}\frac{\theta_{air}}{K_{air}}\frac{dP_{air}}{dt} - P_{ice}\frac{\theta_{ice}}{K_{ice}}\frac{dP_{ice}}{dt} \\ W_3 = -P_{lw}\frac{d\theta_{lw}}{dt} - P_{air}\frac{d\theta_{air}}{dt} - P_{ice}\frac{d\theta_{ice}}{dt} \\ W_4 = -P_{lw}\theta_{lw}\mathrm{div}(\boldsymbol{v}_{sp}) - P_{air}\theta_{air}\mathrm{div}(\boldsymbol{v}_{sp}) - P_{ice}\theta_{ice}\mathrm{div}(\boldsymbol{v}_{sp}) \\ W_5 = P_{lw}\frac{\zeta_{lw}}{\rho_{lw}} + P_{air}\frac{\zeta_{air}}{\rho_{air}} + P_{ice}\frac{\zeta_{ice}}{\rho_{ice}} \end{cases} \quad \text{(D-14)}$$

W_3 in Eq. (D-14) can be written as Eq. (D-15).

$$W_3 = -P_{lw}\frac{d\theta_{lw}}{dt} - P_{air}\frac{d\theta_{air}}{dt} - P_{ice}\frac{d\theta_{ice}}{dt} = -P_{lw}\frac{d(nS_{lw})}{dt} - P_{air}\frac{d(nS_{air})}{dt} - P_{ice}\frac{d(nS_{ice})}{dt} = -P_{lw}\frac{d(n(S_{lw}+S_{ice}-S_{ice}))}{dt} - P_{air}\frac{d(n(1-S_{lw}-S_{ice}))}{dt} - P_{ice}\frac{d(nS_{ice})}{dt} = -n\left[(P_{lw} - P_{air})\frac{d(S_{lw}+S_{ice})}{dt} +\right.$$

$$(P_{ice} - P_{lw})\frac{dS_{ice}}{dt}\Big] - \Big[P_{lw}S_{lw}\frac{dn}{dt} + P_{air}S_{air}\frac{dn}{dt} + P_{ice}S_{ice}\frac{dn}{dt}\Big] \quad \text{(D-15)}$$

W_4 in Eq. (D-14) can be written as Eq. (D-16).

$$W_4 = -P_{lw}\theta_{lw}\mathrm{div}(\boldsymbol{v}_{sp}) - P_{air}\theta_{air}\mathrm{div}(\boldsymbol{v}_{sp}) - P_{ice}\theta_{ice}\mathrm{div}(\boldsymbol{v}_{sp}) = -(1-\theta_{sp})(P_{lw}S_{lw} + P_{air}S_{air} + P_{ice}S_{ice})\mathrm{div}(\boldsymbol{v}_{sp}) = -(P_{lw}S_{lw} + P_{air}S_{air} + P_{ice}S_{ice})\mathrm{div}(\boldsymbol{v}_{sp}) - (P_{lw}S_{lw} + P_{air}S_{air} + P_{ice}S_{ice})\left(\frac{d\theta_{sp}}{dt} + \frac{\theta_{sp}}{K_{sp}}\frac{dP_{sp}}{dt}\right) = -\mathrm{tr}\left((P_{lw}S_{lw} + P_{air}S_{air} + P_{ice}S_{ice})\boldsymbol{\delta}\cdot\mathrm{grad}\,\boldsymbol{v}_{sp}\right) + (P_{lw}S_{lw} + P_{air}S_{air} + P_{ice}S_{ice})\frac{dn}{dt} - (P_{lw}S_{lw} + P_{air}S_{air} + P_{ice}S_{ice})\frac{\theta_{sp}}{K_{sp}}\frac{dP_{sp}}{dt} \quad \text{(D-16)}$$

Eq. (D-17) can be obtained by substituting Eqs. (D-15) and (D-16) into Eq. (D-14).

$$W = \mathrm{tr}\left((\boldsymbol{\sigma} - \theta_{ice}\boldsymbol{q}_{ice} - (P_{lw}S_{lw} + P_{air}S_{air} + P_{ice}S_{ice})\boldsymbol{\delta})\cdot\mathrm{grad}\,\boldsymbol{v}_{sp}\right) - n\Big[(P_{lw} - P_{air})\frac{d(S_{lw}+S_{ice})}{dt} + (P_{ice} - P_{lw})\frac{dS_{ice}}{dt}\Big] - \Big[(P_{lw}S_{lw} + P_{air}S_{air} + P_{ice}S_{ice})\frac{\theta_{sp}}{K_{sp}}\frac{dP_{sp}}{dt} + \Big(P_{lw}\frac{\theta_{lw}}{K_{lw}}\frac{dP_{lw}}{dt} + P_{air}\frac{\theta_{air}}{K_{air}}\frac{dP_{air}}{dt} + P_{ice}\frac{\theta_{ice}}{K_{ice}}\frac{dP_{ice}}{dt}\Big)\Big] + \Big(P_{lw}\frac{\zeta_{lw}}{\rho_{lw}} + P_{air}\frac{\zeta_{air}}{\rho_{air}} + P_{ice}\frac{\zeta_{ice}}{\rho_{ice}}\Big) \quad \text{(D-17)}$$

The bulk moduli of soil solid particles, pore-liquid-water, and pore-ice are negligible in comparison to the bulk modulus of air (i.e., Eqs. (D-18)).

$$\begin{cases}\frac{1}{K_{air}} = \frac{1}{K_{air}} \\ \frac{1}{K_\alpha} \cong 0 \quad (\alpha = sp, lw, ice)\end{cases} \quad \text{(D-18)}$$

Eq. (D-18) and Eq. (D-17) can be simplified as Eq. (D-19).

$$W = \mathrm{tr}\left((\boldsymbol{\sigma} - \theta_{ice}\boldsymbol{q}_{ice} - (P_{lw}S_{lw} + P_{air}S_{air} + P_{ice}S_{ice})\boldsymbol{\delta})\cdot\mathrm{grad}\,\boldsymbol{v}_{sp}\right) - n\Big[(P_{lw} - P_{air})\frac{d(S_{lw}+S_{ice})}{dt} + (P_{ice} - P_{lw})\frac{dS_{ice}}{dt}\Big] - \Big(P_{air}\frac{\theta_{air}}{K_{air}}\frac{dP_{air}}{dt}\Big) + \Big(P_{lw}\frac{\zeta_{lw}}{\rho_{lw}} + P_{air}\frac{\zeta_{air}}{\rho_{air}} + P_{ice}\frac{\zeta_{ice}}{\rho_{ice}}\Big) \quad \text{(D-19)}$$

Eq. (D-19) can be modified to take the form of effective stress $\boldsymbol{\sigma}'$ that can be mathematically represented as Eq. (D-20). Eq. (D-20) is the same equation as obtained by other methods in this

study. However, if pore-ice stress is treated as a part of soil solid, Eq. (D-20) can be extended to Eq. (D-21), which is the same equation obtained in the literature (Xu et al., 2020).

$$\boldsymbol{\sigma}' = \boldsymbol{\sigma} - \theta_{ice}\boldsymbol{q}_{ice} - (\boldsymbol{P}_{lw}S_{lw} + \boldsymbol{P}_{air}S_{air} + \boldsymbol{P}_{ice}S_{ice}) \quad \text{(D-20)}$$

$$\boldsymbol{\sigma}' = \boldsymbol{\sigma} - (\boldsymbol{P}_{lw}(S_{lw} - S_{ice}) + \boldsymbol{P}_{air}S_{air}) \quad \text{(D-21)}$$

This appendix has similarities as the framework summarized in the literature (Borja, 2006; Zhao et al., 2010; Xu et al., 2020). However, the approach summarized in this appendix regards pore-ice similar to soil solids in comparison with the Xu et al., 2020 model.

5.10 List of symbols

a_{fx}, n_{fx}, and m_{fx}	model parameters in Fredlund and Xing model (Fredlund and Xing, 1994)
a_{vg}, n_{vg}, and m_{vg}	model parameters in van Genuchten model (van Genuchten, 1980)
A, A_{lv}, and B	positive model parameters in the study
$A_{lv,ref}$ *and* A_{ref}	model parameters at reference state
G, F, H, U, and Φ_G	Gibbs free energy, Helmholtz free energy, enthalpy, internal energy, the grand potential, respectively
L_A	the specific latent heat
m	mass
M_{lw}	the molar mass of water
n	porosity of soils
N	total number of substances
N_i, μ_i, and c_i	the number, the chemical potential, and the concentration of the ith substances, respectively
P_{atm}	the standard atmosphere pressure
$P_{lw,0}$	the initial pore-water pressure
Q_{rev}	the heat transfer in reversible process
r	the pore radius
R	the universal gas constant
S_{lw}	degree of saturation
S_{obv} and S_{cal}	the observed and the calculated degree of saturations, respectively
$\bar{S}_{obv}$ and $\bar{S}_{cal}$	the average values of the observed and the calculated degree of

	saturations, respectively.
S_{sat} and S_{res}	saturated and residual degree of saturation, respectively
S_{ufw}	unfrozen water content
T_{f0} and $P_{lw,0}$	initial freezing temperature and the pore liquid water pressure at this point, respectively
T_{ff0}	freezing temperature at residual degree of saturation
V, P, S^E, and T	volume, pressure, entropy, and temperature, respectively. And the subscripts lw, ice, and air represent the values for pore -water, -ice, and -air, respectively
$V_{lw,0}$ and $S_{lw,0}$	initial volume and initial degree of saturation of water before freezing, respectively
$w_{lw,ini}$	the initial water content
ΔV and Δv	volume and specific volume difference in phase change, respectively
γ_{iw} and γ_{wa}	the ice-liquid water and pore water-air interfacial free energies, respectively
λ_{bc}	model parameter in Brooks and Corey model (Brooks and Corey, 1964)
λ_{km}	the ratio of soil matric suction over cryogenic pressure (Koopmans and Miller, 1966)
μ_i and N_i	chemical potential and the number of particles of the i-th substance, respectively
μ_i*	standard chemical potential
ξ_{ini}	a model parameter for evaluating initial water content effect
ρ_{lw} and ρ_{ice}	densities of pore liquid water and pore ice, respectively
ψ	soil suction
ψ_{AEV}	air-entry value

CHAPTER 6

Conclusions and Future Work

6.1 Major conclusions

The major conclusions from the undertaken PhD research work are summarized in this section.

6.1.1 Major conclusions from research contents summarized in Chapter 3

In Chapter 3, a reasonable hypothesis is introduced based on the features of pore-size distribution (PoSD) curve for predicting the bimodal soil-water characteristic curve (SWCC). Volumetric water content relationships corresponding to the macropores and micropores in the PoSD curve for bimodal SWCC were developed extending this hypothesis. Two sets of bimodal SWCC equations are successfully derived from the traditional unimodal SWCC equations: namely, van Genuchten (1980) and Fredlund and Xing (1994) equations.

In addition, the calibration processes for the proposed equations are built. A graphical construction method and regression method are separately developed to estimate the key features for bimodal SWCC. The two parameters (i.e., pore size influence factor, α_H and best-fit smoothening parameter λ_β) were used as tools to evaluate the contribution of the micropores and macropores. Rational description of the bimodal SWCC is possible using the proposed bimodal SWCC equations.

6.1.2 Major conclusions from research contents summarized in Chapter 4

In Chapter 4, a new model (i.e., Eqs. (4.11)) is proposed for predicting main wetting SWCC curve the from main drying curve. The wetting SWCC along with its hysteretic features were predicted for a variety of soils using simple equations based on the PoSD curve that were linked to the well-known SWCC fitting equations and a set of boundary conditions. Three methods for predicting scanning curves as well as the corresponding calibration processes are derived for coarse-grained soils (i.e., Eqs. (4.15), (4.17) and (4.19)). Comprehensive comparisons were provided using these equations, between the experimental results and the predicted SWCCs of both coarse-grained soils.

In addition, the SWCCs of fine-grained soils were successfully predicted taking account of the influence of stress state and soil structure associated with different initial water contents (i.e. Eqs. (4.31)). The multi-parametric influences for modelling SWCCs are also evaluated and

discussed (i.e., Eq. (4.34)) and a modified SWCC model (i.e., Eq. (4.37)) is proposed based on van Genuchten equation.

6.1.3 Major conclusions from research contents summarized in Chapter 5

In Chapter 5, novel equations for SFCCs (i.e., Eqs. (5.22) and (5.25)) are derived for modeling the THMC behaviors of unsaturated frozen soils. Each of the parameters in these models are well-defined and have physical meaning (e.g., Eqs. (5.26)) that can be explained using thermodynamics principles. The proposed models were validated using the published experimental results from the literature starting from the initial freezing point.

The hysteretic effects that influence the SFCC behavior are reasonably explained by the proposed pore water/ice volume and temperature relationship (i.e., Eqs. (5.26)). The distinguished zones in two branches of SFCCs (e.g., soil freezing and thawing curves) are comprehensively characterized with detailed explanation using the proposed models.

The salinity and initial water content effects on the SFCCs are also incorporated into the proposed models (i.e., Eqs. (5.37) and (5.41)). The proposed SFCC model is also capable of providing direct links with available SWCC models in the literature as shown in Eq. (5.42). The models proposed in this Chapter are valuable tools for modeling the influence of complex THMC behaviors of unsaturated soils extending thermodynamics principles.

6.2 Recommendations for future work

The framework developed in this PhD thesis is promising and can be used in the prediction and interpretation of the THMC behavior of unsaturated soils for all environments (i.e., for unfrozen and frozen unsaturated soils). The studies are particularly promising for modeling the unfrozen and frozen unsaturated soils considering the anticipated influence of climate changes associated with global warming. However, there is a need and opportunity to further the research undertaken in this PhD thesis.

Some recommendations for future research are summarized below.

(i) There is a limited understanding related to the solid skeleton stress for unsaturated unfrozen and frozen unsaturated soils using independent stress state variables. More fundamental research studies are required in this direction.

(ii) Research related to soil freezing characteristic curves (SFCCs) is rather limited in the literature. There is a need for proposing SFCC equations that can be used in modelling considering the influence of various environmental factors.

(iii) There is a need for proposing simple equations or relationships that can be useful for the SWCCs considering THMC effects.

(iv) There is an urgent need for developing constitutive models that can be useful for explaining behaviors of unsaturated soils addressing effects associated with climate change.

REFERENCES

Ahuja, L. R., Naney, J. W., and Williams, R. D. (1985). Estimating soil water characteristics from simpler properties or limited data. Soil Science Society of America Journal, 49(5), 1100-1105.

Aina, P. O., and Periaswamy, S. P. (1985). Estimating available water-holding capacity of western Nigerian soils from soil texture and bulk density, using core and sieved samples. Soil Science, 140(1), 55-58.

Alonso, E. E., Gens, A., and Josa, A. (1990). A constitutive model for partially saturated soils. Géotechnique, 40(3), 405-430.

Alonso, E.E., Pereira, J.M., Vaunat, J., and Olivella, S. (2010). A microstructurally based effective stress for unsaturated soils. Géotechnique, 60(12), 913-925.

Alves, R. D., Gitirana Jr, G. d. F. N., and Vanapalli, S. K. (2020). Advances in the modeling of the soil-water characteristic curve using pore-scale analysis. Computers and Geotechnics, 127, 103766.

Amanabadi, S., Vazirinia, M., Vereecken, H., Vakilian, K. A., and Mohammadi, M. H. (2020). Comparative study of statistical, numerical and machine learning-based pedotransfer functions of water retention curve with particle size distribution data. Eurasian Soil Science, 52(12), 1555-1571.

Antinoro, C., Bagarello, V., Ferro, V., Giordano, G., and Iovino, M. (2014). A simplified approach to estimate water retention for Sicilian soils by the Arya-Paris model. Geoderma, 213, 226-234.

Arya, L. M., and Paris, J. F. (1981). A physicoempirical model to predict the soil moisture characteristic from particle-size distribution and bulk density data. Soil Science Society of America Journal, 45(6), 1023-1030.

Arya, L. M. and Dierolf, T. S. 1992. Predicting soil moisture characteristics from particle-size distribution: An improved method to calculate pore radii from particle radii. In *Proceedings of the International Workshop on Indirect Methods for Estimating the Hydraulic Properties of Unsaturated Soils* (pp. 115-125). University of California Press, Riverside, CA.

Arya, L. M., Leij, F. J., van Genuchten, M. T., and Shouse, P. J. (1999). Scaling parameter to predict the soil water characteristic from particle-size distribution data. Soil Science Society of America Journal, 63(3), 510-519.

Arya, L. M., Bowman, D. C., Thapa, B. B., and Cassel, D. K. (2008). Scaling soil water characteristics of golf course and athletic field sands from particle-size distribution. Soil Science Society of America Journal, 72(1), 25-32.

Assouline, S., Tessier, D., and Bruand, A. (1998). A conceptual model of the soil water retention curve. Water Resources Research, 34(2), 223-231.

Aubertin, M., Bussiere, B., and Chapuis, R. P. (1996). Hydraulic conductivity of homogenized tailings from hard rock mines. Canadian Geotechnical Journal, 33(3), 470-482.

Bai, R. Q., Lai, Y. M., Zhang, M. Y., and Ren, J. G. (2020). Study on the coupled heat-water-vapor mechanics process of unsaturated soils. Journal of Hydrology, 585, 124784.

Bai, R. Q., Lai, Y. M., Zhang, M. Y., and Yu, F. (2018). Theory and application of a novel soil freezing characteristic curve. Applied Thermal Engineering, 129, 1106-1114.

Baker, L., and Ellison, D. (2008). Optimisation of pedotransfer functions using an artificial neural network ensemble method. Geoderma, 144(1-2), 212-224.

Banin, A., and Anderson, D. M., (1974). Effects of salt concentration changes during freezing on the unfrozen water content of porous materials. Water Resources Research, 10(1), 124-128.

Barbour, S. L., and Yang, N. (1993). A review of the influence of clay-brine interactions on the geotechnical properties of Ca-montmorillonitic clayey soils from western Canada. Canadian Geotechnical Journal, 30(6), 920-934.

Basile, A., and D'Urso, G. (1997). Experimental corrections of simplified methods for predicting water retention curves in clay-loamy soils from particle-size determination. Soil Technology, 10(3), 261-272.

Bird, N. R. A., Bartoli, F., and Dexter, A. R. (1996). Water retention models for fractal soil structures. European Journal of Soil Science, 47(1), 1-6.

Bird, N. R. A., Perrier, E., and Rieu, M. (2000). The water retention function for a model of soil structure with pore and solid fractal distributions. European Journal of Soil Science, 51(1), 55-63.

Bishop, A. W. (1959). The principle of effective stress. Teknik Ukeblad, 39, 859-863.

Bishop, A. W., and Blight, G. E. (1963). Some aspects of effective stress in saturated and partly saturated soils. Geotechnique, 13(3), 177-197.

Black, P. B., and Tice, A. R. (1989). Comparison of soil freezing curve and soil water curve data for Windsor sandy loam. Water Resources Research, 25(10), 2205-2210.

Bouma, J. (1989). Using soil survey data for quantitative land evaluation. In *Advances in Soil Science* (Vol. 9, pp. 177-213). Springer Verlag, New York.

Borja, R.I. (2006). On the mechanical energy and effective stress in saturated and unsaturated porous continua. International Journal of Solids and Structures, 43(6), 1764-1786.

Børgesen, C. D., and Schaap, M. G. (2005). Point and parameter pedotransfer functions for water retention predictions for Danish soils. Geoderma, 127(1-2), 154-167.

Børgesen, C. D., Iversen, B. V., Jacobsen, O. H., and Schaap, M. G. (2008). Pedotransfer functions estimating soil hydraulic properties using different soil parameters. Hydrological Processes, 22(11), 1630-1639.

Brakensiek, D. L. (1977). Estimating the effective capillary pressure in the Green and Ampt infiltration equation. Water Resources Research, 13(3), 680-682.

Brakensiek, D. L., Engleman, R. L., and Rawls, W. J. (1981). Variation within texture classes of soil water parameters. Transactions of the ASAE, 24(2), 0335-0339.

Brooks, R. H., and Corey, A. T. (1964). Hydraulic properties of porous media, Colorado State

University, Fort Collins, Colorado, USA.

Bruand, A. (1990). Improved prediction of water-retention properties of clayey soils by pedological stratification. Journal of Soil Science, 41(3), 491-497.

Bruand, A., Baize, D., and Hardy, M. (1994). Prediction of water retention properties of clayey soils: validity of relationships using a single soil characteristic. Soil Use and Management, 10(3), 99-103.

Brutsaert, W. (1966). Probability laws for pore-size distributions. Soil Science, 101(2), 85-92.

Burger, C. A., and Shackelford, C. D. (2001). Soil-water characteristic curves and dual porosity of sand-diatomaceous earth mixtures. Journal of Geotechnical and Geoenvironmental Engineering, 127(9), 790-800.

Cameron, D. R. (1978). Variability of soil water retention curves and predicted hydraulic conductivities on a small plot. Soil Science, 126(6), 364-371.

Campbell, G. S. (1974). A simple method for determining unsaturated conductivity from moisture retention data. Soil Science, 117(6), 311-314.

Carsel, R. F., and Parrish, R. S. (1988). Developing joint probability distributions of soil water retention characteristics. Water Resources Research, 24(5), 755-769.

Cary, C. E., and Zapata, C. E. (2016). Pore water pressure response of soil subjected to dynamic loading under saturated and unsaturated conditions. International Journal of Geomechanics, 16(6), D4016004.

Chai, J., and Khaimook, P. (2020). Prediction of soil-water characteristic curves using basic soil properties. Transportation Geotechnics, 22, 100295.

Chai, M. T., Zhang, J. M., Zhang, H., Mu, Y. H., Sun, G. C., and Yin, Z. H. (2018). A method for calculating unfrozen water content of silty clay with consideration of freezing point. Applied Clay Science, 161, 474-481.

Chan, T. P., and Govindaraju, R. S. (2004). Estimating soil water retention curve from particle-size distribution data based on polydisperse sphere systems. Vadose Zone Journal, 3(4), 1443-1454.

Chen, R. P., Liu, P., Liu, X. M., Wang, P. F., and Kang, X. (2019). Pore-scale model for estimating the bimodal soil-water characteristic curve and hydraulic conductivity of compacted soils with different initial densities. Engineering Geology, 260, 105199.

Chen, X. Y., Zhang, L. L., Zhang, L. M., Zhou, Y. D., Ye, G. L., and Guo, N. (2021). Modelling rainfall-induced landslides from initiation of instability to post-failure. Computers and Geotechnics, 129, 103877.

Cheng, Q., Ng, C. W. W., Zhou, C., and Tang, C. S. (2019). A new water retention model that considers pore non-uniformity and evolution of pore size distribution. Bulletin of Engineering Geology and the Environment, 78(7), 5055-5065.

Cheng, Q., Tang, C. S., Xu, D., Zeng, H., and Shi, B. (2021). Water infiltration in a cracked soil considering effect of drying-wetting cycles. Journal of Hydrology, 593, 125640.

Chin, K. B., Leong, E. C., and Rahardjo, H. (2010). A simplified method to estimate the soil-water characteristic curve. Canadian Geotechnical Journal, 47(12), 1382-1400.

Chiu, C. F., Yan, W. M., and Yuen, K. V. (2012). Estimation of water retention curve of granular soils from particle-size distribution - a Bayesian probabilistic approach. Canadian Geotechnical Journal, 49(9), 1024-1035.

Clapp, R. B., and Hornberger, G. M. (1978). Empirical equations for some soil hydraulic properties. Water Resources Research, 14(4), 601-604.

Colins, I. F., and Houlsby, G. T. (1997). Application of thermomechanical principles to the modelling of geotechnical materials. Proceedings of the Royal Society of London Series A, 453(1964), 1975-2001.

Comegna, V., Damiani, P., and Sommella, A. (1998). Use of a fractal model for determining soil water retention curves. Geoderma, 85(4), 307-323.

Cornelis, W. M., Ronsyn, J., Van Meirvenne, M., and Hartmann, R. (2001). Evaluation of pedotransfer functions for predicting the soil moisture retention curve. Soil Science Society of America Journal, 65(3), 638-648.

Cosby, B. J., Hornberger, G. M., Clapp, R. B., and Ginn, T. R. (1984). A statistical exploration of the relationships of soil moisture characteristics to the physical properties of soils. Water Resources Research, 20(6), 682-690.

Coussy, O. (2005). Poromechanics of freezing materials. Journal of the Mechanics and Physics of Solids, 53(8), 1689-1718.

Cresswell, H. P., and Paydar, Z. (1996). Water retention in Australian soils. I. Description and prediction using parametric functions. Australian Journal of Soil Research, 34(2), 195-212.

Cunningham, M. R., Ridley, A. M., Dineen, K., and Burland, J. B. (2003). The mechanical behaviour of a reconstituted unsaturated silty clay. Géotechnique, 53(2), 183-194.

Dash, J. G., Rempel, A. W., and Wettlaufer, J. S. (2006). The physics of premelted ice and its geophysical consequences. Reviews of Modern Physics, 78(3), 695-741.

Delage, P., Cui, Y. J., and Tang, A. M. (2010). Clays in radioactive waste disposal. Journal of Rock Mechanics and Geotechnical Engineering, 2(2), 111-123.

Della Vecchia, G., Dieudonné, A. -C., Jommi, C., and Charlier, R. (2015). Accounting for evolving pore size distribution in water retention models for compacted clays. International Journal for Numerical and Analytical Methods in Geomechanics, 39(7), 702-723.

Denbigh, K. G. (1981). The principles of chemical equilibrium: With applications in chemistry and chemical engineering. Cambridge University Press, Cambridge, UK.

De Jong, R., and Loebel, K. (1982). Empirical relations between soil components and water retention at 1/3 and 15 atmospheres. Canadian Journal of Soil Science, 62(2), 343-350.

Dijkerman, J. C. (1988). An Ustult-Aquult-Tropept catena in Sierra Leone, West Africa, II. Land qualities and land evaluation. Geoderma, 42(1), 29-49.

D'Onza, F., Gallipoli, D., Wheeler, S., Casini, F., Vaunat, J., Khalili, N., Laloui, L., Mancuso, C., MašíN, D., Nuth, M., Pereira, J. M., and Vassallo, R. (2011). Benchmark of constitutive models for unsaturated soils. Géotechnique, 61(4), 283-302.

Drotz, S. H., Tilston, E. L., Sparrman, T., Schleucher, J., Nilsson, M., and Öquist, M. G. (2009). Contributions of matric and osmotic potentials to the unfrozen water content of frozen soils. Geoderma, 148(3-4), 392-398.

Enninful, H. R. N. B., Schneider, D., Kohns, R., Enke, D., and Valiullin, R. (2020). A novel approach for advanced thermoporometry characterization of mesoporous solids: Transition kernels and the serially connected pore model. Microporous and Mesoporous Materials, 309, 110534.

Farrell, D. A., and Larson, W. E. (1972). Modeling the pore structure of porous media. Water Resources Research, 8(3), 699-706.

Fayer, M. J., and Simmons, C. S. (1995). Modified soil water retention functions for all matric suctions. Water Resources Research, 31(5), 1233-1238.

Feng, M., and Fredlund, D. G. (1999). Hysteretic influence associated with thermal conductivity sensor measurements. In *Proceedings of the 52nd Canadian Geotechnical Conference* (pp. 651-657). Regina, Canada.

Fredlund, D. G., and Morgenstern, N. R. (1977). Stress state variables for unsaturated soils. Journal of the Geotechnical Engineering Division, 103(5), 447-466.

Fredlund, D. G., and Rahardjo, H. (1993). Soil mechanics for unsaturated soils. John Wiley & Sons, New York.

Fredlund, D. G., and Xing, A. (1994). Equations for the soil-water characteristic curve. Canadian Geotechnical Journal, 31(4), 521-532.

Fredlund, D. G., Xing, A., and Huang, S. (1994). Predicting the permeability function for unsaturated soils using the soil-water characteristic curve. Canadian Geotechnical Journal, 31(4), 533-546.

Fredlund, D.G., Sheng, D.C., and Zhao, J.D. (2011). Estimation of soil suction from the soil-water characteristic curve. Canadian Geotechnical Journal, 48(2), 186-198.

Fredlund, D.G., Rahardjo, H., and Fredlund, M.D. (2012). Unsaturated soil mechanics in engineering practice. John Wiley & Sons, Hoboken, New Jersey.

Fredlund, M. D., Fredlund, D. G., and Wilson, G. W. (1997). Prediction of the soil-water characteristic curve from grain-size distribution and volume-mass properties. In *Proceedings of the 3rd Brazilian Symposium on Unsaturated Soils* (Vol. 1, pp. 13-23). Rio de Janeiro, Brazil.

Fredlund, M. D., Wilson, G. W., and Fredlund, D. G. (2002). Use of the grain-size distribution for estimation of the soil-water characteristic curve. Canadian Geotechnical Journal, 39(5), 1103-1117.

Fomby, T. B., Hill, R. C., and Johnson, S. R. (1984). Advanced Econometric Methods, first ed. Springer, New York.

Fu, Q., Hou, R. J., Li, T. X., Wang, M., and Yan, J. W. (2018). The functions of soil water and heat transfer to the environment and associated response mechanisms under different snow cover conditions. Geoderma, 325, 9-17.

Fu, Y. P., Liao, H. J., Chai, X. Q., Li, Y., and Lv, L. L. (2020). A hysteretic model considering contact angle hysteresis for fitting soil-water characteristic curves. Water Resources Research, 57, e2019WR026889.

Gallipoli, D., Wheeler, S. J., and Karstunen, M. (2003). Modelling the variation of degree of saturation in a deformable unsaturated soil. Géotechnique, 53(1), 105-112.

Gallipoli, D. (2012). A hysteretic soil-water retention model accounting for cyclic variations of suction and void ratio. Géotechnique, 62(7), 605-616.

Garcia, E., Oka, F., and Kimoto, S. (2010). Instability analysis and simulation of water infiltration into an unsaturated elasto-viscoplastic material. International Journal of Solids and Structures, 47(25-26), 3519-3536.

Gardner, W. R. (1958). Some steady-state solutions of the unsaturated moisture flow equation with application to evaporation from a water table. Soil Science, 85(4), 228-232.

Garg, A., Garg, A., and Tai, K. (2013). A multi-gene genetic programming model for estimating stress-dependent soil water retention curves. Computational Geosciences, 18(1), 45-56.

Ghanbarian-Alavijeh, B., and Hunt, A. G. (2012). Comparison of the predictions of universal scaling of the saturation dependence of the air permeability with experiment. Water Resources Research, 48(8).

Ghosh, R. K. (1980). Estimation of soil-moisture characteristics from mechanical properties of soils. Soil Science, 130(2), 60-63.

Gillham, R. W., Klute, A., and Heermann, D. F. (1976). Hydraulic properties of a porous medium: measurement and empirical representation. Soil Science Society of America Journal, 40(2), 203-207.

Gitirana Jr, G.de.F.N., and Fredlund, D.G. (2004). Soil-water characteristic curve equation with independent properties. Journal of Geotechnical and Geoenvironmental Engineering, 130(2), 209-212.

Gonçalves, M. C., Pereira, L. S., and Leij, F. J. (1997). Pedo-transfer functions for estimating unsaturated hydraulic properties of Portuguese soils. European Journal of Soil Science, 48(3), 387-400.

Groenevelt, P. H., and Grant, C. D. (2004). A new model for the soil-water retention curve that solves the problem of residual water contents. European Journal of Soil Science, 55(3), 479-485.

Gupta, S. C., and Larson, W. E. (1979). Estimating soil water retention characteristics from particle size distribution, organic matter percent, and bulk density. Water Resources Research, 15(6), 1633-1635.

Haghverdi, A., Cornelis, W. M., and Ghahraman, B. (2012). A pseudo-continuous neural network approach for developing water retention pedotransfer functions with limited data. Journal of Hydrology, 442-443, 46-54.

Hansson, K., Šimůnek, J., Mizoguchi, M., Lundin, L. -C., and van Genuchten, M. T. (2004). Water flow and heat transport in frozen soil: Numerical solution and freeze-thaw applications. Vadose Zone Journal, 3(2), 527-533.

Haverkamp, R., and Parlange, J. Y. (1986). Predicting the water-retention curve from particle-size distribution. Soil Science, 142(6), 325-339.

He, H. L., Flerchinger, G. N., Kojima, Y., Dyck, M., and Lv, J. L. (2021). A review and evaluation of 39 thermal conductivity models for frozen soils. Geoderma, 382, 114694.

Hogarth, W. L., Hopmans, J., Parlange, J. -Y., and Haverkamp, R. (1988). Application of a simple soil-water hysteresis model. Journal of Hydrology, 98(1-2), 21-29.

Houlsby, G. T., and Puzrin, A. M. (2000). A thermomechanical framework for constitutive models for rate-independent dissipative materials. International Journal of Plasticity, 16(9), 1017-1047.

Houlsby, G. T. (1997). The work input to an unsaturated granular material. Géotechnique, 47(1), 193-196.

Hu, G. J., Zhao, L., Zhu, X. F., Wu, X. D., Wu, T. H., Li, R., Xie, C. W., and Hao, J. M. (2020). Review of algorithms and parameterizations to determine unfrozen water content in frozen soil. Geoderma, 368, 114277.

Hu, R., Chen, Y. F., Liu, H. H., and Zhou, C. B. (2013). A water retention curve and unsaturated hydraulic conductivity model for deformable soils: consideration of the change in pore-size distribution. Géotechnique, 63(16), 1389-1405.

Huang, G., and Zhang, R. (2005). Evaluation of soil water retention curve with the pore-solid fractal model. Geoderma, 127(1-2), 52-61.

Hutson, J. L., and Cass, A. (1987). A retentivity function for use in soil-water simulation models. Journal of Soil Science, 38(1), 105-113.

Ito, M., and Azam, S. (2013). Engineering properties of a vertisolic expansive soil deposit. Engineering Geology, 152(1), 10-16.

Jaafar, R., and Likos, W. J. (2011). Estimating water retention characteristics of sands from grain size distribution using idealized packing conditions. Geotechnical Testing Journal, 34(5), 103594.

Jain, S. K., Singh, V. P., and van Genuchten, M. T. (2004). Analysis of soil water retention data using artificial neural networks. Journal of Hydrologic Engineering, 9(5), 415-420.

Jennings, J. E. B., and Burland, J. B. (1962). Limitations to the use of effective stresses in partly saturated soils. Géotechnique, 12(2), 125-144.

Jensen, D. K., Tuller, M., de Jonge, L. W., Arthur, E., and Moldrup, P. (2015). A new two-stage approach to predicting the soil water characteristic from saturation to oven-dryness. Journal of Hydrology, 521, 498-507.

Jin, X., Yang, W., Gao, X .Q., Zhao, J. Q., Li, Z. C., and Jiang, J. X. (2020). Modeling the unfrozen water content of frozen soil based on the absorption effects of clay surfaces. Water Resources Research, 56(12), e2020WR027482.

Kern, J. S. (1995). Evaluation of soil water retention models based on basic soil physical properties. Soil Science Society of America Journal, 59(4), 1134-1141.

Khalili, N., and Khabbaz, M. H. (1998). A unique relationship for χ for the determination of the shear strength of unsaturated soils. Géotechnique, 48(5), 681-687.

Khalili, N., Witt, R., Laloui, L., Vulliet, L., and Koliji, A. (2005). Effective stress in double porous media with two immiscible fluids. Geophysical Research Letters, 32(15), L15309.1-L15309.5.

Khlosi, M., Cornelis, W. M., Gabriels, D., and Sin, G. (2006). Simple modification to describe the soil water retention curve between saturation and oven dryness. Water Resources Research, 42(11), W11501.

Khosravi, A., and McCartney, J. S. (2012). Impact of hydraulic hysteresis on the small-strain shear modulus of low plasticity soils. Journal of Geotechnical and Geoenvironmental Engineering, 138(11), 1326-1333.

Koekkoek, E. J. W., and Booltink, H. (1999). Neural network models to predict soil water retention. European Journal of Soil Science, 50(3), 489-495.

Kong, L. M., Yu, A. L., Liang, K., and Qi, J. L. (2022). Influence of bimodal structure on the soil freezing characteristic curve in expansive soils. Cold Regions Science and Technology, 194, 103437.

Koopmans, R. W. R., and Miller, R. D. (1966). Soil freezing and soil water characteristic curves. Soil Science Society of America Journal, 30(6), 680-685.

Kosugi, K. I. (1994). Three-parameter lognormal distribution model for soil water retention. Water Resources Research, 30(4), 891-901.

Kozlowski, T. (2007). A semi-empirical model for phase composition of water in clay-water systems. Cold Regions Science and Technology, 49(3), 226-236.

Kurylyk, B. L., and Watanabe, K. (2013). The mathematical representation of freezing and thawing processes in variably-saturated, non-deformable soils. Advances in Water Resources, 60, 160-177.

Lamorski, K., Pachepsky, Y., Sławiński, C., and Walczak, R. T. (2008). Using support vector machines to develop pedotransfer functions for water retention of soils in Poland. Soil Science Society of America Journal, 72(5), 1243-1247.

Langman, J. B., Blowes, D. W., Amos, R. T., Atherton, C., Wilson, D., Smith, L., Sego, D. C., and Sinclair, S. A. (2017). Influence of a tundra freeze-thaw cycle on sulfide oxidation and metal leaching in a low sulfur, granitic waste rock. Applied Geochemistry, 76, 9-21.

Lei, X. Q., Wong, H., Fabbri, A., Limam, A., and Cheng, Y. M. (2016). A chemo-elastic-plastic model for unsaturated expansive clays. International Journal of Solids and Structures,

88-89, 354-378.

Leong, E. C., and Rahardjo, H. (1997). Review of soil-water characteristic curve equations. Journal of Geotechnical and Geoenvironmental Engineering, 123(12), 1106-1117.

Le Pense, S., Arson, C., and Pouya, A. (2016). A fully coupled damage-plasticity model for unsaturated geomaterials accounting for the ductile-brittle transition in drying clayey soils. International Journal of Solids and Structures, 91, 102-114.

Likos, W. J., Lu, N., and Godt, J. W. (2014). Hysteresis and uncertainty in soil water-retention curve parameters. Journal of Geotechnical and Geoenvironmental Engineering, 140(4), 04013050.

Li, D. F., Gao, G. Y., Shao, M. A., and Fu, B. J. (2016). Predicting available water of soil from particle-size distribution and bulk density in an oasis-desert transect in northwestern China. Journal of Hydrology, 538, 539-550.

Li, R. P., Shi, H. B., Flerchinger, G. N., Akae, T., and Wang, C. S. (2012). Simulation of freezing and thawing soils in Inner Mongolia Hetao Irrigation District, China. Geoderma, 173-174, 28-33.

Li, T., Chen, Y. Z., Han, L. J., Cheng, L. H., Lv, Y. H., Fu, B. J., Feng, X. M., and Wu, X. (2021). Shortened duration and reduced area of frozen soil in the Northern Hemisphere. The Innovation, 2(3), 100146.

Li, X. S. (2005). Modelling of hysteresis response for arbitrary wetting/drying paths. Computers and Geotechnics, 32(2), 133-137.

Li, X., Zhang, L. M., and Fredlund, D. G. (2009a). Wetting front advancing column test for measuring unsaturated hydraulic conductivity. Canadian Geotechnical Journal, 46(12), 1431-1445.

Li, X., Zhang, L. M., and Li, J. H. (2009b). Development of a modified axis translation technique for measuring SWCCs for gravel soils at very low suctions. Geotechnical Testing Journal, 32(6), 478-488.

Li, X., Li, J. H., and Zhang, L. M. (2014). Predicting bimodal soil-water characteristic curves and permeability. Computers and Geotechnics, 57, 85-96.

Li, Y., Chen, D., White, R. E., Zhu, A., and Zhang, J. (2007). Estimating soil hydraulic properties of Fengqiu County soils in the North China Plain using pedo-transfer functions. Geoderma, 138(3-4), 261-271.

Li, Y., and Vanapalli, S. K. (2021). A novel modeling method for the bimodal soil-water characteristic curve. Computers and Geotechnics, 138, 104318.

Li, Y., and Vanapalli, S. K. (2022a). Prediction of soil-water characteristic curves using two artificial intelligence (AI) models and AI aid design method for sands. Canadian Geotechnical Journal, 59(1), 129-143.

Li, Y., and Vanapalli, S. K. (2022b). Models for predicting the soil-water characteristic curves for coarse and fine-grained soils. Journal of Hydrology, 612.

Li, Y., Rahardjo, H., Satyanaga, A., Rangarajan, S., and Lee, D. T.-T. (2022). Soil database development with the application of machine learning methods in soil properties prediction. Engineering Geology, 306, 106769.

Liu, S. Y., Yasufuku, N., Liu, Q., Omine, K., and Hemanta, H. (2013). Bimodal and multimodal descriptions of SWCC for structural soils. Water Science and Technology, 67(8), 1740-1747.

Liu, Z., and Yu, X. (2013). Physically based equation for phase composition curve of frozen soils. Transportation Research Record, 2349(1), 93-99.

Lu, N., and Likos, W. J. (2006). Suction stress characteristic curve for unsaturated soil. Journal of Geotechnical and Geoenvironmental Engineering, 132(2), 131-142.

Lu, N., Godt, J. W., and Wu, D. T. (2010). A closed-form equation for effective stress in unsaturated soil. Water Resources Research, 46(5).

Matsumoto, M., Saito, S., and Ohmine, I. (2002). Molecular dynamics simulation of the ice nucleation and growth process leading to water freezing. Nature, 416, 409-413.

Mayr, T., and Jarvis, N. J. (1999). Pedotransfer functions to estimate soil water retention parameters for a modified Brooks-Corey type model. Geoderma, 91(1-2), 1-9.

Mbagwu, J. S. C., and Mbah, C. N. (2008). Estimating water retention and availability in Nigerian soils from their saturation percentage. Communications in Soil Science and Plant Analysis, 29(7-8), 913-922.

McCuen, R. H., Rawls, W. J., and Brakensiek, D. L. (1981). Statistical analysis of the Brooks-Corey and the Green-Ampt parameters across soil textures. Water Resources Research, 17(4), 1005-1013.

McKee, C. R., and Bumb, A. C. (1987). Flow-testing coalbed methane production wells in the presence of water and gas. SPE Formation Evaluation, 2(04), 599-608.

Merdun, H. (2010). Alternative methods in the development of pedotransfer functions for soil hydraulic characteristics. Eurasian Soil Science, 43(1), 62-71.

Mermoud, A., and Xu, D. (2006). Comparative analysis of three methods to generate soil hydraulic functions. Soil and Tillage Research, 87(1), 89-100.

Meskini-Vishkaee, F., Mohammadi, M. H., and Vanclooster, M. (2014). Predicting the soil moisture retention curve, from soil particle size distribution and bulk density data using a packing density scaling factor. Hydrology and Earth System Sciences, 18(10), 4053-4063.

Miguel, M. G., and Bonder, B. H. (2012). Soil-water characteristic curves obtained for a colluvial and lateritic soil profile considering the macro and micro porosity. Geotechnical and Geological Engineering, 30, 1405-1420.

Min, T. K., and Huy, P. T. (2010). A soil-water hysteresis model for unsaturated sands based on Fuzzy set plasticity theory. KSCE Journal of Civil Engineering, 14(2), 165-172.

Minasny, B., and McBratney, A. B. (2002). The neuro-m method for fitting neural network parametric pedotransfer functions. Soil Science Society of America Journal, 66(2), 352-361.

Minasny, B., Hopmans, J. W., Harter, T., Eching, S. O., Tuli, A., and Denton, M. A. (2004). Neural networks prediction of soil hydraulic functions for alluvial soils using multistep outflow data. Soil Science Society of America Journal, 68(2), 417-429.

Minasny, B., McBratney, A. B., and Bristow, K. L. (1999). Comparison of different approaches to the development of pedotransfer functions for water-retention curves. Geoderma, 93(3-4), 225-253.

Mishra, S., Parker, J. C., and Singhal, N. (1989). Estimation of soil hydraulic properties and their uncertainty from particle size distribution data. Journal of Hydrology, 108, 1-18.

Mitchell, J. K. and Soga, K. (2005). Fundamentals of soil behavior. John Wiley & Sons, Hoboken, New Jersey.

Mohammadi, M. H., and Vanclooster, M. (2011). Predicting the soil moisture characteristic curve from particle size distribution with a simple conceptual model. Vadose Zone Journal, 10(2), 594-602.

Moreira de Melo, T., and Pedrollo, O. C. (2015). Artificial neural networks for estimating soil water retention curve using fitted and measured data. Applied and Environmental Soil Science, 2015, 1-16.

Mualem, Y. (1976). A new model for predicting the hydraulic conductivity of unsaturated porous media. Water Resources Research, 12(3), 513-522.

Mualem, Y., and Miller, E. E. (1979). A hysteresis model based on an explicit domain-dependence function. Soil Science Society of America Journal, 43(6), 1067-1073.

Nam, S., Gutierrez, M., Diplas, P., Petrie, J., Wayllace, A., Lu, N., and Muñoz, J. J. (2010). Comparison of testing techniques and models for establishing the SWCC of riverbank soils. Engineering Geology, 110(1-2), 1-10.

Nandagiri, L., and Prasad, R. (1997). Relative performances of textural models in estimating soil moisture characteristic. Journal of Irrigation and Drainage Engineering, 123(3), 211-214.

Nasta, P., Kamai, T., Chirico, G. B., Hopmans, J. W., and Romano, N. (2009). Scaling soil water retention functions using particle-size distribution. Journal of Hydrology, 374(3-4), 223-234.

Nemes, A., Schaap, M. G., Leij, F. J., and Wösten, J. H. M. (2001). Description of the unsaturated soil hydraulic database UNSODA version 2.0. Journal of Hydrology, 251(3-4), 151-162.

Nemes, A., Schaap, M. G., and Wösten, J. H. M. (2003). Functional evaluation of pedotransfer functions derived from different scales of data collection. Soil Science Society of America Journal, 67(4), 1093-1102.

Nemes, A., Rawls, W. J., and Pachepsky, Y. A. (2006). Use of the nonparametric nearest neighbor approach to estimate soil hydraulic properties. Soil Science Society of America Journal, 70(2), 327-336.

Ng, C. W. W., and Pang, Y. W. (2000). Influence of stress state on soil-water characteristics and slope stability. Journal of Geotechnical and Geoenvironmental Engineering, 126(2), 157-166.

Ng, C. W. W., Ni, J. J., and Leung, A. K. (2020). Effects of plant growth and spacing on soil hydrological changes: A field study. Géotechnique, 70(10), 867-881.

Nimmo, J. R., Herkelrath, W. N., and Laguna Luna, A. M. (2007). Physically based estimation of soil water retention from textural data: General framework, new models, and streamlined existing models. Vadose Zone Journal, 6(4), 766-773.

Nishimura, S., and Wang, J. Y. (2018). A simple framework for describing strength of saturated frozen soils as multi-phase coupled system. Géotechnique, 69(8), 659-671.

Niu, G., Cui, Y. J., Pereira, J. M., Shao, L., and Sun, D. A. (2021). Determining Bishop's parameter χ based on pore size distribution. Géotechnique Letters, 11(1), 1-28.

Ni, J. J., Cheng, Y. F., Wang, Q. H., Ng, C. W. W., and Garg, A. (2019). Effects of vegetation on soil temperature and water content: field monitoring and numerical modelling. Journal of Hydrology, 571(4), 494-502.

Nuth, M., and Laloui, L. (2008). Effective stress concept in unsaturated soils: Clarification and validation of a unified framework. International Journal for Numerical and Analytical Methods in Geomechanics, 32(7), 771-801.

Oh, S., Lu, N., Kim, Y. K., Lee, S. J., and Lee, S. R. (2012). Relationship between the soil-water characteristic curve and the suction stress characteristic curve: Experimental evidence from residual soils. Journal of Geotechnical and Geoenvironmental Engineering, 138(1), 47-57.

Pachepsky, Y. A., Shcherbakov, R. A., and Korsunskaya, L. P. (1995). Scaling of soil water retention using a fractal model. Soil Science, 159(2), 99-104.

Pachepsky, Y. A., Timlin, D., and Varallyay, G. (1996). Artificial neural networks to estimate soil water retention from easily measurable data. Soil Science Society of America Journal, 60(3), 727-733.

Pachepsky, Y., Rawls, W., Gimenéz, D., and Watt, J. P. C. (1998). Use of soil penetration resistance and group method of data handling to improve soil water retention estimates. Soil and Tillage Research, 49(1-2), 117-126.

Pachepsky, Y. A., and Rawls, W. J. (1999). Accuracy and reliability of pedotransfer functions as affected by grouping soils. Soil Science Society of America Journal, 63(6), 1748-1757.

Pachepsky, Y. and Rawls, W. J. (2004). *Development of Pe dotransfer Functions in Soil Hydrology*. Elsevier, Amsterdam.

Parlange, J.- Y. (1976). Capillary hysteresis and the relationship between drying and wetting

curves. Water Resources Research, 12(2), 224-228.

Patil, N. G., and Rajput, G. S. (2009). Evaluation of water retention functions and computer program “Rosetta” in predicting soil water characteristics of seasonally impounded shrink-swell soils. Journal of Irrigation and Drainage Engineering, 135(3), 286-294.

Perrier, E., Rieu, M., Sposito, G., and de Marsily, G. (1996). Models of the water retention curve for soils with a fractal pore size distribution. Water Resources Research, 32(10), 3025-3031

Pham, H. Q., Fredlund, D. G., and Barbour, S. L. (2003). A practical hysteresis model for the soil-water characteristic curve for soils with negligible volume change. Géotechnique, 53(2), 293-298.

Pham, H. Q., Fredlund, D. G., and Barbour, S. L. (2005). A study of hysteresis models for soil-water characteristic curves. Canadian Geotechnical Journal, 42(6), 1548-1568.

Pham, H. Q., and Fredlund, D. G. (2008). Equations for the entire soil-water characteristic curve of a volume change soil. Canadian Geotechnical Journal, 45(4), 443-453.

Pidgeon, J. D. (1972). The measurement and prediction of available water capacity of ferrallitic soils in Uganda. Journal of Soil Science, 23(4), 431-441.

Poulovassilis, A. (1970). Hysteresis of pore water in granular porous bodies. Soil Science, 109(1), 5-12.

Pouragha, M., Eghbalian, M., Wan, R., and Wong, T. (2020). Derivation of soil water retention curve incorporating electrochemical effects. Acta Geotechnica, 16(4), 1147-1160.

Pouragha, M., Kruyt, N. P., and Wan, R. (2021). Non-coaxial plastic flow of granular materials through stress probing analysis. International Journal of Solids and Structures, 222-223, 111015.

Pouya, A., Vu, M. N., Ghabezloo, S., and Bendjeddou, Z. (2013). Effective permeability of cracked unsaturated porous materials. International Journal of Solids and Structures, 50(20-21), 3297-3307.

Puhlmann, H., and von Wilpert, K. (2012). Pedotransfer functions for water retention and unsaturated hydraulic conductivity of forest soils. Journal of Plant Nutrition and Soil Science, 175(2), 221-235.

Qader, S. H., Dash, J., Alegana, V. A., Khwarahm, N. R., Tatem, A. J., and Atkinson, P. M. (2021). The role of earth observation in achieving sustainable agricultural production in arid and semi-arid regions of the world. Remote Sensing, 13, 3382.

Qi, S. C., and Vanapalli, S. K. (2015). Hydro-mechanical coupling effect on surficial layer stability of unsaturated expansive soil slopes. Computers and Geotechnics, 70, 68-82.

Qian, J. G., Lin, Z. Q., and Shi, Z. C. (2022). Soil-water retention curve model for fine-grained soils accounting for void ratio-dependent capillarity. Canadian Geotechnical Journal, 59(4), 498-509.

Qiao, Y. F., Tuttolomondo, A., Lu, X. B., Laloui, L., and Ding, W. Q. (2021). A generalized water retention model with soil fabric evolution. Geomechanics for Energy and the

Environment, 25, 100205.

Rahardjo, H., Kim, Y., and Satyanaga, A. (2019). Role of unsaturated soil mechanics in geotechnical engineering. International Journal of Geo-Engineering, 10(1).

Rahimi, A., and Rahardjo, H. (2016). New approach to improve soil-water characteristic curve to reduce variation in estimation of unsaturated permeability function. Canadian Geotechnical Journal, 53(4), 717-725.

Rajkai, K., and Várallyay, G. (1992). Estimating soil water retention from simpler properties by regression techniques. In *Proceedings of the International Workshop on Indirect Methods for Estimating the Hydraulic Properties of Unsaturated Soils* (pp. 417-426). University of California, Riverside, CA.

Rajkai, K., Kabos, S., Van Genuchten, M. T., and Jansson, P. E. (1996). Estimation of water-retention characteristics from the bulk density and particle-size distribution of Swedish soils. Soil Science, 161(12), 832-845.

Rao, S. M., and Shivananda, P. (2005). Role of osmotic suction in swelling of salt-amended clays. Canadian Geotechnical Journal, 42(1), 307-315.

Rao, S. M., and Thyagaraj, T. (2007). Swell-compression behaviour of compacted clays under chemical gradients. Canadian Geotechnical Journal, 44(5), 520-532.

Rawls, W. J., Brakensiek, D. L., and Saxtonn, K. E. (1982). Estimation of soil water properties. Transactions of the ASAE, 25(5), 1316-1320.

Rawls, W. J., and Brakensiek, D. (1985). Prediction of soil water properties for hydrologic modeling. In *Watershed Management in The Eighties* (pp. 2930-299). Reston, VA.

Rawls, W. J., Gish, T. J., and Brakensiek, D. L. (1991). Estimating soil water retention from soil physical properties and characteristics. In *Advances in Soil Science* (pp. 213-234). Springer, New York, NY. USA.

Ren, J. P., and Vanapalli, S. K. (2019). Comparison of soil-freezing and soil-water characteristic curves of two Canadian soils. Vadose Zone Journal, 18(1), 1-14.

Ren, J. P., and Vanapalli, S. K. (2020). Effect of freeze-thaw cycling on the soil-freezing characteristic curve of five Canadian soils. Vadose Zone Journal, 19(1), e20039.

Resurreccion, A. C., Moldrup, P., Tuller, M., Ferré, T. P. A., Kawamoto, K., Komatsu, T., and de Jonge, L. W. (2011). Relationship between specific surface area and the dry end of the water retention curve for soils with varying clay and organic carbon contents. Water Resources Research, 47(6), W06522.

Romano, N., and Santini, A. (1997). Effectiveness of using pedo-transfer functions to quantify the spatial variability of soil water retention characteristics. Journal of Hydrology, 202(1-4), 137-157.

Romano, N., and Palladino, M. (2002). Prediction of soil water retention using soil physical data and terrain attributes. Journal of Hydrology, 265(1-4), 56-75.

Romero-Ruiz, A., Linde, N., Keller, T., and Or, D. (2018). A review of geophysical methods for soil structure characterization. Reviews of Geophysics, 56(4), 672-697.

Rong, W., and McCartney, J. S. (2021). Undrained seismic compression of unsaturated sand. Journal of Geotechnical and Geoenvironmental Engineering, 147(1), 04020145.

Ross, P. J., and Smettem, K. R. J. (1993). Describing soil hydraulic properties with sums of simple functions. Soil Science Society of America Journal, 57(1), 26-29.

Sakaki, T., Komatsu, M., and Takahashi, M. (2014). Rules-of-thumb for predicting air-entry value of disturbed sands from particle size. Soil Science Society of America Journal, 78(2), 454-464.

Satyanaga, A., Rahardjo, H., Leong, E.C., and Wang, J.Y. (2013). Water characteristic curve of soil with bimodal grain-size distribution. Computers and Geotechnics, 48, 51-61.

Satyanaga, A., Rahardjo, H., and Zhai, Q. (2017). Estimation of unimodal water characteristic curve for gap-graded soil. Soils and Foundations, 57(5), 789-801.

Saxton, K. E., Rawls, W. J., Romberger, J. S., and Papendick, R. I. (1986). Estimating generalized soil-water characteristics from texture. Soil Science Society of America Journal, 50(4), 1031-1036.

Saxton, K. E., and Rawls, W. J. (2006). Soil water characteristic estimates by texture and organic matter for hydrologic solutions. Soil Science Society of America Journal, 70(5), 1569-1578.

Schaap, M. G., and Bouten, W. (1996). Modeling water retention curves of sandy soils using neural networks. Water Resources Research, 32(10), 3033-3040.

Schaap, M. (1998). Using neural networks to predict soil water retention and soil hydraulic conductivity. Soil and Tillage Research, 47(1-2), 37-42.

Schaap, M. G., Leij, F. J., and van Genuchten, M. T. (1998). Neural network analysis for hierarchical prediction of soil hydraulic properties. Soil Science Society of America Journal, 62(4), 847-855.

Schaap, M. G., Leij, F. J., and van Genuchten, M. T. (2001). Rosetta: A computer program for estimating soil hydraulic parameters with hierarchical pedotransfer functions. Journal of Hydrology, 251(3-4), 163-176.

Scheinost, A. C., Sinowski, W., and Auerswald, K. (1997). Regionalization of soil water retention curves in a highly variable soilscape, I. Developing a new pedotransfer function. Geoderma, 78(3-4), 129-143.

Sheng, D. C., Fredlund, D. G., and Gens, A. (2008). A new modelling approach for unsaturated soils using independent stress variables. Canadian Geotechnical Journal, 45(4), 511-534.

Sheng, D. C., and Zhou, A. N. (2011). Coupling hydraulic with mechanical models for unsaturated soils. Canadian Geotechnical Journal, 48(5), 826-840.

Schneider, M., and Goss, K.-U. (2012). Prediction of the water sorption isotherm in air dry soils. Geoderma, 170, 64-69.

Sillers, W. S., and Fredlund, D. G. (2001). Statistical assessment of soil-water characteristic curve models for geotechnical engineering. Canadian Geotechnical Journal, 38(6), 1297-1313.

Simms, P. H., and Yanful, E. K. (2001). Measurement and estimation of pore shrinkage and pore distribution in a clayey till during soil-water characteristic curve tests. Canadian Geotechnical Journal, 38(4), 741-754.

Siemens, G. A., Take, W. A., and Peters, S. B. (2014). Physical and numerical modeling of infiltration including consideration of the pore-air phase. Canadian Geotechnical Journal, 51(12), 1475-1487.

Smettem, K. R. J., and Gregory, P. J. (1996). The relation between soil water retention and particle size distribution parameters for some predominantly sandy Western Australian soils. Australian Journal of Soil Research, 34(5), 695-708.

Sun, D. A., Sheng, D. C., and Sloan, S. W. (2007a). Elastoplastic modelling of hydraulic and stress-strain behaviour of unsaturated soils. Mechanics of Materials, 39(3), 212-221.

Sun, D. A., Sheng, D. C., and Xu, Y. F. (2007b). Collapse behaviour of unsaturated compacted soil with different initial densities. Canadian Geotechnical Journal, 44(6), 673-686.

Sun, D. A., Sheng, D. C., Cui, H. B., and Sloan, S. W. (2007c). A density-dependent elastoplastic hydro-mechanical model for unsaturated compacted soils. International Journal for Numerical and Analytical Methods in Geomechanics, 31(11), 1257-1279.

Sun, D. A., Cui, H. B., and Sun, W. J. (2009). Swelling of compacted sand–bentonite mixtures. Applied Clay Science, 43(3-4), 485-492.

Sung, S. G., Lee, I. M., Cho, G. C., and Reddi, L. N. (2005). Estimation of soil-water characteristics using liquid limit state. Géotechnique, 55(7), 569-573.

Tamari, S., Wösten, J. H. M., and Ruiz-Suárez, J. C. (1996). Testing an artificial neural network for predicting soil hydraulic conductivity. Soil Science Society of America Journal, 60(6), 1732-1741.

Tang, C. S., Cui, Y. J., Shi, B., Tang, A. M., and Liu, C. (2011). Desiccation and cracking behaviour of clay layer from slurry state under wetting–drying cycles. Geoderma, 166(1), 111-118.

Tani, M. (1982). The properties of water-table rise produced by a one-dimensional, vertical, unsaturated flow. Journal of Japan Forestry Society, 64, 409-418.

Tarantino, A. (2009). A water retention model for deformable soils. Géotechnique, 59(9), 751-762.

Tarantino, A., and Col, E.D. (2008). Compaction behaviour of clay. Géotechnique, 58(3), 199-213.

Teng, J. D., Kou, J. Y., Yan, X. D., Zhang, S., and Sheng, D. C. (2020). Parameterization of soil freezing characteristic curve for unsaturated soils. Cold Regions Science and Technology, 170, 102928.

Teng, J. D., Liu, J. L., Zhang, S., and Sheng, D. C. (2022). Frost heave in coarse-grained soils:

Experimental evidence and numerical modelling. Géotechnique (Accepted).

Teng, J. D., Zhong, Y., Zhang, S., and Sheng, D. C. (2021). A mathematic model for the soil freezing characteristic curve: The roles of adsorption and capillarity. Cold Regions Science and Technology, 181, 103178.

Terzaghi, K. (1943). Theoretical soil mechanics. Wiley, New York.

Tietje, O., and Tapkenhinrichs, M. (1993). Evaluation of pedo-transfer functions. Soil Science Society of America Journal, 57(4), 1088-1095.

Tinjum, J. M., Benson, C. H., and Blotz, L. R. (1997). Soil-water characteristic curves for compacted clays. Journal of Geotechnical and Geoenvironmental Engineering, 123(11), 1060-1069.

Tomasella, J., and Hodnett, M. G. (1998). Estimating soil water retention characteristics from limited data in Brazilian Amazonia. Soil Science, 163(3), 190-202.

Tomasella, J., Hodnett, M. G., and Rossato, L. (2000). Pedotransfer functions for the estimation of soil water retention in Brazilian soils. Soil Science Society of America Journal, 64(1), 327-338.

Tomasella, J., Pachepsky, Y., Crestana, S., and Rawls, W. J. (2003). Comparison of two techniques to develop pedotransfer functions for water retention. Soil Science Society of America Journal, 67(4), 1085-1092.

Tsaparas, I., Rahardjo, H., Toll, D. G., and Leong, E. G. (2002). Controlling parameters for rainfall-induced landslides. Computers and Geotechnics, 29(1), 1-27.

Tyler, S. W., and Wheatcraft, S. W. (1989). Application of fractal mathematics to soil water retention estimation. Soil Science Society of America Journal, 53(4), 987-996.

Tuller, M., and Or, D. (2005). Water films and scaling of soil characteristic curves at low water contents. Water Resources Research, 41(9).

Twarakavi, N. K. C., Sakai, M., and Šimůnek, J. (2009). An objective analysis of the dynamic nature of field capacity. Water Resources Research, 45(10).

Uchaipichat, A., and Khalili, N. (2009). Experimental investigation of thermo-hydro-mechanical behaviour of an unsaturated silt. Géotechnique, 59(4), 339-353.

Ungaro, F., Calzolari, C., and Busoni, E. (2005). Development of pedotransfer functions using a group method of data handling for the soil of the Pianura Padano-Veneta region of North Italy: water retention properties. Geoderma, 124(3-4), 293-317.

van den Berg, M., Klamt, E., van Reeuwijk, L. P., and Sombroek, W. G. (1997). Pedotransfer functions for the estimation of moisture retention characteristics of Ferralsols and related soils. Geoderma, 78(3-4), 161-180.

van Genuchten, M. T. (1980). A closed-form equation for predicting the hydraulic conductivity of unsaturated soils. Soil Science Society of America Journal, 44(5), 892-898.

Van Looy, K., Bouma, J., Herbst, M., Koestel, J., Minasny, B., Mishra, U., Montzka, C., Nemes, A., Pachepsky, Y. A., Padarian, J., Schaap, M. G., Tóth, B., Verhoef, A., Vanderborght, J., Ploeg, M. J., Weihermüller, L., Zacharias, S., Zhang, Y. G., and Vereecken, H.

(2017). Pedotransfer Functions in Earth System Science: Challenges and Perspectives. Reviews of Geophysics, 55(4), 1199-1256.

Vanapalli, S. K., Fredlund, D. G., Pufahl, D. E., and Clifton, A. W. (1996). Model for the prediction of shear strength with respect to soil suction. Canadian Geotechnical Journal, 33(3), 379-392.

Vanapalli, S. K., Sillers, W. S., and Fredlund, M. D. (1998). The meaning and relevance of residual state to unsaturated soils. In *51st Canadian Geotechnical Conference* (pp. 4-7). Edmonton, Alberta, Canada.

Vanapalli, S. K., Fredlund, D. G., and Pufahl, D. E. (1999). The influence of soil structure and stress history on the soil-water characteristics of a compacted till. Géotechnique, 49(2), 143-159.

Vanapalli, S. K., and Catana, M. C. (2005). Estimation of the soil-water characteristic curve of coarse-grained soils using one point measurement and simple properties. In *Proceedings of the International Symposium on Advanced Experimental Unsaturated Soil Mechanics* (pp. 401-407). Trento, Italy.

Vanapalli, S. K. (2009). Shear strength of unsaturated soils and its applications in geotechnical engineering practice. In *Proceedings of the 4th Asia Pacific Conference on Unsaturated Soils* (pp. 579-598). Newcastle, Australia.

Vereecken, H., Maes, J., Feyen, J., and Darius, P. (1989). Estimating the soil moisture retention characteristic from texture, bulk density, and carbon content. Soil Science, 148(6), 389-403.

Vereecken, H., Maes, J., and Feyen, J. (1990). Estimating unsaturated hydraulic conductivity from easily measured soil properties. Soil Science, 149(1), 1-12.

Vereecken, H., Weynants, M., Javaux, M., Pachepsky, Y., Schaap, M. G., and van Genuchten, M. T. (2010). Using pedotransfer functions to estimate the van genuchten-mualem soil hydraulic properties: A review. Vadose Zone Journal, 9(4), 795-820.

Vereecken, H., Schnepf, A., Hopmans, J. W., Javaux, M., Or, D., Roose, T., Vanderborght, J., Young, M. H., Amelung, W., Aitkenhead, M., Allison, S. D., Assouline, S., Baveye, P., Berli, M., Brüggemann, N., Finke, P., Flury, M., Gaiser, T., Govers, G., Ghezzehei, T., Hallett, P., Hendricks Franssen, H. J., Heppell, J., Horn, R., Huisman, J. A., Jacques, D., Jonard, F., Kollet, S., Lafolie, F., Lamorski, K., Leitner, D., McBratney, A., Minasny, B., Montzka, C., Nowak, W., Pachepsky, Y., Padarian, J., Romano, N., Roth, K., Rothfuss, Y., Rowe, E. C., Schwen, A., Šimůnek, J., Tiktak, A., Van Dam, J., van der Zee, S. E. A. T. M., Vogel, H. J., Vrugt, J. A., Wöhling, T., and Young, I. M. (2016). Modeling soil processes: Review, key challenges, and new perspectives. Vadose Zone Journal, 15(5), 1-57.

Vereecken, H., Amelung, W., Bauke, S. L., Bogena, H., Brüggemann, N., Montzka, C., Vanderborght, J., Bechtold, M., Blöschl, G., Carminati, A., Javaux, M., Konings, A. G., Kusche, J., Neuweiler, I., Or, D., Steele-Dunne, S., Verhoef, A., Young, M., and Zhang,

Y. (2022). Soil hydrology in the Earth system. Nature Reviews Earth & Environment, 3(9), 573-587.

Visser, W. V. (1966). Progress in the knowledge about the effect of soil moisture content on plant production. In *Technical bulletin*, No. 5. Institute for land and water management research, Wageningen, The Netherlands.

Vugmeyster, L., Hagedorn, B., Clark, M. A., Sletten, R. S. (2017). Evaluating the effect of grain size and salts on liquid water content in frozen soils of Antarctica by combining NMR, chemical equilibrium modeling, and scattered diffraction analysis. Geoderma, 299, 25-31.

Wagner, B., Tarnawski, V. R., Wessolek, G., and Plagge, R. (1998). Suitability of models for the estimation of soil hydraulic parameters. Geoderma, 86(3-4), 229-239.

Wagner, B., Tarnawski, V. R., Hennings, V., Müller, U., Wessolek, G., and Plagge, R. (2001). Evaluation of pedo-transfer functions for unsaturated soil hydraulic conductivity using an independent data set. Geoderma, 102(3-4), 275-297.

Walczak, R. T., Moreno, F., Sławiński, C., Fernandez, E., and Arrue, J. L. (2006). Modeling of soil water retention curve using soil solid phase parameters. Journal of Hydrology, 329(3-4), 527-533.

Wan, R., Pouragha, M., Eghbalian, M., Duriez, J., and Wong, T. (2019). A probabilistic approach for computing water retention of particulate systems from statistics of grain size and tessellated pore network. International Journal for Numerical and Analytical Methods in Geomechanics, 43(5), 956-973.

Wan, X. S., and Yang, Z. H. (2020). Pore water freezing characteristic in saline soils based on pore size distribution. Cold Regions Science and Technology, 173, 103030.

Wang, C., Lai, Y. M., and Zhang, M. Y. (2017). Estimating soil freezing characteristic curve based on pore-size distribution. Applied Thermal Engineering, 124, 1049-1060.

Watanabe, K., and Mizoguchi, M. (2002). Amount of unfrozen water in frozen porous media saturated with solution. Cold Regions Science and Technology, 34(2), 103-110.

Webb, S. W. (2000). A simple extension of two-phase characteristic curves to include the dry region. Water Resources Research, 36(6), 1425-1430.

Wei, C. F., and Dewoolkar, M. M. (2006). Formulation of capillary hysteresis with internal state variables. Water Resources Research, 42 (7), 1-16.

Wheeler, S. J., Sharma, R. S., and Buisson, M. S. R. (2003). Coupling of hydraulic hysteresis and stress-strain behaviour in unsaturated soils. Géotechnique, 53(1), 41-54.

Wheeler, S. J., and Sivakumar, V. (1995). An elasto-plastic critical state framework for unsaturated soil. Géotechnique, 45(1), 35-53.

Williams, J., Prebble, R. E., Williams, W. T., and Hignett, C. T. (1983). The influence of texture, structure and clay mineralogy on the soil moisture characteristic. Australian Journal of Soil Research, 21(1), 15-32.

Williams, R. D., and Ahuja, L. R. (1992). Evaluation of similar-media scaling and a one-parameter model for estimating the soil water characteristic. Journal of Soil Science, 43(2), 237-248.

Wilson, G. V., Jardine, P. M., and Gwo, J. P. (1992). Modeling the hydraulic properties of a multiregion soil. Soil Science Society of America Journal, 56(6), 1731-1737.

Wijaya, M., Leong, E. C. (2016). Equation for unimodal and bimodal soil-water characteristic curves. Soils and Foundations, 56(2), 291-300.

Wösten, J. H. M., and van Genuchten, M. T. (1988). Using texture and other soil properties to predict the unsaturated soil hydraulic functions. Soil Science Society of America Journal, 52(6), 1762-1770.

Wösten, J. H. M., Finke, P. A., and Jansen, M. J. W. (1995). Comparison of class and continuous pedotransfer functions to generate soil hydraulic characteristics. Geoderma, 66(3-4), 227-237.

Wösten, J. H. M., Pachepsky, Y. A., and Rawls, W. J. (2001). Pedotransfer functions: bridging the gap between available basic soil data and missing soil hydraulic characteristics. Journal of Hydrology, 251(3-4), 123-150.

Xiao, Z. A., Lai, Y. M., and Zhang, J. (2020). Method for calculating the liquid water fraction of saline soil during the freezing process. Permafrost and Periglacial Processes, 32(1), 92-101.

Xiao, Z. A., Zhu, L. Z., and Hou, Z. R. (2022). The change mechanism and a prediction model of unfrozen water content in sodium chloride soil. Geoderma, 419, 115881.

Xu, M. J., Cao, Y. L., Ni, P. P., and Mei, G. X. (2020). Infiltration analysis of perforated storm sewer: finite difference modelling versus field tests. Journal of Hydrology, 590, 125421.

Xu, X. T., Bai, R. Q., Lai, Y., Zhang, M. Y., and Ren, J. G. (2020). Work conjugate stress and strain variables for unsaturated frozen soils. Journal of Hydrology, 528, 124537.

Xu, Y. F., Matsuoka, H., and Sun, D. A. (2003). Swelling characteristics of fractal-textured bentonite and its mixtures. Applied Clay Science, 22(4), 197-209.

Yang, X. H., and Vanapalli, S. K. (2020). Model for predicting the variation of shear stress in unsaturated soils during strain-softening. Canadian Geotechnical Journal, 58(10), 1513-1526.

Yang, X. H., and Vanapalli, S. K. (2023). Mechanisms and modeling methods of strain-softening behavior of unsaturated soils. International Journal of Geomechanics, 23(5).

Yin, P. H., and Vanapalli, S. K. (2018). Model for predicting tensile strength of unsaturated cohesionless soils. Canadian Geotechnical Journal, 55(9), 1313-1333.

Zacharias, S., and Wessolek, G. (2007). Excluding organic matter content from pedotransfer predictors of soil water retention. Soil Science Society of America Journal, 71(1), 43-50.

Zapata, C. E., Houston, W. N., Houston, S. L., and Walsh, K. D. (2000). Soil-water characteristic curve variability. In Advances in Unsaturated Geotechnics (pp. 84-124). Denver, CO.

Zhai, Q., Rahardjo, H., and Satyanaga, A. (2017). Effects of residual suction and residual water content on the estimation of permeability function. Geoderma, 303, 165-177.

Zhai, Q., Rahardjo, H., Satyanaga, A., and Priono. (2017). Effect of bimodal soil-water characteristic curve on the estimation of permeability function. Engineering Geology, 230, 142-151.

Zhai, Q., Rahardjo, H., and Satyanaga, A. (2018). A pore-size distribution function based method for estimation of hydraulic properties of sandy soils. Engineering Geology, 246, 288-292.

Zhai, Q., Rahardjo, H., Satyanaga, A., and Dai, G. (2020). Estimation of the soil-water characteristic curve from the grain size distribution of coarse-grained soils. Engineering Geology, 267, 105502.

Zhan, T. L. T., Jia, G. W., Chen, Y. M., Fredlund, D. G., and Li, H. (2012). An analytical solution for rainfall infiltration into an unsaturated infinite slope and its application to slope stability analysis. International Journal for Numerical and Analytical Methods in Geomechanics, 37(12), 1737-1760.

Zhang, C., and Lu, N. (2020). Unified effective stress equation for soil. Journal of Engineering Mechanics, 146(2).

Zhang, C., and Lu, N. (2021). Soil sorptive potential–based paradigm for soil freezing curves. Journal of Geotechnical and Geoenvironmental Engineering, 147(9), 04021086.

Zhang, L. H., Ma, W., and Yang, C. S. (2018). Investigation on the effects of freeze-thaw action on the pore water pressure variations of soils. Journal of Offshore Mechanics and Arctic Engineering, 140(6), 062001.

Zhang, L. M., and Chen, Q. (2005). Predicting bimodal soil-water characteristic curves. Journal of Geotechnical and Geoenvironmental Engineering, 131(5), 666-670.

Zhang, H., Zhang, J. M., Zhang, Z. L. and Chai, M. T. (2016). Investigation of the pore-water pressure of saturated warm frozen soils under a constant load. Journal of Offshore Mechanics and Arctic Engineering, 138(6), 062001.

Zhang, W. J., and Lin, M. F. (2019). Evaluating the dual porosity of landfilled municipal solid waste. Environ. Environmental Science and Pollution Research, 26, 12080-12088.

Zhang, Y., and Schaap, M. G. (2017). Weighted recalibration of the Rosetta pedotransfer model with improved estimates of hydraulic parameter distributions and summary statistics (Rosetta3). Journal of Hydrology, 547, 39-53.

Zhao, C. F., Yin, Z. Y., Misra, A., and Hicher, P. Y. (2018). Thermomechanical formulation for micromechanical elasto-plasticity in granular materials. International Journal of Solids and Structures, 138, 64-75.

Zhao, C. G., Liu, Y., and Gao, Y. P. (2010). Work and energy equations and the principle of

generalized effective stress for unsaturated soils. International Journal for Numerical and Analytical Methods in Geomechanics, 34(9), 920-936.

Zhou, A. N. (2013). A contact angle-dependent hysteresis model for soil-water retention behaviour. Computers and Geotechnics, 49, 36-42.

Zhou, A. N., and Sheng, D. C. (2015). An advanced hydro-mechanical constitutive model for unsaturated soils with different initial densities. Computers and Geotechnics, 63, 46-66.

Zhou, A.N., Sheng, D. C., and Carter, J. P. (2012a). Modelling the effect of initial density on soil-water characteristic curves. Géotechnique, 62(8), 669-680.

Zhou, A.N., Sheng, D. C., Sloan, S. W., and Gens, A. (2012b). Interpretation of unsaturated soil behaviour in the stress - saturation space, I: volume change and water retention behaviour. Computers and Geotechnics, 43, 178-187.

Zhou, A.N., Sheng, D. C., and Li, J. (2014). Modelling water retention and volume change behaviours of unsaturated soils in non-isothermal conditions. Computers and Geotechnics, 55, 1-13.

Zhou, J. Z., Wei, C. F., Lai, Y. M., Wei, H. Z., and Tian, H.H. (2018). Application of the generalized Clapeyron equation to freezing point depression and unfrozen water content. Water Resources Research, 54**(**11), 9412-9431.

Zhou, Y., Zhou, J., Shi, X. Y., and Zhou, G. Q. (2019). Practical models describing hysteresis behavior of unfrozen water in frozen soil based on similarity analysis. Cold Regions Science and Technology, 157, 215-223.

Zhu, C. M., Ye, W. M., Chen, Y. G., Chen, B., and Cui, Y. J. (2013). Influence of salt solutions on the swelling pressure and hydraulic conductivity of compacted GMZ01 bentonite. Engineering Geology, 166, 74-80.

Zhu, S. R., Wu, L. Z., and Peng, J. B. (2020). An improved Chebyshev semi-iterative method for simulating rainfall infiltration in unsaturated soils and its application to shallow landslides. Journal of Hydrology, 590, 125157.

Zhuang, J., Jin, Y., and Miyazaki, T. (2001). Estimating Water Retention Characteristic from Soil Particle-Size Distribution Using a Non-Similar Media Concept. Soil Science, 166(5), 308-321.

Zou, G., Li, Y., Wang, Y., Liu, D. L., Liu, X., Li, Y., and Wu, J. (2015). Pedo-transfer functions for estimating the hydraulic properties of paddy soils in subtropical central China. Archives of Agronomy and Soil Science, 62(7), 982-993.